Fabrication and Applications of Nanoporous Alumina Membranes

Lee, Kah Peng

Award date:
2013

Awarding institution:
University of Bath

Fabrication and Applications of Nanoporous Alumina Membranes

Kah Peng Lee

A thesis submitted for the degree of Doctor of Philosophy

University of Bath

Department of Chemical Engineering

August 2013

Acknowledgements

The process of completing this thesis and PhD project has been challenging and yet rewarding. This thesis would not have been possible without the valuable assistance and encouragement from supportive colleagues, friends and family.

Firstly, I am grateful to University of Bath for funding my studentship and other financial supports for attending conferences and laboratory consumables.

I would like to first thank my supervisor, Dr. Davide Mattia for his continuous support and guidance throughout the course of this research. In addition, I have been given many opportunities to attend international meetings and be involved in collaboration work. His advice and experience sharing about development of academic career are also very much appreciated. I would also like to acknowledge my second supervisor, Dr. Tom Arnot for the constructive discussions and useful feedback on some of my work.

I would like to thank Dr. Hannes Richter for hosting my 3-month visit in Germany. This has been a great exposure and unforgettable experience. Dr. Chris Brown and Dr. Karen Edler have also generously allowed me to use their research equipment for some preliminary studies. Being a member of the faculty fellowship academy, I wish to thank Professor Julian Chaudhuri, Dr. Andrew Heath and Dr. Jeanette Muller for this opportunity of skill development. Not to forget, the other administrative and technical staff in the Department of Chemical Engineering, thank you for your support during my time at the University. In particular, this PhD project would not be possible without the help from Fernando Acosta, John Bishop, Paul Frith and Nick Gathercole.

I have received great support from my fellow colleagues in the department and also resident tutoring team. It has been a great pleasure to work with them. Also, many thanks to friends I met in Bath for the precious friendship, emotional support, care and wonderful time we have been sharing. In particular, Hannah Leese, Paulina Morawska and Li Min Chua have been sharing a lot of my up and down moments, outside and inside of work. I also cannot express how fortunate I feel for the cherished time I have been (and will be) sharing with Colin McClure.

Finally, I would like to thank my family for their constant love, despite the distance.

Fabrication and Applications of Nanoporous Alumina Membranes

Kah Peng Lee
(Supervised by Dr. Davide Mattia)

Department of Chemical Engineering, University of Bath, BA2 7AY, UK.

Abstract:

The performance of membranes in various processes is largely dependent on their morphological properties. Thus, membrane structure has been continuously optimised for different applications. Anodic alumina membranes (AAMs) exhibit self-ordered pore structure and the pore size can be tuned in the sub-micrometre range. The aim of this PhD project is to propose and develop AAMs for the applications of membrane filtration and emulsification with potential for scale-up.

In the project, the AAMs were initially fabricated in flat sheet form to optimise the process parameters to obtain membranes with a high quality of pore structure. The membrane pore diameter can be readily controlled by the anodization voltage. While AAMs are normally symmetric, by manipulating the anodization voltage, asymmetric AAMs consists of stem pores and active pores have been successfully made. After that, the flat AAMs with symmetric and homogeneous structure were used as a platform to study for surface modification and fluid transport in nano-channels. The surface chemistry and wettability of the membranes has been altered by grafting of silane molecules and carbon coating by chemical vapour deposition. Fluid flow measurement through pristine AAMs with pore diameter in the 20 nm to 100 nm range shows flow enhancement effect, experimentally for the first time, can occur in hydrophilic materials.

Subsequently, tubular AAMs were fabricated using aluminium alloy tubes, to be assessed for ultrafiltration and membrane emulsification processes. The pore structure of the tubular AAMs was analogous to flat membranes. Despite the reduced pore circularity and hexagonal arrangement originated from the presence of impurities in the starting materials, the narrow pore size distribution was not compromised. In a selectivity-permeability analysis, the asymmetric tubular AAMs outperformed most of the commercial ceramic membranes but their flux was very low when compared to polymeric membranes. A bovine serum albumin filtration test showed that complete pore blocking-cake filtration model can be used to describe the fouling behaviour. Finally, symmetric tubular membranes were used to study dead-end and cross-flow emulsification processes. The resulting emulsions show low polydispersity. Using a membrane with 25 nm average pore diameter, the obtained average droplet size was as low as 120 nm during a cross-flow emulsification. This is by far the smallest achieved average droplet size by cross-flow membrane emulsification.

Table of Contents

List of Figures

List of Tables

Abbreviations

AAM	Anodized alumina membrane
BSA	Bovine serum albumin
CFD	Computational fluid dynamics
CNT	Carbon nanotube
DLS	Dynamic light scattering
HLB	Hydrophile-lipophie balance
HPLC	High performance liquid chromatography
IFT	Interfacial tension
MF	Microfiltration
NF	Nanofiltration
MWCO	Molecular weight cut-off
o/w	Oil in water
PBR	Pilling-Bedworth ratio (for volume expansion)
PBS	Phosphate buffer saline
PCTE	Polycarbonate track etched
PDI	Polydispersity index
PEG	Polyethylene glycol
PEO	Polyethylene oxide
PP	Polypropylene
PTFE	Polytetrafluoroethylene
RO	Reverse osmosis
RSA	Rigid star amphiphile
sccm	Standard cubic centimetre
SEM	Scanning electron microsope
SiC	Silicon carbide
SPG	Shirasu porous glass (membrane)
TEM	Transmission electron microscope
TFC-PA	Thin film composite polyamide
UF	Ultrafiltration
w/o	Water in oil

Nomenclatures (SI unit)

English letters:

A	Membrane area (m^2)
B	Thickness of barrier oxide layer (m)
B_U	Anodizing ratio ($m\ V^{-1}$)
c	Empirical proportionality constant for droplet pore size (-)
C_a	Average solute concentration at both sides of membrane ($mol\ m^{-3}$)
C_m	Solute concentration at the membrane surface ($mol\ m^{-3}$)
C_p	Solute concentration of the permeate ($mol\ m^{-3}$)
C_s	Solute concentration ($mol\ m^{-3}$)
Ca	Capillary number (-)
D	Diffusivity ($m^2\ s^{-1}$)
D_d	Droplet diameter (m)
$D_{4,3}$	Average particle size by volume (m)
D_c	Interpore distance (m)
D_p	Pore diameter (m)
E	Electric field ($V\ m^{-1}$)
f	Friction factor (-)
f^0_{aw}	Frictional coefficient of solute with water in free solution ($kg\ s^{-1}\ mol^{-1}$)
F	Force (N)
F_b	Buoyant force (N)
F_i	Inertial force (N)
F_d	Drag force (N)
F_γ	Force caused by interfacial tension (N)
g	Gravity acceleration ($m\ s^{-2}$)
h	Height of droplet (m)
H	Pendant droplet shape dependent empirical parameter (-)
j	Total current density ($A\ m^{-2}$)
j_a	Anion contributing current density during anodization ($A\ m^{-2}$)
j_c	Cation contributing current density during anodization ($A\ m^{-2}$)
j_e	Electron contributing current density during anodization ($A\ m^{-2}$)
j_i	Ionic current density ($A\ m^{-2}$)
j_0	Temperature- & metal-related factor for anodization current density ($A\ m^{-2}$)
J_s	Solute flux ($mol\ m^{-2}\ s^{-1}$)
J_w	Volumetric water flux ($m\ s^{-1}$)
J_{wo}	Initial water flux ($m\ s^{-1}$)
k_x	Wall correction factor (-)
K_b	Fouling constant for complete pore blocking mechanism (s^{-1})
K_c	Fouling constant for cake filtration mechanism ($s\ m^{-2}$)
K_i	Fouling constant for intermediate pore blocking mechanism (m^0)
K_s	Fouling constant for standard pore blocking mechanism ($m^{-0.5}\ s^{-0.5}$)
L_p	Pure water permeability ($m^3\ m^{-2}\ s^{-1}\ Pa^{-1}$)
n	Number of pores (-)
$n(r)$	Pore size distribution (-)
P	Pressure (Pa)

P_c	Critical pressure for droplet formation (Pa)
P_s	Solute permeability (m s^{-1})
q	The ratio of solute radius to pore radius (-)
r	Distance along the capillary axis from the centre (m)
r_d	Radius of droplet (m)
r_p	Pore radius (m)
r_s	Solute radius (m)
R	Rejection (-)
R_a	Average roughness (nm)
R_{RMS}	Root mean squared roughness (nm)
Re	Reynolds number (-)
S	Shape factor for pendant drop (-)
S_o	Observed sieving coefficient (-)
S_a	Actual sieving coefficient (-)
S_D	Steric hindrance factor corresponds to diffusive solute flux (-)
S_F	Steric hindrance factor corresponds to convective solute flux (-)
t	time (s)
U	Anodization voltage (V)
V	Axial velocity of water (m s^{-1})
V_c	Average velocity of the continuous phase (m s^{-1})
v_s	Velocity of solute (m s^{-1})
v_w	Velocity of solvent (m s^{-1})
We	Weber number (-)
x	Depth along the membrane thickness (m)

Greek symbols:

β	Temperature- and metal-dependent parameters for anodization current density (m V^{-1})
γ	Interfacial tension (N m^{-1})
δ_m	Membrane thickness (m)
ΔP	Transmembrane pressure (Pa)
ΔP_{eff}	Effective transmembrane pressure (Pa)
$\Delta \Pi$	Osmotic pressure difference (Pa)
$\Delta \rho$	Density difference between the two liquid phases (kg m^{-3})
ε	Flow enhancement factor (-)
λ_B	Proportionality constant for thickness of barrier oxide layer (m)
λ_c	Proportionality constant for interpore distance (m)
λ_p	Proportionality constant for pore diameter (m)
μ	Absolute viscosity (Pa s)
φ	Porosity (-)
ρ	Density of continuous phase (kg m^{-3})
ρ_d	Density of disperse phase (kg m^{-3})
σ	Reflection coefficient (-)
θ	Interfacial contact angle (°)
τ_w	Wall shear stress (Pa)

1. Introduction

As an emerging technology, membrane processes have become increasingly important in various industries. A significant breakthrough for industrial applications of synthetic membranes started in the 1960s, although the earliest recorded study of membrane phenomena can be traced back to the middle of the 18th century (Fane *et al.*, 2008). As shown in Table 1.1, the initial development from the 18th to early 20th century is the discovery of various mass transport phenomena across membranes. Then, it moved onto development of membrane materials for practical applications. In particular, the membrane filters developed by Professor Zsigmondy were first commercially produced by Sartorius GmbH. These membrane filters found immediate application in the field of microbiology and assessment of safe drinking water.

As highlighted, in the 1960s, the development of asymmetric membranes greatly improves the membrane perm-selectivity, making membrane technology competitive with other separation processes. The advancement in effective packing of membranes into modular elements was an important step to bring membrane separation into large scale industry. With nearly half a century of rapid development, various membrane processes have found numerous industrial applications, which cover water and dairy purification, sea and brackish water desalination, food and beverage production, gas and vapour separation, hemodialysis, etc (Richardson *et al.*, 1997). Membrane technology has greatly enhanced the capabilities to restructure production processes, protect the environment and public health, as well as provide new technologies for sustainable growth.

As the core of membrane processes, various membrane materials have been developed for different processes. Different membrane materials offer different characteristics such as perm-selectivity, wettability, chemical resistance, biocompatibility, fouling tendency, etc., and therefore are suitable for different applications. Despite the successful implementation of membrane processes in various industries, continuous development is needed to further improve the current process efficiency and introduce novel processes for broader applications.

Table 1.1 The historical milestones of membrane technological development (pre-2000s) (Fane *et al.*, 2008).

Year	Development/discovery	Scientist(s)
1748	Discovery of osmosis phenomenon	A. Nollet
1833	The law of gaseous diffusion	T. Graham
1855	Phenomenological laws of diffussion	A. Fick
1860-1880s	Semipermeable membranes: osmotic pressure	M. Traube, W. Pfeffer, J.W. Gibbs, J.H. van't Hoff
1907-1920	Porous membrane filters	R. Zsigmondy
1920s	Research on reverse osmosis	L. Michaelis, E. Manegod, J.W. McBain
1930s	Electrodialysis membranes	T. Teorell, K.H. Meyer, J.F. Sievers
1950s	Electrodialysis, micro- and ultra-filtration, hemodialysis and ion-exchange membranes	Many
1963	**Defect-free, high flux, asymmetric reverse osmosis membranes**	**S. Loeb, S. Sourirajan**
1968	**Spiral wound RO module**	**J. Westmorland**
1977	Thin film composite membranes	J. Cadotte
1970-1980	Membrane and process improvements	Many
1980s	Industrial membrane gas separation processes	J.M.S Henis, M.K. Tripodi
1990s	Hybrid and novel membrane processes	Many

On the other hand, the recent emergence of nanotechnology and nano-fabrication techniques has led membrane material research and development into another phase, offering the opportunities of tuning the membrane structure, morphology or surface properties at the nanoscale (Lee *et al.*, 2011). This offers a new degree of freedom to optimise the membrane structure or chemistry for specific applications. As an example, the ability to control membrane pore size in sub-nanometre can be highly desirable for gas separation processes, since the gas molecules are often in Angstrom dimension. Therefore, a new class of material, metal-organic-framework with intrinsic Angstrom scale pore size has been tested for gas separation and promising results in term of selectivity and permeability have been achieved. (Bae *et al.*, 2010)

1.1 Aims and Scopes

Anodized alumina membrane (AAM) is a unique nano-structured material that exhibit self-ordered pore structure (Sulka, 2008). The pore structure can be readily tuned by altering the fabrication procedures. Despite these advantages, the usage of AAMs is still limited to small scale applications such as nano-fabrication and laboratory scale filtration. It is mainly due to the production scale of the AAM is small, expensive and limited to flat sheet configuration. Further testing for larger scale applications such as filtration and catalysis is hence restricted. Therefore, the aim of this work is to propose AAM, as a novel class of membrane material, to be used for scale-up membrane processes. To achieve this, there are two focuses of this project, namely the material development and characterisation, as well as evaluation for membrane processes, specifically ultrafiltration and membrane emulsification. The following research activities are necessary to achieve the aim and objectives of this project:

Material development and characterisation

- Fabricate AAMs in small scale, i.e. flat sheet form, to investigate the effect of various fabrication parameters on the resulting membrane morphology, i.e. pore diameter, thickness and porosity. This can lead to the development for the method to tailor the structure of AAMs by the manipulation of the fabrication conditions for different applications.
- Perform surface modification on the AAMs to alter the surface chemistry of the membranes. This is to alter the wettability of the membrane surface, which is influential for filtration and emulsification processes.
- Conduct fluid flow measurement across the membrane to investigate the effect of AAM pore structure on mass transport. This is to understand the effect of the fluid-fluid or fluid-solid interaction in mass transport at the nanoscale. A measurement rig with high accuracy and sensitivity is to be designed and constructed, given that the available sample size is small.
- Fabricate AAMs in a scalable geometry, i.e. tubular form, by using more economical starting materials. Design and improve the fabrication rig and standard procedures to obtain good quality and reproducible samples. Compare the resulting membrane morphology to that of flat membranes.

Process evaluation

- Evaluate the tubular AAMs for different membrane applications:
    - AAMs fabricated here have the pore diameter range for ultrafiltration process. The membrane properties such as mechanical rigidity,

permeability, selectivity and fouling mechanism are to be examined. Compare AAMs with other state-of-the-art commercial UF membranes.

- AAMs contain uniform nanoporous structure which is desirable for membrane emulsification but very limited research has been done on this. Using basic formulation (sunflower oil and water), conduct experiments with varied process parameters to obtain emulsions with well-defined droplet size in the nanometre range. The suitability of AAMs with other popular membranes for emulsification processes. Using the experimental results, model the process to correlate with different process conditions.

1.2 Thesis structure

This thesis is divided into eight chapters.

Following the Introduction, Chapter 2 provides a comprehensive literature background of the current work, overviewing the previous work in the relevant areas. The detailed preparation procedures of AAMs will be presented in Chapter 3. This chapter include the details of the starting materials, development of experimental rigs and also the analytical techniques used to characterise the AAMs.

The analysis of the resulting morphology of the fabricated flat AAMs can be found in Chapter 4. This provides an in-depth analysis of the effects of each process parameters to the resulting membrane morphology. This systematic study enables the tuning of membrane structure for different applications, by controlling the fabrication process parameters. Chapter 5 examines the wettability of the surfaces of flat AAMs after surface modification, and also the fluid flow measurement across the ‘nano-channels’ before and after surface modification.

In Chapter 6 and 7, tubular AAMs are introduced for the applications of ultrafiltration and membrane emulsification, respectively. In particular, the ultrafiltration performance is examined based on clean water permeability, solute rejection, molecular weight cut-off rating and fouling tendency. For membrane emulsification, both dead-end and cross-flow modes are investigated at varied process parameters, such as applied pressure, cross-flow velocity and

membrane pore diameter. In both cases, the performance of AAMs is compared with other state-of-the-art membranes.

Finally, Chapter 8 draws conclusions from the experimental findings in this work. A proposal for further investigation in this area of research will also be presented.

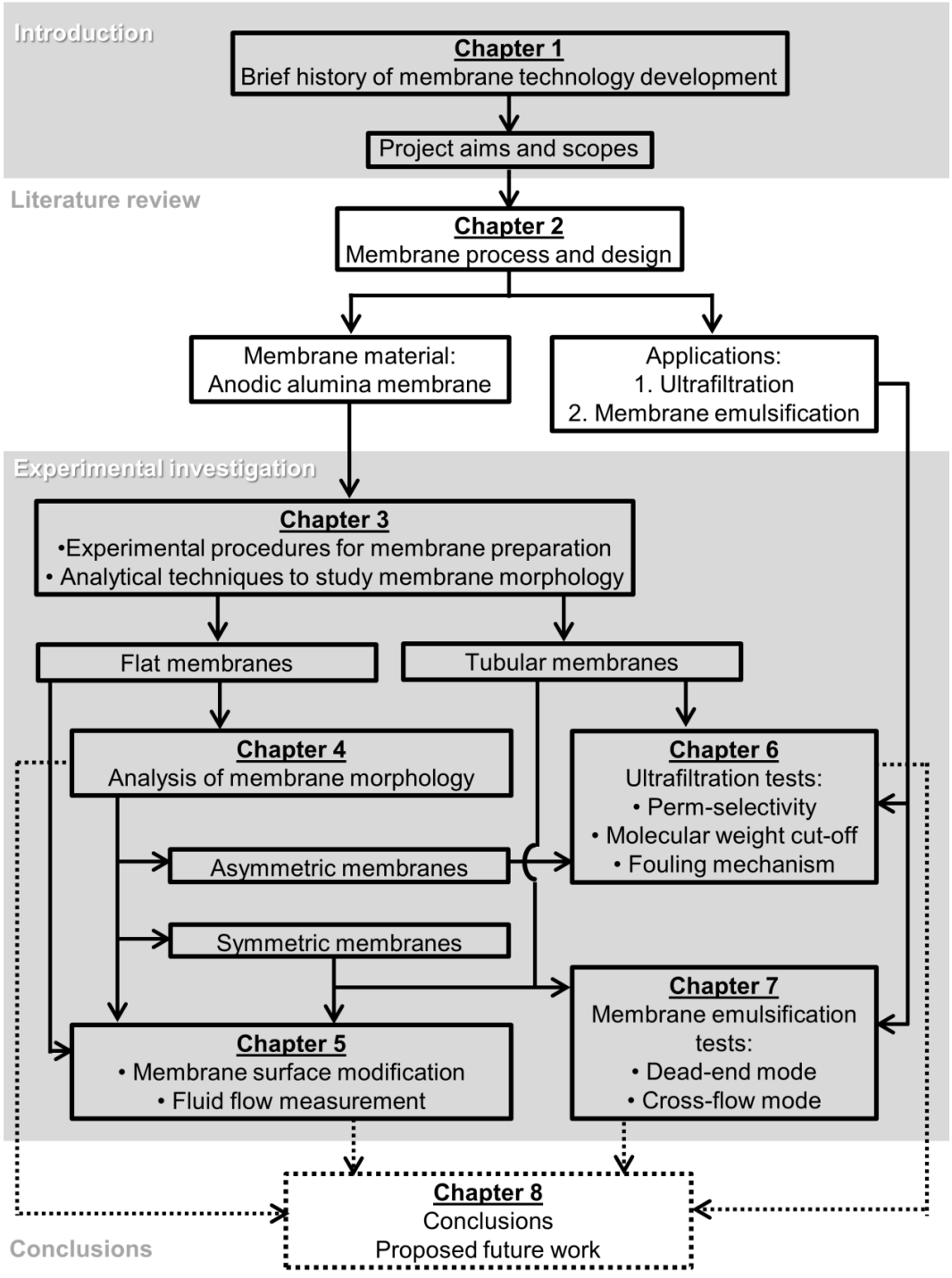

Figure 1.1 The structure of the thesis

2. Literature Review

In this chapter, the development of membranes and membrane processes is reviewed. This will lead to the recent advancement of nanostructured membranes for enhanced membrane performance. This PhD project specifically focuses on the development of anodic alumina membranes (AAMs) for filtration applications. Therefore, the fundamentals of AAM formation and previously related work are comprehensively studied in this section. This chapter also includes the theories and recent development in ultrafiltration and membrane emulsification processes. The focus is placed on the basic understanding of each component, for example, the formation mechanisms of AAMs, mass transport in ultrafiltration and droplet formation mechanism in membrane emulsification.

2.1 Membrane technology

'Membrane', a word derived from Latin word 'membrana', has different meanings in different domains. In association with separation, concentration or purification processes, a membrane is defined as a thin semipermeable layer separating two phases and able to selectively restrict the transport of one or more components, as shown schematically in Figure 2.1 (Howell *et al.*, 1993). Alternatively, a membrane is a material through that one component can pass more readily than others. The components that pass through the membrane are defined as permeate and those which are retained, form the retentate. (Mulder, 1996)

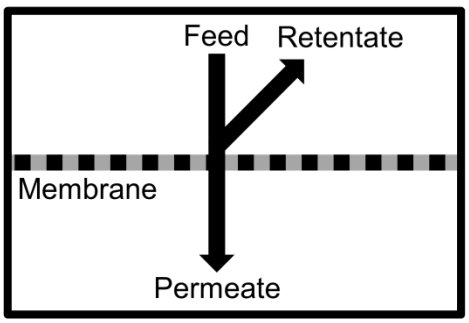

Figure 2.1 Fundamentals of membrane and membrane separation processes (adapted from Fane *et al.*, 2008).

2.1.1 Membrane processes

Membrane-based processes have been increasingly used for a range of industrial applications due to the advantages of efficient separation, continuous, automatic and economical operation at ambient conditions, compact and simple integration into existing processes as well as energy savings (Mulder, 1996). As tabulated in Table 2.1, the application and driving force of various membrane processes are listed. A separate category of novel membrane processes and hybrid processes is included to show the growth of membrane technology into applications beyond separation. Different membrane processes can also be combined together to overcome the limitations of individual systems, and to maximize the productivity of the target separation processes (Fane *et al.*, 2008).

Table 2.1 Various membrane processes (Fane *et al.*, 2008).

Conventional membrane separation processes		
Process	Driving force	Application
Microfiltration (MF)	Hydrostatic pressure difference (< 2 bar)	Retaining bacteria or solid particles (0.1 - 10 μm)
Ultrafiltration (UF)	Hydrostatic pressure difference (1 - 10 bar)	Retaining viruses and macromolecules (2 - 100 nm)
Nanofiltration (NF)	Hydrostatic pressure difference (10 - 70 bar)	Retaining divalent ions, sugar and dye (1 - 5 nm)
Reverse osmosis (RO)	Hydrostatic pressure difference (10 - 100 bar)	Retaining monovalent ions; desalination (< 1 nm)
Gas separation	Partial pressure difference (1-100 bar)	CO_2 capture from power plant and H_2 purification
Membrane distillation	Temperature and partial pressure difference	Desalination and other water purification processes
Pervaporation	Temperature & partial pressure difference (<1 bar)	Separation of ethanol from water
Dialysis	Concentration difference	Biomedical devices, e.g. hemodialysis
Electrodialysis	Electrical potential difference	Desalination, water softening, glycerin purification
New or integrated membrane processes		
Process	Description or application	
Membrane emulsification	Produce higher quality emulsions with improved energy efficiency	
Membrane contactor	Provide direct contact surface for mass transfer between phases, e.g. oxygenator	
Membrane bioreactor	Combination of UF or MF with bioreactor for efficient wastewater treatment	
Forward osmosis	Low fouling filtration process	
Reversed electrodialysis	Energy extraction when fresh water flows into sea water	
Controlled release	Delivery of active ingredients at a specified rate, e.g. drug delivery	
Electro osmosis	Microscale flow induced by voltage: lab-on-a-chip application	

2.1.2 Membrane filtration operation modes

Membrane filtration can be operated basically in two modes: dead-end and cross-flow, as shown in Figure 2.2. In dead-end filtration, the entire feed stream flows towards the membrane perpendicularly, so that the retained substances accumulate and deposit on the membrane surface (Richardson *et al.*, 1997). In cross-flow filtration, the feed stream flows parallel to the membrane surface and only a fraction of the feed stream permeates through the membranes under the driving pressure. Moving the feed flow tangentially to the membrane surface, cross-flow filtration can result in much higher permeation flux as the stream continuously removes retained materials, reducing the accumulation of retained substances. (Cheremisinoff, 1998; Baker, 2004)

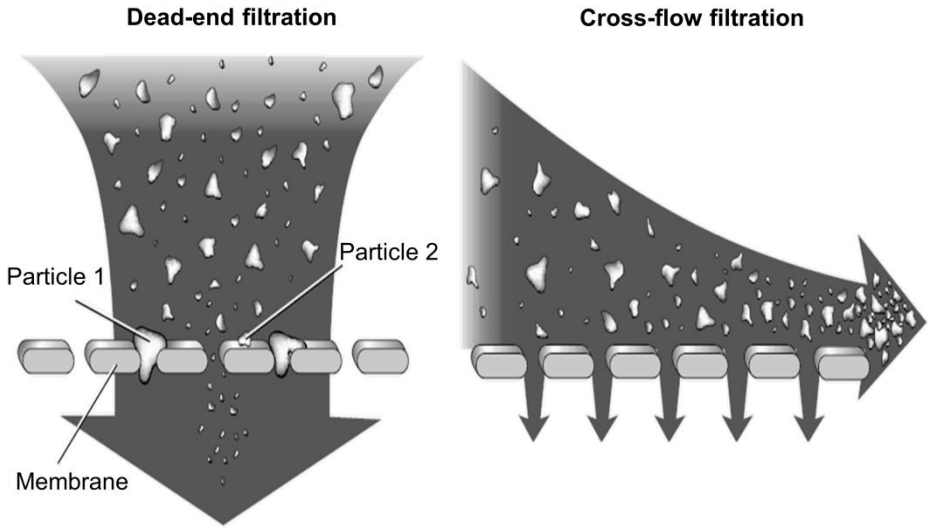

Figure 2.2 Schematics of dead-end and cross-flow filtrations. Particles may be retained by sieving when they are larger than the membrane's pore size (particle 1), or they are attached or adsorbed to the membrane surface (particle 2). Adapted from (Brainerd, 2001).

The dead-end mode tends to be used in conventional filtration processes with dilute feeds, such as filtration of surface water or secondary effluents in wastewater industry (Fane *et al.*, 2008). The absence of an axial shear along the membrane surface, which distinguishes the dead-end mode from the cross-flow mode, causes the formation of cake over the operating time (Mulder, 1996). This increases the solute/retained particle concentration of the feed and therefore the quality of the permeate will decrease with time (Belfort *et al.*, 1994). Therefore, periodic backwash is required to control the cake formation and fouling. This will

be further discussed in the membrane fouling section. Dead-end filtration is less used for industrial applications due to the instantaneous flux decline (Belfort *et al.*, 1994). However, it is effectively used for bench scale and pilot scale tests.

In contrast, cross-flow filtration provides significant built-in advantages over dead-end mode and it is widely used in most commercial large-scale pressure driven membrane processes (Porter, 1990). In practice, the flux declines with time due to concentration polarisation and membrane fouling, however, less severe than dead-end filtration (Cheremisinoff, 1998; Mulder, 1996). The flux can be optimised by modifying certain operating parameters such as the transmembrane pressure and shear rate. Nevertheless, more complex equipment and higher energy consumption is needed for cross-flow filtration to circulate the feed flow, compared to dead-end filtration (Henry, 1972).

2.1.3 Membrane configurations

For practical applications, membranes are configured into different modular forms. Generally, there are four types of membrane modules, namely flat sheet, tubular, spiral wound and hollow fibre, as illustrated in Figure 2.3. The key properties of efficient membrane modules are high packing density, enhanced hydrodynamics that reduces effect of concentration polarization and membrane fouling, low operating and maintenance costs as well as cost-efficient production (Strathmann, 2001). Table 2.2 summarises and compares the properties of each membrane modular design.

Table 2.2 Comparison of different membrane modules(Mulder, 1996).

	Flat plate	Tubular	Spiral wound	Hollow fibre
Packing density	Moderate (300-500 m^2m^{-3})	Low (<100 m^2m^{-3})	High (600-800 m^2m^{-3})	Very high (>6000 m^2m^{-3})
Investment	High	Low - high	Low	Moderate
Energy	Moderate	High	Moderate	Low
Variable costs	Average	Low- high	Low	Average
Fouling tendency	Average	Low	Average	Low - high
Cleanability	Good	Good	Difficult	Good
Replacement	Sheet	Tubes	Element	Element
Manufacturing	Simple	Simple	Complex	Moderate

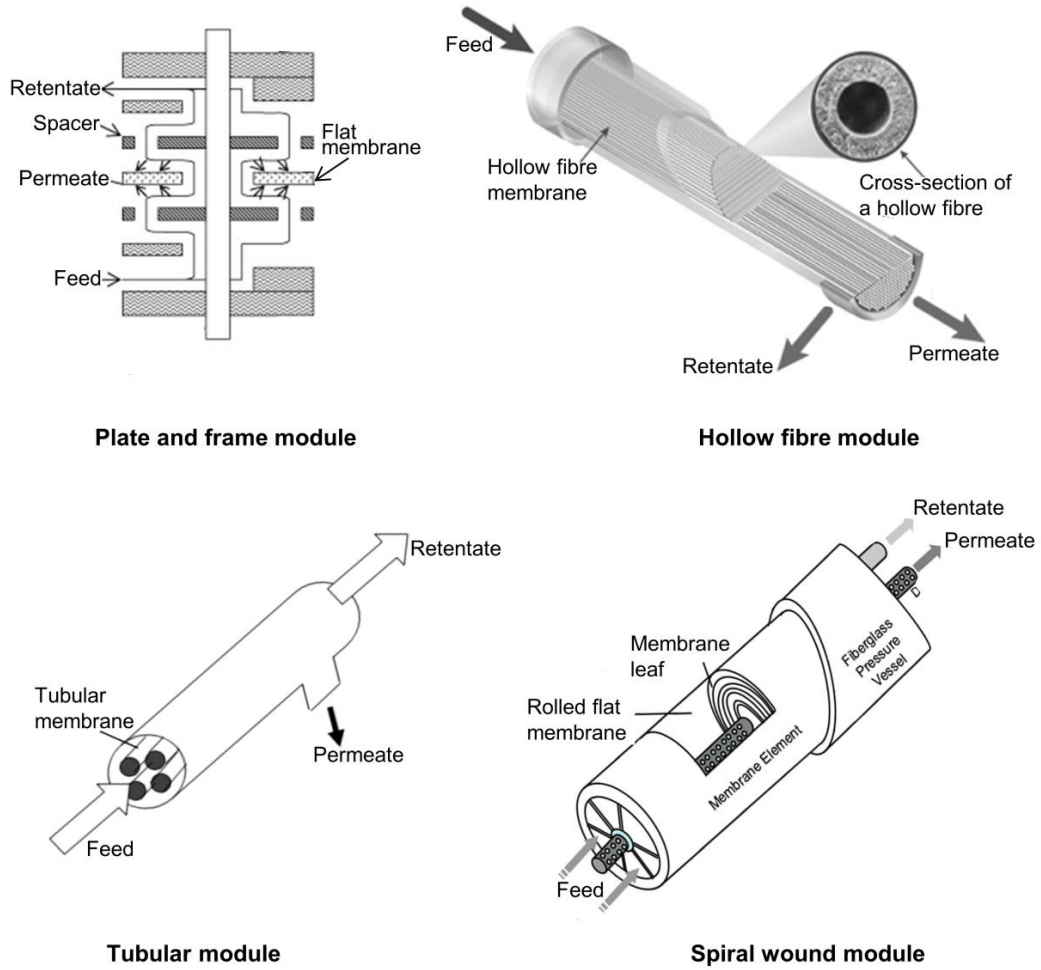

Figure 2.3 Different membrane module designs. Adapted from (Mulder, 1996).

2.1.4 Membrane material

There are many ways to classify synthetic membranes, for example, by membrane material, morphology, surface properties or preparation method (Fane *et al.*, 2008). Membranes can be made of polymers, ceramics and metals. As the core of membrane processes, membranes are developed to cater for the needs of different processes, such as high temperature operation, acidic environment or high operating pressure. Generally, the key properties of good membrane material are high selectivity, permeability and durability. (Ho and Sirkar, 1992)

Polymeric membranes lead the commercial membrane market since the introduction of membrane processes into industrial applications in the 1960s, because they are very competitive in performance and economics (Green and Perry, 2007). The consideration for suitable membrane forming polymers includes the chain rigidity, chain interactions, stereoregularity, and polarity of

their functional groups (Zeman and Zydney, 1996). Cellulose acetate, polysulfone, polyether sulfone, polyacrilonitrile, polyamide, and polyvinylidene fluoride are among the most common polymers for membrane preparation. Depending on the polymeric materials, there are different membrane preparation techniques, such as phase inversion, track etching, coating and interfacial polymerisation. Most polymeric membranes were fabricated by a form of phase inversion known as immersion precipitation (Richardson *et al.*, 1997). The ultimate membrane structure is a function of phase separation and mass transfer rate; variation of the process conditions will hence produce membranes with different separation characteristics (Strathmann and Kock, 1977). Ideally, membranes should have high porosity to ensure high fluxes and a narrow pore size distribution to ensure good selectivity (Zeman and Zydney, 1996).

A significant recent advance in the development of ceramic membranes has resulted in increasing application in commercial MF and UF processes (Richardson *et al.*, 1997). They are mostly composed of metal oxide materials, for example, alumina, zirconia and titania. Table 2.3 lists various methods to form ceramic membranes. The selection of a preparation method depends on the desired membrane structure and the intended application. For example, sol-gel route is prominent in preparing nanoporous ceramic membranes while chemical vapour deposition is well-known in producing dense ceramic membranes (Leo, 2008). Ceramic membranes are mostly used in processes under harsh operating conditions where polymeric membranes cannot be used, such as high temperature for steam sterilisation in biotechnological and food application (Fane *et al.*, 2008). Table 2.4 provides the general overview of the advantages and disadvantages offered by polymeric, inorganic and mixed-matrix membranes.

Table 2.3 Preparation methods of ceramic membranes (Leo, 2008).

Process	Materials
Thermal sintering	Alumina, Silica, Titania, Zirconia
Sol-gel	Alumina, Silica, Titania, Zirconia
Chemical vapour deposition	Silica
Pyrolysis	Silicon carbide, Silicon nitride
Hydrothermal treatment	Silicalite
Anodic oxidation	Alumina (amorphous)
Phase separation/leaching	Silica
Dynamic membranes	Zirconia (amorphous)

Table 2.4 Comparison of the properties for polymeric, inorganic and mixed-matrix membranes. Adapted from (Ismail *et al.*, 2011).

Properties	Polymeric membranes	Ceramic membranes	Mixed matrix membranes
Permeability	High	Low	High
Separation performance	Moderate	Moderate	Enhanced
Cost	Economical	Expensive	Moderate
Packing density	High	Low	High
Chemical & thermal stability	Moderate	High	High
Mechanical strength	Good	Poor	Excellent
Compatibility to solvent	Limited	Wide range	Limited
Swelling	Frequent	Free of swelling	Free of swelling
Handling	Robust	Brittle	Robust

The advancements in membrane characterization techniques have given a better understanding of, and insight into, the membrane structure at the nanoscale (Matsuura, 2001). This enables the correlation of membrane structure with membrane performance, and hence optimisation of membrane structure can bring improved membrane performance. As an example, Atomic Force Microscopy (AFM) was used to confirmed that surface roughness of an RO membrane can greatly enhance permeability, whilst at the same time maintaining high salt rejection due to an increase in effective membrane surface area (Hirose *et al.*, 1996).

The recent emergence of nanotechnology and nano-fabrication techniques has led membrane material research and development into another phase, offering the opportunities of tuning the membrane structure, morphology or surface properties at the nanoscale (Lee *et al.*, 2011). Figure 2.4 shows some examples of nano-structured membranes, with the pore size varying from UF to RO range.

Mixed matrix membranes mentioned in Table 2.4 are prepared by incorporation of inorganic nanoparticles, such as zeolite, titania, silver, silica or carbon nanotubes into the polymer matrix of membranes. The functions of the inorganic nanoparticles vary according to the material, e.g. titania nanoparticles improve

the photocatalytic property of the membrane for fouling prevention whereas silica nanoparticles can modify the morphology of the membrane to improve the permeability and selectivity (Li and Wang, 2010). Zeolite membranes represent the opportunities to fabricate membranes with uniform pore size, where the intercrystalline channel form the porous network for mass transport (Li *et al.*, 2007). Both nanotubes and aquaporin proteins were incorporated into membranes due to their high water conductivity, showing the potential for high flux membrane development (Lee *et al.*, 2011). On the other hand, NF polymeric membranes formed by rigid star amphipliles (RSA) can be controlled carefully to form smooth, uniform and ultra-thin active layer at the precision of nanometre, improving the selectivity and permeability of NF membranes (Lu *et al.*, 2007). Despite being costly, microfabrication techniques offer a route to create different pore geometries and slit-pore has been found to have exceptional separation properties (Kanani *et al.*, 2010).

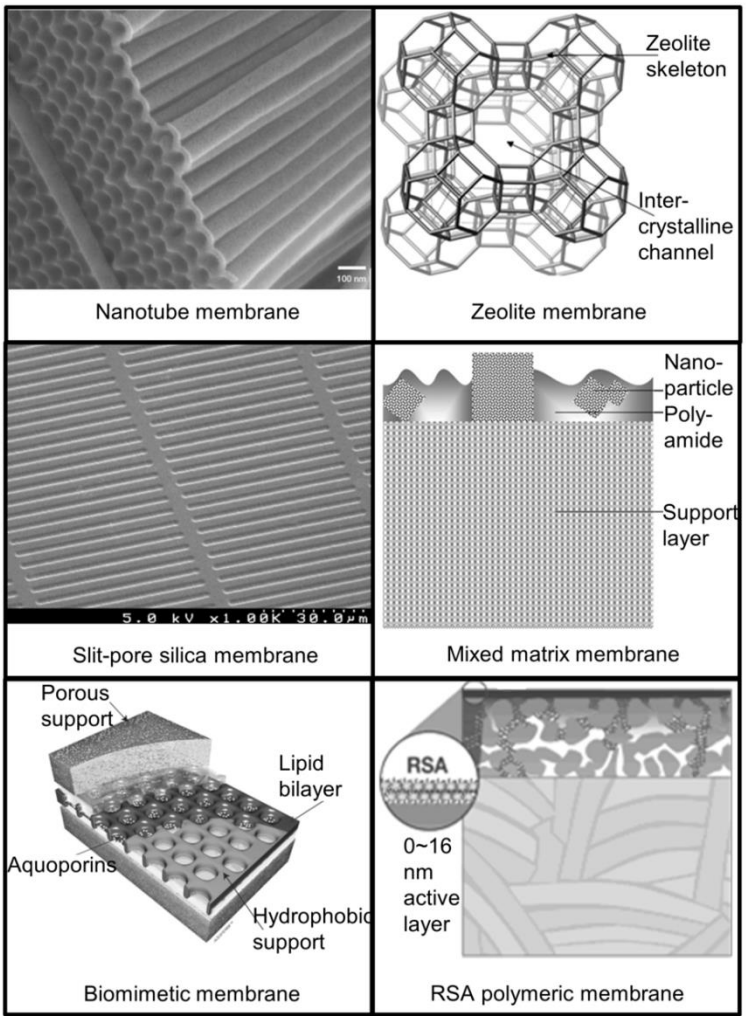

Figure 2.4 Various nano-structured membranes (Martin and Kohli, 2003; Li *et al.*, 2007; Lopez *et al.*, 2006; Jeong *et al.*, 2007; Kumar *et al.*, 2007; Lu *et al.*, 2007).

2.2 Anodic alumina membrane

Recently, nanoporous anodic alumina membranes (AAMs), self-ordered nanostructured membranes with a hexagonal arrangement of monodisperse nanopores, have become a popular template system for the synthesis of various functional nanostructures (Lee *et al.*, 2006). It has also become increasingly of interest to the research community of lab-scale molecular separation, catalysis, energy storage, drug delivery as well as biosensing (Mutalib Md Jani *et al.*, 2009). This profound interest is due to the salient features of AAMs: they can be easily fabricated and the desired structure can be easily controlled via fabrication process parameters.

2.2.1 Principles of aluminium anodization

Anodization of aluminium is a well-established process for production of protective and decorative coating on its metal surface (Diggle *et al.*, 1969). Anodization of aluminium is an electrochemical oxidation process carried out by applying a positive voltage to aluminium in an electrolyte and results in the formation and subsequent thickening of its oxide.

The formation of alumina is a highly thermodynamically favourable reaction. The spontaneous reaction of oxidation for aluminium is driven by a significant Gibb's free energy change, as shown in equation 2.1. Aluminium also readily reacts with water in aqueous environments, but yields various stable by products including alumina (Al_2O_3), aluminium hydroxide ($Al(OH)_3$, aluminium ions (Al^{3+}) and aluminate ions (AlO_2^-). For the aluminium-water system, six reactions are known to occur (Equations 2.1 to 2.6), assuming the absence of complexing agents with aluminium (Pourbaix, 1966).

$$2Al + 3H_2O \rightarrow Al_2O_3 + 6H^+ + 6e^-;\ \Delta G^o = -871\ kJ\ mol^{-1} \quad 2.1$$

$$Al^{3+} + 2H_2O = AlO_2^- + 4H^+ \quad 2.2$$

$$2Al^{3+} + 3H_2O = Al_2O_3 + 6H^+ \quad 2.3$$

$$Al_2O_3 + H_2O = 2AlO_2^- + 2H^+ \quad 2.4$$

$$Al = Al^{3+} + 3e^- \quad 2.5$$

$$Al + 2H_2O = AlO_2^- + 4H^+ + 3e^- \quad 2.6$$

The anodization of aluminium thermodynamically depends on the pH value, which is determined by electrolyte type and concentration, as well as temperature (Diggle *et al.*, 1969). When aluminium is anodized in neutral, weak acidic or basic solutions such as boric acid or ammonium borate, the growth of the oxide is thermodynamically favoured as reaction 2.1. A compact oxide layer, called a barrier-type oxide (Figure 2.5), is known to grow in these conditions (Diggle *et al.*, 1969). If aluminium is anodized in a strong acid such as perchloric acid ($HClO_4$), aluminium is ionised and dissolved into the solution. This process is known as electro-polishing of aluminium, which proceeds by the reaction 2.6 (Bockris *et al.*, 1989). In mild acidic solutions such as diluted sulphuric, phosphoric, chromic and oxalic acids, it is well-known that porous alumina grows as a result of anodization (Diggle *et al.*, 1969). It is widely believed that combination of the oxidation reaction 2.1 and the aluminium dissolution reaction 2.6 occurs that causes the formation of porous alumina (Diggle *et al.*, 1969).

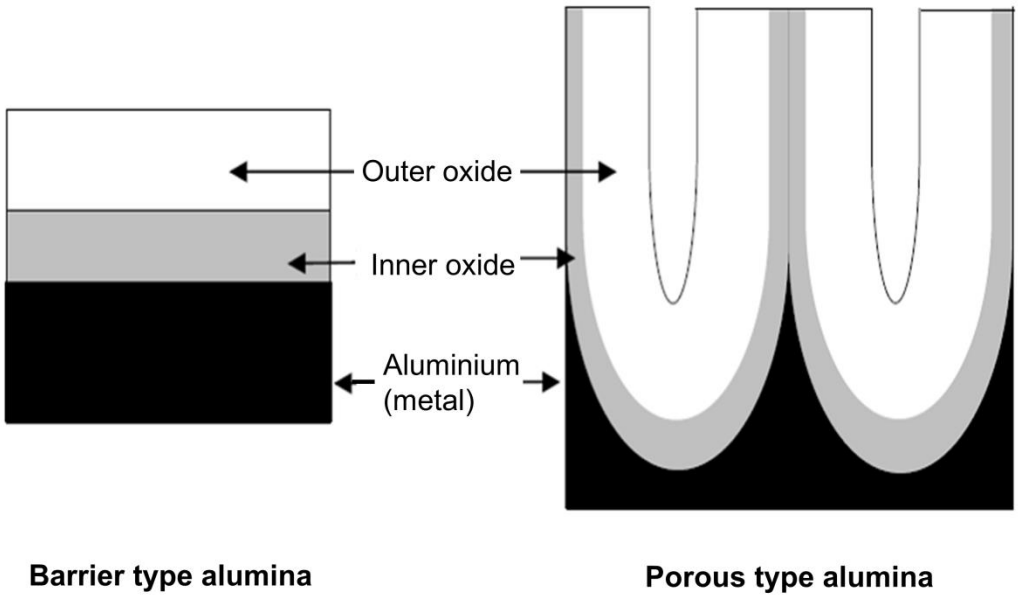

Figure 2.5 Schematic illustration of barrier type and porous type anodic alumina.

2.2.2 Kinetics and interfacial reactions

Aluminium anodization proceeds through a few kinetic steps associated with transport of different ionic species, e.g. Al^{3+} and OH^-. It has been concluded that anodic oxides grow simultaneously at both interfaces, i.e. at the metal/oxide interface by transport of hydroxide ions and at the oxide/electrolyte interface by transport of aluminium ions (Thompson *et al.*, 1987; Thamida and Chang, 2002).

As shown in Figure 2.6, firstly, hydroxide ions transfer occurs at the oxide/electrolyte by the water splitting reaction. The hydroxide ions then migrate across the oxide to the metal/oxide interface driven by the high electric field across the oxide, which is in the order of 10^6 to 10^7 V cm^{-1} (Diggle *et al.*, 1969). Finally, the hydroxide ions react with aluminium metal to form alumina. Simultaneously, aluminium metal is ionised, transferred to the oxide/electrolyte interface and reacts with hydroxide ions to form alumina. At the same time the protons present also cause the dissolution of alumina formed at the oxide/electrolyte interface.

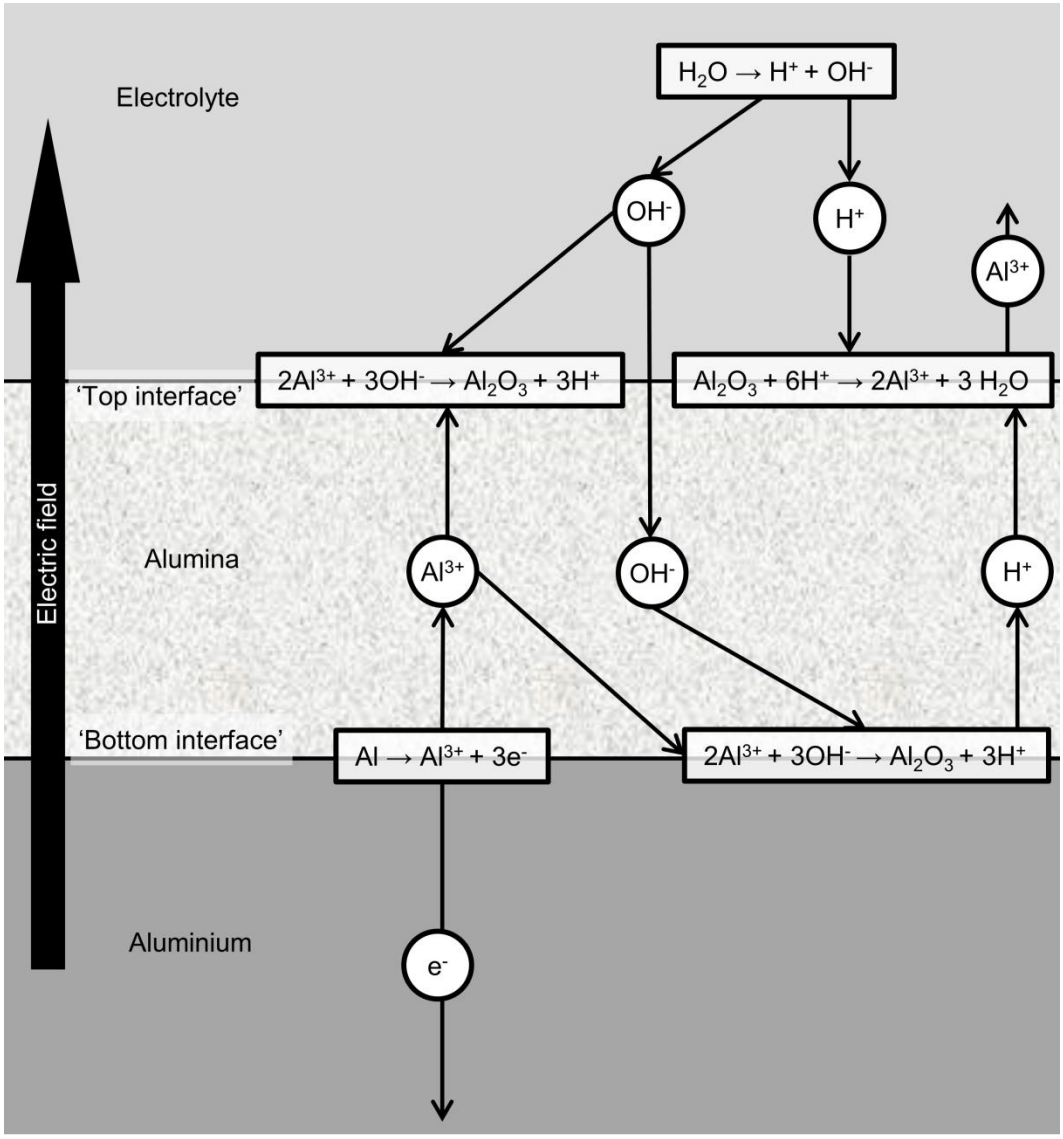

Figure 2.6 Migration of various ions during aluminium anodization and formation of oxide at both the top and bottom interfaces (Thamida and Chang, 2002).

The current density passing across the oxide film can be written as (Bojinov, 2010):

$$j = j_a + j_c + j_e \quad (2.7)$$

where j_a, j_c and j_e are the anion-contributing, cation-contributing and electron-contributing current density, respectively. Due to the low electronic conductivity of alumina, the ionic current density ($j_i = j_a + j_c$), is the predominant mode to transport the charges. The relationship between the ionic current, j_i and the electric field, E can be expressed by the Guntherschultze-Betz equation (Lohrengel, 1993):

$$j_i = j_0 e^{\beta E} \quad (2.8)$$

where both j_0 and β are temperature- and metal-dependent parameters. For alumina, the E, j_0 and β are in the range of 10^6 to 10^7 Vcm^{-1}, 1 x 10^{-16} to 3 x 10^{-2} mA cm^{-2} and 1 x 10^{-7} to 5.1 x 10^{-6} cm V^{-1}, respectively (Lohrengel, 1993). Based on equation 2.8, the rate-limiting steps of the alumina formation are determined by the ionic transport at the oxide/electrolyte interface, within the bulk oxide or at the metal/oxide interface, as described in Figure 2.6.

2.2.3 Current transient and pore formation steps

The growth of anodic porous alumina forms the basis for the fabrication of anodized alumina membranes. The structural evolution of pore formation can be monitored through the anodic current density in a potentiostatic mode, or the formation voltage in galvanostatic mode (Thompson *et al.*, 1978). Figure 2.7(a) shows schematic diagram of the transition of current density during potentiostatic anodization. Initially, the steep drop of current density represents the gradual growth of the barrier type oxide (Step 1). In phenomenological terms, the resistance of the non-conductive oxide layer is increasing due to the thickening of the oxide. At step 2, the current density passes the minimum value where the electric field is focused locally on fluctuations of the surface. Embryonic pore structures start to develop at the electrolyte/oxide interface, as illustrated by the TEM micrograph in Figure 2.7(b). Further anodizing results in electric field- and temperature-enhanced dissolution of the oxide. This leads to well-developed pore structures with a scalloped barrier layer at the metal/oxide interface (Step 3). Hence, current density increases to its peak due to the drop in overall resistance

when the porous structure is forming. In Step 4, due to pore formation competition, some pores stop growing which leads to slight decrease in field current density. Finally, the current density reaches equilibrium due to steady-state growth of pores.

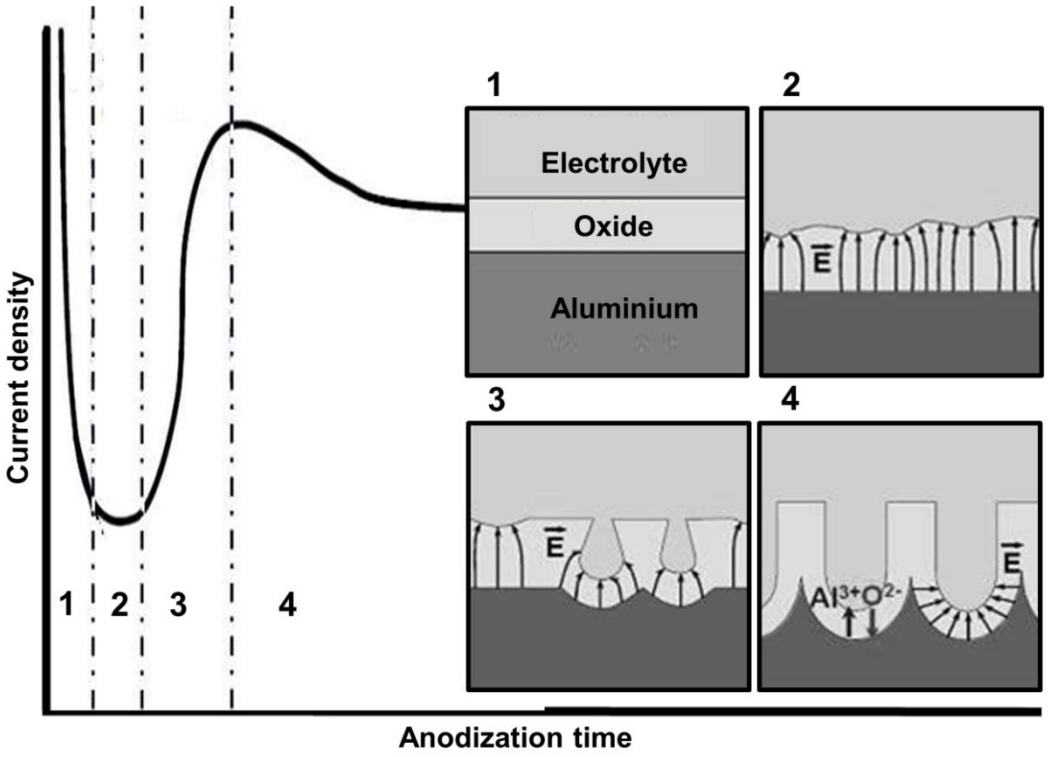

(a)

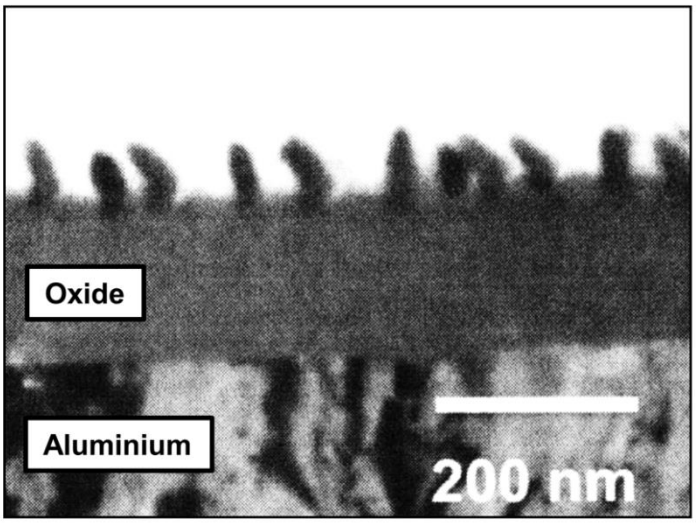

(b)

Figure 2.7 (a) Transient curve of potentiostatic current density and corresponding schematics of pore structure evolution, and (b) TEM micrograph of step 2, 150,000X magnification (Choi, 2004; Thompson *et al.*, 1978).

2.2.4 AAM structure and anodization conditions

Typically, the anodic voltages and current densities are in the range of 10 – 200 V and 0.1 – 100 mA cm^{-2}, respectively (Choi, 2004). Figure 2.8 illustrates a schematic and a SEM micrograph showing the structure of porous anodic alumina. Porous alumina consists of vertically aligned cellular and cylindrical pores with diameters in the range of 10 – 300 nm. A scallop-shaped barrier layer at the base of the pores separates the porous layer from the aluminium substrate.

While the thickness of porous anodic alumina is a coulombic function (Petukhov *et al.*, 2012), its structure largely depends on the anodization voltage. Interpore distance, pore diameter and thickness of barrier layer at the pore base are concluded to be linearly proportional to the anodization voltage and independent of the electrolytes used (O'Sullivan and Wood, 1970). The research to date has produced a set of phenomenological equations that can predict the pore diameter, D_p, interpore distance, D_c, and thickness of barrier oxide layer, B, for porous anodic alumina produced from potentiostatic anodization voltage, U (Zaraska *et al.*, 2010b).

$$D_p = \lambda_p U \tag{2.9}$$

$$D_c = \lambda_c U \tag{2.10}$$

$$B = \lambda_B U \tag{2.11}$$

where λ_p, λ_c and λ_B are proportionality constants for pore diameter, interpore distance and thickness of barrier oxide layer, respectively. Previous reports have shown these three proportionality constants are normally in the range of 0.9 – 1.3 nm V^{-1}, 2.5 – 3.0 nm V^{-1}, and 1.1 – 1.4 nm V^{-1}, respectively (Poinern *et al.*, 2011).

For a perfectly structured AAM with hexagonally packed pore arrays, the porosity, φ, can be calculated by equation 2.12a. It should be noted that, for a perfectly self-organised AAM formed during optimal anodization conditions, the porosity should be approximately 10% (Nielsch *et al.*, 2002).

$$\varphi = \frac{\pi}{2\sqrt{3}}\left(\frac{D_p}{D_c}\right)^2 \tag{2.12a}$$

For actual membranes, where there is a distribution in pore size:

$$\varphi = \sum_{i=1}^{n} \frac{\pi D_{p,i}^2}{4A} \approx \frac{n\pi D_p^2}{4A} \tag{2.12b}$$

where A is the membrane area and n is the number of pores.

Since kinetics of anodization is a function of electric field as shown in equation 2.8, the ratio of the thickness of the barrier layer to the anodic voltage is an important parameter to understand anodization kinetics. This parameter is defined as anodizing ratio, B_U, representing the ratio of the barrier layer across the anodization voltage and therefore also the growth rate of the oxide:

$$B_U = \frac{B}{U} \qquad 2.13$$

From the equations, it can be deduced that the smaller the anodizing ratio is, the higher the porous alumina growth rate is. In general, the anodizing ratio decreases as the activity of the electrolytes increases, and so the growth rate of porous oxide (O'Sullivan and Wood, 1970). The activity of electrolytes can be controlled by types of acids, concentration of acids as well as temperature. For example, sulphuric acid has a higher activity than phosphoric acid, and hence porous alumina film grows faster in sulphuric acid if other anodization conditions are similar. These characteristics are believed to arise from the coupled interplay of film formation and dissolution under the electric field which was discussed in Section 2.2.3 (O'Sullivan and Wood, 1970). In this regard, it is worth noting that the anodizing ratio of a planar barrier type oxide, which is formed in a weak electrolyte that does not dissolve alumina, is about 1.4 nm V^{-1}, larger than that of porous type oxides.

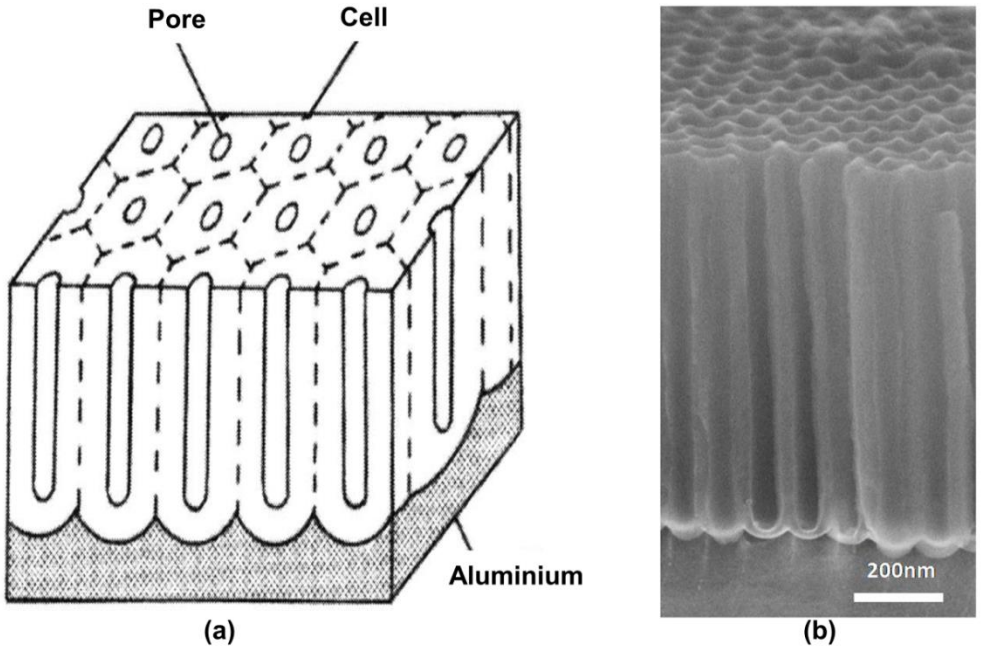

Figure 2.8 (a) Schematic of ideal porous structure of anodic alumina (Masuda *et al.*, 1997) and (b) SEM micrograph showing cross-section of an anodic alumina membrane, 65,000X magnification (Haspert, 2010).

2.2.5 AAM pore formation and pore ordering mechanism

Though great experimental progress has been made on morphology modulation, critical aspects of the formation mechanism of porous anodized alumina including pore initiation, separation, and growth, are still a subject of debate (Su *et al.*, 2012). The most widely accepted and discussed model is the field-assisted dissolution theory which was first proposed by Hoar and Mott in 1959, and later supported by experimental evidence (Hoar and Mott, 1959; O'Sullivan and Wood, 1970). More recently, a controversial field-assisted plastic flow model was proposed to question the validity of field-assisted dissolution model, and a series of experimental investigations were recently presented. (Sato, 1971; Garcia-Vergara *et al.*, 2006a). Other models suggested were mainly the variations of these two theories (Sulka, 2008).

2.2.5.1 Field-assisted dissolution model

The formation of porous type alumina by anodization has distinctive features that contrast with that of barrier type counterpart, which shed light on the mechanisms of pore formation (Diggle *et al.*, 1969). First of all, the growth of porous alumina under constant voltage anodization can, in principle, be indefinite whereas barrier alumina stops growing when its thickness limits the electric field across the oxide. Second, according to the mass balance, the mass of the metallic aluminium consumed during anodization does not fully correspond to the alumina formed (Garcia-Vergara *et al.*, 2006b). Moreover, the anodizing ratio of the barrier layer of a porous alumina, ~1.2 nm V^{-1}, is smaller than that of the barrier type alumina, ~1.4 nm V^{-1}, showing a higher alumina growth rate. Therefore, it can be deduced that a dynamic equilibrium is established between formation and dissolution of alumina at the metal/oxide and oxide/electrolyte interfaces, respectively (O'Sullivan and Wood, 1970). However, the chemical dissolution rate of alumina as represented by equation 2.4 is several orders of magnitude smaller than the formation rate at steady-state. Even the proposal of local Joule heating at the base of pores is insufficient to elevate the dissolution rate to form the dynamic equilibrium (O'Sullivan and Wood, 1970).

The field-assisted dissolution model was therefore proposed to explain the enhanced rate of alumina dissolution in presence of an electric field (Hoar and

Mott, 1959). Local variations in field strength can appear on a surface with defects, impurities, ridges, or of different geometry. This non-uniform current distribution leads consequently to the enhanced field-assisted dissolution of alumina and local thickening of the film (O'Sullivan and Wood, 1970). As shown in Figure 2.9, the strength of the electric field is greatly increased at the pore bottom due to the hemispherical scalloped geometry. Therefore, the dissolution rate of the alumina is also increased at the pore base and the overall dynamic equilibrium between dissolution and formation can be established. The experimental verification by O'Sullivan and Wood has provided fundamental understanding of the mechanism (O'Sullivan and Wood, 1970). First, it was suggested that the origin of the oxygen ions in the formed alumina are mostly from water, as confirmed by oxygen isotopic analysis. The interfacial reaction of breaking Al-O bonds in the aluminium lattice was considered as the rate-limiting step for dissolution of the oxide. The applied electric field across the oxide stretches the Al-O bond, which then lower the effective activation energy for the dissolution, and thus significantly enhance the dissolution rate of alumina.

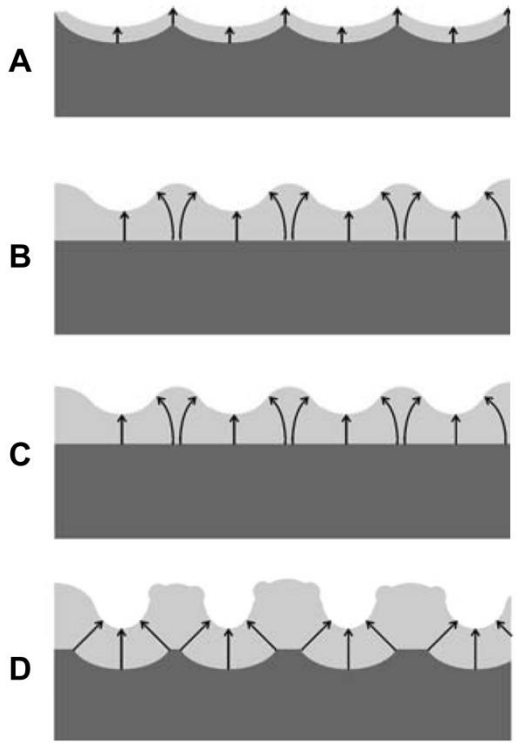

Figure 2.9 Schematic diagram showing current distribution during pore initiation and development of pores on anodized alumina (Sulka, 2008).

Based on field-assisted dissolution model, Parkhutik and Shershulsky calculated the electric field distribution in the oxide using the Laplace equation and presented the first analytical correlation between the pore structure and the electric field in the oxide (Parkhutik and Shershulsky, 1992). It was also demonstrated theoretically that interpore distance has a linear dependence on anodization voltage in a steady-state. After that, this model was modified by using a linear and weakly non-linear stability analysis to predict the critical electrolyte pH (<1.77) for pore formation (Thamida and Chang, 2002). During anodization, the volume expansion associated with conversion of aluminium into alumina will cause elastic stress whereas the curvature at the pore bottom will incur Laplace pressure. The inclusion of the effects of these stresses on the dissolution rate of the oxide for analysis will enable the prediction for the self-ordered porous structure of anodized alumina (Singh *et al.*, 2006). Unfortunately, despite showing the correlation of porous structure with anodization conditions, these analytical models shows large discrepancy in fitting the experimental data, due to the very limited information on the kinetics of the field-assisted dissolution of alumina (Friedman *et al.*, 2007).

2.2.5.2 Field-assisted plastic flow model

An oxygen tracer study of porous alumina film during anodization, which indicated an efficiency of film growth close to 60%, revealed that pore formation did not cause loss of oxygen from the film, i.e. field-assisted dissolution of alumina did not occur (Siejka and Ortega, 1977). The mechanism of loss of aluminium to the electrolyte, giving rise to the reduced efficiency, was attributed to field-ejection of Al^{3+} ions. This behaviour runs counter to the field-assisted dissolution theory and hence a field-assisted plastic flow model for pore formation in a steady-state was proposed (Garcia-Vergara *et al.*, 2006b).

In this model, it is suggested that steady-state growth of pores is maintained by plastic flow of the oxide film under growth stresses during anodization in acidic electrolytes. To verify this model, a tungsten tracer study was performed to visualise the mass transport in the porous alumina film with the aid of transmission electron microscopy (TEM). As shown in Figure 2.10, a thin layer of tungsten tracer was introduced in the middle of an aluminium substrate. As anodization continued, the tungsten tracer entered the oxide in the form of

tungsten oxide showing an evenly inverted distribution in the scalloped barrier layer. This contrasts the field-assisted dissolution theory, for which the tungsten tracer at the pore base would be expected to lie ahead of the tungsten at the cell boundary (Figure 2.10(c)), due to the proposed outward transport of the ions driven by the concentrated electric field at the bottom of the pore (Garcia-Vergara *et al.*, 2007). On the other hand, from the distribution of tungsten tracer, it can be concluded that the pores are created by flow of oxide from the pore bases to the cell walls in acidic electrolyte, as depicted in Figure 2.10(d). The oxide flow arises at the pore base is attributed to compressive stress originating from competition of strong anion adsorption with deposition of oxygen and also volume expansion due to aluminium oxidation (Houser and Hebert, 2009).

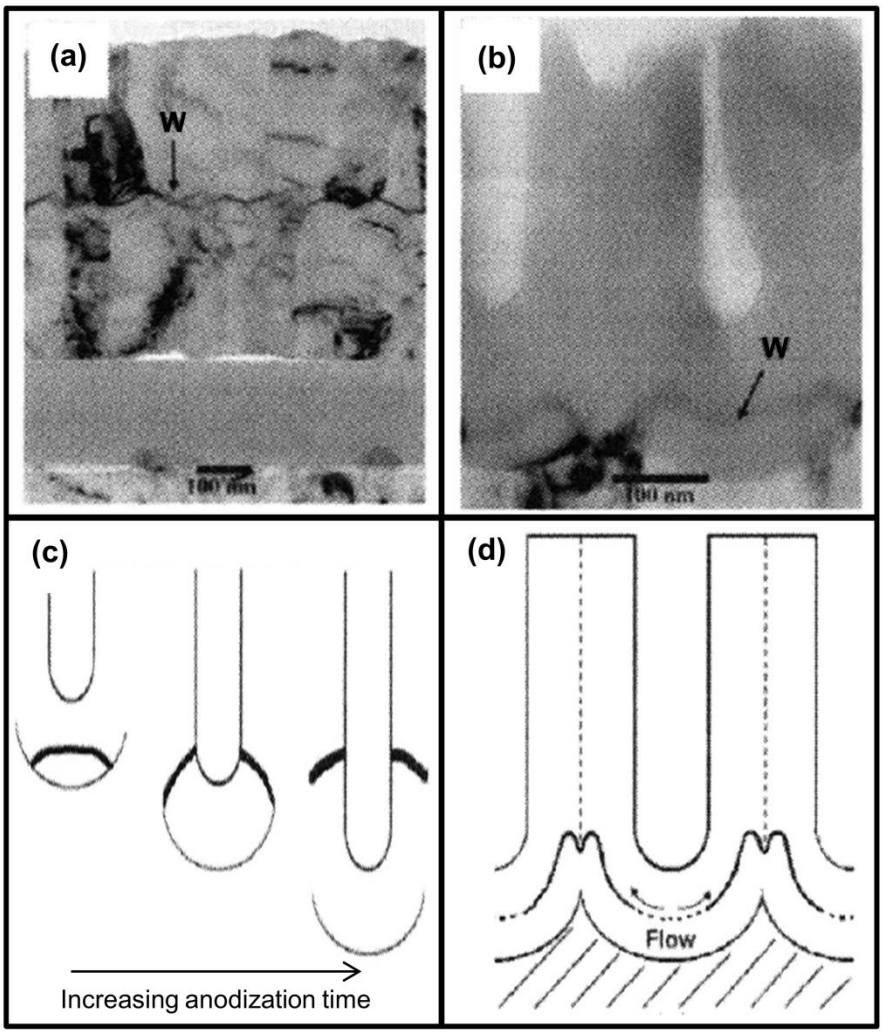

Figure 2.10 TEM micrographs showing the position of tungsten tracer in (a) aluminium before anodization and (b) anodic alumina after anodization. Proposed distribution of the tungsten tracer according to (c) field assisted dissolution mechanism or (d) plastic flow mechanism. (Garcia-Vergara *et al.*, 2006b).

To further complicate the matter, through a series of tungsten tracer studies in various electrolytes, it was concluded that steady state growth of porous alumina were governed by plastic flow of the oxide in phosphoric and sulphuric acids, and by field-assisted dissolution mechanism in chromic acid and alkaline solutions (Garcia-Vergara *et al.*, 2007). Moreover, studies using similar approach but different tracer species, i.e. neodymium and hafnium have shown opposite results which conform to the field assisted dissolution model instead of plastic flow model (Garcia-Vergara *et al.*, 2008). Therefore, a tracer study alone can neither verify the plastic flow of the oxide nor can it disprove the field assisted dissolution theory.

2.2.5.3 Pore-ordering mechanism

The structure of AAMs has been discussed in Section 2.2.4 and shown in Figure 2.8. The understanding of the mechanism for the self-organisation of pore structure is still very limited and only a few methodical experiments on this topic have been reported (Jessensky *et al.*, 1998; Nielsch *et al.*, 2002; Ono *et al.*, 2004).

The origin of self-ordering structure of AAMs is often associated with the volume expansion, also known as the Pilling-Bedworth ratio (PBR) (Xu and Gao, 2000). It is defined as the ratio of the volume of alumina, which is produced by the anodizing process, to the consumed aluminium volume. The theoretical PBR value for porous alumina formation by anodization with a 100% current efficiency is 1.6. Therefore the aluminium specimen volume increases significantly during anodization, as shown schematically in Figure 2.11.

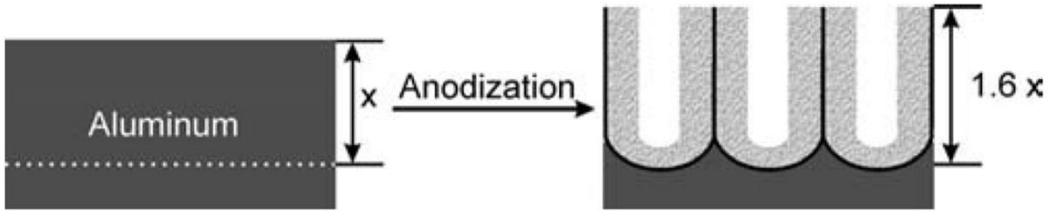

Figure 2.11 Volume expansion observed during anodization of aluminium at 100% current efficiency (Sulka, 2008).

Experimental values of PBR, however, always differ from the theoretical predictions due to lower current efficiency of anodization, and usually vary from 0.9 to 1.6 (Sulka, 2008). The first experimental measurements were performed for aluminium anodization in oxalic and sulphuric acid solutions (Jessensky *et al.*, 1998). It was concluded that increasing the anodizing potential increases the PBR and the optimal conditions of voltage and solution pH for highly self-ordered pore structure occur at moderate volume expansion (PBR = 1.22). Jessensky's theory concluded that the mechanical stress at the aluminium/alumina interface causes repulsive forces between the neighbouring pore channels, which promote the self-organisation of pore structure (Jessensky *et al.*, 1998).

Li *et al.* performed aluminium anodization in phosphoric, oxalic and sulphuric acid solutions and reported that a volume expansion of approximately 1.4 yields an optimal self-ordered structure (Li *et al.*, 1998a). Based on the volume expansion and the porosity, they calculated the compressive stress in alumina to be 4 GPa. Nielsch *et al.* measured the porosity under conditions of ordering and found that the porosity was about 10% for various optimal self-ordering anodization voltages and concentrations of electrolytes that corresponded to a volume expansion of about 1.2 (Nielsch *et al.*, 2002). By increasing the PBR to above 1.3, a decrease in the size of the ordered domains was observed. Their results were explained based on Jessensky's theory which raises a few questionable controversies (Jessensky *et al.*, 1998). First, the validity of the simple argument based on the volume expansion has been denied by many experimental findings. Second, the measured stresses are in fact tensile with most of the stress present in the aluminium beneath the alumina which is clearly in contradiction with the Jessensky's model that is based on pore repulsion due to compressive stresses (Krishnan, 2005).

Similarly, Ono et al. performed anodization in various electrolytes and reported the porosity as a function of anodization voltage (Ono *et al.*, 2004). The porosity value approaches 10% at high voltages close to the breakdown voltages (discussed in Section 2.2.6.2). Self-ordering was also observed under these conditions, and therefore it is suggested that high current density or high electric field strength is the key controlling factor for self-organisation.

2.2.6 Fabrication procedures of AAM

The unique structure of self-ordered nanoporous AAMs make them attractive for many applications. Significant efforts, therefore, have been placed to optimise the multistage techniques to prepare free standing open through anodized alumina membranes.

2.2.6.1 Pre-treatment

The quality of the aluminium substrate, e.g. surface roughness, crystalline structure and purity of aluminium have a significant impact on the resulting nano-structure formed during anodization (Sulka, 2008). Aluminium substrates always have a pre-existing oxide layer over its surface which is produced by the ambient oxygen in the atmosphere. In addition, the mechanical, thermal and chemical processing of aluminium during machining can cause the presence of surface scratches, pits, impurities and grain boundaries. These surface and intrinsic properties of the aluminium will affect the pore formation and nucleation during anodization (Zaraska *et al.*, 2010b).

Typically, the pre-treatment of an aluminium substrate begins with annealing. Annealing is a heat treatment cycle at temperatures of about two thirds of the metal melting point (400 ~ 500 °C for aluminium) to recover the metal from stress induced during machining and also reduce the microscopic defects (Benum and Nes, 1997). The results of annealing include improved dislocation ordering, reduction of dislocation density, nucleation and growth of new grains leading to the formation of a recrystallized structure, as can be seen by comparison between Figure 2.12(a) and (b). As the aluminium grain size increases during annealing, the surface roughness also increases (Figure 2.12(c) and (d)). Good hexagonal pore arrangement was obtained by anodization of aluminium annealed at 500 °C (Rahimi *et al.*, 2012).

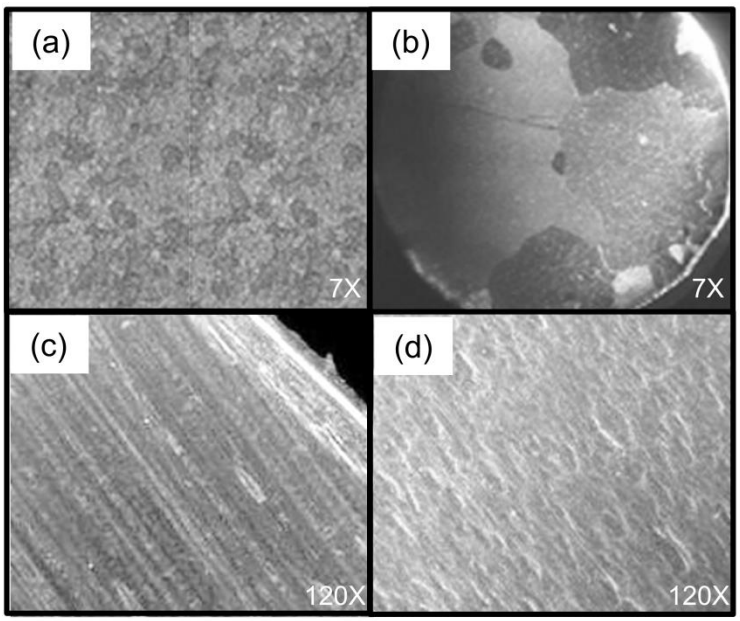

Figure 2.12 Optical micrographs of aluminium substrates annealed at (a) 200 °C and (b) 500 °C. The SEM micrographs of aluminium substrates (c) before and (d) after annealing (Rahimi *et al.*, 2012; Sulka, 2008).

Subsequently, all the organic contaminants present on the surface arising from processing and handling, are removed by ultrasonication in solvents such as acetone or ethanol. The most common defects at macroscopic scale such as roughness, cavities and cracks can prevent self-organisation of the pore structure and hence another step is required to remove them (Alam *et al.*, 2011). Relative to mechanical and chemical polishing, electro-polishing is the fastest and most reproducible method to reduce these macroscopic defects as well as the oxide layer formed with ambient oxygen (Rahimi *et al.*, 2012). A nearly perfect hexagonal close packed ordered pore arrays with big domain size was obtained from anodization on electro-polished aluminium substrate (Wu *et al.*, 2002). In addition, a significant difference in current density during anodization was found between electro-polished and non-electro-polished specimens. The higher anodization current density was attributed to the breakdown of the oxide layer on the non-electro-polished substrate, resulting in a less ordered pore structure (Wu *et al.*, 2002).

As described in Section 2.2.1, based on the mechanism of electro-polishing, temperature and activity of the acidic electrolyte (type and concentration) are the main process parameters. From the wealth of past literature, the so-called L_1 solution (a mixture of 62 ml perchloric acid, 700 ml ethanol, 100 ml butyl

cellosolve and 137 ml distilled water) has been extensively studied since it produces different nanoscale patterns under different electro-polishing conditions (Ricker *et al.*, 1996; Bandyopadhyay *et al.*, 1996). Several other electrolytes such as perchloric acid-ethanol mixture (Ma *et al.*, 2009), phosphoric acid, sulphuric acid chromic acid or a mixture of them (Jessensky *et al.*, 1998; Sulka, 2008) have also been reported. Interestingly, the perchloric acid-ethanol mixture is the most popular recipe in most cases and produces better surface smoothness among them (Jessensky *et al.*, 1998).

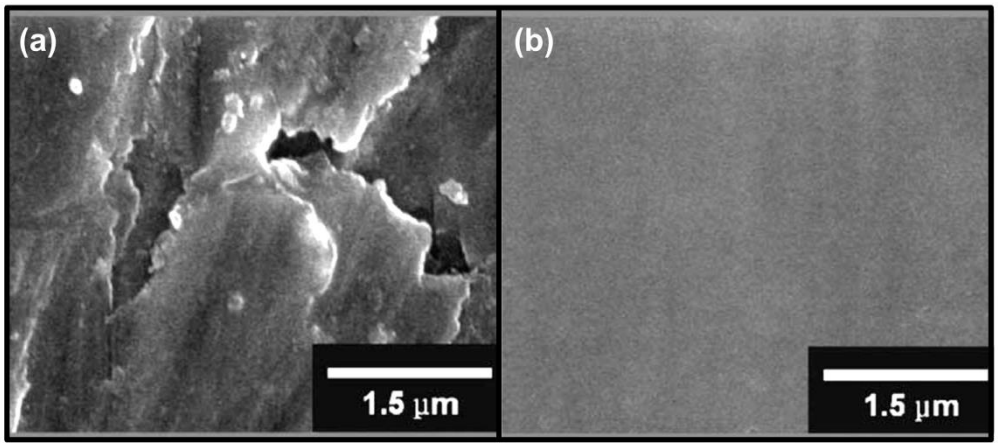

Figure 2.13 SEM micrographs of aluminium substrate (a) before and (b) after electro-polishing, 14,000X magnification (Hwang *et al.*, 2005).

2.2.6.2 Anodization

As discussed before, the self-assembled structure of porous alumina can only be obtained under some specific conditions. Generally, a mild anodization process leading to porous alumina formation is conducted at low temperatures and employs mainly sulphuric, oxalic and phosphoric acids as electrolyte (Sulka, 2008). Depending on the activity of the electrolyte, there is a certain range of voltage for each electrolyte which can be applied for anodization without burning or breakdown the formed oxide film (as shown in Figure 2.14). While the breakdown voltage depends on the electrolyte concentration, typically, breakdown voltages for phosphoric, oxalic and sulphuric acid solutions at 0.3 M concentration are 200 V, 120 V and 30 V, respectively (Krishnan, 2005).

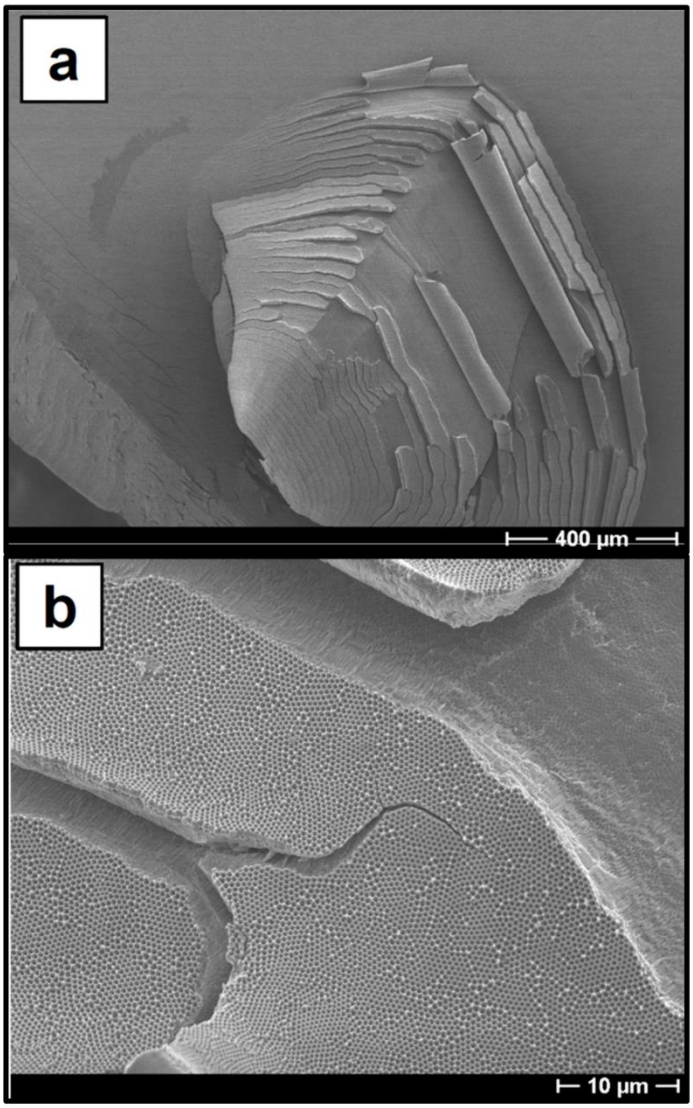

Figure 2.14 SEM micrographs at different magnification (a) 55X and (b) 1,500X showing porous alumina after electrical breakdown predominantly caused by high-field anodization (Krishnan, 2005).

In addition, there is a certain anodization voltage (self-ordering regime) for each specific electrolyte for the best arrangement of porous structure can be obtained, as shown in Figure 2.15. The degree of pore ordering is reduced when anodization is conducted at a voltage outside the self-ordering regimes. There has been a continuing effort to identify the optimal anodization conditions for different or a mixture of electrolytes. This includes acetic, citric, chromic, glycolic, malic, malonic, and tartaric acids, however, phosphoric, oxalic and sulphuric acids are the most widely used electrolytes with well-established optimal anodization conditions (Sulka *et al.*, 2002).

The initial observation of self-organisation of AAMs was originated from mild anodization (O'Sullivan and Wood, 1970). The rate of oxide growth is low in mild anodization is low due to the low current density (Jessensky *et al.*, 1998). More recently, hard anodization, also known as high-field anodization has been successfully applied for the formation of self-organised AAMs (Lee *et al.*, 2006). As tabulated in Table 2.5, the passing current density used in hard anodization is much higher than in mild anodization, resulting in high rate of alumina growth. Therefore, hard anodization enables the fabrication of thicker AAMs, albeit with the price of lower porosity. It should be noted that the application of high electric field promotes significant evolution of heat, which needs to be rapidly transferred from the sample in order to prevent burning or breakdown.

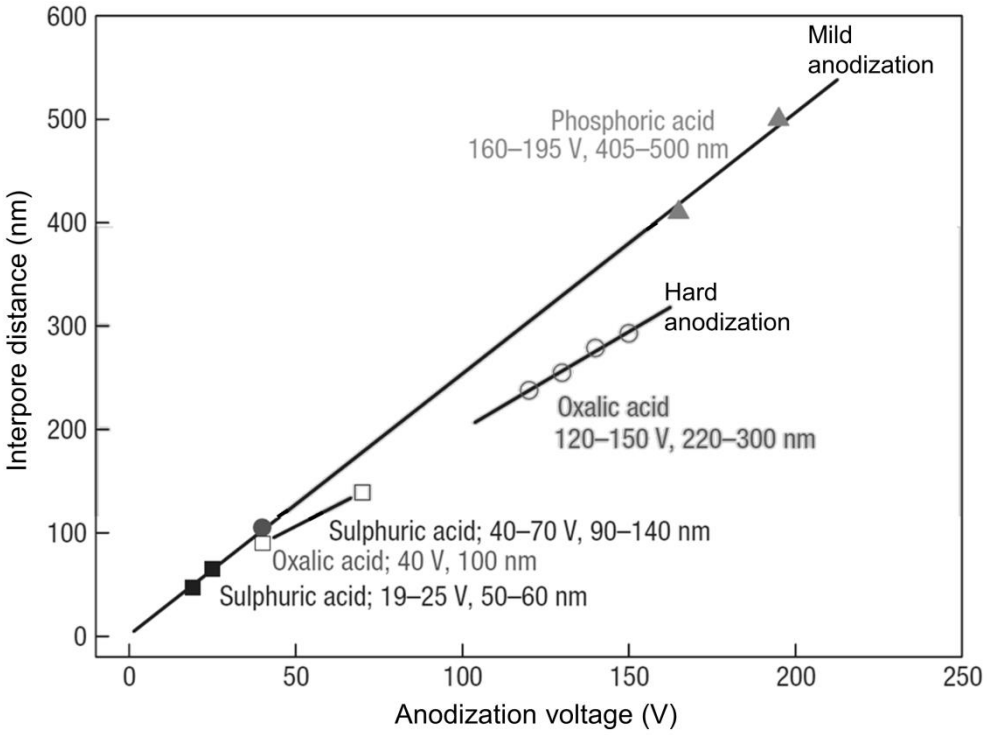

Figure 2.15 Self-ordering regimes (electrolyte, voltage and interpore distance) of various anodization conditions (Lee *et al.*, 2006). Summary of self-ordering voltages and corresponding interpore distance in conventional mild anodization in sulphuric (filled squares), oxalic (filled circles) and phosphoric acid (filled triangles). The open squares and open circles corresponds to sulphuric and oxalic acid in hard anodization.

Table 2.5 Comparison between mild and hard anodization in 0.3 M oxalic acid at 1°C (Lee *et al.*, 2006).

	Mild anodization	Hard anodization
Typical voltage (V)	40	110-150
Current density (mA cm^{-2})	5	30-250
Film growth rate (μm h^{-1})	2 (linear)	50-70 (non-linear)
Porousity (%)	10	3.3-3.4
Interpore distance (nm)	100	220-300
Typical pore diameter (nm)	40	49-59
Typical pore density (cm^{-2})	1.0×10^{10}	$1.3\text{-}1.9 \times 10^{9}$
Proportionality constant for interpore distance (nm V^{-1})	2.5	2.0
Water content (wt %)	0.3-0.4	0.1
Carbon content (wt %)	2.4	1.8
Density (g cm^{-3})	2.8	3.1

During the initial stage of anodization, before arriving to the steady-state growth of oxide, pore-branching and pore-merging occur and irregular pore shapes are formed due to the competition of neighbouring pores growth. Therefore, one-step anodization normally results in an irregular pore structure at the top, in contrast to the highly self-ordered pore bottom. To eliminate this irregularity, a two-step anodization method was proposed and this has been widely adapted nowadays to obtain reproducible highly self-ordered AAMs (Masuda and Fukuda, 1995). In the two-step anodization, after pre-treatment, a short first-step anodization is performed until the current profile reaches Stage 4, as shown in Figure 2.7, indicating the end of competition of neighbouring pore growth. The alumina film formed is then removed by wet chemical etching in a mixture of phosphoric and chromic acids, at a temperature of 60 to 80 °C. The length of the time required for the etching depends heavily on the thickness of the oxide grown, as a result of different anodization conditions. Then, a template is created for the second-step anodization with similar conditions to the first-step. Bypassing the competition stage of pore growth, an enhanced structure is achieved. Multiple cycles of pre-anodization and subsequent oxide removal have been proposed, however, the pore structure was not distinctive from two-step anodization (Li *et al.*, 1998b; Sulka *et al.*, 2002).

2.2.6.3 Post-treatment

To produce free-standing AAMs, the anodized alumina samples have to be detached from the residual non-anodized aluminium and the scalloped-shaped barrier layer at the pore bottom. The removal of residual aluminium can be achieved by using electrochemical etching in 20% hydrochloric acid, with an operating voltage between 1 and 5 V (Mata-Zamora and Saniger, 2005). However, a wet chemical method is the most widely used approached. For this procedure, the anodized sample is normally immersed in a solution made of copper (II) chloride and hydrochloric acid (O'Sullivan and Wood, 1970; Masuda *et al.*, 1997). Other solutions or liquids that are infrequently used are saturated mercury chloride (Sulka *et al.*, 2002), bromine in methanol (Liu *et al.*, 2000) and saturated copper sulphate (Ding *et al.*, 2005).

After that, the scalloped-shaped pore bottoms are exposed. Usually, the removal of barrier oxide layer, also known as pore opening is performed by wet chemical etching. To prevent pore widening at the top surface of the membrane, only the bottom side of the membrane is exposed to a phosphoric acid solution, with the opening time depending directly on the barrier layer thickness, as a consequence of different anodization conditions (Sulka, 2008). Other than phosphoric acid, chromic and sulphuric acids have also been used. The etching rate however, varies with different acids and also the temperature. Hence, an electrochemical detection method was proposed to detect the pore opening process to obtain reproducible results (Lillo and Losic, 2009).

Instead of removing the residual aluminium and barrier oxide layer separately, some electrochemical methods claim to be able to achieve reproducible, clean, one-step detachment of the porous alumina from the aluminium and barrier layer. These include barrier layer thinning process, cathodic polarization and anodic voltage pulse detachment (Nielsch *et al.*, 2000; Shaban *et al.*, 2010; Shiyong *et al.*, 2007). Nevertheless, there are drawbacks associated with the surface structure resulted from each of these methods. The barrier layer thinning achieved by a successive reduction of the anodization voltage created branched pore arrays. The AAMs obtained from anodic voltage pulse detachment have a rough pore bottom surface. More work on cathodic polarization method is needed to determine the optimum reaction conditions to obtain accurate pore-opening result.

2.2.7 AAMs of other geometry

AAMs are mostly fabricated in the form of flat membranes in most pervious work because they are mostly used for small scale applications such as nano-fabrication and drug delivery. For industrial membrane processes, it is crucial to have a membrane geometry that allows efficient packing into modular form. As such, tubular AAMs were prepared initially via the anodizing the outer surface of aluminium alloy tubes in oxalic acid (Itoh *et al.*, 1996). Then the same group of researchers improved the mechanical strengths of the tubular AAMs by anodizing the inner surface of aluminium alloy tubes (Itoh *et al.*, 1998). The later AAMs could withstand a pneumatic pressure up to 32.6 MPa as compared to 10.6 MPa in the former AAMs. This is attributed to a residual compressive stress formed in the alumina during the 'inside-out' anodization process. The effect of anodization conditions on the structural properties were found to be analogous to the flat counterpart (Belwalkar *et al.*, 2008). It should be pointed out that all tubular AAMs were prepared from alloy, instead of highly pure aluminium tube due to its low availability and high cost. Therefore, as expected, the pore structure is less uniform than AAMs prepared from highly pure aluminium (Zaraska *et al.*, 2010b).

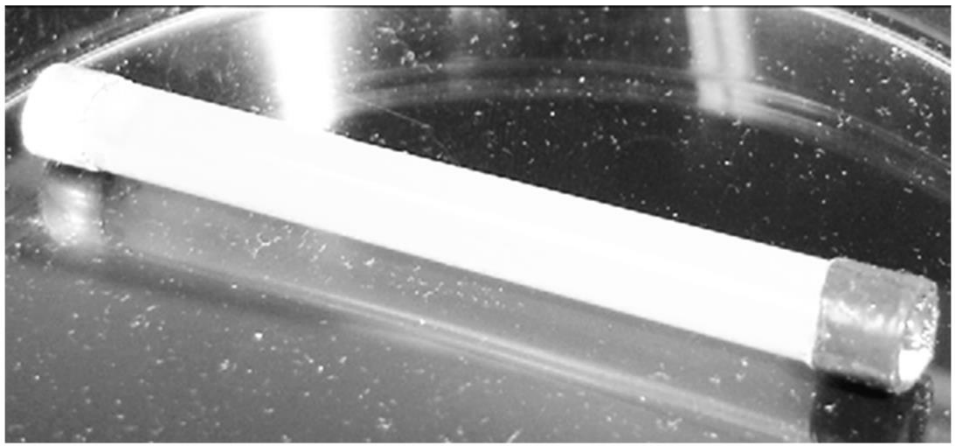

Figure 2.16 A tubular AAM sample (Belwalkar *et al.*, 2008).

2.3 Ultrafiltration

Ultrafiltration (UF) is a pressure-driven membrane separation process which rejects suspended solid particles or dissolved macromolecules (Ho and Sirkar, 1992). The selectivity of the semipermeable membranes mainly depends on the pore size, which can range from 2 nm for a tight UF membrane to 100 nm for a rather loose UF membrane (Ho and Sirkar, 1992). The applications of UF can be found in various industries, such as biochemical process, water treatment and food industry. It is due to its effectiveness and efficiency in purification, concentration, fractionation or removal of macromolecules or fine particle suspensions at ambient temperature (Porter, 1990). As shown in Figure 2.17, the state-of-the-art commercial UF membranes are asymmetric in structure, i.e. a thin active layer that has smaller pore size that is responsible for the selectivity on top of a thicker support layer which is responsible for mechanical robustness (Ho and Sirkar, 1992). In contrast to symmetric membranes, this structure enables good separation without compromising the solvent permeability.

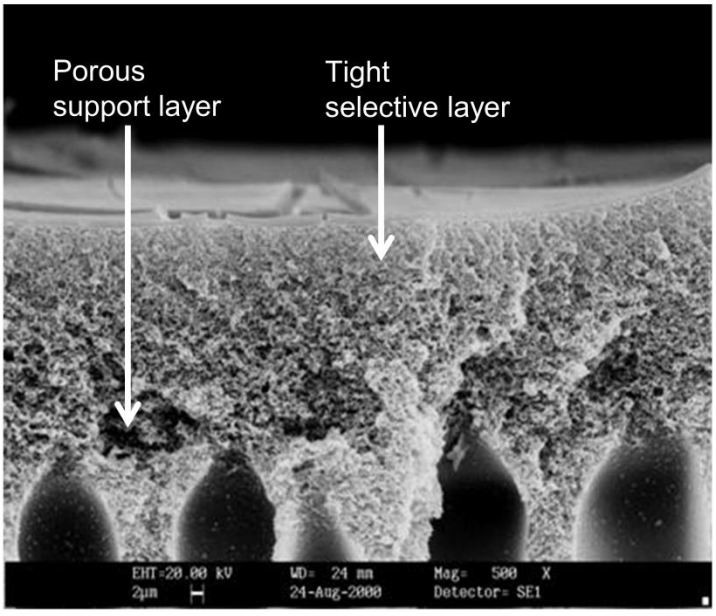

Figure 2.17 SEM micrograph of an asymmetric UF membrane structure, 900X magnification.

UF membranes are manufactured in various materials, tailored for different applications. They are mostly polymeric, such as polysulfone (PS), polyethersulfone (PES), cellulose acetate (CA), polyacrylonitrile (PAN), Polyvinylidene fluoride (PVDF), etc. Polymeric membranes offer a number of

advantages such as low fabrication cost, high permeability and good selectivity as discussed in Table 2.4 before. However, polymeric UF membranes suffer from severe fouling and swelling, and often cannot sustain harsh or extreme operating conditions, i.e. high temperature, acidic or alkaline environment (Porter, 1990). In contrast, ceramic membranes made of metal oxides are increasingly popular for harsh operating environment, despite their higher cost and lower permeability. To compare the performance of various UF membranes commercially available, a graphical framework has been developed based on permeability-selectivity analysis using bovine serum albumin (BSA) as a model sieving solute (Mehta and Zydney, 2005). As can be seen in Figure 2.18, results for a number of different UF membranes fall along, below, or slight above, a theoretical 'upper bound' curve that reflects the current state-of-the-art performance of commercial UF membranes. This theoretical 'upper bound' is based on the modelling analysis of solute and solvent transport through membranes, which is discussed in the following subsection. The permeability-selectivity trade-off curve clearly shows that polymeric membranes outperform commercial ceramic ones, particularly in term of permeability. This is mainly caused by the lower porosity to thickness ratio of ceramic membranes.

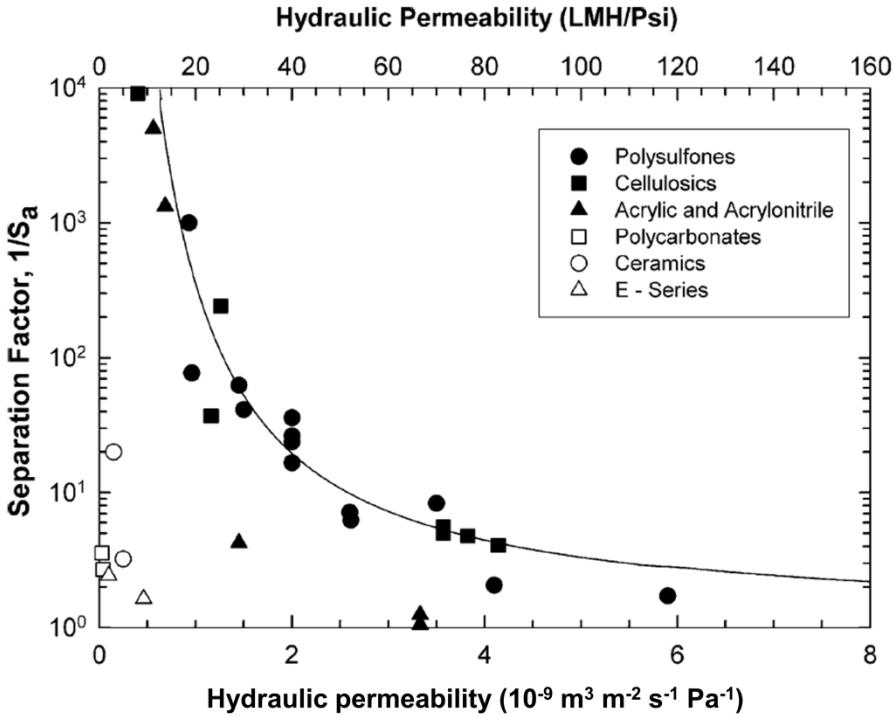

Figure 2.18 Permeability-selectivity framework developed to compare various commercial UF membranes (Mehta and Zydney, 2005).

2.3.1 Membrane properties

In contrast to RO or NF membranes, UF and MF membranes are widely accepted to be porous (Zeman and Zydney, 1996). Therefore, of special importance for UF and MF membranes are the pore statistics, e.g. pore size, pore density and bulk porosity, which are important parameter determining their use in separation. Except for some specially designed membranes with uniform pore sizes, most UF membranes have a pore size distribution. There are a number of techniques developed to determine membrane pore size (distribution) (Ho and Sirkar, 1992):

- Bubble point-breakthrough pressure method measures the pressure required to force one immiscible fluid through the pores of a membrane previously filled with another immiscible fluid. The name of the method comes came from the original approach of placing a water-filled membrane with air impingement from below. Based on Young-Laplace, the largest pores open at lowest pressure; thus gradual increment of air pressure and monitoring of air passage can provide an estimation of pore size distribution (Capannelli *et al.*, 1983). Mercury porosimetry and liquid-liquid displacement are variation of this method. This method requires relatively high pressure for UF membrane range. Therefore, this can either compact polymeric membranes causing distortion of the pore structure, or cause breakage or cracks in ceramic membranes.

- Permporometry is a method where a mixture of non-condensable gas and condensable vapour is fed to a porous membrane and the permeation rate of non-condensable gas is measured (Cuperus *et al.*, 1992). As stated in Kelvin's theory, in a capillary having a small pore size, vapour condenses at vapour pressure lower than the saturated vapour pressure. It is clear that capillary condensation occurs in a smaller pore at lower relative pressure of vapour. Since the condensed vapour can be assumed to block the permeation of non-condensable gas, it is possible to estimate pore size distribution by measuring the permeation rate as a function of the vapour pressure of condensable gas in the feed stream. This method has been claimed to accurately characterise the interconnecting active pores, which are responsible for actual membrane performance.

- Direct observation by electron microscopy can only be used with dry membranes to measure surface porosity and pore size. This method is coupled with image analysis and statistical techniques to quantify the pore size distribution (Martínez-Villa *et al.*, 1988). This method is limited in resolution of the microscopy, especially imaging process can be challenging at high magnification, due to the non-conductive nature of polymeric and ceramic membranes.

- Gas adsorption method, by measuring the partial pressure on curved surface, can analyse pore size distribution based on Kelvin equation (Dollimore and Heal, 1978). This method however cannot eliminate the contribution from 'dead-end' pores that has no significance on transport characteristics.

- Nuclear magnetic resonance method can be used to determine the pore size distribution of water-saturated membranes via spin-lattice relaxation measurements (Glaves and Smith, 1989). This method is, however, very uncommon due to the difficulty in determining the constants needed to correlate the relaxation time with pore radius.

- Solute retention method is by far the most widely used method for UF membranes. This method characterises the pore size of a given UF membrane by measuring the rejection of various solutes of increasing molecular weight or hydrodynamic sizes. Since the early applications of UF membranes were targeted at separation of macromolecules, which are often characterised by their molecular weight, the term molecular weight cut-off (MWCO) is widely used in the industry and defined as the molecular weight above which rejections are expected to be higher than 90% (Sarbolouki, 1984). Figure 2.19 is a graphical representation of solute rejection data for ideal and real membranes, which are also commonly known as MWCO curves. The sharp pore size distribution shown for the ideal membrane is never seen in practice. Unfortunately, there is not any standard procedure established for MWCO tests, e.g. the molecular weight and types of solutes, transmembrane pressure, the filtration time, the stirring, etc.

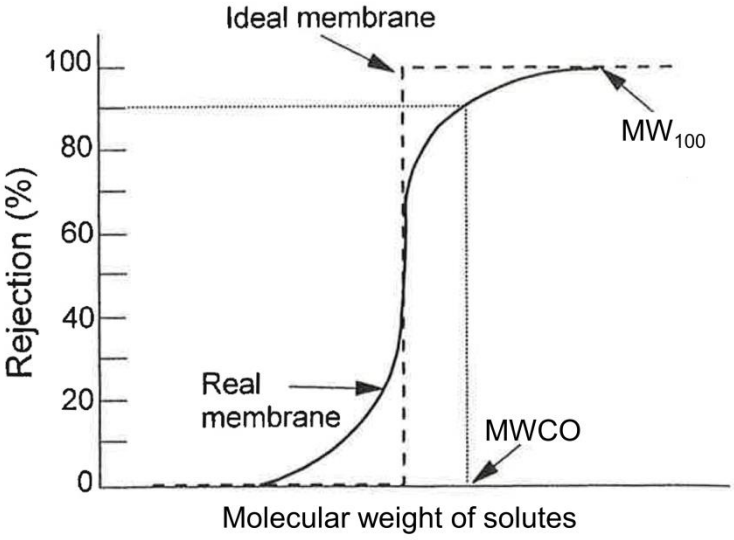

Figure 2.19 A typical example of a molecular weight cut off curve. Ideal membrane with monodispersed pore diameter has a sharp cut-off curve where total rejection is obtained for any solute larger than the pore diameter. In reality, membranes have a range of pore diameter and hence the MWCO curve provide ratings of ideal and real membranes (Cheryan, 1998).

2.3.2 Mass transport in ultrafiltration membranes

Several mathematical models have been developed in the literature to describe the transport mechanism through membranes. Ultrafiltration, due to the porous structure, has most frequently been visualised as sieve filtration (Cheryan, 1998).

2.3.2.1 Solvent flux and flow enhancement

Kedem and Katchalsky phenomenologically derived the following solvent transport equation based on non-equilibirium thermodynamics (Kedem and Katchalsky, 1958):

$$J_w = L_p(\Delta P - \sigma \Delta \Pi) \qquad 2.14$$

where J_w is volumetric water flux, L_p is pure water permeability, ΔP is the transmembrane pressure, σ is the reflection coefficient which represents rejection capability and $\Delta \Pi$ is the osmotic pressure difference. To simplify further derivation, the effective pressure difference, ΔP_{eff} is defined as:

$$\Delta P_{eff} = (\Delta P - \sigma \Delta \Pi)$$

Fluid flow through each pore is conventionally described by the Hagen-Poiseuille equation. For an idealised UF membrane consisting of a parallel array of cylindrical pores having a distribution of pore radii, the pure water permeability can be written as (Mehta and Zydney, 2005):

$$L_p = \frac{\varphi}{8\mu\delta_m} \frac{\int_0^\infty n(r_p) r_p^4 dr_p}{\int_0^\infty n(r_p) r_p^2 dr_p} \quad 2.15$$

where δ_m is the membrane thickness, μ is the solvent viscosity, r_p is pore radius and $n(r_p)$ is the pore size distribution. If mean pore radius is used, equation 2.15 can be simplified as (Mulder, 1996):

$$L_p = \frac{\varphi \bar{r}_p^2}{8\mu\delta_m} \quad 2.16$$

The Hagen-Poiseuille equation was derived based on the assumption of non-slip boundary condition, i.e. zero velocity at the pore wall. While the equation has been widely used and validated for macroscopic hydrodynamics, recently, a lot of experimental and simulation results have provided evidence of slip behaviour, especially at the nanoscale. In particular, there are many experimental work reported a so-called flow enhancement effect being observed in carbon nanotubes (CNTs) with diameter from 1 to 44 nm, in the order of 10 to 10^5 (Majumder *et al.*, 2005; Holt *et al.*, 2006; Whitby *et al.*, 2008; Qin *et al.*, 2011; Du *et al.*, 2011). To take this observed enhanced flow into account, a flow enhancement factor, ε, has been defined as a measure of the deviation of experimental results from the no-slip Hagen-Poiseuille equation:

$$\varepsilon = \frac{Q_{exp}}{Q_{HP}}$$

where Q_{exp} is the numerically or experimentally observed volumetric flow rate whereas Q_{HP} is the no-slip theoretical volumetric flow rate.

It is generally accepted that the origin of the high flow rates observed resides in the unfavourable interaction of water with the hydrophobic surface of CNTs. This would result in the slippage of water molecules at the CNT wall, leading to high flow velocities. Water slip on hydrophobic surfaces is a well-documented phenomenon, whereas its occurrence on hydrophilic surfaces is still a matter of debate. While simulation results show the flow enhancement effect in silicon and silicon carbide nanotubes, as well as water slippage on magnesium oxide surface, there is still a lack of experimental evidence (Joseph and Aluru, 2008; Khademi and Sahimi, 2011; Ho *et al.*, 2011). It has been argued that the

discrepancy of Hagen-Poiseuille equation in estimating nanoscale flow is mainly due to the absence of an explicit term that takes liquid-solid wall interaction into account (Mattia and Calabrò, 2012). Therefore, a mathematical model was developed, which makes explicit the contribution of tube characteristic dimensions (radius and length, for membrane the length is equivalent to its thickness) and of the solid-liquid interaction parameters (surface diffusion, D_s and work of adhesion, W_A) to the flow enhancement effect (Mattia and Calabrò, 2012):

$$\varepsilon \approx 8\mu \frac{\delta_m}{r_p^2} \frac{D_S}{W_A} \qquad 2.17$$

This model has shown the capability to explain the flow enhancement experimental results mentioned earlier.

2.3.2.2 Solute flux and rejection

According to the transport equations obtained from non-equilibrium thermodynamic model, the solute flux, J_s can be written as (Kedem and Katchalsky, 1958):

$$J_s = P_s\left(C_m - C_p\right) + (1-\sigma)J_w C_a \qquad 2.18$$

where P_s is the solute permeability, C_m, C_p and C_a are the concentrations at the membrane surface, of the permeate and of an average for both sides the membrane, respectively. Both P_s and σ can be determined by empirical curve-fitting as described elsewhere (Nakao and Kimura, 1981). Via integration of the differential form of equation 2.18 across the membrane thickness, the real rejection, R of the membrane can be obtained (Spiegler and Kedem, 1966):

$$R = 1 - \frac{C_p}{C_m} = \frac{\sigma(1-F)}{(1-\sigma F)} \qquad 2.19$$

where

$$F = e^{\left[-\frac{J_W(1-\sigma)}{P_S}\right]}$$

To account for transcapillary transport, ‘pore theory’ that describes solute flux as a combination of filtration and diffusion flows was proposed (Pappenheimer *et al.*, 1951). Both these flows are impeded by steric hindrance at the pore/capillary entrance and frictional forces within the pores. Then, this theory was modified to adopt Haberman and Sayre’s correction of the frictional forces to relate to Kedem

and Katchalsky non-equilibrium thermodynamic model described above (Kedem and Katchalsky, 1958; Haberman *et al.*, 1958).

When spherical solutes move within a pore filled with liquid, the drag force acting on each solute, F_{drag} is enhanced by the presence of the pore wall. F_{drag} can be expressed as:

$$F_{drag} = 6\pi\mu r_s \frac{v_s - v_w g(q)}{f(q)} \quad 2.20$$

where $q = \frac{r_s}{r_p}$, r_s is the radius of solute, v_s and v_w are the velocity of solute and solvent, respectively. *f(q)* and *g(q)* are called the wall correction factors for diffusive and convective flows, respectively. They were derived theoretically by Haberman and Sayre, 1958 based on the motion of fluid spheres in a long cylinder:

$$f(q) = \frac{1 - 2.5105q + 2.0865q^3 - 1.7068q^5 + 0.72603q^6}{1 - 0.75857q^5} \quad 2.21$$

$$g(q) = \frac{1 - \frac{2}{3}q^2 - 0.20217q^5}{1 - 0.75857q^5} \quad 2.22$$

To consider the frictional effect, two steric hindrance factors, S_F and S_D, corresponding to convective and diffusive solute flux, respectively, were introduced. Subsequently, the solute flux can be expressed as (Renkin, 1954):

$$J_s = -Df(q)\frac{dC_s}{dx} + v_w C_s g(q) - \frac{\bar{V}_s}{f^0_{aw}} C_s f(q) \frac{dP}{dx} \quad 2.23$$

where D is the diffisivity, C_s is the solute concentration, x is the depth along the membrane thickness, f^0_{aw} is the frictional coefficient of solute with water in free solution and P is the pressure.

It was assumed that water flows through the capillary according to Poiseuille's law:

$$v_w = V\left[1 - \left(\frac{r}{r_p}\right)^2\right]$$

where V is the axial velocity of water and r is the distance along the capillary axis. Furthermore, the third term on the right side of equation 2.23 is negligible because $V_s C_s$ is very small. Thus, equation 2.23 can be simplied as (Verniory *et al.*, 1973):

$$J_s = DS_D f(q)\left(\frac{\varepsilon}{\delta_m}\right)(C_m - C_p) + S_F g(q) J_w C_a \quad 2.24$$

Comparing equation 2.24 with equation 2.18, the following relations can be obtained:

$$P_s = DS_D f(q)\left(\frac{\varepsilon}{\delta_m}\right)$$

$$\sigma = 1 - S_F g(q)$$

where

$S_D = (1-q)^2$ and

$S_F = (1-q)^2(1+2q-q^2)$

This model developed based on 'pore theory' has been successfully used to model the transport of macromolecules such as dextran and PEG in symmetric AAMs (Ichimura *et al.*, 2000).

2.3.3 Membrane fouling

Flux decline (or increased transmembrane pressure) and changing of selectivity are often observed during UF operation. This is as a result of concentration polarisation and fouling, with the former increasing the membrane surface concentration and the latter providing a secondary barrier for solvent permeation (Field, 2010). Fouling is defined as a process resulting in loss of performance of a membrane due to the deposition of suspended or dissolved substances on external surfaces, at the pore openings or within the pores (Koros *et al.*, 1996). The occurrence of fouling depends on the solute and membrane property, which determines the solute-membrane interaction, as well as the hydrodynamic condition used during operation. Fouling may take the following forms (Bacchin *et al.*, 2006):

- Adsorption occurs when specific interactions between the membrane and solute exist. A monolayer of particles and solutes can form even in the absence of permeation flux, leading to an additional hydraulic resistance. If the degree of adsorption is concentration-dependent, then concentration polarization exacerbates the amount of adsorption.

- Pore blockage can occur when filtering because the solute size is larger than the membrane pore size. This leads to a reduction in flux due to the closure or partial closure of pores.

- Deposition of particles can grow layer by layer at the membrane surface, leading to a significant additional hydraulic resistance. This is often referred to as a cake resistance.

- Gel formation occurs, for certain macromolecules, when the level of concentration polarization is severe. The gel is formed in the immediate vicinity of the membrane surface, for example, a solution of highly concentrated proteins.

The effects of such fouling types on the membrane pore size distribution and membrane flux are schematically illustrated in Figure 2.20. Based on the fouling mechanism, different mathematical models have been proposed to describe the fouling phenomena and predict the membrane flux (Field, 2010).

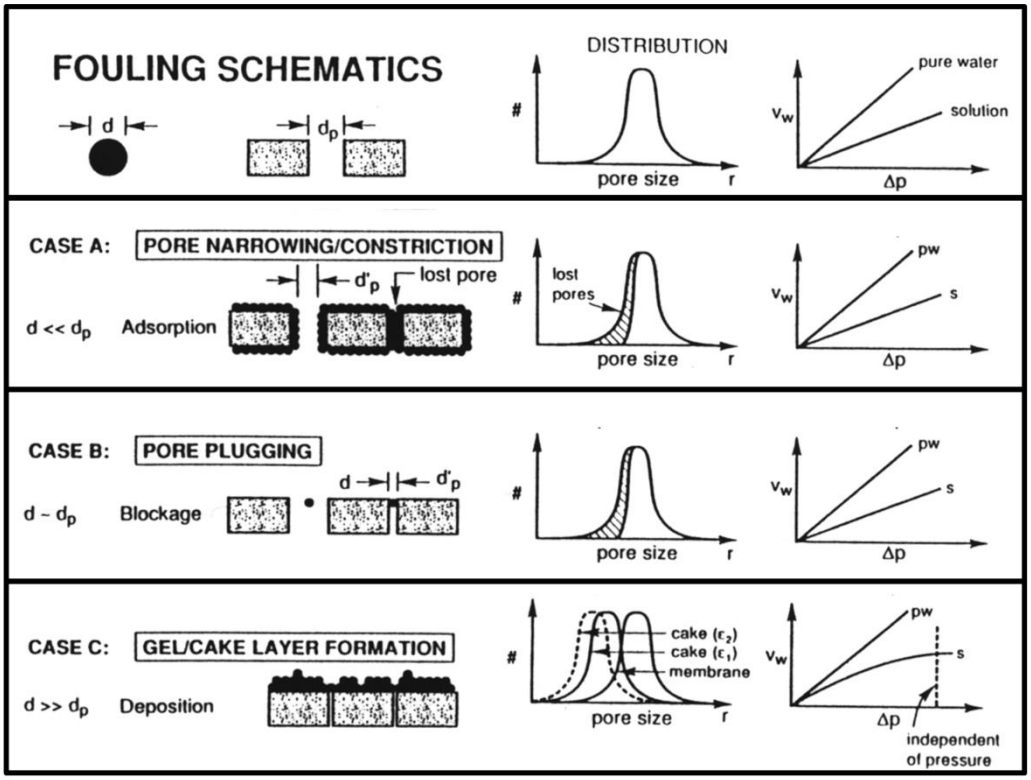

Figure 2.20 Schematics of fouling occurrence with impacts on typical pore size distribution as well as membrane flux (Belfort *et al.*, 1994).

Modelling of membrane filtration with the presence of fouling can be performed by considering the fouling resistances in series with the membrane resistance. Due to the fouling in UF mainly occurred by surface pore blocking and cake formation, the 'standard' classical fouling models proposed by Hermia have been widely accepted to analyse fouling phenomena (Marshall *et al.*, 1993; Hermia, 1982). As shown in Figure 2.21, the four models are complete pore blocking, standard pore blocking, intermediate pore blocking and cake filtration.

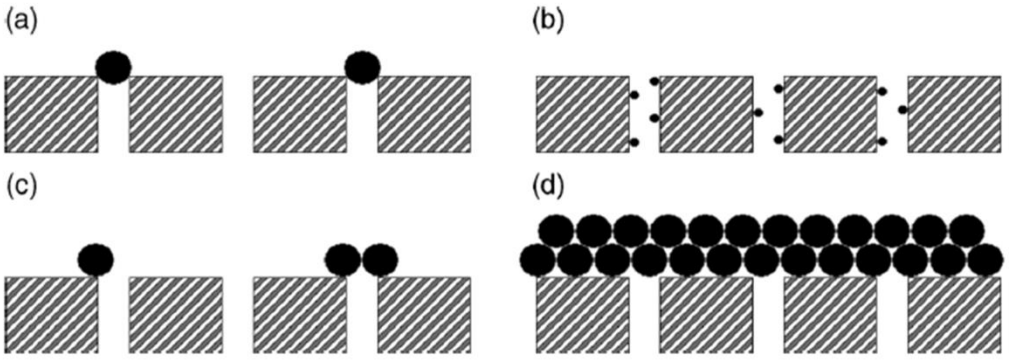

Figure 2.21 Schematics of different fouling mechanisms for porous membranes. (a) Complete pore blocking; (b) standard pore blocking; (c) intermediate pore blocking and (d) cake filtration (Field, 2010).

The original unifying equation took the following form (Hermia, 1982):

$$\frac{d^2t}{dV^2} = k\left(\frac{dt}{dV}\right)^n \qquad 2.25$$

where V is the accumulated permeate volume over time t, k is fouling constant and n is the index that corresponds to different fouling mechanisms. In this equation, the significance of the index n becomes clear. The smaller the value n, the greater the decrease of the rate for flux decline caused by the corresponding fouling mechanism. The transport equations in Table 2.6 are the integral form of equation 2.25 based on different index n. These equations are only applicable to dead-end filtration or limited to the initial time periods of cross-flow membrane operation (Field, 2010). Although these four classical models are most often used for analysis, there is considerable experimental evidence showing a transition in the fouling behaviour, with the initial flux decline associated with pore blocking followed by cake formation (Bolton *et al.*, 2006). For example, an experiment based on the dead-end filtration of bovine serum albumin (BSA) through polycarbonate track-etched membranes has shown a two-stage fouling

phenomenon (Ho and Zydney, 2000). Initially, fouling occurred in the form of complete pore blocking. The deposited aggregates were assumed to be permeable. Flow through the blocked areas resulted in the deposition of a cake, further reducing the permeate flux. Following this, as shown in Table 2.7 ,five new fouling models that accounted for the combined effects of the different individual douling mechanisms were developed (Bolton *et al.*, 2006).

Table 2.6 Fouling mechanisms, phenomenological background and transport equations (Field, 2010; Hermia, 1982).

Fouling mechanism	n	Phenomenological background and impact on mass transport	Transport equation in dead-end mode[a]
Complete pore blocking	2	Particles larger than the pore size completely block membrane pores. Reduction of the active membrane area. Depends on feed velocity.	$J_w = J_{w0}K_bAt$
Standard pore blocking	1.5	Particles smaller than pore size enter the pores and get either adsorbed or deposited onto the pore walls. This restrict the flow of permeate. Increase in membrane resistance due to pore size reduction. Internal pore blockage is independent of feed velocity. Mitigation by cross-flow is absent.	$J_w = J_{w0}\left(1 + \frac{1}{2}K_s\sqrt{AJ_{w0}}t\right)^{-2}$
Intermediate pore blocking	1	Particles reaching surface may seal a pore, or bridge a pore or partially block it, or adhere on inactive regions. Reduction of active membrane area. The effect is similar to pore blocking but less severe.	$J_w = J_{w0}(1 + K_i(AJ_{w0})t)^{-1}$
Cake filtration	0	Formation of a cake on the membrane surface by particles which neither enter nor seal the pores. The overall resistance becomes the resistance of the cake plus the resistance of the membrane (which may already be fouled by other mechanisms).	$J_w = J_{w0}(1 + K_C(AJ_{w0})^2t)^{-\frac{1}{2}}$

[a] where J_{wo} is the initial water flux, A is the membrane area, t is the time and K_b, K_s, K_i and K_c are fouling constant corresponds to each fouling mechanism, respectively.

Table 2.7 Summary of the five new combined fouling models (Bolton *et al.*, 2006).

Model	Equation
Cake filtration-complete pore blocking	$V = \frac{J_{w0}}{K_b}\left\{1 - e^{\left[\frac{-K_b}{K_c J_{w0}^2}\left(\sqrt{1+2K_c J_{w0}^2 t}-1\right)\right]}\right\}$
Cake filtration-intermediate pore blocking	$V = \frac{1}{K_i}\ln\left\{1 + \frac{K_i}{K_c J_{w0}}\left[\left(\sqrt{1 + 2K_c J_{w0}^2 t} - 1\right)\right]\right\}$
Complete pore blocking-standard pore blocking	$V = \frac{J_{w0}}{K_b}\left(1 - e^{\frac{-2K_b t}{2+K_s J_{w0} t}}\right)$
Intermediate pore blocking-standard pore blocking	$V = \frac{1}{K_i}\ln\left(1 + \frac{-2K_i J_{w0} t}{2 + K_s J_{w0} t}\right)$
Cake filtration-standard pore blocking	$V = \frac{2}{K_s}\left[\beta\cos\left(\frac{2\pi}{3} - \frac{1}{3}\cos^{-1}\alpha\right) + \frac{1}{3}\right]$ where $\alpha = \frac{8}{27\beta^3} + \frac{4K_s}{3\beta^3 K_c J_{w0}} - \frac{4K_s^2 t}{3\beta^3 K_c}$, $\beta = \sqrt{\frac{4}{9} + \frac{4K_s}{3K_c J_{w0}} + \frac{2K_s^2 t}{3K_c}}$

2.4 Membrane emulsification

Emulsions play an important role in the formulation of foods, cosmetics and pharmaceuticals. Conventionally, they are prepared via the creation of turbulence that induces shear stress by using colloid mills, rotor-stator systems and high pressure homogenizers. The choice of specific method is usually based on the application of the resulting emulsion, the apparent viscosity, the amount of mechanical energy required and the heat-exchange demands (Friberg *et al.*, 2003). However, there are emerging techniques to form emulsions such as microfluidics and membrane emulsification (Joscelyne and Trägårdh, 2000). Particularly, there has been an increasing interest in membrane emulsification since its first success in making an emulsion with uniform particle size using porous glass membranes in the late 1980s (Nakashima and Shimizu, 1986). This method involves using a low pressure to disperse an immiscible liquid through a membrane into another phase. This technique is highly attractive given its simplicity, high process flexibility, low energy and surfactant consumption as well as producing a narrow droplet size distribution (Wedlock, 1994).

2.4.1 Fundamentals of membrane emulsification

Emulsion is defined as a dispersion of one liquid phase in another immiscible liquid phase that are made using mechanical shear (Bibette *et al.*, 1999). As shown in Figure 2.22, the phase that forms discontinuous droplets is known as disperse phase whereas the bulk phase is denoted as continuous phase. Figure 2.22 also illustrates that both oil in water (o/w) and water in oil (w/o) can be created. Emulsions are normally metastable. The large surface energy as a result of large interfacial areas between the two immiscible phases and interfacial tension cause the coalescence of droplets (Mason *et al.*, 2006). The interfacial tension can be significantly reduced by the addition of amphiphilic surface-active molecules, or 'surfactants', that is highly soluble in one of the liquid phases. Surfactants prefentially adsorb at interfaces, since their molecule structures have non-polar lipophilic tails that prefer to be in oil and polar hydrophilic head groups that prefer to reside in water phase. Therefore, it is necessary to add a surfactant to produce an emulsion with long term stability (Bibette *et al.*, 1999).

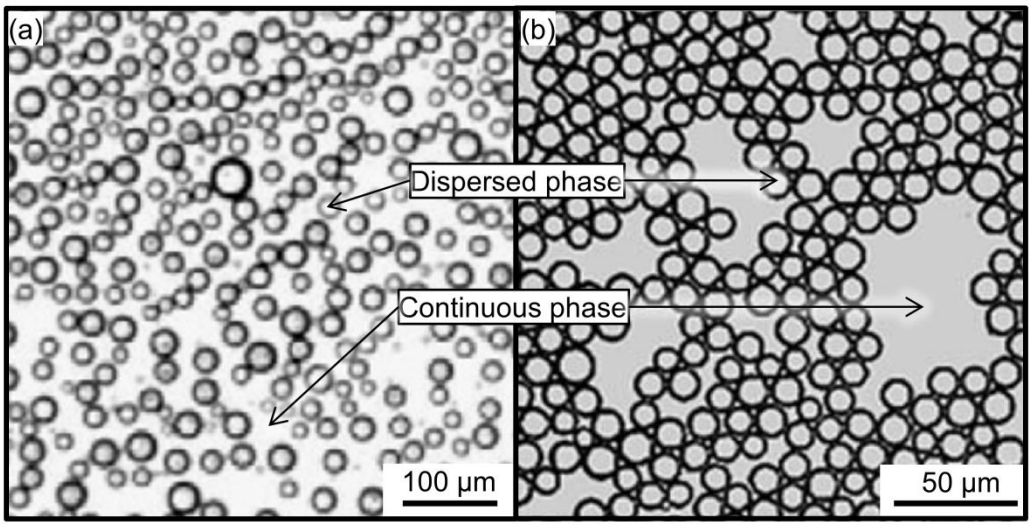

Figure 2.22 Optical micrographs of uniform (a) sunflower oil droplets in water and (b) water droplets in kerosene emulsions formed by membrane emulsification process (Cheng *et al.*, 2006; Wagdare *et al.*, 2010).

In membrane emulsification, the membrane used should be wetted by the continuous phase before the emulsification process to prevent the membrane surface from wetting with the disperse phase. This is to facilitate the detachment of disperse phase droplet into the continuous phase, which is discussed in the Section 2.4.2. Therefore, hydrophilic membranes are suitable for o/w emulsions

whereas the hydrophobic ones are only used for making w/o emulsions (Cheng *et al.*, 2008). Similar to filtration, membrane emulsification can be operated in dead-end or cross-flow mode (Figure 2.23). In its simplest form, dead-end membrane emulsification only employs pressure to force the disperse phase through a porous membrane into the continuous phase. Droplets are not subjected to shear stress and hence the specific energy consumption is low, 10^4 to 10^6 Jm^{-3} in contrast to 10^6 – 10^8 Jm^{-3} when using conventional methods (Lambrich and Schubert, 2005). However, to obtain an extra degree of freedom to control droplet size, external stress can be induced by stirring the continuous phase or by rotating a tubular membrane during the process (Vladisavljević and Williams, 2005). In cross-flow mode, the tangential flow of the continuous phase can induce shear stress to facilitate the detachment of the disperse droplets (Lambrich and Schubert, 2005). Cross-flow systems have shown potential for large scale applications; for example. they are widely used by the dairy industry in Japan (Nakashima *et al.*, 2000).

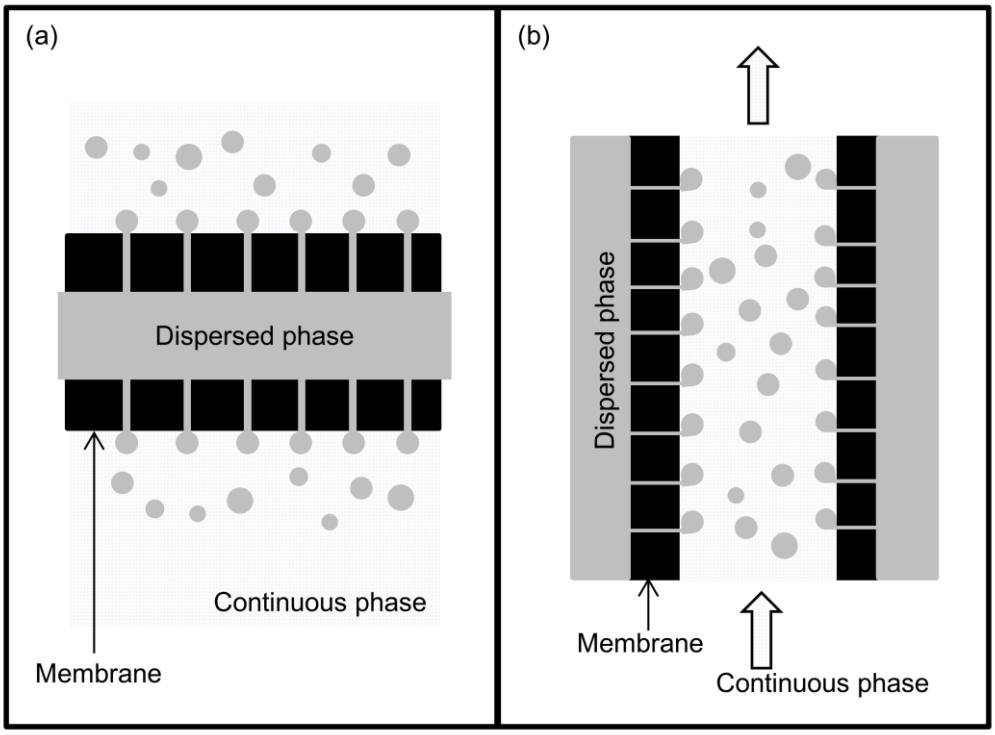

Figure 2.23 Schematics of membrane emulsification operated at (a) dead-end mode and (b) cross-flow mode.

2.4.2 Droplet formation mechanism and force balance

Assuming that membrane pores are cylindrical, the pressure required to disperse the oil phase through the pores can be estimated from capillary pressure:

$$P_c = \frac{2\gamma \cos\theta}{r_p} \qquad 2.26$$

Where P_c is the critical pressure (minimum pressure to make disperse phase permeate), γ is the interfacial tension between the two liquid phases and θ is the interface contact angle of the two liquid phases with the pore wall.

A simplified theoretical approach to describe the evolution and detachment of a droplet from an individual pore was proposed (Peng and Williams, 1998). The process involves two stages, namely *droplet growth* when the droplet inflates at the pore tip and *droplet detachment* when the droplet breaks off and then moves away from the pore tip. Spherical droplet tends to be formed under the action of solely interfacial forces, i.e. simple dead-end mode (Figure 2.24a). As demonstrated in Figure 2.24, the presence of shear stress, induced by cross-flow, stirring or membrane rotation, can distort the shape of the droplet. The deformation of the spherical shape depends on the magnitude of the induced shear. Buoyancy force may also slightly change the shape of the droplet. In addition, all the wetting interaction (interfacial force) between the liquid phases can affect good droplet formation. In general, the cases represented by Figure 2.24c & d should be avoided to ensure well defined droplet size distribution. The formation of droplet is hence closely related to the balance of forces.

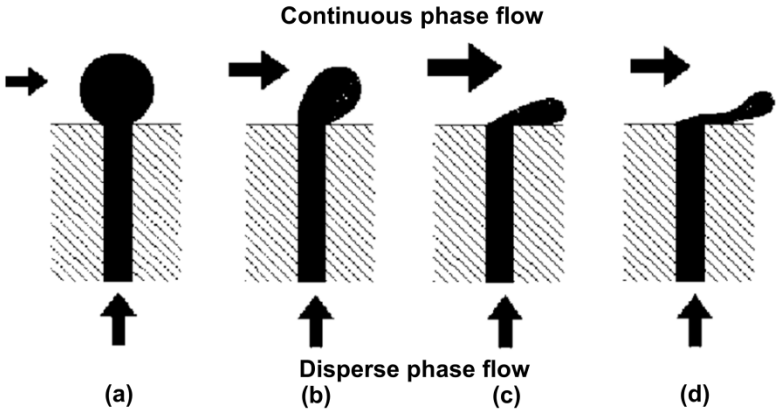

Figure 2.24 Illustration of droplet formation and detachment from a pore tip under different conditions: (a) negligible or low shear force; (b) high shear force in comparison to interfacial tension; (c) very small contact angle or extremely high shear force and (d) membrane surface wetted by disperse phase. (Peng and Williams, 1998).

The force balance analysis can be performed by considering the dynamic of motion for a spherical particle immersed in a fluid Figure 2.25a. A droplet formed through a small pore may be subjected to the following four external forces Figure 2.25b:

- F_d is a drag force induced by cross flow. The direction of the force is parallel to the membrane surface. In term of friction factor, f, the drag force can be expressed as:

  $$F_d = 3\pi f k_x \rho V_c^2 r_d^2 \quad 2.27$$

  where k_x is the wall correction factor ((O'Neill, 1967), ρ is the density of continuous phase, V_c is the average velocity of the continuous phase and r_d is the radius of the droplet.

- F_γ is a force caused by the interfacial tension. It represents the effect of the adhesion of the droplet around the edge of the pore opening. This can be written as:

  $$F_\gamma = 2\pi\gamma r_p \quad 2.28$$

- F_b is the buoyant force arising from the difference between the densities of the two phases. This is significant only if the continuous phase is stagnant, i.e. simple dead-end membrane emulsification. In cross-flow mode, this force is very negligibly small when compared to F_d and F_γ. This can be calculated by:

  $$F_b = \frac{4}{3}\pi r_d^3(\rho - \rho_d)g \quad 2.29$$

  where ρ_d is the density of the disperse phase and g is the gravity acceleration.

- F_i is an inertial force caused by dispersed phase flow moving through the pore capillary as it inflates the droplet. The direction of the force is normal to the membrane surface. Similar to F_b, this force is only significant if external shear is absent, due to the low Reynolds number of the disperse phase flow. This force can be expressed by:

  $$F_i = \rho_d \pi r_p^2 V_d^2 \quad 2.30$$

  where V_d is the average velocity of the disperse phase within the pore.

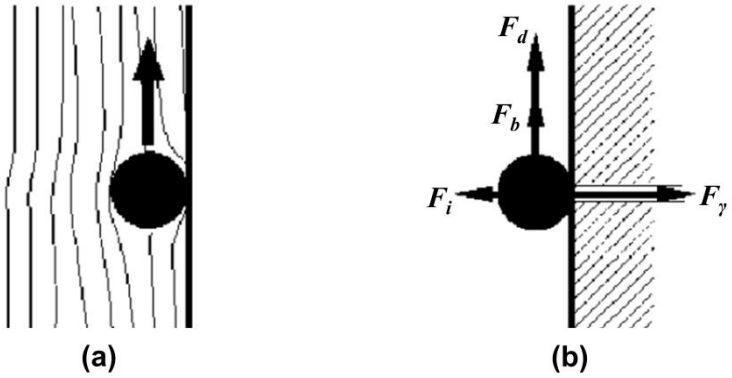

Figure 2.25 (a) Flow of immersed particle and (b) forces acting on a droplet formed at a membrane pore (Peng and Williams, 1998).

Generally, dispersed droplet deforms in the direction influenced by the buoyant and inertia forces in dead-end membrane emulsification. However, in cross-flow configuration, the droplet deforms in the direction of the shear force. The interfacial force can be separated into two parts: one acting to oppose shear force and one is perpendicular to the membrane surface. Hence, the droplet should start to detach when the magnitude of the shear force is sufficient to overcome the interfacial force (Peng and Williams, 1998).

2.4.3 Process parameters of membrane emulsifications

There are nearly 100 of previous investigation of membrane emulsification processes, with varying process parameters. In particular, Vladisavljević and William, as well as Charcosset *et al.* have summarised and listed these valuable information in their reviews (Vladisavljević and Williams, 2005; Charcosset *et al.*, 2004). In this section, the influence of each process parameter on the quality of emulsion formed is discussed.

2.4.3.1 Membrane properties: material, pore size and porosity

Shirasu porous glass (SPG) membrane, which is designed for membrane emulsification, is most widely investigated membrane material (Nakashima and Shimizu, 1986). Other membranes used in making emulsions include alumina, zirconia, silica, polytetrafluoroethylene (PTFE), polypropylene (PP),

polycarbonate track etched (PCTE) and thin film composite polyamide (TFC-PA) membranes. As discussed before, the wettability of the membranes decides their suitability for o/w or w/o systems.

It is widely accepted that the average droplet radius, r_d is linearly proportional to the average membrane pore radius r_p, for a given operating condition (Charcosset *et al.*, 2004):

$$r_d = c r_p \qquad 2.31$$

where c is an empirical proportionality constant. For SPG membranes, c normally ranges from 2 to 10 due to different operating conditions. For other membranes, the values reported for c are higher, typically from 3 to 50 (Charcosset *et al.*, 2004). The polydispersity index (PDI) is typically defined as the ratio of the size distribution's width to its average (Bibette *et al.*, 1999). Typically, emulsions with defined dispersity (PDI < 0.2) can be produced if the membrane pore size distribution is sufficiently narrow (Mason *et al.*, 2006; Charcosset *et al.*, 2004). SPG and PCTE membranes are among the membranes with well-defined pore size distribution to produce emulsions with narrow droplet size distribution.

Finally, the porosity of the membrane surface, which is related to the interpore distance, is another important parameter for membrane emulsification. It is because when interpore distance is too small, i.e. high porosity, this may allow contact of two adjacent droplets, leading to coalescence. However, a low porosity has the disadvantage of low dispersed phase flux.

2.4.3.2 Process parameters: cross-flow velocity and applied pressure

As discussed, the force balance plays an important role in droplet formation and detachment. The cross-flow velocity of the continuous phase and permeate rate of disperse phase are not only important to define the composition of the emulsion formulation, but are also influential to the force balance. The cross-flow velocity has a positive relationship with wall shear stress, which in turn facilitates droplet detachment. Therefore, droplet size becomes smaller when cross-flow velocity is increased (Peng and Williams, 1998). At high transmembrane pressure, the flux of the disperse phase is increased. This comes at the expense of increased average droplet size and also it distribution, as a result of higher tendency of droplet coalescence.

2.4.3.3 Phase properties: surfactants, viscosity and pH

As discussed before, surfactants are crucial for the formation of emulsions with long term stability. It has also been shown that the type of surfactant used can influence the droplet size (Schröder *et al.*, 1998). For example, droplet size obtained with surfactant Tween 20 are about twice the size of the droplets stabilised with sodium dodecyl sulphate (SDS), in agreement with the ratio of equilibrium interfacial tensions. In general, the selection of surfactants is based on a numerical hydrophile-lipophile balance (HLB) scheme, a system that classifies the tendency of surfactants to disperse in polar or non-polar liquids.

According to pore flow model, the higher the viscosity is, the lower the disperse phase flux is. This can cause an increment in droplet size as a result of reduction in inertia force. Since viscosity is a function of temperature, temperature can hence affect the droplet size distribution too.

Generally, pH is a parameter which is product dependent. However, membrane surface properties are often pH dependent. For example, ceramic membranes exhibit iso-electric point at a given pH, normally in the range of pH 5.2 to 8. Beyond this range, the surface charge can cause disastrous consequences on the resulting emulsion droplet size (Joscelyne and Trägårdh, 2000).

2.4.4 Mini-, Micro- and Nano-emulsions

Conventionally, most emulsions contain droplets with diameter in micrometre range, > 1 μm. Recently, emulsions with smaller droplet size are of great scientific interest, because of their unique properties in translucency and stability (Mason *et al.*, 2006). In the beginning, it is important to define the terminology being used to describe emulsions of ultra-small droplet size. Firstly, nano-emulsion is a common metastable (only kinetically stable) emulsion system, with droplet size in the nanometre range (McClements, 2012). However, the definite upper droplet size limit for nano-emulsions is not well-defined yet, with papers reporting 500 nm (Anton *et al.*, 2008), 200 nm (Huang *et al.*, 2010) and 100 nm (McClements, 2012). Micro-emulsions, in contrast to what the name suggests, are emulsions with droplet size less than 100 nm but thermodynamically stable. Unlike nano-emulsions, they are not considered as normal class of emulsion because they are formed spontaneously by adding surfactants to completely

eliminate the surface tension (Mason *et al.*, 2006). Therefore, a micro-emulsion is not within the scope of this thesis. Finally, due to the lack of well-defined droplet size for nano-emulsion, the term 'mini-emulsion' has also been suggested to distinguish from traditional emulsion, having a droplet size below 1 μm.

Mini- and nano-emulsions were initially made using ultrasonic and high pressure valve homogenisers. While offering potential in scalability, these two methods are associated with relatively broad droplet size distribution and high energy consumption (Koroleva and Evgenii, 2012). On the other hand, microfluidics and membrane emulsification have the combined advantage of narrow droplet size distribution and low energy consumption, but no emulsion made can achieve droplet size below 200 nm to date. Finally, two techniques have been developed to overcome these problems, namely phase inversion temperature and emulsion inversion point methods. However, these methods still suffer from physical limitations such as low flexibility on emulsion composition and emulsion formation is highly temperature sensitive (Koroleva and Evgenii, 2012).

Nano-emulsions appear visibly different from normal emulsions with microscale droplets since the droplets can be much smaller than optical wavelength of the visible spectrum. Nano-emulsions with droplet size in the tens of nanometres are (nearly) transparent. However, when the droplet radius approaches 100 nm, nano-emulsions appear hazy, and above this, in the submicron range, they appear white or milky due to significant multiple scattering (Mason *et al.*, 2006). On the other hand, nano-emulsions exhibit enhanced stability against gravitationally driven coalescence. Brownian motion, caused by entropic driving forces, keeps the droplets suspended even for long period (Bernardi *et al.*, 2011).

The compositional flexibility of nano-emulsions offers a wide range of applications. For example, the incorporation of fluorescent dyes and other active molecules into nano-emulsions makes them potentially useful to explore properties of living cells and for drug delivery (Bhalodia *et al.*, 2010). The small size of droplets is also likely to increase the transport efficiency of active molecules within the droplets. Nano-emulsions also show potential in bringing new technology in printing industry that will enable high resolution printing (Mason *et al.*, 2006). Nano-emulsions also show promising application in nutraceuticals, for example, adding nutritional compounds to beverages without altering its colour (Donsì *et al.*, 2010).

2.5 Summary

Following the introduction of the development of membrane technology, this chapter gives an overview on the topics of anodic alumina membranes, ultrafiltration and membrane emulsification. AAM is a unique nano-structured material that exhibit self-ordered pore structure. While the precise formation mechanism is still a subject of investigation, the fabrication technique is well-established. In particular, it offers the advantage of an easy control of the pore structure by altering the anodization conditions. However, the usage of AAMs is still limited to small scale applications such as nano-fabrication and laboratory scale filtration. Nevertheless, there is increasing interest in developing AAMs for larger scale application. The recent efforts include the investigation of fabrication of AAMs into tubular form and the use of AAMs for gas separation and hemodialysis.

Considering the uniform pore structure and the ease of precisely controlling it at the nanoscale, AAM is a good candidate membrane material for UF and membrane emulsification processes. For UF, a uniform pore structure is desirable to have sharp selectivity cut-off. This has so far only been achieved by PCTE membranes which have a very low porosity and hence low permeability. The ability to engineer the pore structure of AAM also enables the possibility to optimise the permeability and selectivity. Nevertheless, further investigation of transport properties and fouling behaviour of AAMs is necessary.

In the previous studies of membrane emulsification, most of the membranes used were in MF range. AAMs have a uniform pore structure and can easily be fabricated to have pore diameter below 100 nm, thereby offering the possibility to produce emulsions with small droplet size and well-defined distribution. However, the droplet formation is a function of many process parameters (e.g. cross-flow velocity, transmembrane pressure, surfactant type and concentration). Therefore, empirical data is needed to validate the suitability of AAMs for membrane emulsification process.

3. Materials, Fabrication and Characterisation

Anodic alumina membranes (AAMs) are currently produced commercially by two companies, namely Whatman Inc., England with a trade name Anodisc® and Synkera, US with a trade name Unikera®. However, Anodisc® contain structural defects and irregularities, and both of them have a limited range of pore diameters available, as discussed in more detailed in Section 3.1.1. Therefore, in this work, AAMs were fabricated in house to offer more control over the pore structure via optimisation. Based on the experience from making flat disc form AAMs, a novel apparatus was designed to fabricate AAMs in tubular form. Particularly, the apparatus for fabricating tubular AAMs was modified and improved in several stages to obtain homogenous samples and reproducibility was improved. Subsequently, asymmetric AAMs were developed by manipulating the anodization voltage. Finally, the chapter will end with the characterisation techniques that were used to analyse the pore structure of the AAMs.

3.1 Flat disc symmetric AAMs

Despite the commercial availability of AAMs, there are a number of crucial drawbacks that prevented them from being used in this work. Details of these structural limitations are summarised below and followed by a description of the procedures for the in house production of the membranes.

3.1.1 Commercial AAMs

Anodisc® has been the first commercial AAM targeted for laboratory scale filtration, due to its resistance to aggressive organic solvents. Recently, its application has been extended to template fabrication of one-dimensional nano-structured materials (Martin, 1994). However, they are only available in small disc form (13 – 47 mm) and average pore diameter of 200, 200/100 and 200/20 nm, where the former is symmetric and the two later are asymmetric in structure. Moreover, the pore structure of these commercial AAMs has never been optimized and contains structural defects and irregularities (Figure 3.1). As can

be seen from the topography, the pore arrangement is less-ordered and the pore shape significantly deviates from circularity. Branching of pores can be observed from both the topography and cross-section of the membranes. Most probably, this is a result of successive anodization processes used to produce the AAMs commercially (Mattia, 2007).

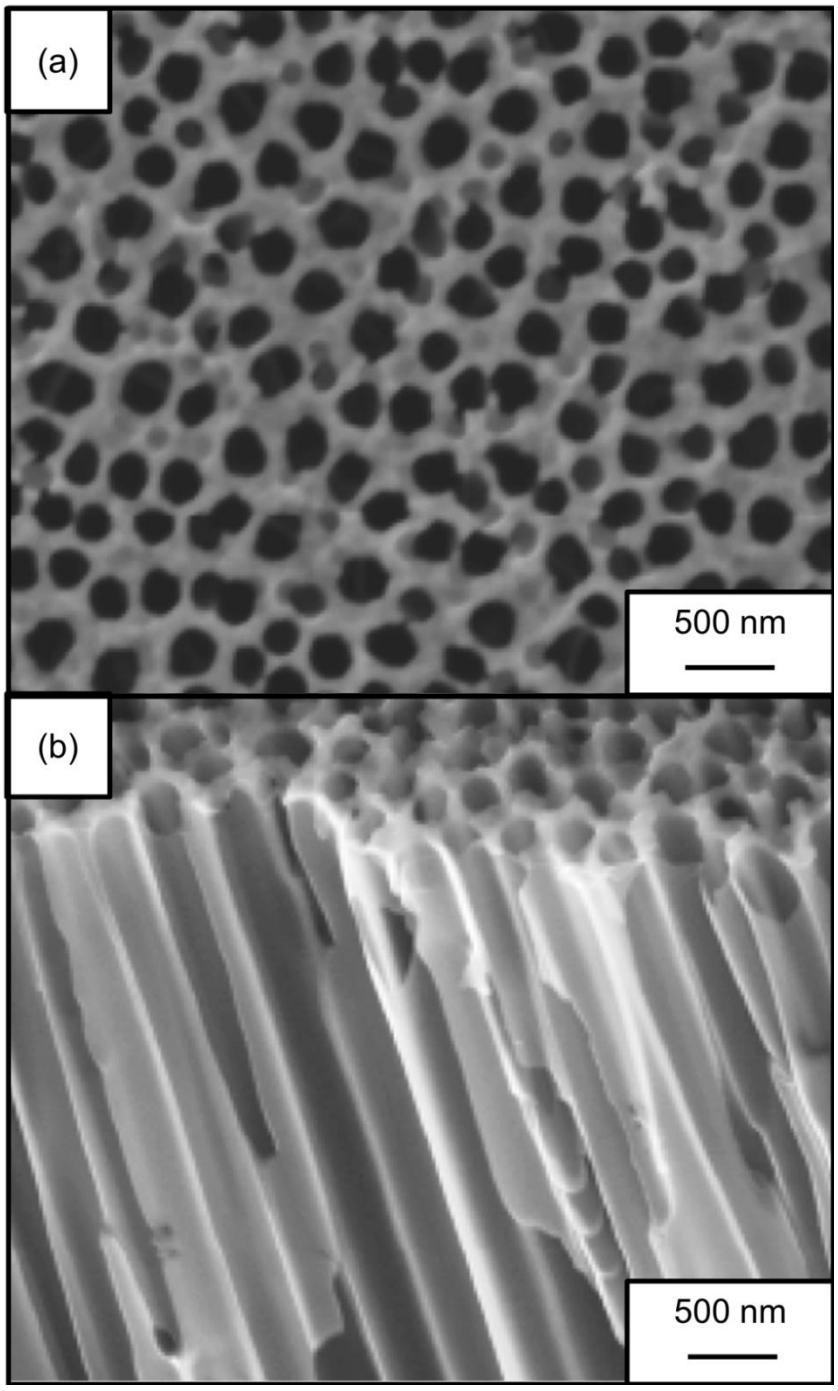

Figure 3.1 SEM micrographs showing the (a) topography, 26,000X magnification and (b) cross-section of an Anodisc® membrane , 26,000X magnification (Mattia, 2007). Numerous pore branchings and irregular pore shape can be observed.

On the other hand, although Unikera® shows a highly uniform pore structure, it has lower than expected porosity (Figure 3.2). The reported values are in the range of 7 to 10 % whereas normal AAMs have porosity in the range of 10 to 20 % (O'Sullivan and Wood, 1970). Despite the difference seems small in this case, however, this difference can lead to at least 30% loss in flux, which will be further discussed later. This difference is believed to be due to an electrochemical technique being used for post-anodization treatment which causes the pore to be not completely opened through (Shiyong *et al.*, 2007). Detailed comparison of different techniques for post-anodization treatment is further discussed later.

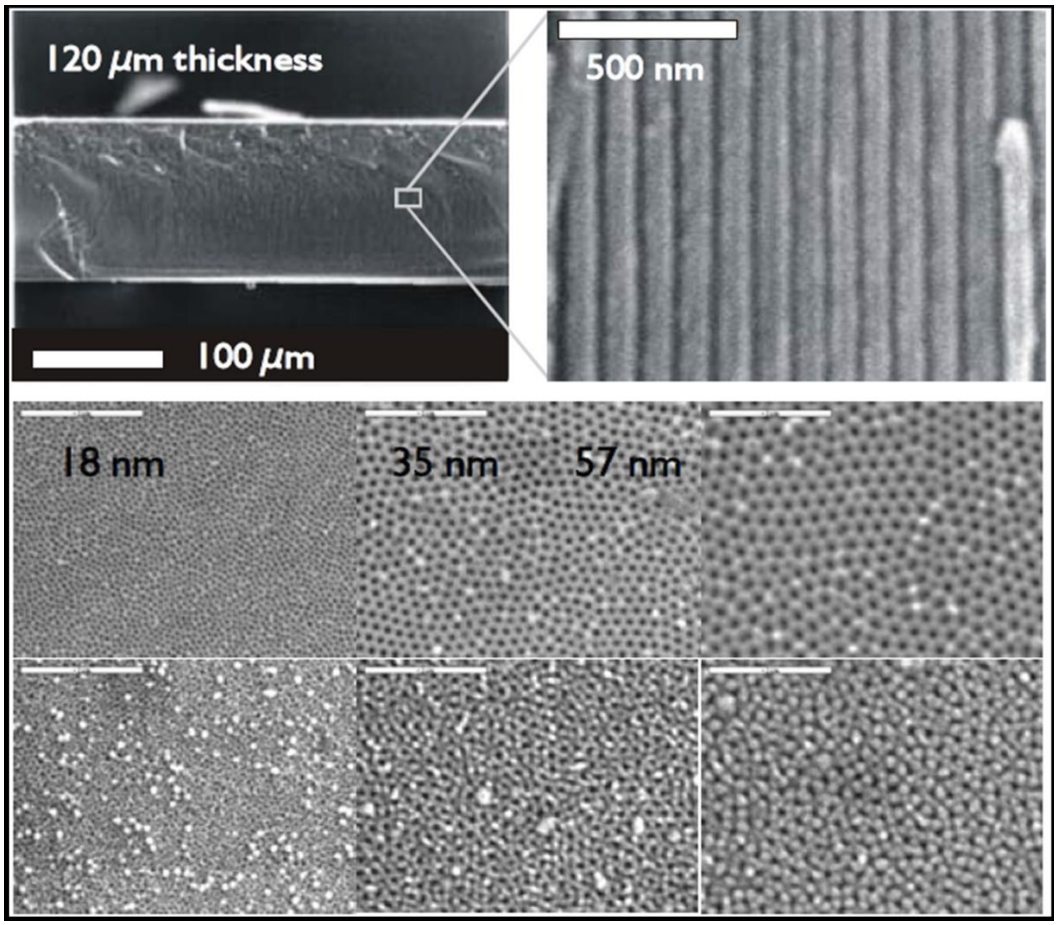

Figure 3.2 SEM micrographs from Synkera Inc. product brochure showing the topography and cross-section of Unikera® membranes. The upper two images show the cross-section of the membrane at different magnification. The bottom images show the surfaces of both the top (upper row) and bottom (lower row) of membranes having mean pore diameter of 18 nm (left), 35 nm (middle) and 57 nm (right). As can be seen, the bottom surfaces of the membranes show undesirable rougher surface. (See **Section 3.1.2.3** for detailed explanation for this surface roughness).

3.1.2 In-house fabrication of flat disc AAMs

Due to the undesirable properties of the commercial AAMs, samples were prepared in-house to engineer the desired pore structure. The preparation of the membranes can be divided into three stages, namely the pre-treatment, one or two step anodization and post treatment (Figure 3.3).

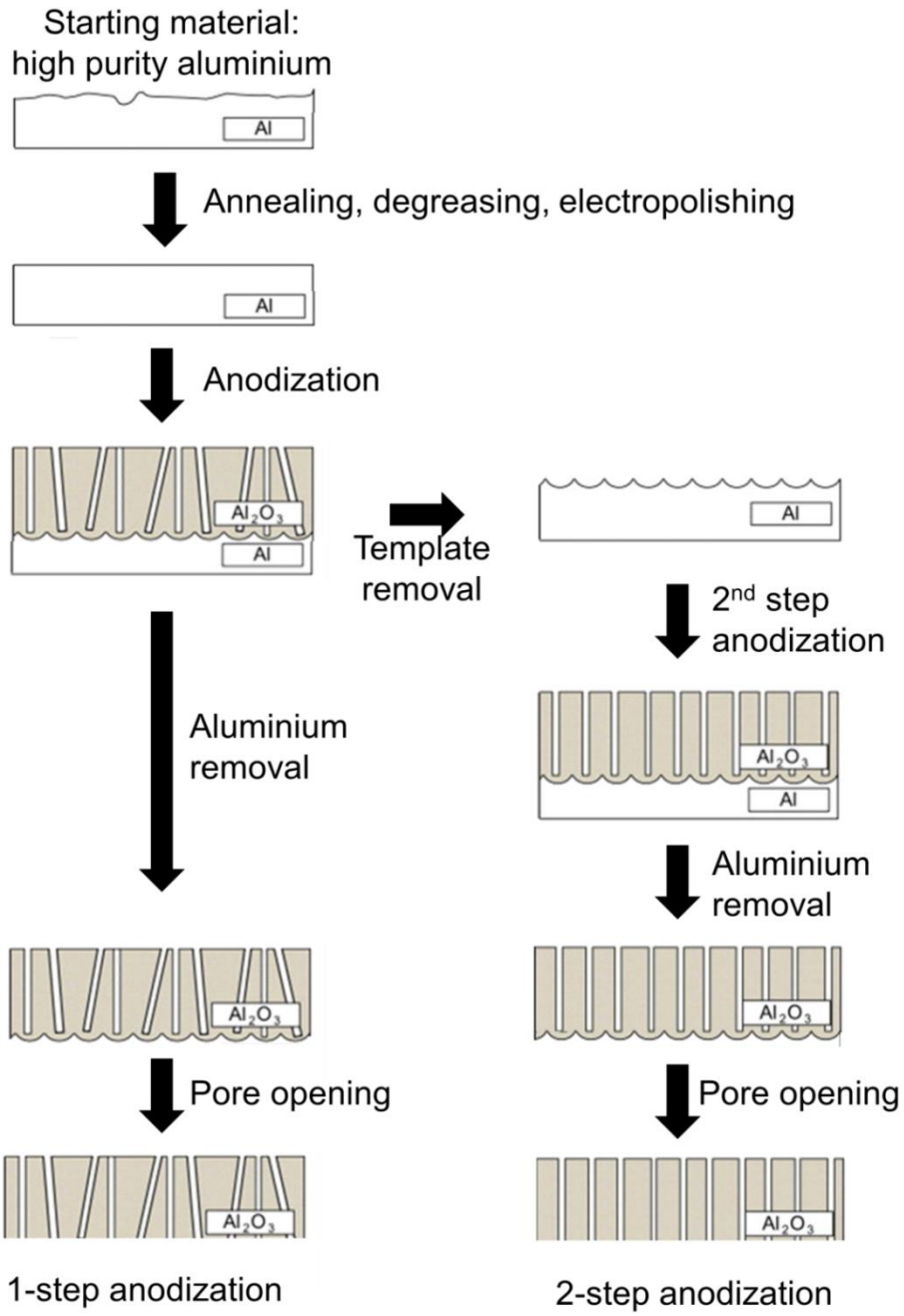

Figure 3.3 Schematic of the multi-step procedures to fabricate flat disc AAMs (Zaraska *et al.*, 2011). The procedures include three stages, namely pre-treatment, anodization and post-treatment. For optimum pore structure, 2-step anodization can be adapted.

3.1.2.1 Starting materials and pre-treatment

High purity aluminium foil (99.99%, 0.25mm thickness, Alfa Aesar was cut into circular discs of 13 mm diameter and annealed in air at 500 ºC (CWF1100, Carbolite) for an hour. During the annealing, the removal of the internal stress, crystal defects and grain boundaries occur, improving the microstructure of aluminium. This process improve the regularity of the pore structure formed later during anodization (Rahimi *et al.*, 2012). Then, the aluminium discs were cleaned by ultra-sonication (Fisher Scientific, FB 15048) in acetone (HPLC grade, 99.5+ %, Fisher) for 10 minutes.

Relative to chemical or mechanical polishing, electro-polishing is the most effective and reproducible method to remove the spontaneously grown oxide layer in air and create a smooth surface, which was proven to improve pore orderliness. There was a range of electro-polishing conditions reported (Sulka, 2008). In this work, the cleaned aluminium discs were electro-polished in a solution of perchloric acid (60-62 %, Fisher) and ethanol (96 %, Fisher) in the volumetric ratio of 1 : 4. The aluminium disc was connected as the anode whereas a solution containing stainless steel beaker was used as the cathode. Using a dry ice-acetone bath to maintain the temperature constant (<-50 °C), the electro-polishing was performed at 20 V (Agilent, E3620A) for 15 minutes to obtain a mirror-like shiny surface as shown in (Figure 3.4).

3.1.2.2 Anodization

Anodization is the crucial process where the structured porous oxide layer was formed. Figure 3.5 and Figure 3.6 show an image and the schematic of the experimental apparatus of AAMs fabrication. By using copper tape, an electro-polished aluminium disc was used as the anode on a sample holder and sealed using an O-ring, leaving an exposed area of 10 mm in diameter for anodization. A 5 mm thick stainless steel (SS316 grade) plate was used as the cathode. The sample holder was immersed in a magnetically stirred electrolyte in a double jacketed beaker, where the desired temperature was controlled and maintained by recirculation of coolant (Thermo Scientific HAAKEC10-K10, DC10-K20 or DC50-K35).

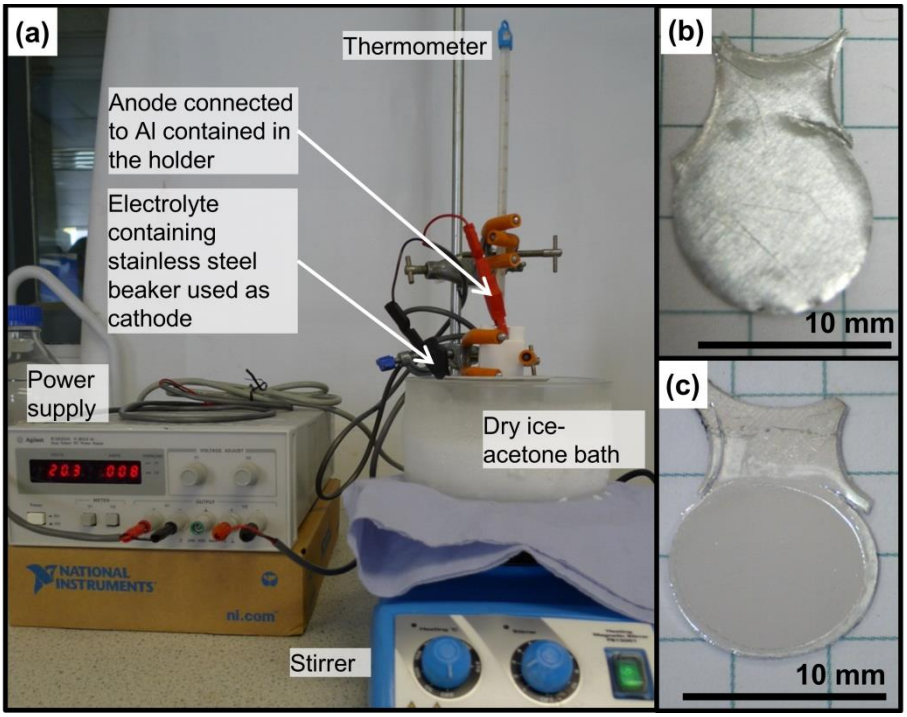

Figure 3.4 (a) The electro-polishing apparatus, and the aluminium substrate (b) before and (c) after electro-polishing.

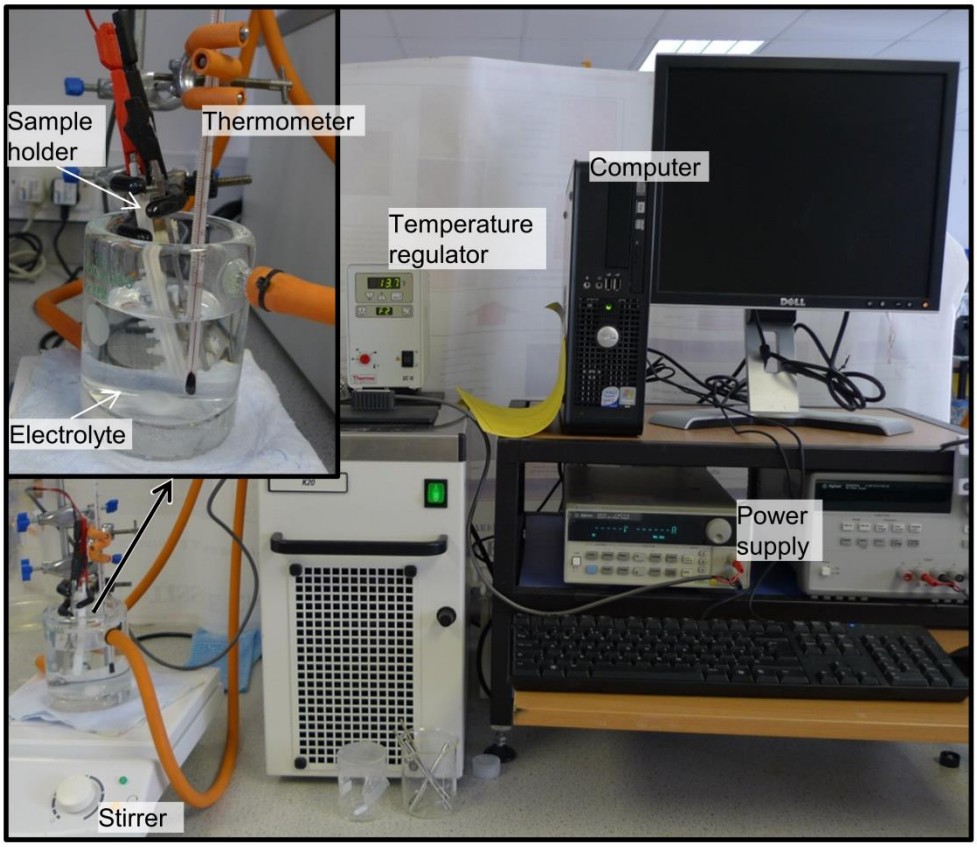

Figure 3.5 The experimental apparatus to fabricate flat AAMs.

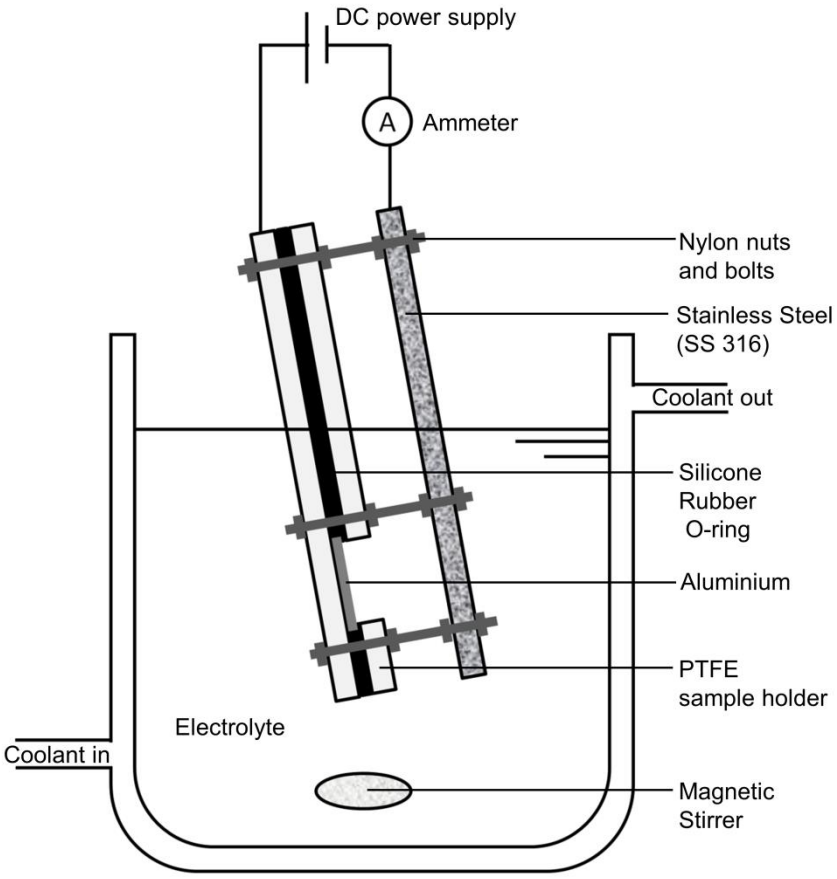

Figure 3.6 The schematic of experimental set up for anodization of aluminium disc. The electro-polished aluminium disc was fixed in place using the holder. The bolts and nuts fixed the distance between anode and cathode, which is in parallel to each other. The holder was inserted into the electrolyte with an angle, instead of perpendicular, to improve the escape of hydrogen bubbles during anodization.

The porous anodic alumina structure formation mechanism and reactions that are taking place during anodization were summarised in Section 2.2.5. As described, the morphology and structure of AAMs depend on the anodization conditions:

- Applied voltage - given the well-known linear dependence of pore diameter with applied voltage, with a constant of about 1.25 nm V^{-1}, the applied voltage was controlled to obtain the desired pore diameter (O'Sullivan and Wood, 1970). Another factor to be considered is the thickness of the membrane, which is proportional to the current density, and therefore also the applied voltage. When the applied voltage is 10 V, the oxide film thickness is only about 20 μm, which poses challenges to handling for post-treatment or further characterisation.

- Electrolyte type and concentration – the activity of electrolyte is closely related to the self-ordered structure formed. In this work, the desired pore diameter is 100 nm and below. Hence, sulphuric acid has been used to produce the smallest pore size, with an applied voltage of 25 V and below. On the other hand, oxalic acid was used for applied voltage in the range of 25 to 80 V. Concentration is an important parameter too that can be used to control the current density during anodization, in order to control the thickness of the AAMs or preventing an excessively aggressive reaction. For example, 0.5 M sulphuric acid was used for anodization at 20 to 25 V whereas 1.0 M was used for anodization below 20 V to obtain sufficient thickness of AAMs. A trial of anodization at 25 V by 1.0 M anodization has resulted in over-heating and affected the nano-structure of the oxide film. When the concentration of the electrolyte is too low, the rate of field assisted dissolution of oxide to form the porous structure is reduced and insufficient to create desired pore diameter and porosity.

- Temperature – the anodization process is highly exothermic, as the reaction rate is positively correlated with current density, and hence the applied voltage. Temperature can change dramatically the pore size distribution as well as the morphology of the resulting membranes (Chung *et al.*, 2011). Normally, anodization in sulphuric acid was performed down to 0 ºC whereas 10 to 13 ºC was normally maintained for anodization in oxalic acid. Exceptionally, anodization at 60 V to 80 V in oxalic acid was performed at lower temperature, nearly 0 ºC to prevent over-heating and aggressive anodization that affects the porous structure.

- Time – the anodization time is related to the final thickness of the membranes. Based on the literature review, anodization was performed for 5 to 7 hours in sulphuric acid and 10 to 12 hours in oxalic acid to obtain sufficient thickness for mechanical integrity . However, for higher voltage anodization, i.e. 80 V in oxalic acid, a shorter time of approximately 4 hours is sufficient due to the high current density.

The voltage bias was induced by a DC power supply (Agilent E3643A, 6645A or 6675A). The voltage and current profile was recorded using a Labview-based data acquisition programme. For clarification, the top surface is referring to the surface where anodization first started whereas the bottom surface is referring to the surface where the anodization ended. This is applied throughout the thesis.

As shown in Figure 3.3, both one-step and two-step anodization had been performed. For the two-step anodization, the oxide layer formed from the one-hour first-step anodization was removed by wet chemical etching using a 1 : 1 mixture of 6 wt% phosphoric acid and 1.8 wt% chromic acid at 60 ºC for 20 minutes. Having formed the template for the secondary growth of the porous alumina, the second-step anodization was performed immediately under the same conditions as the first step but for a longer period of time to obtain sufficient membrane thickness. Figure 3.7 shows sample images of porous oxide layers formed after anodization.

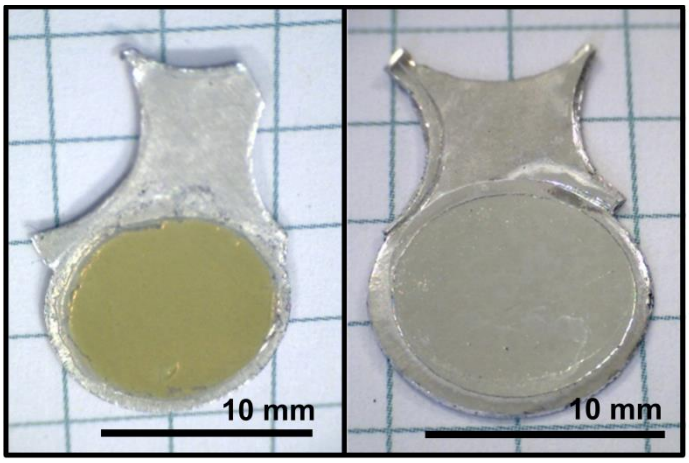

Figure 3.7 The oxide layer formed on aluminium substrate after anodization: (a) yellowish transparent oxide layer was formed by anodization in oxalic acid and (b) colourless transparent oxide layer was formed in sulphuric acid.

3.1.2.3 Post-treatment

After the anodization process, the bottom part of the alumina membrane is covered by the residual aluminium. To expose the bottom surface of the oxide layer, the residual aluminium was removed by a reaction with copper (II) chloride in a 1 : 1 solution of 0.2 M copper (II) chloride dihydrate to 20 wt% hydrochloric acid (Figure 3.8). The reaction produces a copper deposit, water vapour and soluble Al^{3+} ions in water:

$$2Al_{(s)} + 3\,CuCl_2.2H_2O_{(aq)} \rightarrow\ 2AlCl_{3(aq)} + 3Cu_{(s)} + 6H_2O \qquad 3.1$$

The hydrochloric acid facilitates the reaction by:

$$2Al_{(s)} + 6HCl_{(aq)} \rightarrow\ 2AlCl_{3(aq)} + 3H_{2(g)} \qquad 3.2$$

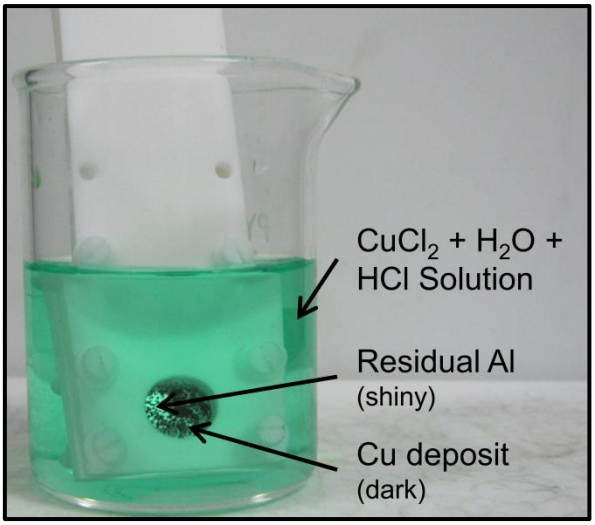

Figure 3.8 The removal of residual aluminium substrate.

Finally, the oxide barrier layer was removed to produce self-standing open-through membranes. It is etched away by 6 wt% phosphoric acid according to the following reaction:

$$\frac{1}{2}Al_2O_3 + \frac{1}{2}H_2O + H^+ \rightarrow Al(OH)_2^+ \quad 3.3$$

$$Al(OH)_2^+ + H^+ \rightarrow Al(OH)^{2+} + H_2O \quad 3.4$$

$$Al(OH)^{2+} + H^+ \rightarrow Al^{3+} + H_2O \quad 3.5$$

However, the etching time and temperature has to be closely monitored to prevent over- or under-etching. Under-etching will result in incomplete removal of barrier layer and hence reduce the porosity of the membrane. Over-etching will cause pore-widening at the bottom surface of the membrane, and hence over-estimating the overall porosity of the membrane. Both cases will affect the uniform and symmetric structure of the membrane and cause inaccuracy in characterising the membrane structure. The different thickness of barrier layer as a function of applied anodization voltage further complicates this process. Therefore, an electrochemical detection method was adapted to precisely control the pore-opening process (Lillo and Losic, 2009).

As shown in Figure 3.9, a membrane was sandwiched between two small electrolyte-containing reservoirs and sealed by using a silicone rubber O-ring. The bottom surface of the membrane, i.e. the oxide barrier layer, was in contact with phosphoric acid, whereas the top surface, i.e. the porous side was in contact

with a 0.2 M potassium chloride solution. By placing an electrode in each solution, a current could be detected when the pores started to open during the etching. The current detection provides the information about different stages of etching, e.g. oxide barrier layer thinning, pore-opening and pore widening. This provides more consistency of the experiment and enables repeatable results. At the end of the pore opening process, free standing AAMs were produced (Figure 3.10).

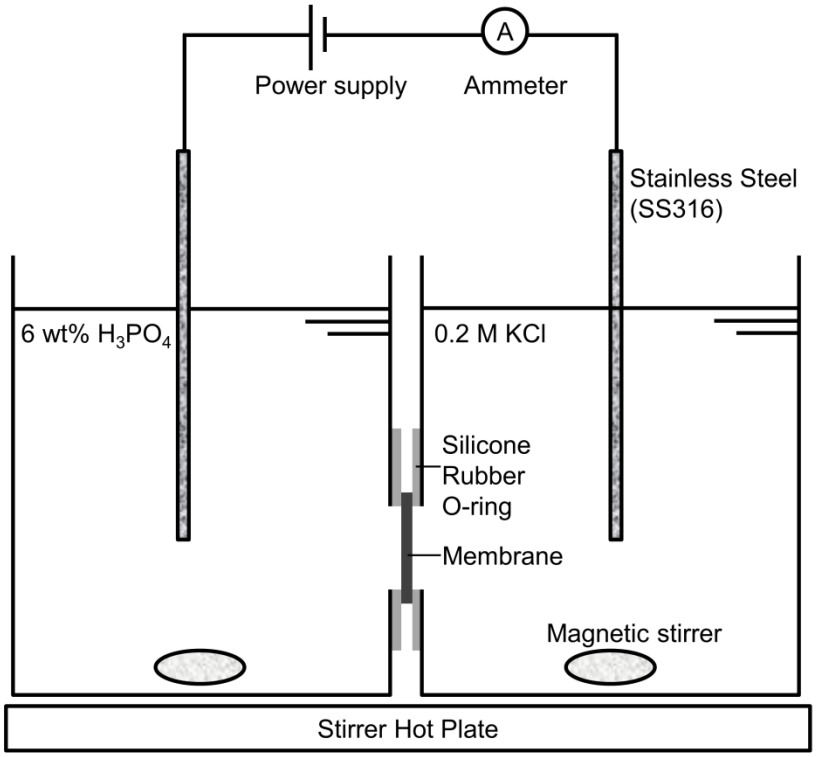

Figure 3.9 The schematic of electrochemical set-up for controlled removal of oxide barrier layer. The bottom surface of the membrane was facing to phosphoric acid solution whereas the top surface was facing the potassium chloride solution to avoid pore widening.

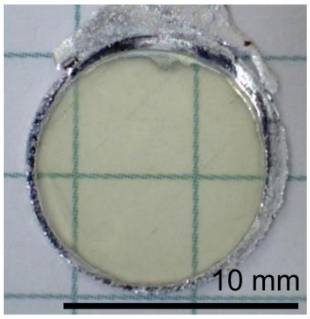

Figure 3.10 A final AAM sample with open-through porous structure after the post-treatment.

Other than the wet chemical procedures used here for post-treatment, an electrochemical method has been proposed to combine residual aluminium removal and oxide barrier layer removal into a single step (Shiyong *et al.*, 2007). This method is based on the dissolution of the oxide barrier layer via an anodic voltage pulse in aqueous perchloric acid solution. Despite providing the convenience of combining two processes into one, this method does not consistently provide completely open pores, while produces some roughness along the hexagonal cells as can be seen from Figure 3.11. Therefore, this method was not employed further.

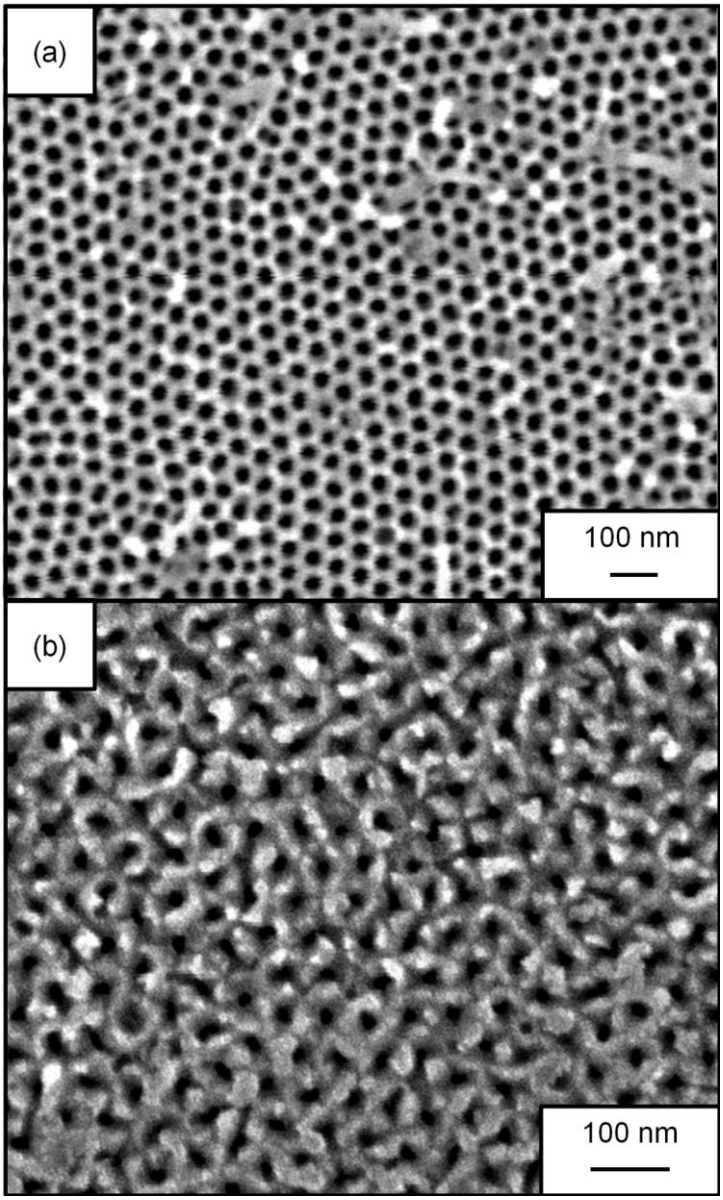

Figure 3.11 SEM micrographs showing the difference between the (a) ordered top surface structure, 80,000X magnification and (b) bottom surface of a membrane that oxide barrier layer was incompletely removed by electrochemical dissolution, 130,000X magnification. Image adapted from (Shiyong *et al.*, 2007).

3.2 Tubular symmetric AAMs

Unlike flat disc AAMs, the process for the fabrication of AAMs in tubular form is less established. As mentioned in Section 2.2.7, several attempts had been reported regarding tubular AAMs. In this work, the fabrication of tubular AAMs was initially started based on these previously reported procedures. The set-up was gradually improved to generate repeatable results and also the method expanded to fabricate multiple membranes simultaneously as well as membrane tube with smaller diameter and asymmetric membranes.

3.2.1 Materials and pre-treatment

While high purity aluminium foil was used to make flat disc membranes, aluminium alloy tubes were used as the starting materials for two reasons, a higher yield strength and lower cost. Two types of alloy were used for comparison, one is a laboratory grade manganese rich aluminium alloy (Al : Mn : Cu = 98.6 : 1.2 : 0.12, Alfa Aesar) whereas the other is an industrial grade A1050 which contains more than 99.5% of aluminium (Haynes tube). Both tubes had an outer diameter of 6.35 mm and a thickness of 0.35 mm and 0.30 mm, respectively. They were cut into 9 cm length sections.

Similar to the flat ones, the aluminium alloy tubes were annealed, degreased and electro-polished prior to anodization. However, during annealing, to make sure the internal stresses relief was homogeneous along the curvature, the tubes were positioned standing straight (Figure 3.12).

Figure 3.12 Arrangement of aluminium alloy tube for annealing process.

Electro-polishing was more challenging for the aluminium alloy tubes, due to the geometry. Initial attempts based on the set-up for flat disc aluminium were only effective for the outer surface area. However, in this work, anodization of inner tube surface was chosen due to it having been reported to produce more mechanically robust membrane in contrast to that of outer surface (Itoh *et al.*, 1998). Therefore, a new set-up was created, as shown in Figure 3.13(a) and (b). A 2 mm diameter stainless steel rod was placed in the middle of the aluminium alloy tube. The stainless steel rod position was fixed by using rubber plugs on both ends, ensuring no short-circuit connection. However, the inner tube provided very limited electro-polishing solution capacity. A tube was therefore connected via the plug to replenish the electro-polishing solution by using a syringe. This set- up provided improved electro-polishing result as compared to the previous attempts (Figure 3.13(c)).

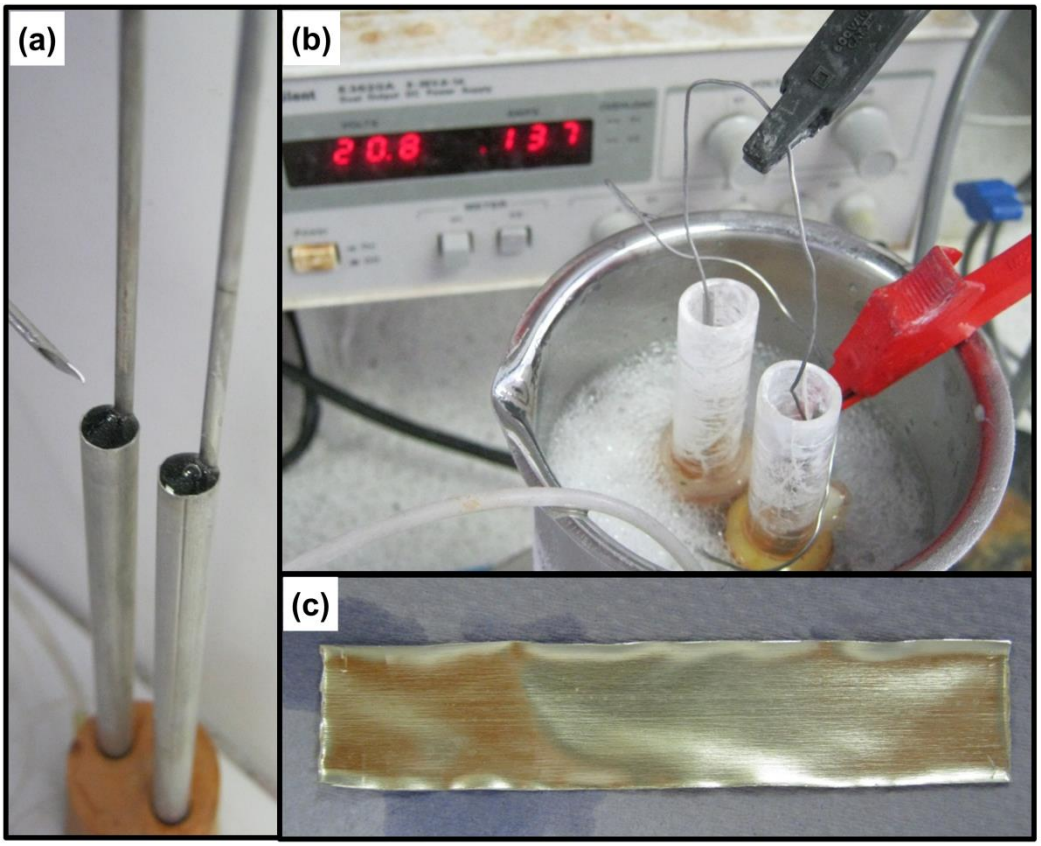

Figure 3.13 (a) electro-polishing solution was filled within the tubes; (b) Electro-polishing set up for aluminium alloy tube and (c) the shiny and smooth inner surface after electro-polishing.

3.2.2 Anodization

Permeability studies of one-step and two-step flat disc AAMs show a very limited difference of below 5% (for experimental details, please see Section 5.2.4). Therefore, one-step anodization was used to fabricate tubular AAMs. To obtain improved mechanical properties of the membrane, the internal surface of the tube was anodized (Itoh *et al.*, 1998). Figure 3.14 and Figure 3.15 show the picture and schematic of the purpose-built rig for the internal anodization of aluminium alloy tube. Similar to electro-polishing, a 2 mm diameter stainless steel rod was fixed in the middle of an aluminium alloy tube by using a plug. The electrolyte was recirculated by using a peristaltic pump, with the pump rate optimised to prevent the ion depletion and overheating within the tube due to the exothermic nature of the reaction. The electrolyte entered the tube via the bottom plug, and left from the top via the holes drilled on the plug. This flow direction also could facilitate hydrogen gas, a byproduct of anodization, to vent off efficiently.

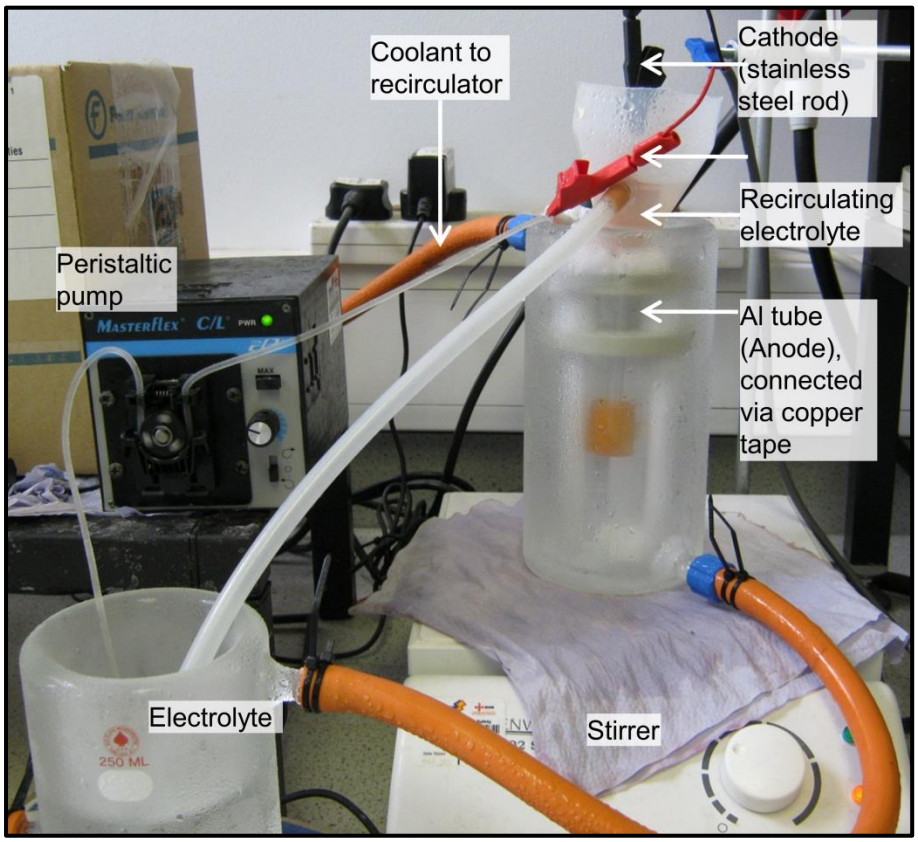

Figure 3.14 The picture of the apparatus for anodization to fabricate tubular AAMs.

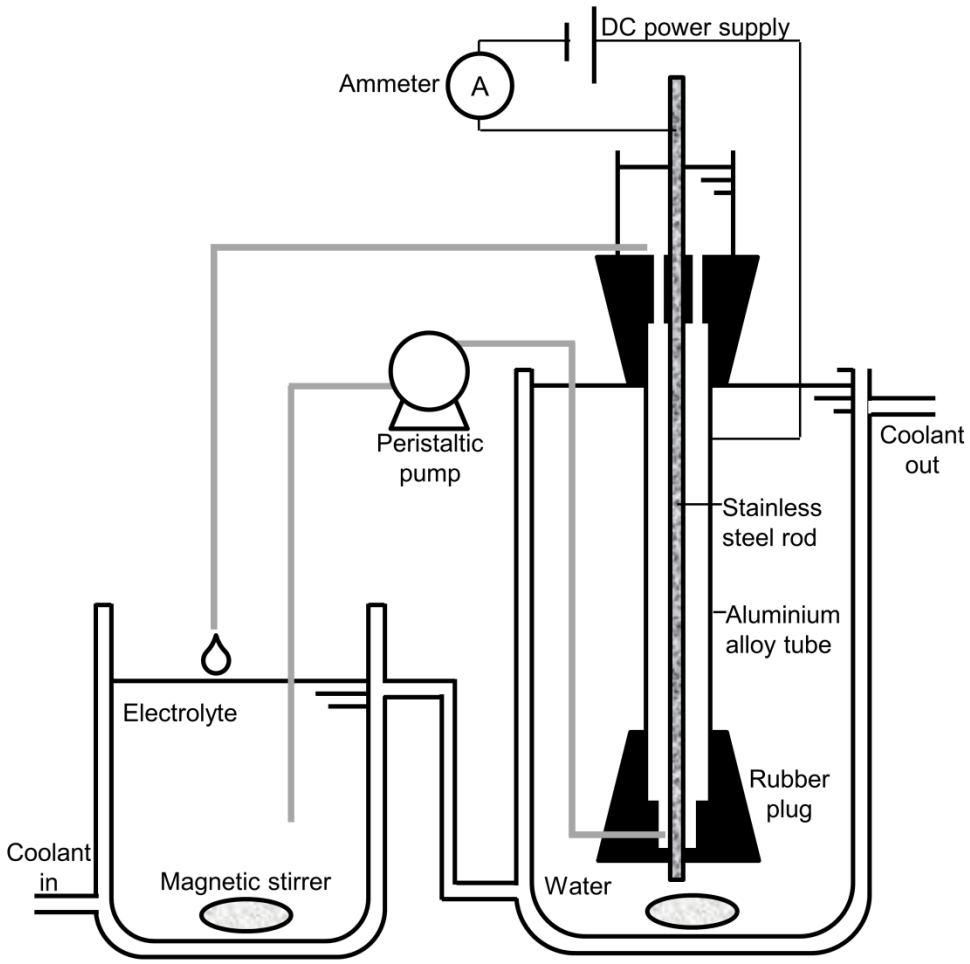

Figure 3.15 The schematic of the experimental set-up for anodization of aluminium alloy tubes. The electrolyte is recirculated via the inner side of the aluminium alloy tube. The temperature is controlled by coolant using double jacketed beakers.

Potentiostatic anodization was performed to fabricate symmetric membranes, in the range from 10 V to 50 V, using the anodization conditions within the self-ordered regime of flat disc AAMs. Due to overheating, anodization was not performed beyond 50 V. There was a trial on anodization at 80 V with reduced concentration of oxalic acid, 0.1 M rather than the commonly used 0.3 M. This resulted in a less-ordered membrane with less orderliness as discussed in Section 6.1. The anodization was performed from 10 to 24 hours, depending on the voltage, to obtain mechanically robust membranes.

Table 3.1 The conditions of anodization for symmetric membranes.

Geometry	Applied voltage (V)	Electrolyte	Temperature (°C)	Time[a] (hr)
Flat	25	0.3 M oxalic acid	13	14
	30		13	14
	40		13	13
	50		13	10
	60		10	10
	70		5	6
	80		0	4
Tubular	40	0.3 M oxalic acid	13	13
	50		13	10
	10	1.0 M sulphuric acid	0	24
	12		0	20
	15		0	18
	20	0.5 M sulphuric acid	0	12
	25		0	10

[a] For flat membranes, this refers to the 2nd-step anodization time.

3.2.3 Post treatment

After the anodization, similar to flat disc AAMs, the residual aluminium was removed by copper chloride (II) to expose the outer surface of the anodic alumina. However, to enable easy handling of the membrane, 2 cm length of residual aluminium at both ends of the tube was masked by adhesive tape. So, only the middle 5 cm of the anodized oxide layer was exposed (Figure 3.16).

The electrochemical detection method could not be used to control the pore opening process for tubular AAMs. This is due to the difficulty of insulating the aluminium substrate from current conduction. Therefore, to investigate the optimum time for the removal of oxide barrier layer, after anodization, the aluminium was removed with 1 cm interval where the other was masked by adhesive tape (Figure 3.17). Next, during pore-opening in phosphoric acid, each bar was exposed to phosphoric acid to different time intervals. The optimum time for pore opening was finally determined after observing each sample using electron microscope. From this experiment, it was also found that the oxide

barrier layer of tubular AAMs was more susceptible to acid attack, and hence the pore-opening was performed at room temperature in contrast to that of flat disc AAMs.

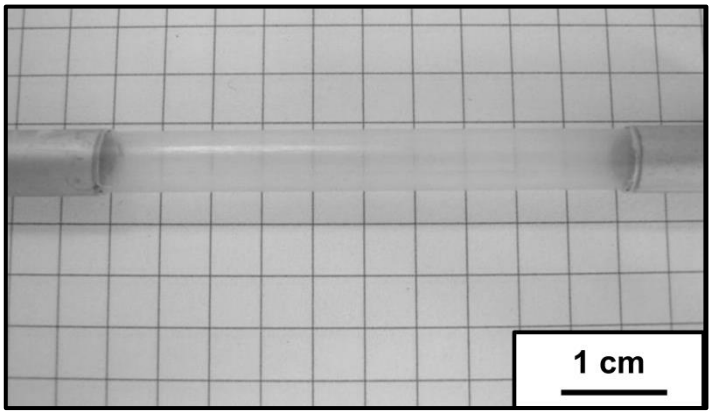

Figure 3.16 A finished tubular AAM sample, with a 50 mm long middle section where residual non-anodized aluminium and oxide barrier layer have been removed.

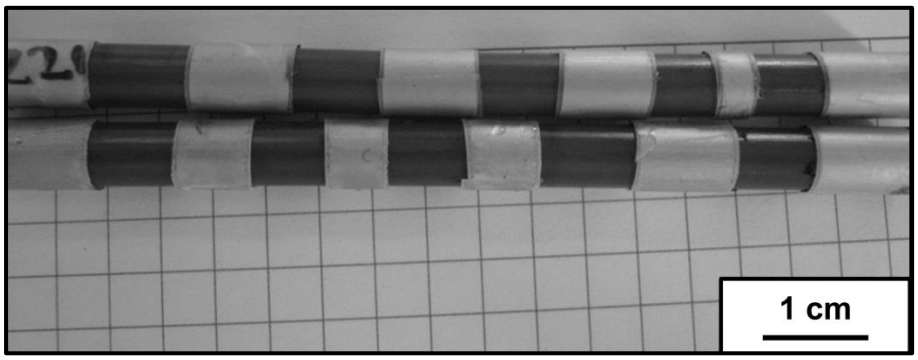

Figure 3.17 A sample made to investigate the optimum time for pore opening.

3.3 Asymmetric membranes

For anodization below 10 V, even a long period of time does not yield a sufficiently thick membrane that is robust enough to be handled. Therefore, asymmetric membranes were prepared in both flat disc and tubular form, where the former was prepared for morphological studies and the latter for testing ultrafiltration performance. The procedures of fabrication were similar to those described above, apart from the control of applied voltage. While potentiostatic anodization was performed to fabricate symmetric membranes, asymmetric structure can be achieved by tuning the applied voltage.

In this work, two methods of applied voltage reduction were used to decrease the pore diameter, as shown in the anodization voltage profile in Figure 3.18. The first method was proposed by (Meng *et al.*, 2005). This method is based on the correlation between pore density and anodization voltage (Nielsch *et al.*, 2002):

$$Pore\ density \propto \frac{1}{\sqrt{U}} \qquad 3.6$$

Based on this, the stem pores (support layer) were formed by an initial potentiostatic anodization. To create multiply branched (n number of branches), the applied voltage was then reduced in a sudden manner by a factor of $n^{-0.5}$. This method can also be used to create several levels by multiple stages of sudden reduction of applied voltage. A caution in using this method, when the voltage reduction is too large, the field-assisted dissolution of oxide barrier layer during anodization will be slowed and hence a longer period of time is needed to dissolve the thicker oxide barrier layer formed in the previous voltage. To resolve this problem, the sample was immersed in a phosphoric acid solution to thin the oxide barrier layer. Nevertheless, it will cause pore-widening at the top surface.

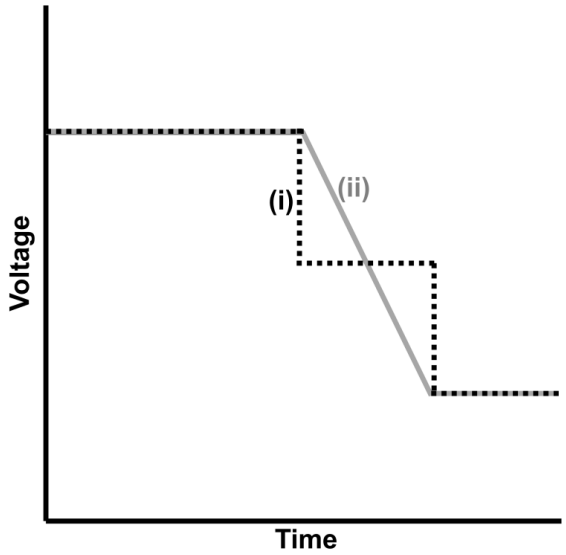

Figure 3.18 Two anodization voltage profiles showing the different methods to develop asymmetric pore structure: (i) by sudden applied voltage reduction to create multiple branched pores and (ii) by gradual anodization voltage reduction to create continual pore branching before reaching final anodization voltage.

The second method involves a slow constant anodization voltage ramp down rate to the final anodization voltage. In this method, the voltage ramp down rate has to be adequately slow, as previous studies (Lee *et al.*, 2012) have shown

that fast ramp rates (> 0.1 V s^{-1}) lead to disordered structures due to an insufficient time for the pore structure to reorganise, especially towards the lower end of the anodization voltage values. In both methods, if the stem pores were formed at a higher voltage in oxalic acid and subsequent voltage reduction will lead to final voltage less than 25 V, it is suggested to change the electrolyte to sulphuric acid to obtain optimum orderliness of pore structure. In the current work, to avoid this procedure for tubular asymmetric AAMs with very low final anodization voltage, the stem pores were anodized at 18 V. Hence, only a single electrolyte, 1.0 M sulphuric acid, is used in this process.

Table 3.2 The conditions of anodization for asymmetric membranes.

Geometry	Applied voltage (V)		Electrolyte	Temperature (°C)	Ramp rate (V s^{-1})	Time (hr)	
	Initial	Final				Initial	Final
Flat	40	20	0.3 M oxalic acid	13	0.2[a]	10	2[a]
	40	5		13	0.01	10	4
Tubular	18	5	1.0 M sulphuric acid	0	0.005	12	4
	18	2		0	0.005	12	4
	18	1		0	0.005	12	4

[a] This membrane's asymmetric structure was achieved by a quick ramp to 20V with an intermediate stage of 28 V. The voltage was maintained for 2 hours before being ramped down to final 20 V. All other asymmetric membranes were fabricated by gradual voltage reduction at the ramp rate of 0.001 V s^{-1}.

3.4 Surface modification

The pristine AAMs are highly hydrophilic. It is the interest of this work to study the transport properties of the membrane with similar structure but different surface chemistry. Two surface modification techniques were used in this work, namely silane functionalization chemistry and chemical vapour deposition (CVD).

3.4.1 Chemical vapour deposition (CVD)

CVD involves the dissociation and/or chemical reaction of gaseous reactants in an activated (heat, light, plasma) environment, followed by the formation of a stable solid product, normally in the form of powders or thin films (Choy, 2003). In

this work, high temperature (at least higher than 600 ºC) was needed to activate the decomposition of the precursor. However, the pristine AAMs produced by electrochemical anodization are amorphous (Mardilovich *et al.*, 1995). It is well-known that alumina undergoes numerous phase transformations above 400 ºC with significant changes in the specific volume (Figure 3.19). As a result, the AAMs tend to bend and roll-up during CVD due to phase change of alumina under rapid temperature rise, as shown in Figure 3.20.

This problem, however, can be resolved with an annealing treatment in air at temperatures higher than that of CVD. For flat disc AAMs, they were placed between two α-alumina plates to keep them flat. The heating rate must be very slow, down to 1 ºC min^{-1}, so that the thermal stresses can be successfully relieved and the volume expansion is slow enough to be counteracted by the compression induced by the alumina plates.

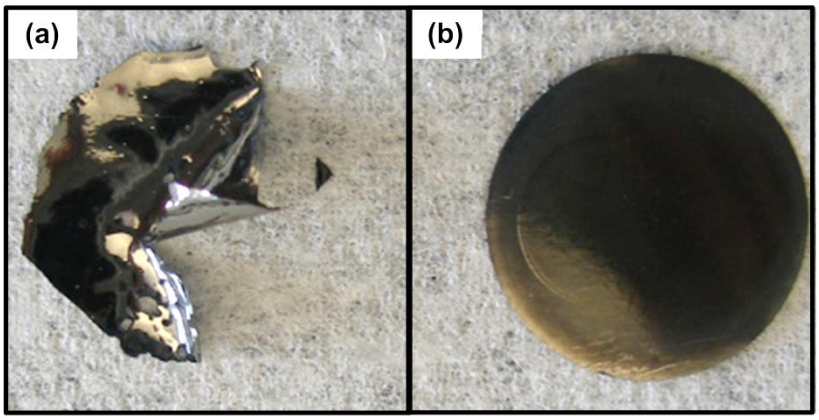

Figure 3.19 Effect of membrane pre-annealing on the shape after CVD deposition: (a) without annealing; (b) pre-annealed at 700 ºC. (Mattia, 2007).

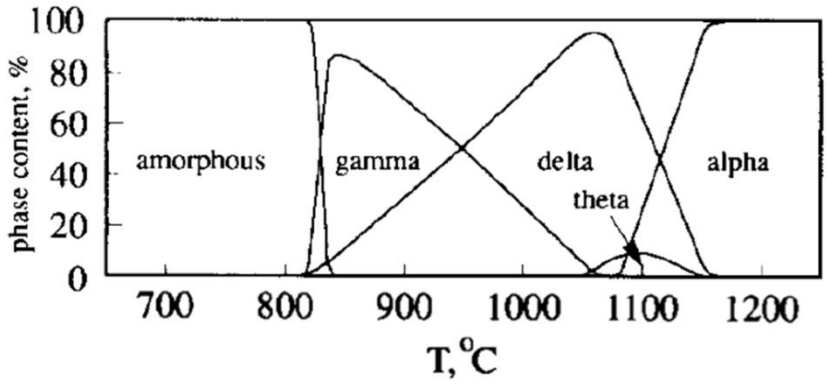

Figure 3.20 Crystal structural phase change of alumina at different temperature. Picture was adapted from Mardilovich *et al*., 1995.

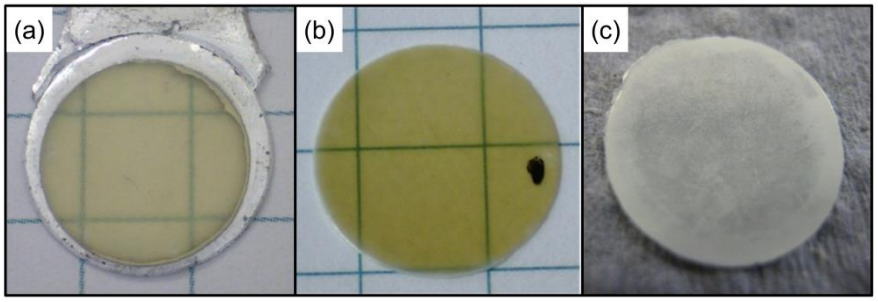

Figure 3.21 Pictures of (a) non-annealed membrane; (b) membrane that is annealed upto 700 °C and; (c) membrane that is annealed upto 1200 °C. At 1200 °C, the membrane turned into white colour from transparent due to the phase transformation into α phase.

As shown in Figure 3.21, the AAMs have been annealed upto 1200 ºC, turning the alumina into the most stable α-alumina phase. There is no further phase transformation occurring beyond this temperature. However, there are advantages and disadvantages to transform the alumina to a highly crystalline form. The main advantage would be that α-alumina is very stable and chemically resistant. However, the highly crystalline phase will increase the brittleness of the membrane for handling. Besides, the pores tend to lose their circularity and polygonise. For relatively low annealing temperatures (600 to 750 ºC), this effect is insignificant due to the alumina crystal structure being still in transitional phase, and hence retaining pore circularity. For higher annealing temperature, i.e. the more crystalline the membrane is, the polygonisation is more evident (Figure 3.22). Therefore, the AAMs were annealed upto 700 ºC - 900 ºC in this work, depending on the target temperature of the subsequent CVD processes.

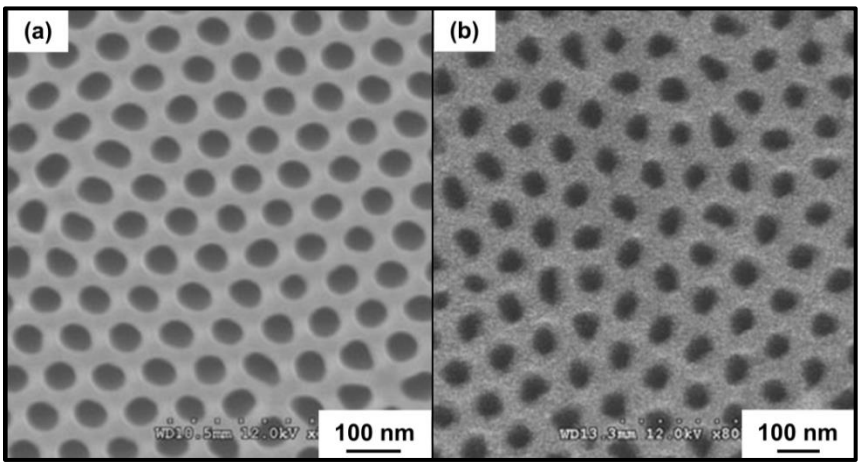

Figure 3.22 SEM micrographs of (a) as anodized membrane showing circular pores, 90,000X magnification and (b) membrane annealed at 1200 °C showing polygonised pores, 70,000X magnification.

In this work, a non-catalytic CVD process was used to deposit homogeneous thin carbon film inside the pores of the AAMs. Figure 3.23 shows schematically the apparatus built for the CVD process. The membranes, as the substrates for deposition, were held perpendicularly to the gas flow via a quartz holder (Figure 3.24). This was then placed into a 1.5 m long quartz tube reactor with a diameter of about 25 mm. Next, the quartz tube reactor was inserted into a tubular furnace (Carbolite, TZF 12/38/850), where the substrates were positioned such that they are in the middle of the heating zone. The tube was connected to gas sources, in this case, ethylene as carbon source, argon and helium as inert gas, which are regulated using mass flow controllers (Omega, FMA 5400/5500). The other end of the quartz tube was connected to a silicone oil containing bubbler. Its role is to prevent the back flow of flue gas, before being vented off via the fume system.

Once the set-up was ready, the reactor was purged using 20 sccm Argon (BOC, research grade, 99.9995%) for about an hour. Then the heating programme was started. The reactor was heated to 670 ºC at a rate of 15 ºC min^{-1}. When it reached 670 ºC, the gas feed was switch to a mixture of ethylene (BOC, research grade, 99.92%) and helium (BOC, research grade, 99.9995%), with a flow rate of 6 sccm and 14 sccm, respectively (Mattia, 2007). This was usually maintained for 6 hours; however, this could be varied to obtain different thickness of coating. The cooling was performed under argon. When it reached room temperature, the membranes were removed from the quartz tube and the membranes were uniformly coated with a thin layer of carbon (Figure 3.25).

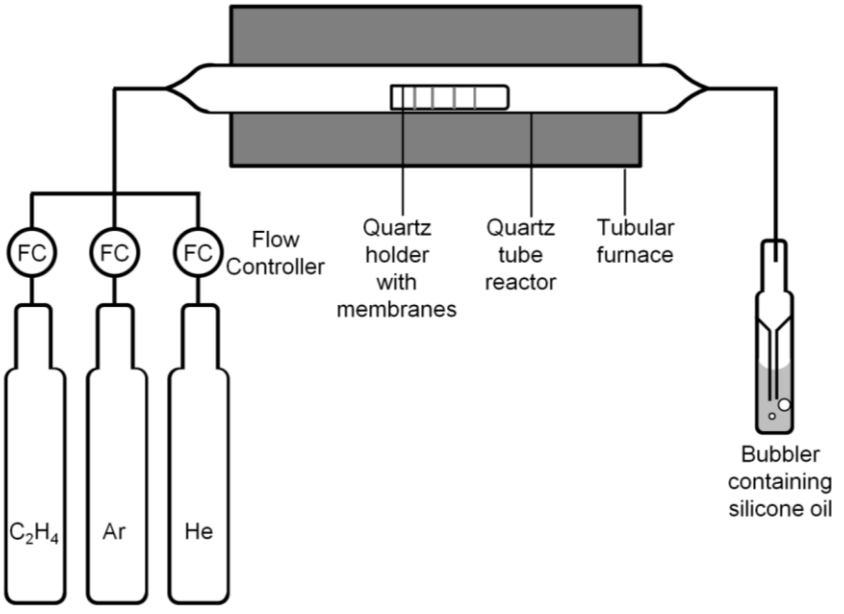

Figure 3.23 Schematic of the CVD apparatus for deposition of carbon film.

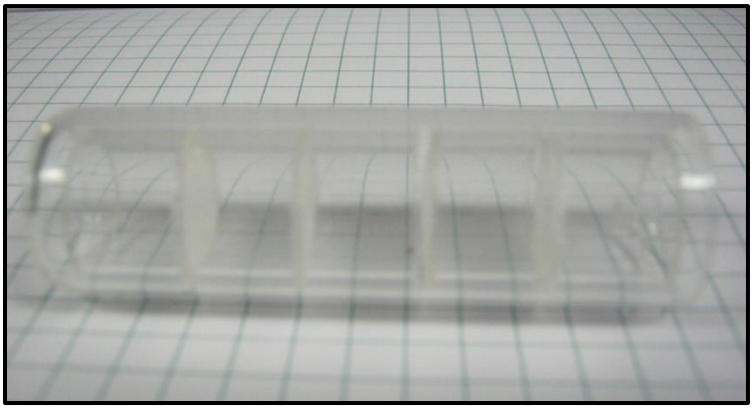

Figure 3.24 AAM substrates held in a quartz holder.

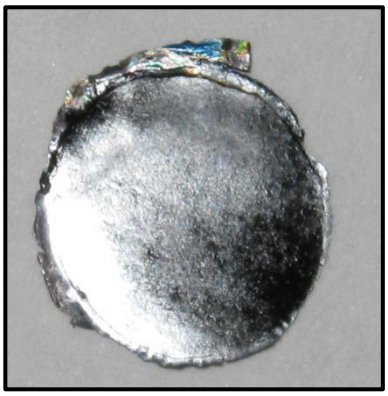

Figure 3.25 Carbon coated AAM.

During the CVD process, the reaction occurring is:

$$C_2H_{4(g)} \rightarrow 2C_{(s)} + 3H_{2(g)} \quad 3.7$$

While the equation above describes the overall reaction of the decomposition of ethylene, there were actually multiple complex intermediate reactions occurring. In particular, soot was consistently being produced as a by-product, which mostly consists of benzene and polyaromatic hydrocarbons (Lucas and Marchand, 1990). A mass spectroscopy analysis of the decomposition for methane revealed the simplified sequence of the intermediate reaction, which is in the order of:

$$methane \rightarrow benzene \rightarrow polyaromatic\ hydrocarbons \rightarrow carbon \quad 3.8$$

Although this study has not been conducted for the decomposition of ethylene, but a similar reaction path is expected. AAMs within the carbon coated membranes can be dissolved by hydrofluoric acid (Cheng *et al.*, 2005) or sodium hydroxide (Martin, 1994) to release the carbon nanotubes. This was done in this

work to verify the coating was homogeneous through the thickness of the AAMs. In short, crushed coated AAMs were immersed in a stirred, 1 M sodium hydroxide solution and heated above 100 °C in refluxing conditions. Nevertheless, the pre-annealing before the CVD process made the alumina templates more crystalline, i.e. more chemically resistant. Therefore, it posed more difficulty to completely remove the alumina templates. Ultra-sonication can significantly speed up the dissolution process. Once the solution cooled down to room temperature, the nanotubes were purified and collected by using a membrane filter under vacuum suction.

3.4.2 Silane functionalization chemistry

Silanes are silicon-containing compounds that have a hydrolytically sensitive centre that can react with inorganic substrate to form stable covalent bonds and possess an organic substitution which alters the surface properties of treated substrates (Lim *et al.*, 2006). Silane chemistry is therefore a popular technique to modify the surface energy or wettability of substrates under normal conditions without imparting chemical reactivity to the substrates.

Most of the widely used organosilanes have one organic substituent and three hydrolysable substituents such as halogens, alkoxy or alkyl groups. In this work, a number of trichlorosilanes were used. As shown in Figure 3.26, the functionalization by silane chemistry involves a number of steps. It begins with hydrolysis of the three labile groups firstly. It is then followed by the condensation of silanes into oligomers, which subsequently form hydrogen bonding with hydroxyl groups on the substrate. Finally, the curing will favour the formation of covalent linkage with the substrate (Abel *et al.*, 2006). Other than functionalization by single type of silane, mixed silanes functionalization has also been performed. By controlling the co-adsorption of different silane molecules with different organic substituents, the surface free energy and wettability can be finely tuned (Lim *et al.*, 2006).

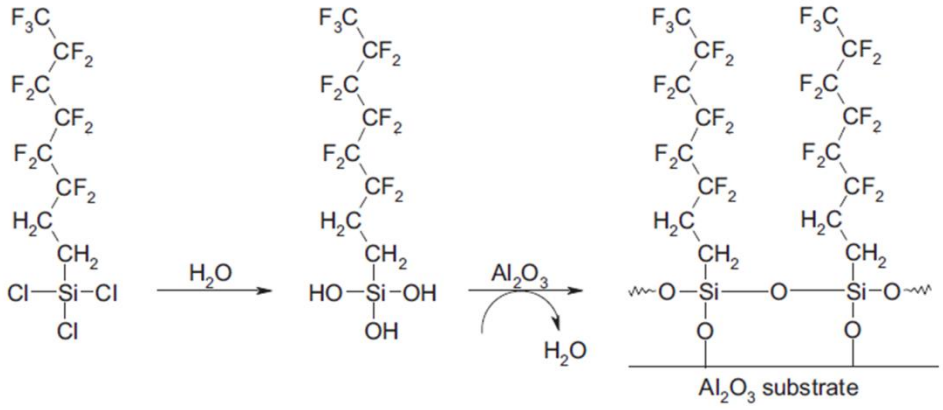

Figure 3.26 Schematic representation for the surface modification of alumina using perfluorinated octyltrichlorosilane.

In the current work, the AAM samples contain hydroxyl groups on the surface. There were previous reports that AAMs' surface can be saturated with hydroxyl groups by boiling them in water, but our result by using perfluorinated octyltrichlorosilane has shown successful surface modification without this step. The samples were immersed in a solution containing about 0.10 to 0.25 % of a single component or a mixture of trichlorosilanes (See Table 3.3) in 40 ml n-hexane. They were placed on a roller mixer to improve mass transfer. After an hour, they were rinsed by hexane to remove excessive silanes that were present on the surface. Finally, the samples were ready after curing in an oven at 100 ºC for an hour.

Table 3.3 Information of trichlorosilanes used in surface modification.

Silane	Chemical structure	Contact angle[a]	Reference
Perfluorinated octyltrichlorosilane	$CF_3(CF_2)_7SiCl_3$	109°	(Aran *et al.*, 2011)
Butyltrichlorosilane	$CH_3(CH_2)_3SiCl_3$	98° ± 2°	(Kluth *et al.*, 1997)
Ethyltrichlorosilane	$CH_3CH_2SiCl_3$	82° ± 2°	(Peor *et al.*, 2008)
Methyltrichlorosilane	CH_3SiCl_3	76° ± 2°	(Wasserman *et al.*, 1989)
3-Cyano-propyltrichlorosilane	$CN(CH_2)_3SiCl_3$	59°	(Nitzan and Margel, 1997)

[a] The contact angle obtained from the literature was self-assembly monolayer coating on non-porous alumina or silicon substrate.

3.5 Membrane characterisation

It is important to characterise the pore structure of the membranes, in order to correlate pore structure parameters, such as porosity, mean pore diameter and thickness with the transport properties of the membranes. Besides, the wetting property of the membranes was also investigated to observe the influence of surface chemistry to fluid transport phenomena.

3.5.1 Scanning electron microscopy (SEM)

There is a number of widely-used established techniques for membrane pore structure characterisation, such as liquid-liquid displacement, gas adsorption porosimetry and mercury porosimetry. For statistically reliable result, sufficient amount of sample in term of mass or surface area is needed. This therefore limited the applicability of the above method for AAMs, which each sample only has a mass of hundreds of milligram. Therefore, the pore structure was observed directly under scanning electron microscopy (SEM).

AAMs are ceramic materials and hence non-conductive, which possess a lot of challenges for SEM imaging. Coating of conductive materials, i.e. gold or platinum was not an option here due to the coating thickness will alter the pore diameter and hence affect the measurement accuracy. In this work, field emission SEM (FE-SEM) was used to improve the resolution of imaging, especially for membranes with smaller mean pore diameter. Two FE-SEM were used in analysing samples, the first one was a Hitachi S-4300 at the Physic Department, University of Oxford whereas the second one was a JEOL 6301F at the Microscopy and Analysis Suite, University of Bath. Low accelerating voltage and short working distance settings were used to minimise charging on the membranes, negating the need for a conductive coating. At low accelerating voltage, both machines can provide the resolution down to about 5 nm. Figure 3.27 shows one of the examples of severely distorted micrographs due to the non-conductive nature of AAMs.

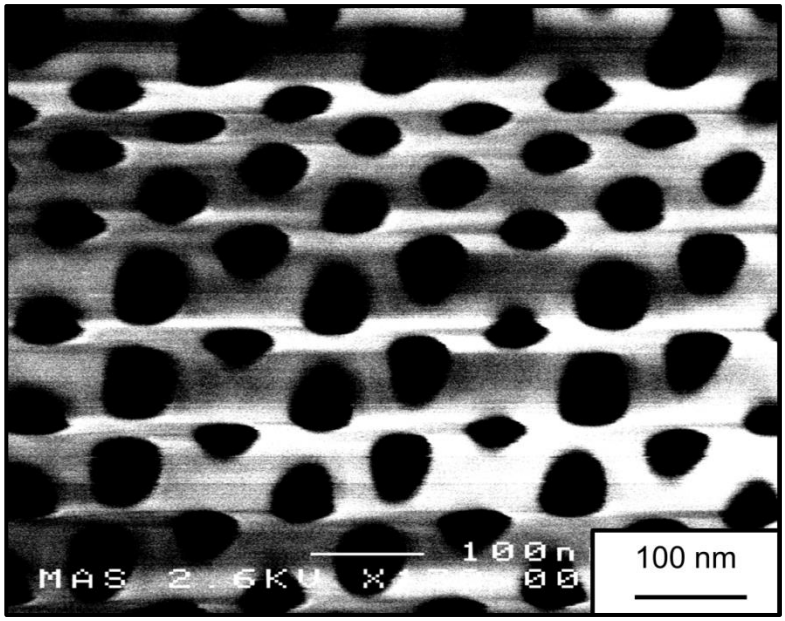

Figure 3.27 An example of distorted image due to severe charging effect, 180,000X magnification.

3.5.2 Image analysis

Statistical image analysis of SEM micrographs using ImageJ software yielded the pore structural characteristics, i.e pore diameter, pore circularity, porosity and pore size distribution. The quality of the SEM micrographs is crucial to ensure accurate estimation of the above parameters; in particular, sharp focus and clear contrast between the pore and surface are desirable.

As shown in Figure 3.28, by using ImageJ, the micrographs were processed firstly by thresholding, i.e. converting greyscale image into binary (black and white) image. Then using the 'analyse particle' function, area, perimeter, feret's diameter and circularity of each 'particle' were quantified. For example, Table 3.4 shows the information obtained from ImageJ based on the particles in Figure 3.28(d), which is the bracketed segment of Figure 3.28(c). Due to feret's diameter being the longest distance between any two tangents contacting the pore boundary, it overestimated the effective pore diameter. This, the feret's diameter was compensated by circularity to obtain the effective pore diameter, which give values in good agreement with previous reported literature (Section 4.2.4). When calculating the pore diameter, the pores at the edges of the bracketed area are excluded, whereas for porosity estimation, they are included.

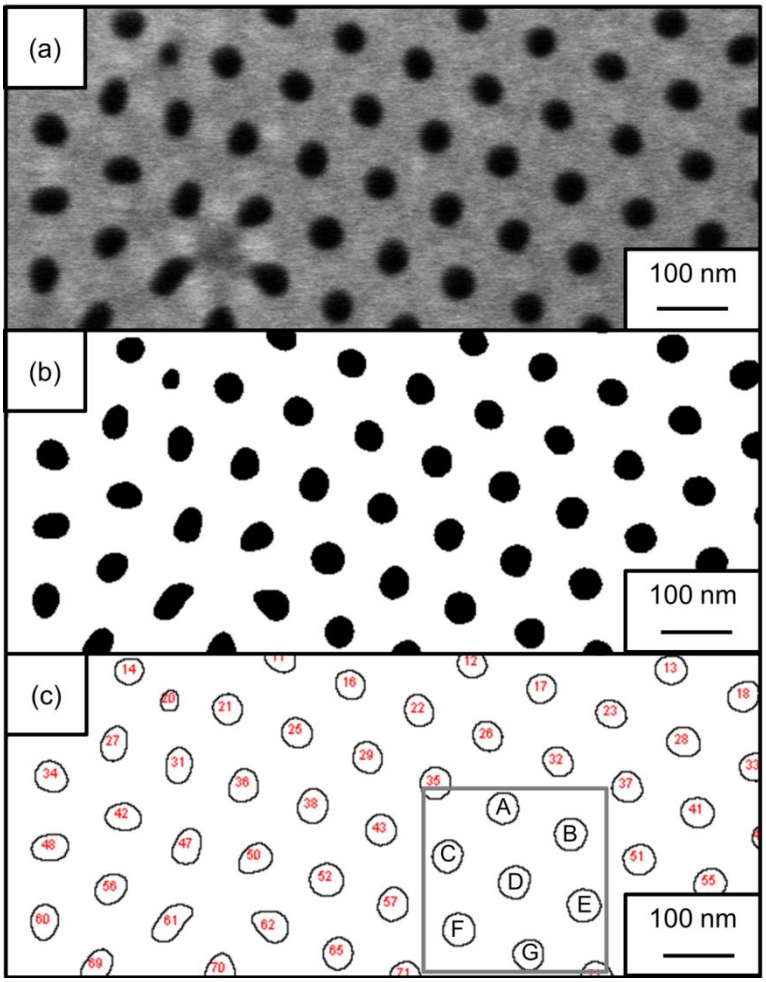

Figure 3.28 (a) Original SEM micrograph of a 40 V AAM; (b) after 'thresold' processing and; (c) analysing 2-D particles based on processed imagewhere information of each pore was presented in Table 3.4, all images have 130,000X maginification.

Table 3.4 Examples of information obtained from image analysis based on Figure 3.28.

Pore label	Area (nm^2)	Perimeter (nm)	Feret's diameter (nm)	Circularity	Effective pore diameter (nm)
A	1683	149	50	0.95	47
B	1887	159	52	0.94	49
C	1775	154	50	0.94	47
D	1630	149	48	0.93	45
E	1749	152	50	0.95	47
F	1782	152	51	0.97	50
G	1795	154	50	0.95	47

3.5.3 Contact angle measurement

Contact angle measurement was performed to study the wettability of the membrane, especially the effect of surface modification. For this, a basic system, which a USB digital microscope with upto 200 times magnification (Veho VMS-004 Discovery Deluxe) is the major component, was used to perform the measurement. An LED light was used for back illumination, providing a clear contrast to determine the contour of a liquid droplet. The sample stage comprises a lab jack that allows the adjustment of height and a spirit level to ensure the plan was flat.

Based on sessile drop technique-goniometer method (de Gennes *et al.*, 2004), a 5 µl of liquid droplet was deposited by a pipette (Poulten-Graf, R780/O) pointed vertically down onto the sample. Small amount of liquid was used, was to minimise the effect of gravity on the shape of the liquid droplet. Then, high resolution images were captured using the digital microscope. Experiments were repeated at least three times on different occasions or locations on the surface for each sample. Finally, the images were analysed using ImageJ software with DropSnake package. This is a semi-manual approach where the contour of the droplet was identified manually where the software determines the tangents of the contour and finally the contact angle.

3.5.4 Membrane roughness measurement

Gwyddion (v2.31) is a modular programme for scanning probe microscopy (SPM) and is used primarily to analyse AFM data. AFM Images can be used within Gwyddion, where they can be made sharper and statistical measurements can be analysed (Bartók *et al.*, 2009). Dr. Hannah Leese has kindly provided the AFM data for the surface roughness measurement. The average roughness, Ra, denotes the arithmetic average of the absolute values of the surface height deviations measured from the centre plane. The root mean square roughness, R_{RMS}, is the standard deviation of the average roughness (Hobbs *et al.*, 2006). They were determined from each scan line for 5 µm x 5 µm AFM images, where the pores excluded from the estimation.

4. Flat AAMs: Morphology

As described in the literature review, the development of flat AAMs is relatively mature (Masuda *et al.*, 1997). Recent development has been focusing on its application in nano-fabrication and therefore there were several attempts in manipulating the membrane structure, i.e branched pores (Petukhov *et al.*, 2012; Meng *et al.*, 2005), perforated pores (Losic, 2009), modulation of pore diameter (Lee *et al.*, 2008) and also other structural modifications.

The use of AAMs is the focus of this project, and hence the membrane material itself forms the backbone of this research work. Therefore, it is crucial to analyse the structure of the AAMs, and also to obtain experience in fabricating desirable membranes by controlling the processing parameters. The detailed procedures of AAMs fabrication have been clearly described in Chapter 3. This chapter provides an in-depth analysis of the pore structure of AAMs obtained from different anodization conditions. AAMs with controlled pore structure were successfully fabricated with high reproducibility. It provides high quality specimens in various experiments which are reported in the subsequent chapters.

4.1 Stability of anodization

Anodization is the crucial step of the formation of porous structure. In this work, potentiostatic anodization was performed. The current density profile, not only indicates the structural evolution of pore formation, but also provides a hint of the quality of the porous structure formed. Therefore, in all cases, a stable current density profile is desirable for potentiostatic anodization (Figure 2.7). As can be seen in Figure 4.1, the anodization current density curves have similar contour as suggested by the pore initiation mechanism shown by Figure 2.7, i.e. the current density quickly drops due to the resistance caused by the initial formation of barrier oxide, followed by a rise due to the formation of porous oxide as a results of field assisted dissolution. Subsequently, the current density gradually decreases as the growth competition among the neighbouring pores reduces and eventually reaches steady-state.

As expected, the overall current density is higher with increasing anodization voltage, except for 70 V which has an equilibrium current density that is lower than that of 60 V. This is attributed to the lower temperature used for anodization

than that of 60 V (see Table 3.1), effectively lowering its rate of reaction. The anodization at 40 V and 50 V, being the optimum condition for oxalic acid electrolyte (see Section 4.2 for more information), has a steady-state current density ranges between 3 to 5 mA cm^{-2}, in good agreement with previous literature (Lee *et al.*, 2006).

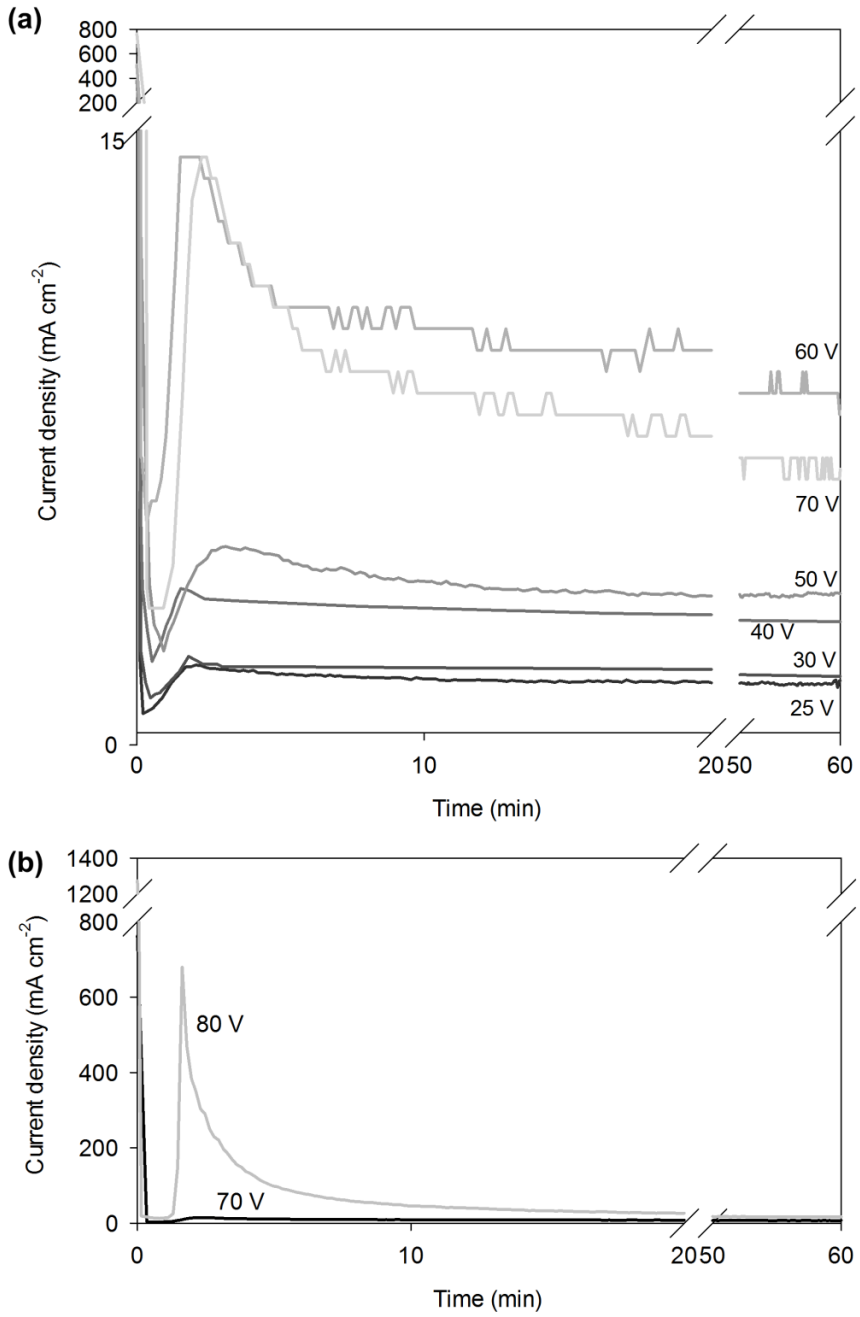

Figure 4.1 (a) Typical first 60-minute current density profiles of aluminium anodization at different voltages and (b) 80 V anodization current density profile. The latter was excluded due to the relatively high current density as can be compared with the 70 V current density profile which was also plotted in (b) for comparison. These current density profiles were obtained according to the flat AAO anodization conditions shown in Table 3.1.

As shown in Figure 4.1(b), the current density for anodization at 80 V is particularly high, as driven by the high voltage, even at low temperature. For stable anodization, effective heat removal is required. Other than burning or electric breakdown which has been discussed in Section 2.2.6.2, undesirable nano-structure could be formed if the anodization was not well controlled. As shown in Figure 4.2, some fibrous structure can be observed growing on top of the AAM surface. The porous structure can be seen underneath the fibrous structure. This is formed as a result of temperature effects and the length of anodization time, which causes the degradation of the porous structure formed initially (Zhang *et al.*, 2005).

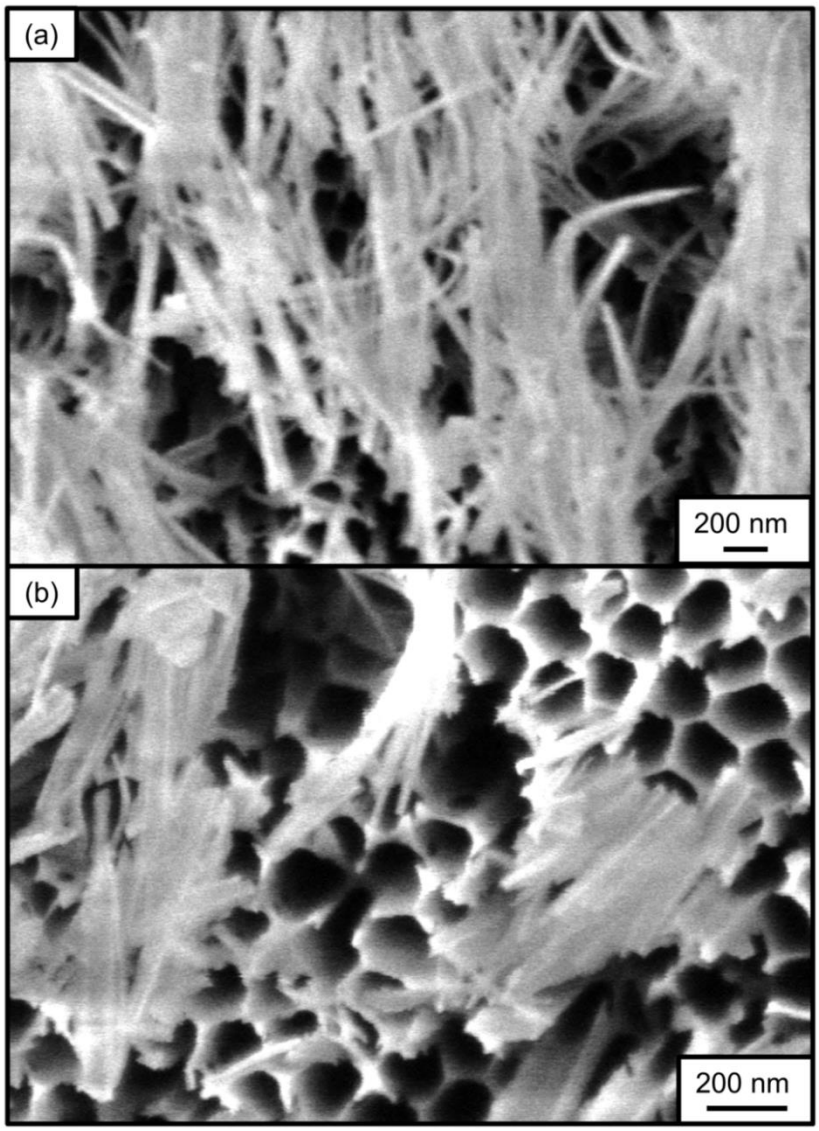

Figure 4.2 SEM micrographs showing (a) a larger area (33,000X magnification) and (b) a closed up view (60,000X magnification) of the top surface of an AAM fabricated at 80 V at 5 °C in 0.3 M oxalic acid. At this condition, undesirable fibrous structure was formed on the top surface.

As described before (Section 2.2.6.1), electro-polishing is an important pre-treatment procedure. The anodization current density profile can reflect the quality of the electro-polishing in providing a smooth surface for pore-initiation. As shown in Figure 4.3, the initial stage of anodization for poorly electro-polished aluminium substrate has a relatively low current density, due to the incomplete removal of the ambient oxide layer on the surface by electro-polishing. Despite the rise in current density after pore formation, its steady-state current density is consistently below that of a well electro-polished sample. This is mainly due to lower pore density obtained for rough aluminium surface (Wu *et al.*, 2002).

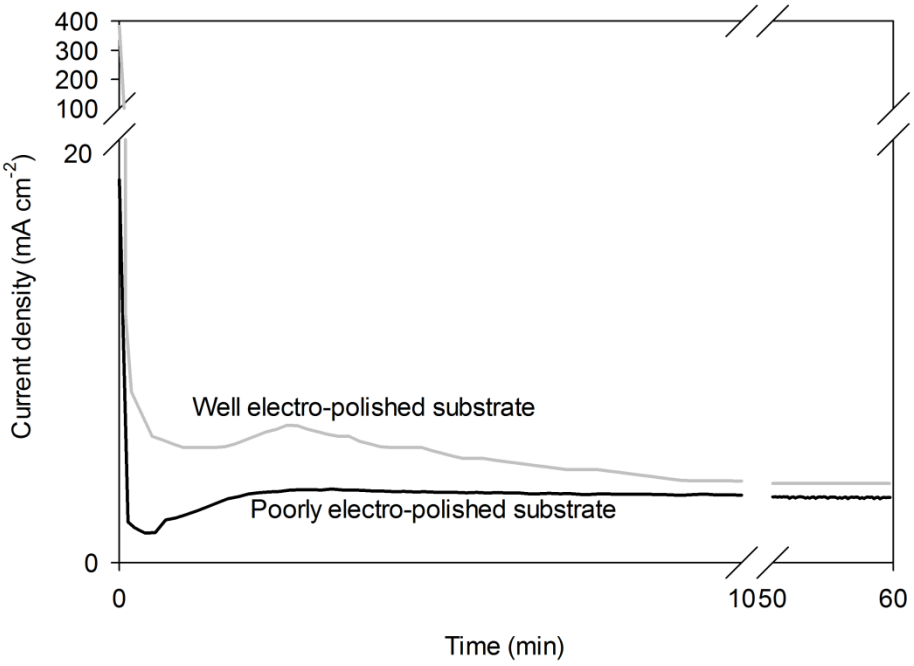

Figure 4.3 Comparison between the anodization current density profiles of AAMs formed on well and poorly electro-polished aluminium substrates. The former sample has a higher current due to lower resistance as a result of good polishing.

During the preparation of anodization, it is very important to provide good sealing around the aluminium substrate. Poor sealing can result in the exposure of the back of the aluminium substrate to the acid electrolyte. In this case, anodic oxide can form at the back of the substrate, causing resistance for the subsequent removal of residual aluminium (Figure 4.4(a)). In extreme cases, if scratches or pointed defects are present at the back of the aluminium substrate, a local field-enhanced dissolution effect will result in a high consumption rate of aluminium, as can be seen in Figure 4.4(b). Typical anodization current densities of these two scenarios are shown in Figure 4.5.

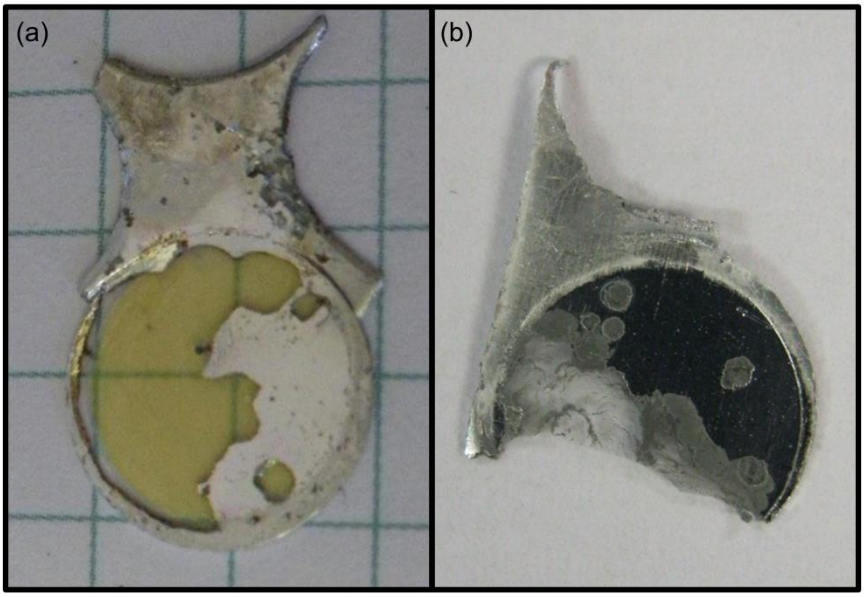

Figure 4.4 Non-usable AAM samples formed due to (a) mild acid attack and (b) aluminium consumption.

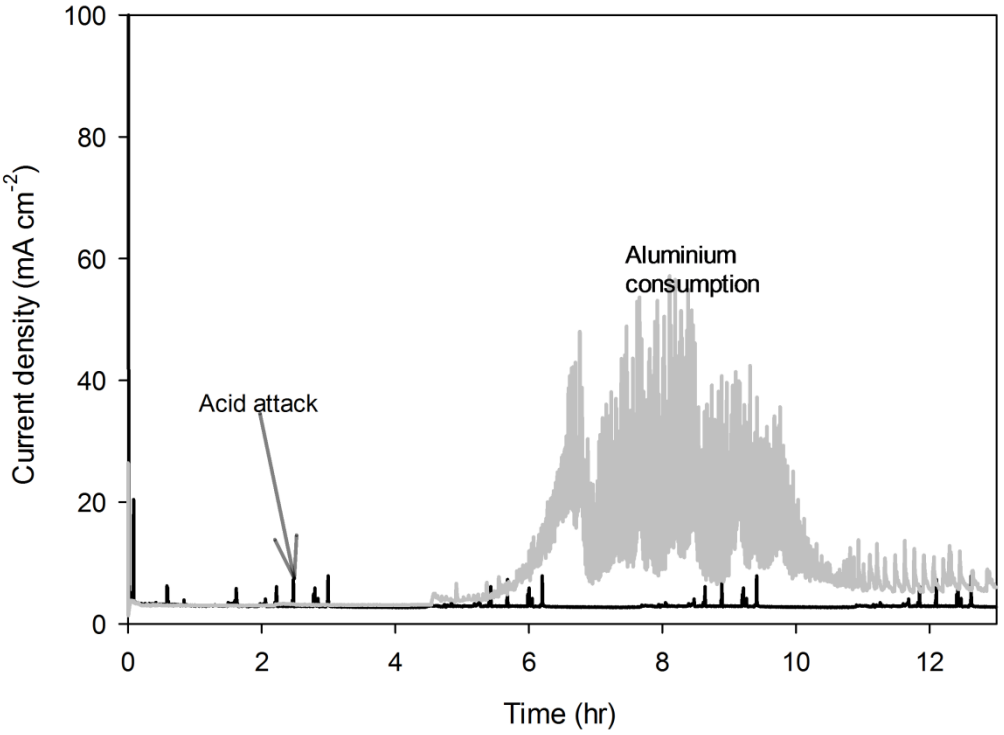

Figure 4.5 Typical anodization current density profiles formed due to the occurrence of mild acid attack or aggressive aluminium consumption.

4.2 Symmetric AAM morphology

Field emission SEM is the main technique used to directly investigate the morphology of AAMs fabricated. In particular, the uniform pore structure and constant cross-section of the AAMs make it feasible and reliable to quantify the pore diameter and porosity via image analysis technique described in Section 3.5.2.

4.2.1 AAM top surface

Top surfaces, where the anodization initiated, are visibly distinctive for AAMs fabricated from one-step and two-step anodization. As expected, the top surface of one-step anodization shows a relatively irregular pore structure (Figure 4.6). The pore shape is less circular, showing some triangular, elliptical or slightly polygonal shape. This is probably due to the equilibrium of the force balance not yet achieved. The presence of smaller pores neighbouring the bigger or major pores gives evidence of the competition of pore growth at the initial stage of anodization. This competition causes branching or blockage of pores, and hence an irregular pore structure at the top surface.

In contrast, the top surfaces of samples prepared by two-step anodization show more uniform pore structure. In particular, a two-step anodized 40 V membrane contains highly circular pores, within the packing of hexagonal cells, as illustrated in Figure 4.7(a). For a 60 V membrane, while a number of branched pores can be observed, the number of branched pores has been decreased significantly relative to the one-step anodized sample (Figure 4.7(b)). In particular, by comparing Figure 4.6(b) and Figure 4.7(b), the degree of opening for the pores is more complete and regular.

The current density profiles of first and second step of anodization are shown in Figure 4.8. In both cases, distinctive transition between the pore evolutionary stages can be observed. However, in the second step of anodization, the current density transition is faster and reaches steady-state in a shorter time. In addition, the minimum current density of the first step anodization is lower than the second step anodization. This implies the template formed during the first step of anodization accelerates the ordered pore initiation process in the second step (Gong *et al.*, 2010).

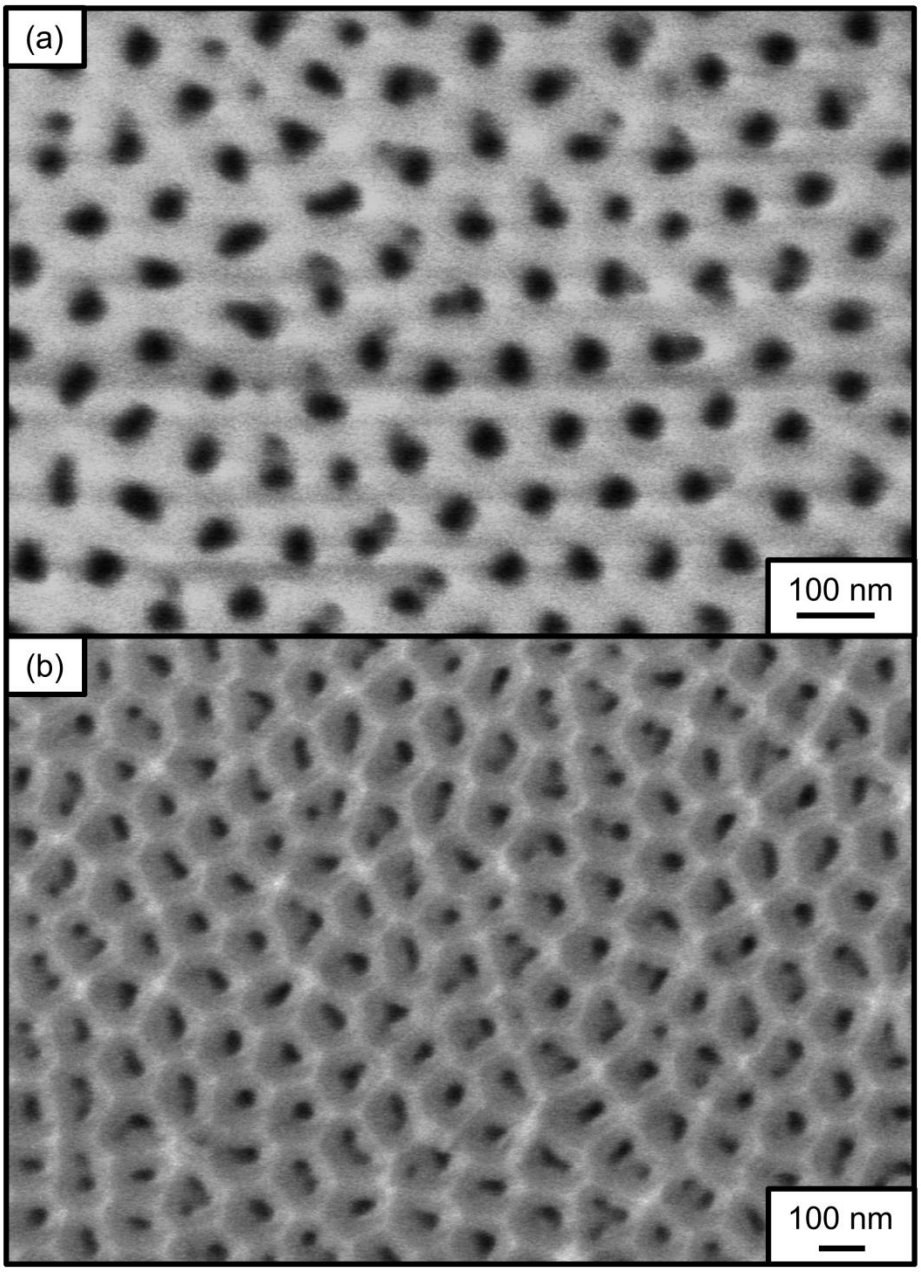

Figure 4.6 SEM micrographs showing the top surfaces of AAMs obtained by 1-step anodization at (a) 40 V (100,000X magnification) and (b) 60 V (60,000X magnification). Numerous branched pores and slightly irregular pore structure can be observed.

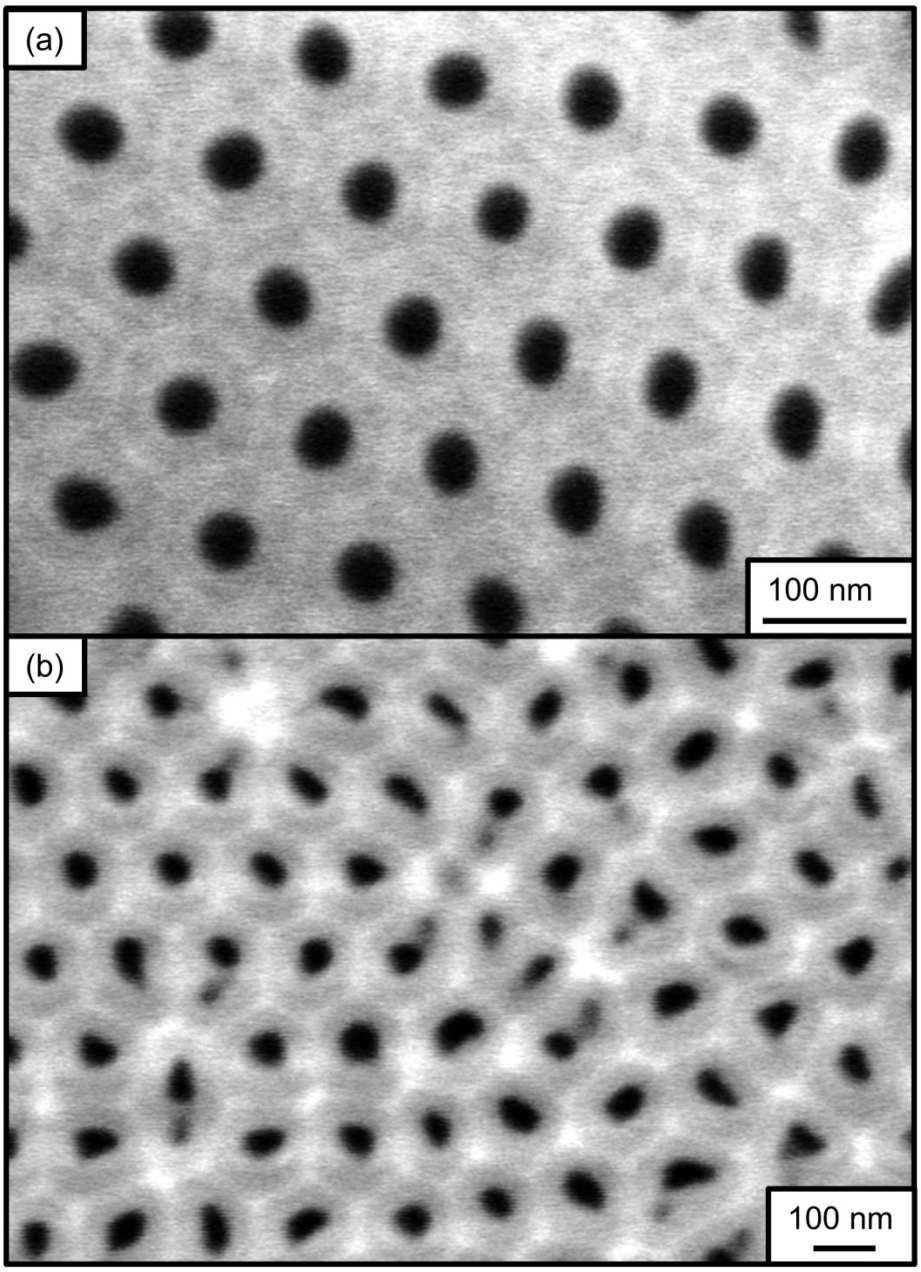

Figure 4.7 SEM micrographs showing the top surfaces of AAMs obtained by 2-step anodization at (a) 40V (190,000X magnification) and (b) 60 V (80,000X magnification). The 40 V membrane exhibits nearly ideal pore structure. For the 60 V membrane, reduced number of branched pores and more circular pore shape are obtained from 2-step anodization.

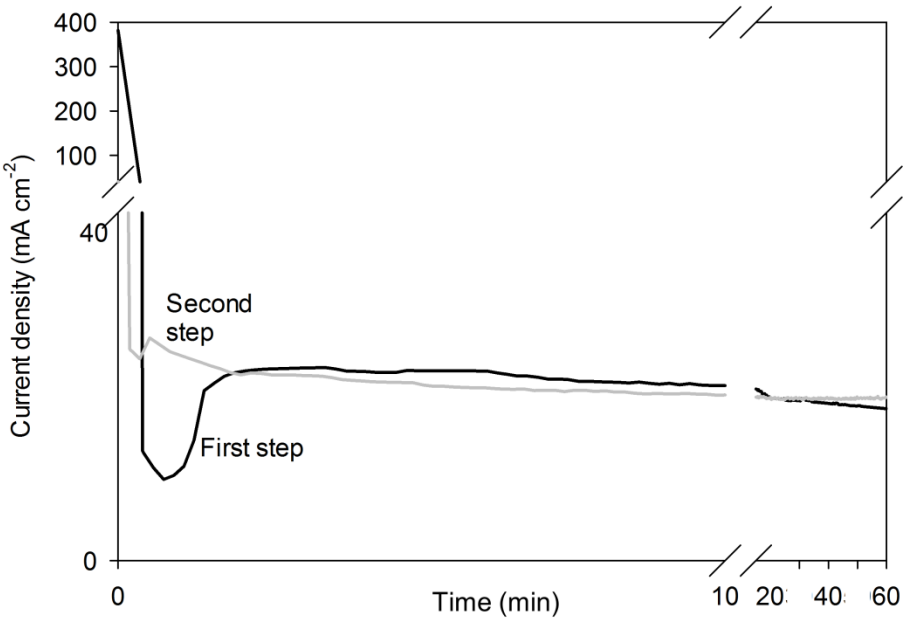

Figure 4.8 Comparison of current density profiles of by first and second step of anodization at 40 V. In second-step anodization, the current stabilises in a shorted time due to the template formed in the first step.

4.2.2 AAM bottom surface

After anodization and removal of the residual aluminium, the bottom surface of the membrane is revealed. This bottom surface, prior to wet chemical etching, is covered by a so called 'scalloped shaped' oxide barrier layer. This is shown by Figure 4.9(a). The oxide barrier layer is etched away by the exposure to acid. As mentioned in Section 2.2.6.3, an electrochemical approach was adapted to monitor the process of pore opening directly.

Figure 4.10 shows a typical current profile recorded during the etching of a 40 V AAM in phosphoric acid. The current profile is featured with a characteristic shape, with four distinctive sections that correspond to different stages of etching. At the beginning of etching, stage (i), the current stays steadily at the minimum. This confirms that the barrier oxide layer is thinning but still compact and blocking flow through the pores. At stage (ii), the plot shows an inflection of the current response with a significant increase in the current signal. This signal corresponds to the initial pore opening, with ion permeation through the etched holes in the barrier layer. The current signal increases as the barrier oxide layer is being removed, i.e. decreasing the resistance for ion transport. At stage (iii), the current profile reaches a maximum and levels off. At this point, the barrier oxide layer is completely removed and further etching (stage (iv)) will not increase further the

current. This is because further etching will only cause pore-widening, this increment in surface porosity has minimal effect in improving the ion transport. These four stages can be clearly visualised in Figure 4.9 (a)-(d).

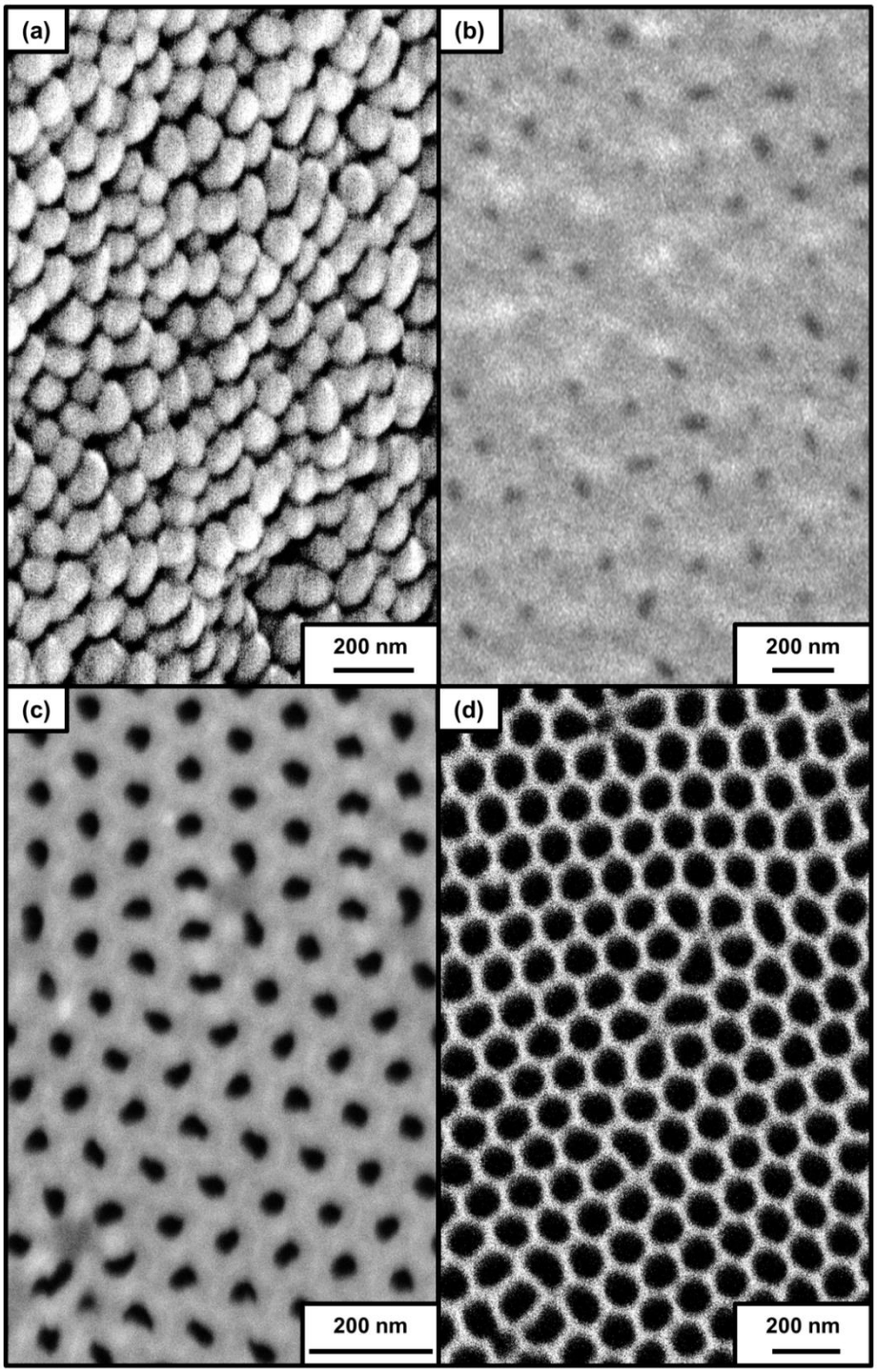

Figure 4.9 SEM micrographs of bottom surfaces for an AAM fabricated at 40 V, showing different degree of pore opening: (a) barrier oxide layer before pore opening (65,000X magnification); (b) partly opened (50,000X magnification); (c) pores are throughly opened (100,000X magnification) and (d) pore widening (55,000X magnification). Each micrograph is corresponding to each stage of pore opening detection shown in Figure 4.10.

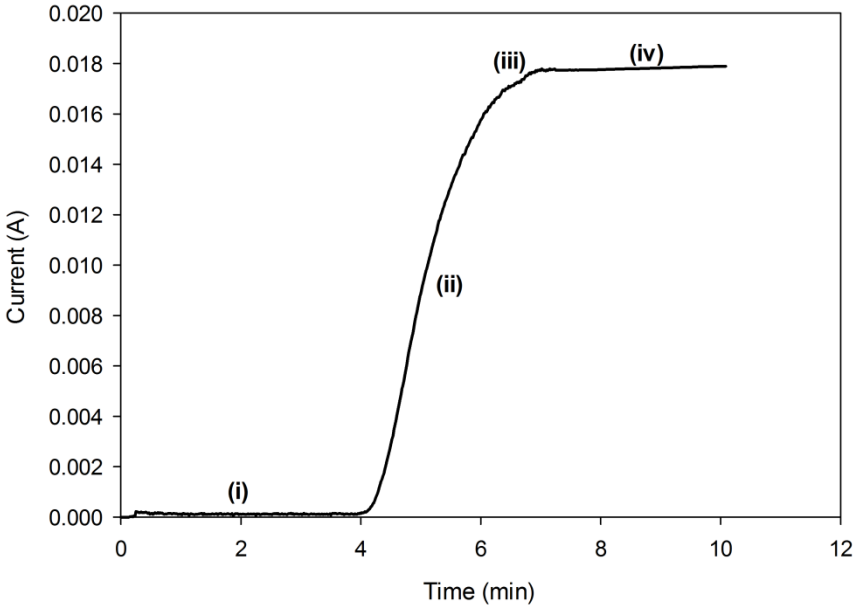

Figure 4.10 A current profile recorded via the electrochemical detection method during the pore opening of a 40 V AAM. The labelled stages, (i), (ii), (iii) and (iv) are corresponding to Figure 4.9(a), (b), (c) and (d), respectively.

As shown in Figure 4.11, the pore opening current profiles vary considerably among the AAMs prepared at different conditions. The well-documented previous studies show that the barrier oxide layer of AAM is proportional to the anodization voltage. Therefore, noticeably, the time required for initiation and completion of pore opening is increasing accordingly. Moreover, the current profile for 25 V AAM shows a slower slope and levels off at a lower peak. This can be attributed to the smaller pore diameter, which is less conductive relative to larger pore diameter. Despite having a larger diameter, the overall thickness of the 80 V AAM poses more resistance for ion conduction through the membrane. Therefore, this result confirms that the pore opening current profiles correspond accurately to the different structures obtained by different anodization conditions.

Nevertheless, the etching conditions, such as type of acid, acid concentration and temperature can alter reaction rate. This detection method is still applicable to provide current profile with distinctive stages. Therefore, the use of this method can achieve reproducible pore-opening results even when the process is conducted under different conditions.

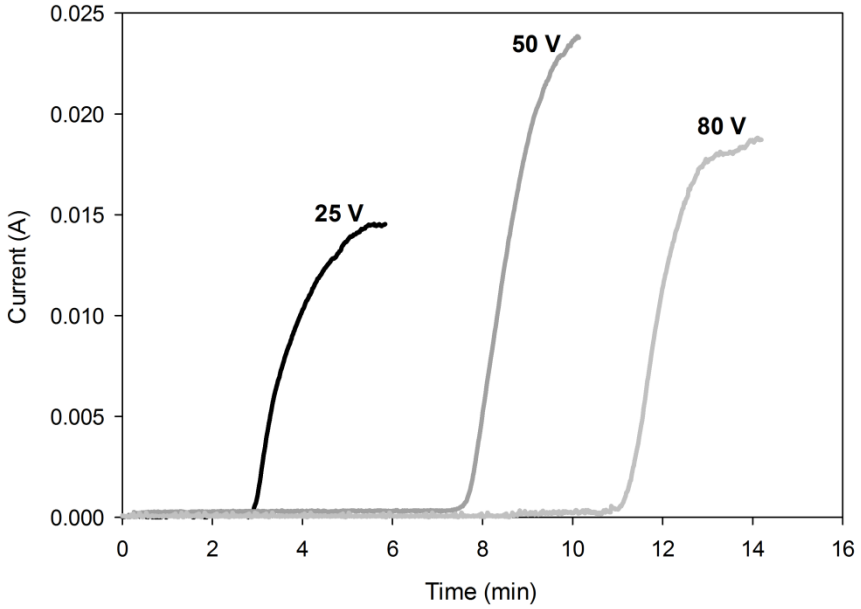

Figure 4.11 A series of pore opening current profiles for AAMs fabricated at different voltages.

4.2.3 AAM pore structure

Figure 4.12 illustrates the SEM micrographs of the bottom surfaces for AAMs fabricated using oxalic acid at different voltages, ranging from 25 to 90 V. As can be seen, the AAMs fabricated in oxalic acid exhibit an optimum self-ordered pore structure at 40 V and 50 V (Figure 4.12(c) and (d)). The circular pores are uniformly packed in the cells with hexagonal arrangement. The degree of ordered arrangement is reduced accordingly when the anodization is deviating further away from 40 V. This is shown by the presence of irregular pore size and pore shapes. For lower anodization voltages, the pore size is fairly homogeneous and the pores are still nearly circular, but elongated. For high anodization voltage, the pore shape deviates greatly, especially a large proportion of triangular or rectangular pores are present. This confirms the claim that states self-ordering process takes place only at an appropriate voltage (Ono *et al.*, 2004).

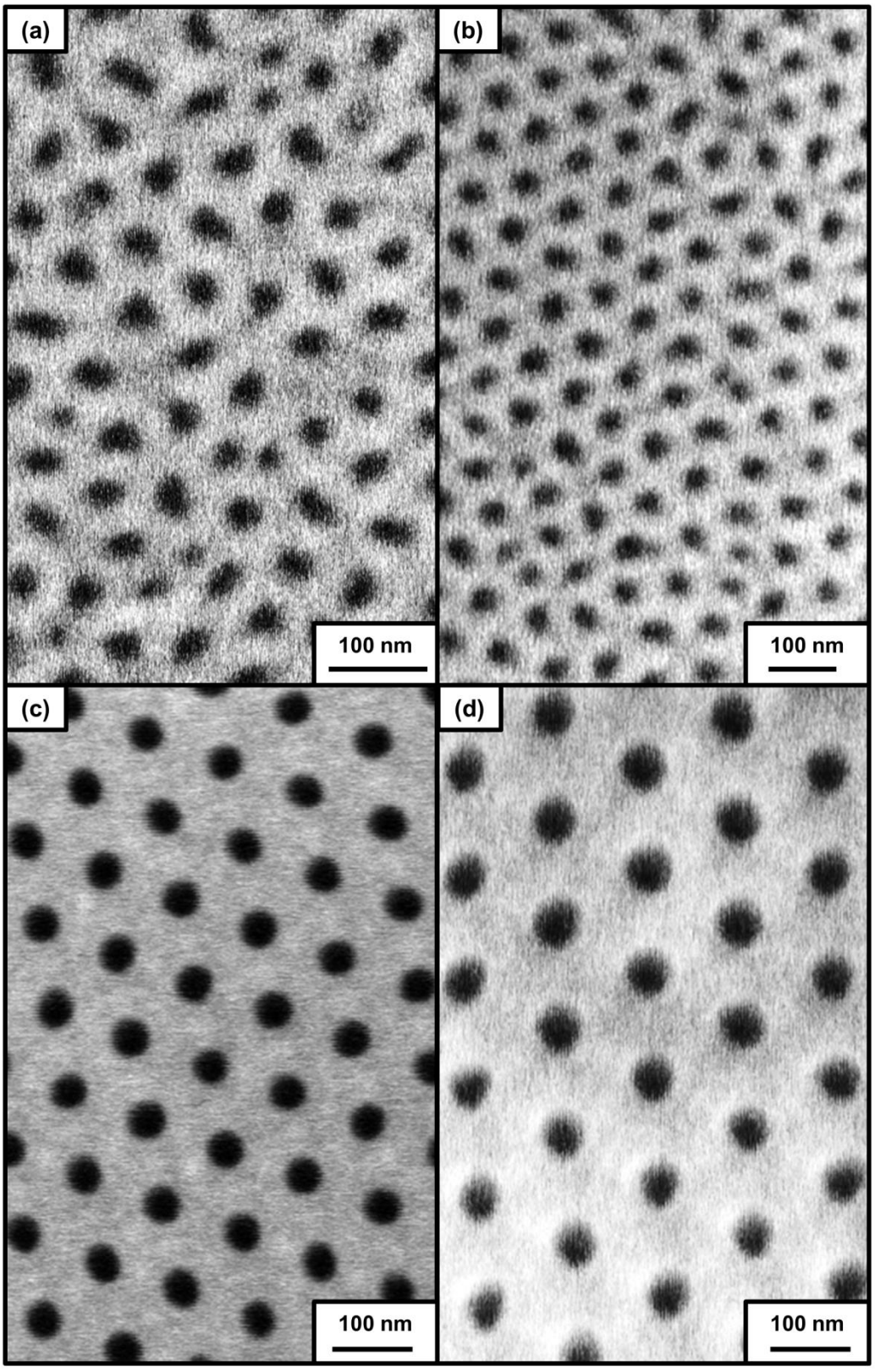
(a)
100 nm
(b)
100 nm
(c)
100 nm
(d)
100 nm

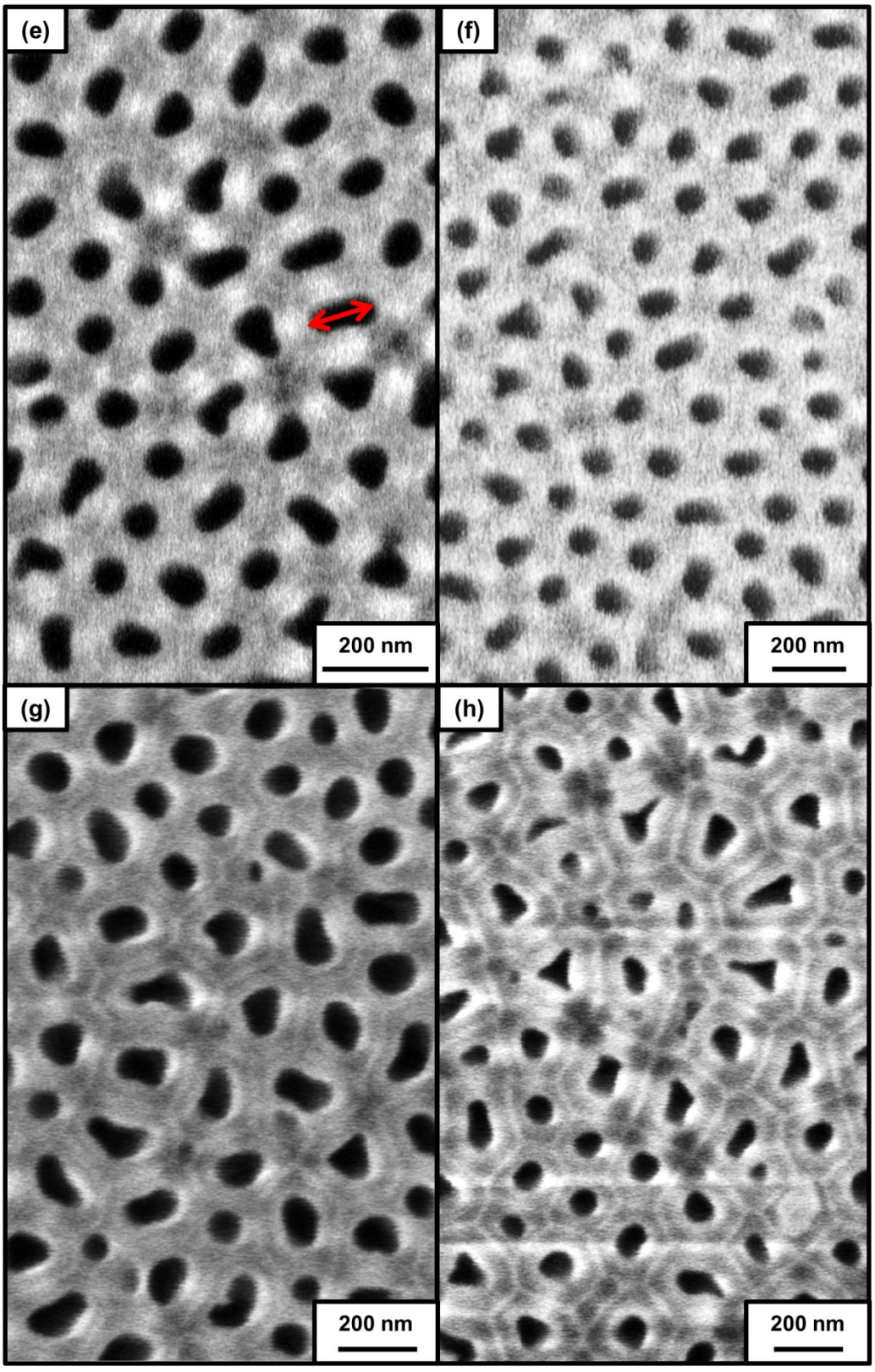

Figure 4.12 SEM micrographs showing the bottom surface of AAMs fabricated at (a) 25V (160,000X magnification); (b) 30 V (110,000X magnification); (c) 40 V (130,000X magnification); (d) 50 V (130,000X magnification); (e) 60 V (85,000X magnification); (f) 70 V (60,000X magnification); (g) 80V (65,000X magnification) and (h) 90 V (55,000X magnification).

In addition to the voltage, the appropriate electrolyte also plays an important role. As shown in Figure 4.13, at 25 V, the AAMs formed in 0.5 M sulphuric acid exhibits higher degree of uniformity than those formed at 0.3 M oxalic acid. The hexagonal pore arrangement and pore size regularity are more clearly observed in the AAM anodized in 0.5 M sulphuric acid. Based on this result, it can be concluded that optimum self-ordering structure can be achieved at moderate electric field, which is a function of the electrolyte activity and anodization voltage. This provides an appropriate balanced force field to facilitate the self-assembly of neighbouring pores. At low electric field, the pore diameter obtained is considerably homogeneous but the stress arisen from volume expansion is too weak to hexagonally arrange the pores periodically (Jessensky *et al.*, 1998). At high electric field, the reaction may be unstable and lead to formation of pores with different diameters. The high growth rate of oxide film also provides very limited time for the self-organised arrangement for the pores (Choi *et al.*, 2009).

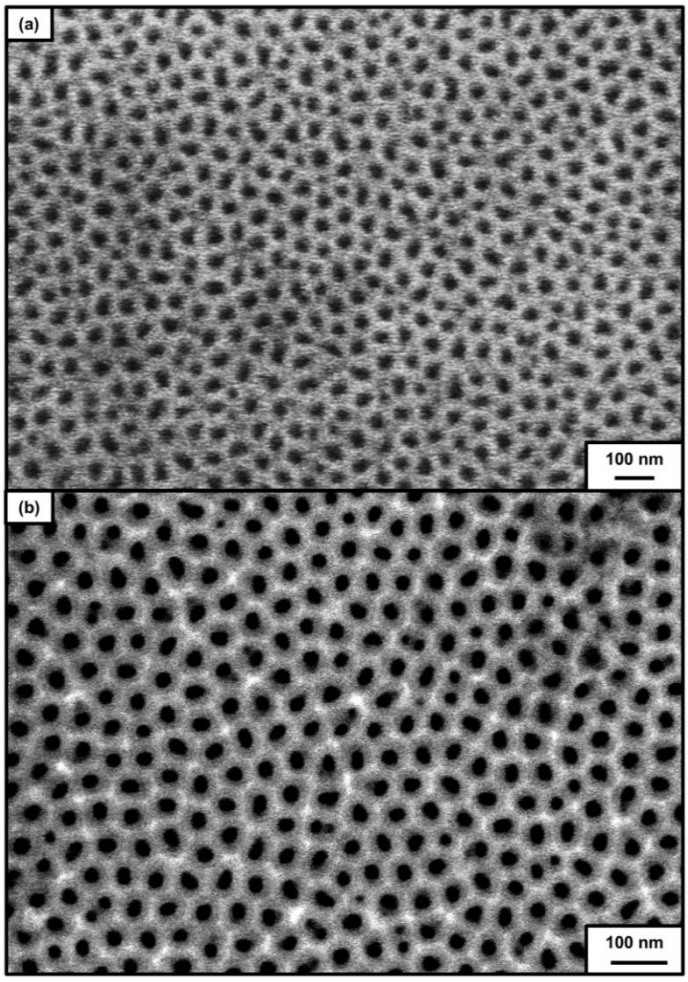

Figure 4.13 Comparison of pore structure between AAMs fabricated in (a) 0.3 M oxalic acid (80,000X magnification) and (b) 0.5 M sulfuric acid at 25 V (120,000X magnification). The latter exhibits a higher order of pore arrangement.

Figure 4.14 shows a large area of a highly uniform pore structure of an AAM anodized at 40 V. The structure is homogenous although some deviations from hexagonal arrangement can be identified along the domain boundaries, which is originated from the crystalline structure of the aluminium before anodization.

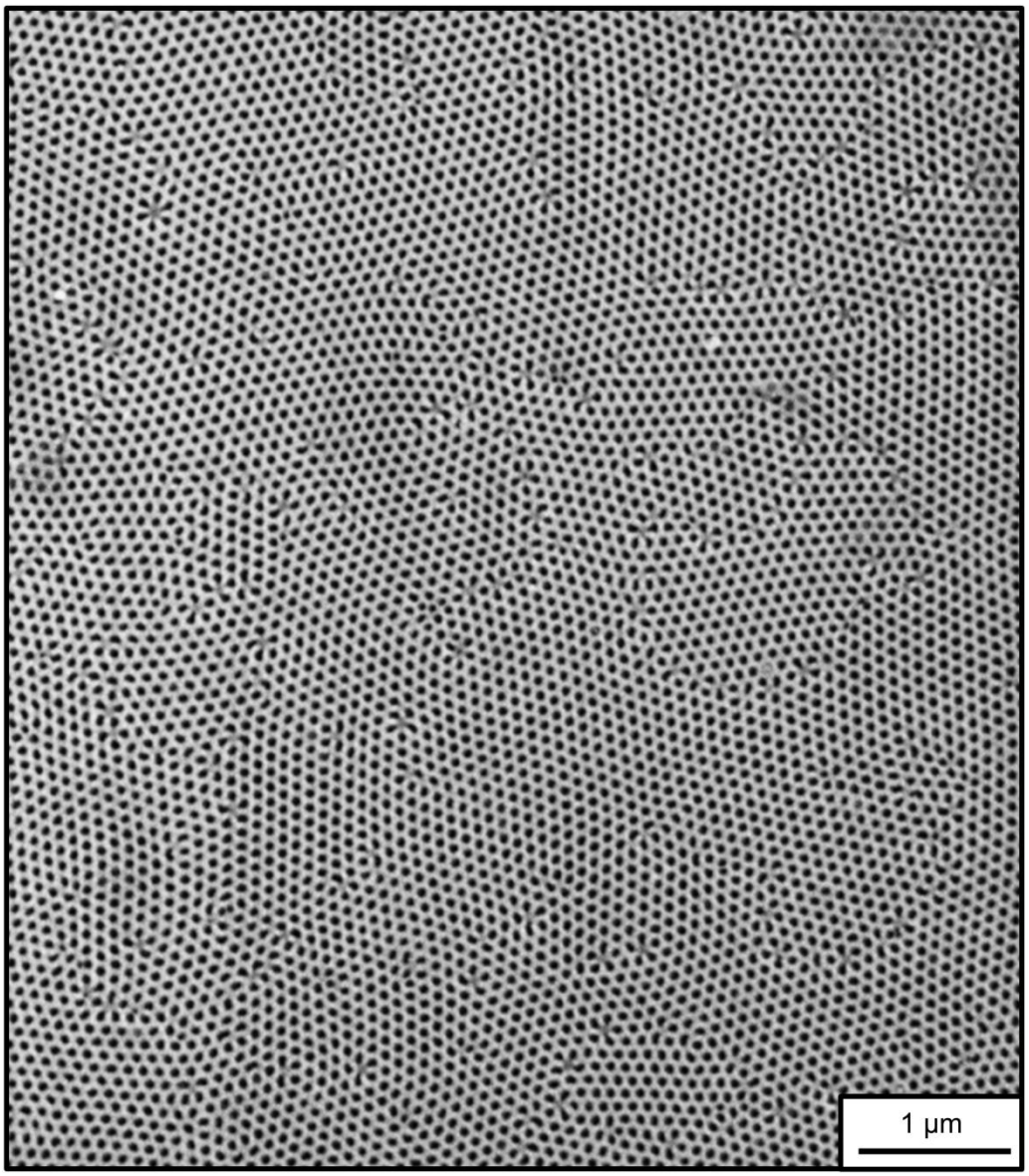

Figure 4.14 SEM micrograph of an AAM sample fabricated at 40 V showing large area of homogenous pore structure (20,000X magnification).

4.2.4 AAM pore diameter and porosity

Using statistical image analysis of SEM micrographs, the pore diameter and porosity of each AAM were obtained. During the image analysis, the given pore diameter is feret's diameter, which is defined as the longest distance between any two tangents contacting the pore boundary (as shown in Figure 4.12(e)). It therefore overestimates the effective pore diameter. For compensation, the feret's diameter obtained was normalised by circularity to obtain the effective pore diameter, which is an analogous method to obtain hydraulic diameter of non-circular pipe conventionally (Richardson *et al.*, 1997). Therefore, for circular pores obtained at optimum anodization conditions, the feret's diameter is close to the effective pore diameter. Their circularity is close to unity and therefore this adjustment is minimal. On the other hand, if the pore shape is less circular, the overestimation of the feret's diameter can be substantial. In this case, the circularity factor will be smaller and provide a good compensation.

Table 4.1 Mean pore diameter and porosity of AAMs fabricated at different voltages in oxalic acid. Two AAM samples were analysed for each anodization condition.

Anodization voltage (V)	Mean pore diameter (nm)	Porosity[a] (-)	Pore density X 10^{13} m^{-2}
25V	31±4	0.14	18.8
	29±3	0.12	18.3
30V	35±4	0.16	16.3
	36±4	0.15	15.0
40V	48±5	0.15	8.2
	47±2	0.15	8.8
50V	56±6	0.17	6.7
	60±5	0.17	5.9
60V	70±5	0.16	4.0
	69±6	0.16	4.1
70V	86±8	0.18	3.0
	82±10	0.17	3.1
80V	96±8	0.18	2.5
	96±10	0.17	2.3

[a] The porosity is estimated based on the topography of the membrane. However, due to the unique structure of the membrane that consists of nano-channels, this porosity can be taken as the bulk porosity.

Table 4.1 summarises the pore diameter and porosity of membranes prepared at different anodization conditions. As shown in Figure 4.15, a linear correlation between the pore diameter and the anodization voltage was observed with a gradient of 1.19 nm V^{-1}. It is in good agreement with previous findings, which predominantly reporting the proportionality factor to be approximately 1.2 nm V^{-1} (O'Sullivan and Wood, 1970). The porosity remains within the range of 0.12 to 0.18. The pore density is decreasing with increasing anodization voltage. This result is well-aligned with previous studies (Sulka, 2008).

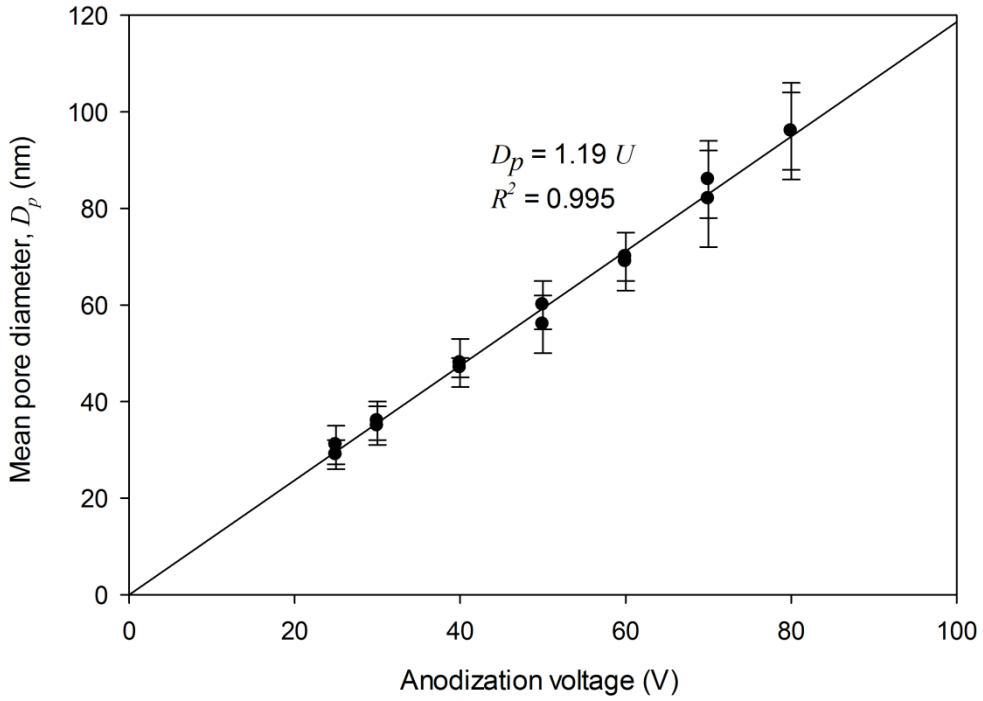

Figure 4.15 Linear relationship between the anodization voltage and pore diameter during anodization process.

Figure 4.16 shows the pore size distribution of AAMs fabricated at low, optimum and high anodization voltage. For 40 V membrane, due to the ordered structure, it is featured with a narrow pore size distribution. For lower and higher anodization voltages, wider pore size distributions were obtained. However, in each membrane, more than 90% of the pores have diameter that falls into a ±15% deviation span of the mean pore diameter.

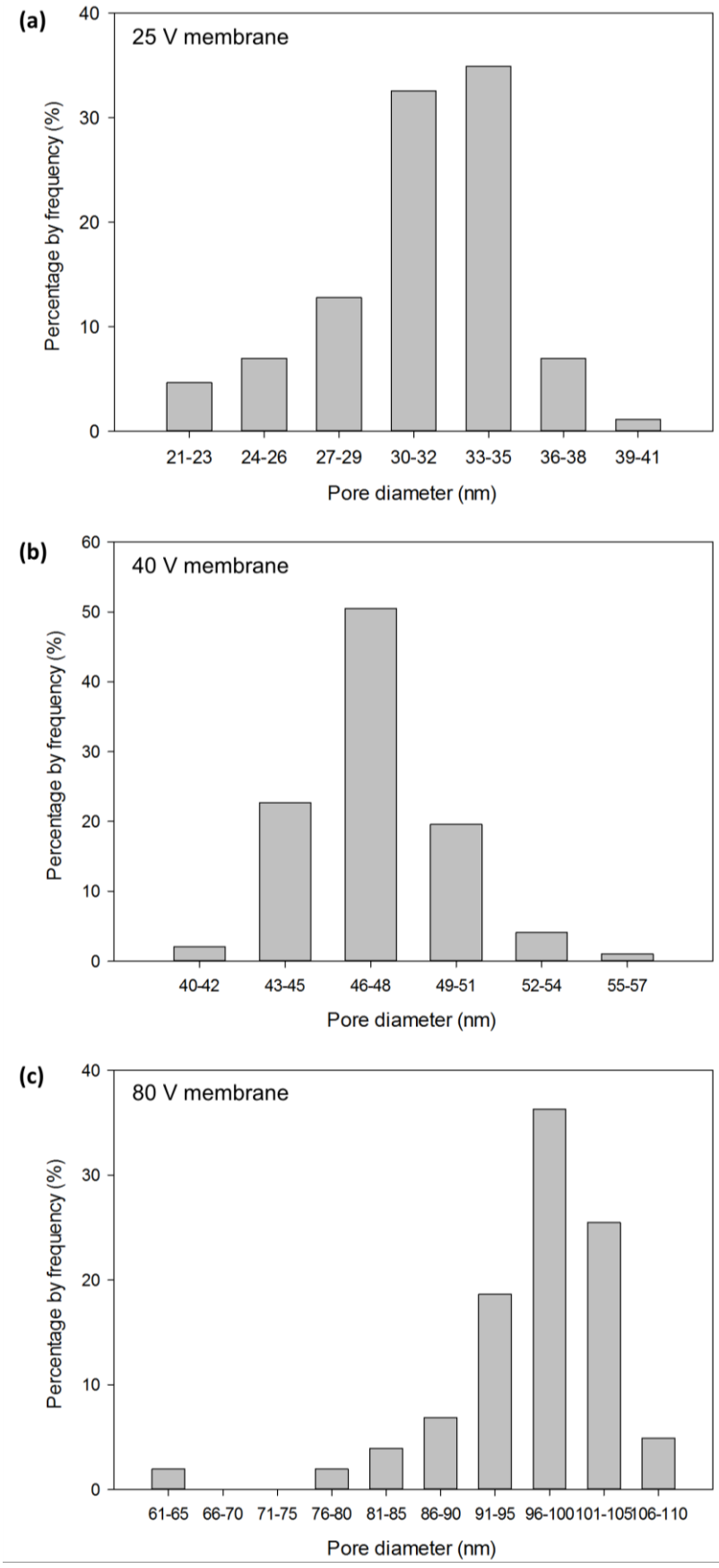

Figure 4.16 Pore diameter distribution of AAMs fabricated at different anodization voltages: (a) 25 V; (b) 40 V and (c) 80 V.

4.2.5 AAM cross-section and thickness

As can be seen in Figure 4.17, the cross-section micrograph shows straight nano-channels that run parallel to each other. The roughness observed at the pore wall was predominantly caused by the snapping of the membrane during sample preparation for field emission SEM, which does not leave a clean edge along the pore wall.

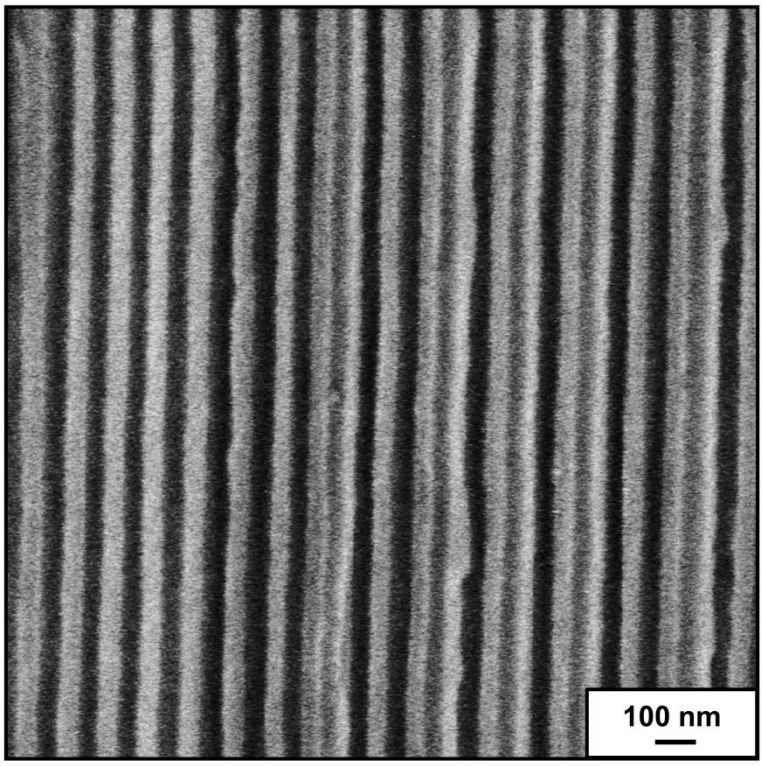

Figure 4.17 SEM micrograph showing the cross-section of a 50 V AAM (60,000X magnification). The porous structure consists of straight nano-channels.

As summarised in Table 4.2, the thickness of AAMs has a positive correlation with anodization voltage. However, the length of hours of anodization is different for each membrane. Long hours are needed for low voltage to create sufficiently thick membrane to be handled robustly. For high voltage, the anodization should be stopped before the growth of fibrous structure. The growth rate of alumina is dynamic during anodization, as a result of increasing electrical resistance arisen from the increasing thickness of porous alumina formed. Nevertheless, the average growth rate was calculated and shows a positive trend with anodization voltage as expected. As shown in Figure 4.18, the growth rate of the alumina is increasing almost exponentially with anodization voltage, in well agreement with

Equation 2.8 where electric field is a linear function of voltage. Nevertheless, the anodization at higher voltages was performed at lower temperature (Table 3.1) and hence the gradient of the plot was skewed, i.e. the plot does not cross the origin as predicted by Equation 2.8.

Table 4.2 The thickness and average growth rate of AAMs at different voltages.

Anodization voltage (V)	Thickness (±5 μm)	Average growth rate (μm hr^{-1})
25V	55	3.93
	55	3.93
30V	60	4.29
	65	4.64
40V	80	6.15
	80	6.15
50V	80	8.00
	105	10.50
60V	130	13.00
	135	13.50
70V	115	19.17
	130	21.67
80V	145	36.25
	120	30.00

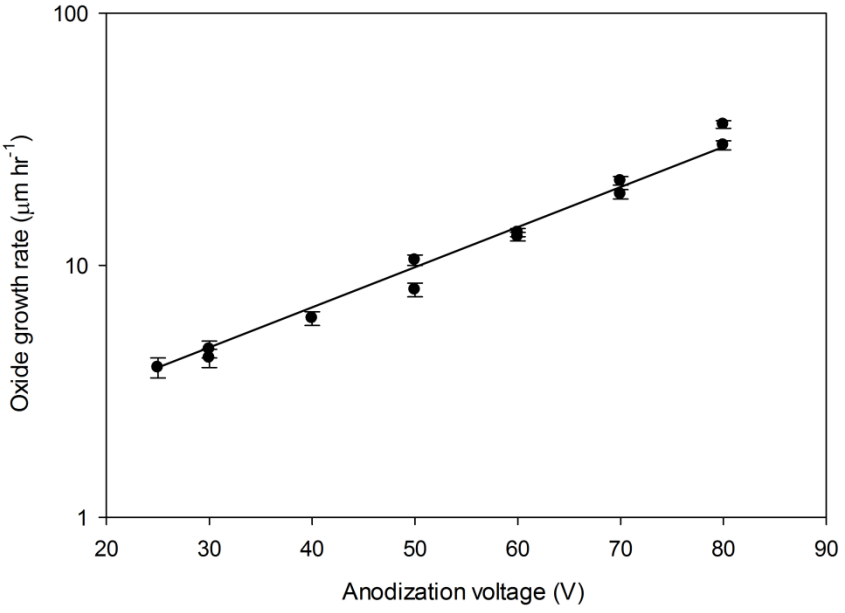

Figure 4.18 The rate of oxide growth during anodization at different voltages.

4.2.6 Membrane surface roughness

Surface roughness is influential to membrane performance, especially for flux, fouling tendency and ease of cleaning. A number of samples were analysed based on the method described in Section 3.5.4 (Figure 4.19). The roughness can generally be affected by a number of factors, such as applied voltage, which influences the rate of alumina dissolution during anodization, and wet chemical etching (acid concentration and temperature) for oxide barrier layer removal. However, as shown in Table 4.3, the surface roughness of AAMs prepared at different conditions is similar and generally in the range of the previously reported value, below 10 nm (Leitao *et al.*, 2012).

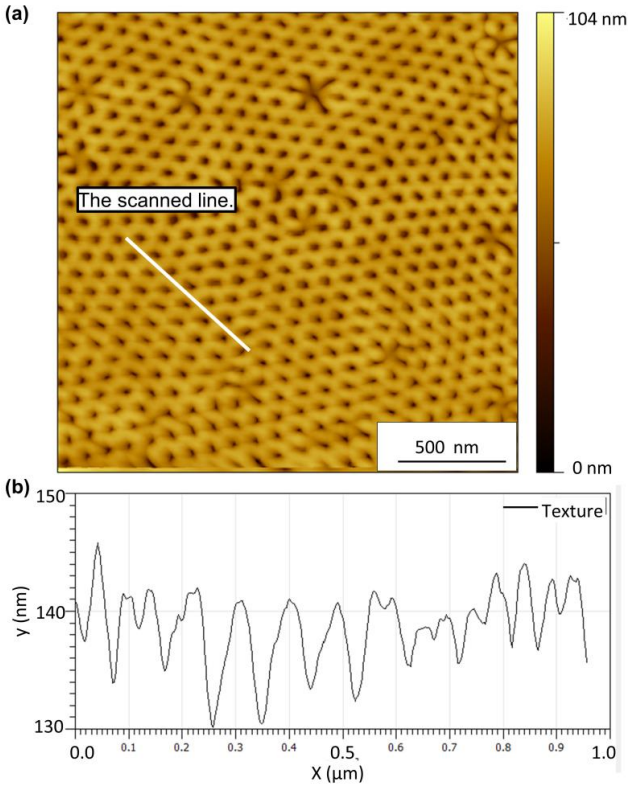

Figure 4.19 (a) An example of AFM micrographs used for surface roughness estimation, 40,000X magnification and (b) The texture profile obtained for a representative line scan by using Gwyddion 2.31.

Table 4.3 The average and root mean squared roughness of AAMs.

Samples	25 V		40 V (1-step)		40 V (2-step)		80 V	
Surface	Top	Bottom	Top	Bottom	Top	Bottom	Top	Bottom
R_a (nm)	2	1	2	2	3	3	5	4
R_{RMS} (nm)	2	1	3	4	4	4	6	4

4.3 Asymmetric membrane morphology

Asymmetric AAMs were made by controlling the voltage during the anodization. Two methods were used to reduce the diameter. First, the anodization voltage was suddenly reduced by a factor of $2^{-0.5}$ to create a Y-branched pores, i.e. one pore channel is branched into two. Figure 4.20 shows the anodization current profile when this scheme is used to fabricate an asymmetric AAM. The current dropped simultaneously with the sudden reduction in voltage. The current density reaches close to zero as the voltage drops suddenly, because of the reduced field strength for the dissolution of the thicker oxide barrier layer formed in the previous higher voltage. However, the current slowly increases as the thinning of the oxide barrier layer. A transient peak which is similar to 3rd stage of pore evolution during anodization (Figure 2.7 – stage 3) is followed, showing the reorganisation of pore structure corresponding to the voltage reduction.

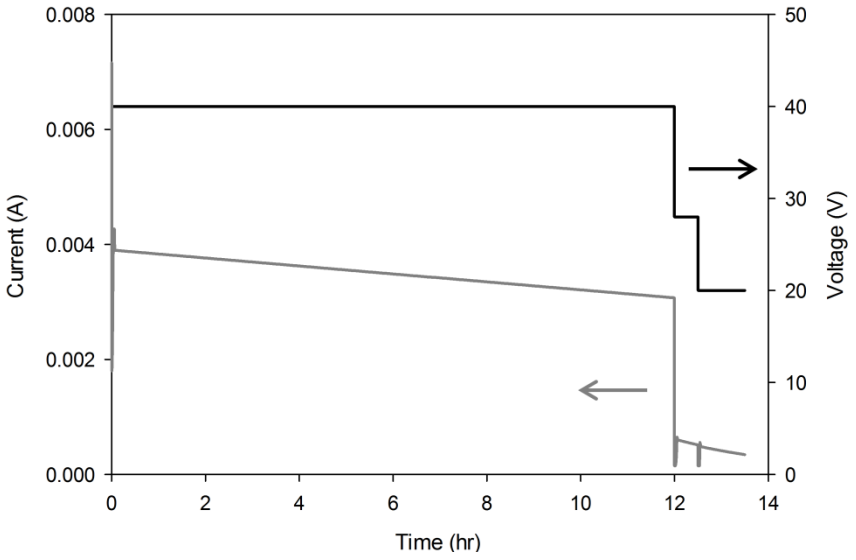

Figure 4.20 Anodization current and voltage profile of an asymmetric AAM fabricated by initial anodization at 40 V and sudden voltage reduction was applied by a factor of $2^{-0.5}$ to induce sudden pore branching.

An example of the morphology obtained with this method is shown in the SEM micrograph of the cross-section at different magnification (Figure 4.21). Figure 4.21(b) shows the symmetric region, or so called stem pores of the membranes with straight pores running in parallel to each other. Figure 4.21(c) illustrates the transition where the sudden change in anodization voltage leads to the branching and re-organisation of the porous structure, with the y-branching clearly shown in Figure 4.21(d). Further reduction of the anodization voltage by the same factor will lead to another generation of pore branching. Multiple branches can be

achieved by reducing the anodization voltage by a factor of $n^{-0.5}$ where n is the desired number of branches.

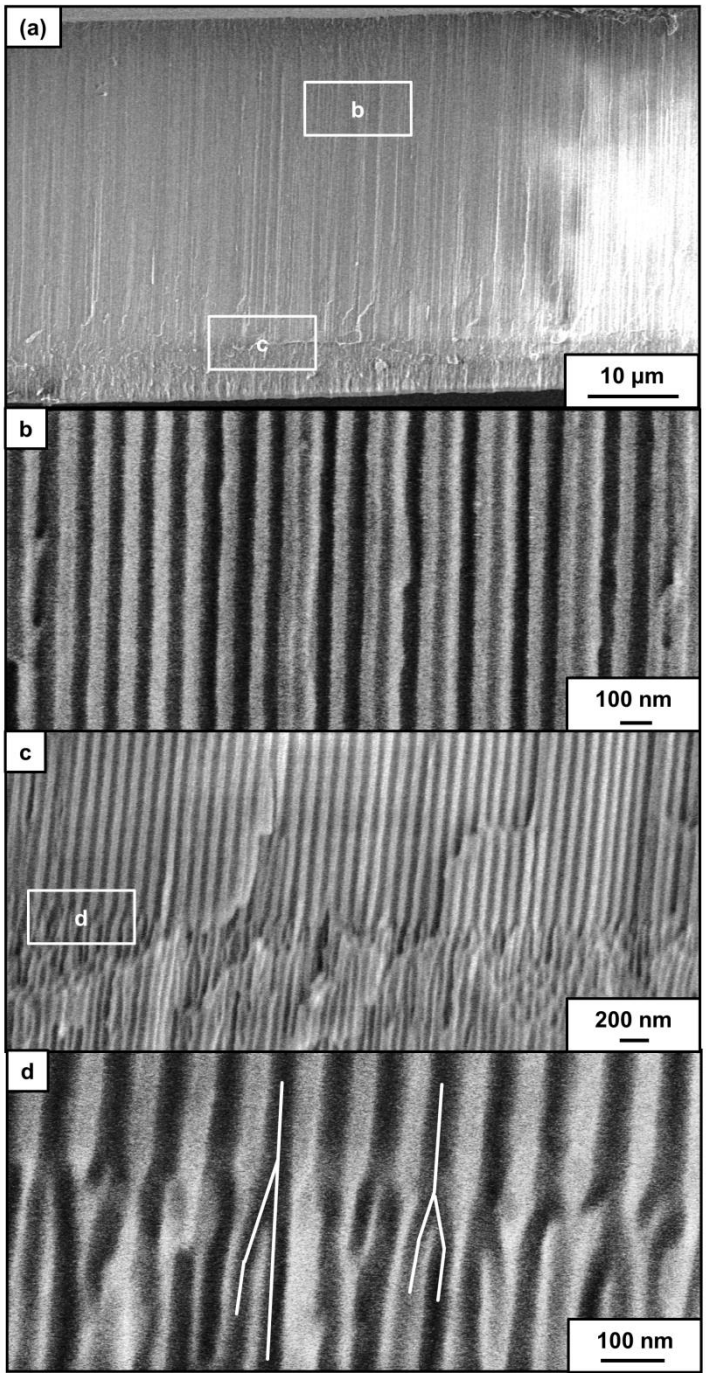

Figure 4.21 SEM micrographs showing the cross-sections of an asymmetric AAM fabricated by sudden voltage reduction, at different level of magnification. (a) shows the overall thickness of the AAM (1,700X magnification). (b) (60,000X magnification) and (c) (28,000X magnification) are the close-up images of the corresponding bracketed area in (a). In particular, (b) shows the cross-section where a symmetric structure/stem pores were developed at the initial potentiostatic condition and (c) shows the cross-section where structure was developed at the sudden reduction of anodization voltage from 40 V to 28 V. (d) is a close-up image (120,000X magnification) of the bracketed area in (c) showing the y-branching.

The second method involved a slow constant anodization voltage ramp down rate to the final anodization voltage, as shown in Figure 4.22. The current profile reduces gradually according to the rate of voltage reduction. Figure 4.23 shows the development of branching pores happens gradually at several depths from the membrane surface. It can be clearly seen that the average pore size decreases from left to right in Figure 4.23(a), leading to smaller pores with higher in density when moving to the right. On the right side is the membrane section where the final anodization voltage was maintained for a period of time, in this case two hours, to form the selective layer of the AAMs. The voltage ramp down rate has to be adequately slow as previous studies have shown that fast ramp rates (>0.001 V s^{-1}) lead to disordered structures due to an insufficient time for pore structure reorganisation, especially towards the lower end of anodization voltage (Lee *et al.*, 2012). Figure 4.23(b) shows the membrane selective layer thickness, which can be controlled by the hold time at the final anodization voltage.

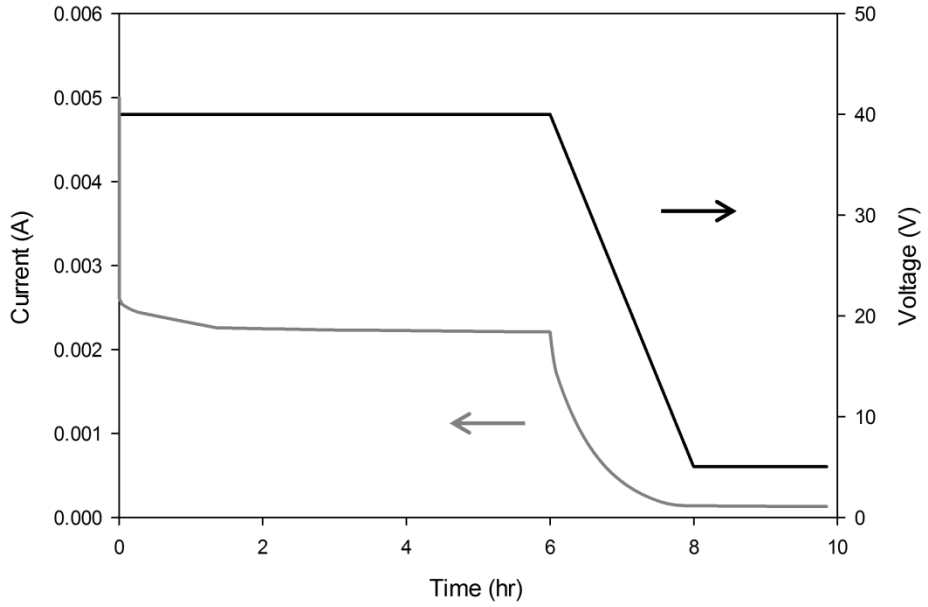

Figure 4.22 Anodization current and voltage profile of an asymmetric AAM fabricated by gradual voltage reduction from 40 V to 5 V, in order to induce continual pore branching.

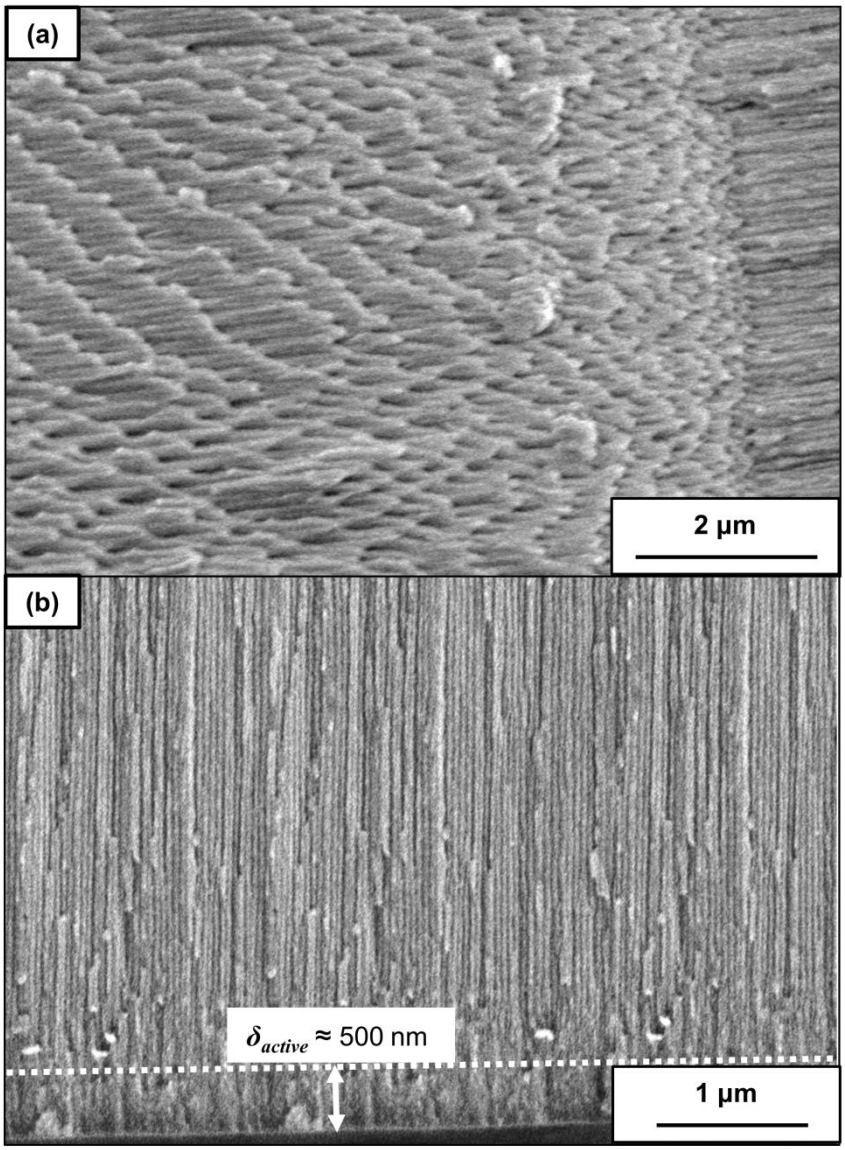

Figure 4.23 SEM micrographs showing the cross-sections of an asymmetric membrane fabricated by a scheme described in Figure 4.22. (a) shows the continual branching over the course of gradual anodization voltage reduction (12,000X magnification) and (b) shows the thickness of the layer formed by the final anodization voltage (20,000X magnification).

4.4 Summary

In this chapter, based on the well-established protocol for AAM synthesis, AAMs of high quality were fabricated with high reproducibility. However, a number of precautions are needed to achieve this result, particularly the control of temperature and electrolyte properties in ensuring the formation of a homogenous porous structure. For higher anodization voltages, inefficient

cooling or long anodization times can cause the formation of a fibrous structure on the top surface of the AAMs. The current density profile during anodization provides an insight into the stability of the reaction and which is reflected on quality of the AAMs formed. This has shown the importance of pre-treatment of aluminium substrates, especially electro-polishing.

Flat and symmetric AAMs have been successfully fabricated from 25 V to 80 V in 0.3 M oxalic acid. For one-step anodization, the AAMs produced have a relatively irregular arrangement of pores at the top surface due to the initial inequilibrium pore growth. Two-step anodization, having pre-textured the surface for second step of anodization, is a method to fabricate AAMs with homogeneous pore structure through the thickness of the membrane. Moreover, the adaptation of the electrochemical detection technique has enabled a good control of wet chemical etching for removing the oxide barrier layer at the bottom surface avoiding over-etching. In good agreement with previous findings, a linear correlation between the pore diameter and the anodization voltage was observed with a gradient of 1.19 nm V^{-1}. As expected, the porosity remains almost constant for AAMs fabricated at different voltages whereas the pore density is reducing with increasing voltage. The AAMs fabricated in oxalic acid exhibit an optimum self-ordered arrangement at 40 V, featured by circular pores with a narrow pore size distribution. The growth rate of the AAM layer, which is a function of temperature, electrolyte type and concentration, and the anodization time are the important parameters determining the membrane thickness.

Finally, by manipulating the anodization voltage, two types of asymmetric membranes with distinctive structure have been successfully fabricated. The first method produces AAM with a defined pore branching region where multiple branched pores can be formed by sudden voltage reduction. The second method creates continual pore branching as a result of gradual ramp down of anodization voltage.

This chapter has shown the method to control the structure of AAM by altering the anodization parameters. This enables the optimisation of the AAM porous structure for different applications, which are further discussed in the following chapters.

5. Flat AAMs: Surface Modification and Fluid Flow Measurement

Given the well-defined and controlled nanoporous structure, flat AAMs are used as a platform to study the wettability of nanostructured surface and fluid flow behaviour at the nanoscale. In this chapter, the effect of the surface modification on flow is discussed, accompanied by a comprehensive investigation of fluid flow at the nanoscale. In particular, a dedicated pressure-driven fluid flow measurement apparatus with high accuracy and sensitivity was designed and constructed. Using this, it is demonstrated for the first time, water slippage can occur in hydrophilic nanochannels. This finding has recently been published in the journal *Nanoscale* (Lee et al., 2012).

5.1 Surface modification

The experimental procedures for the surface modification techniques performed are described in Section 3.1. Silane chemistry offers a convenient approach to alter the wettability of the AAMs. On the other hand, coating by chemical vapour deposition (CVD) is a scalable process to modify the surface chemistry of the AAMs, as well as producing one dimensional nanostructured materials.

5.1.1 Silanization

Pristine AAMs are highly hydrophilic. The typical contact angle of liquid water on non-porous alumina is 12 ± 2° (Megias-Alguacil *et al.*, 2011). Figure 5.1 shows an image that was used to determine the contact angle of a water droplet on a pristine AAM anodized at 40 V. The contact angle is 14 ± 3°, in good agreement to the literature value (Velleman *et al.*, 2009).

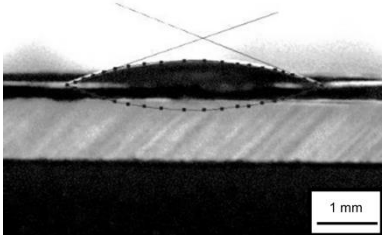

Figure 5.1 A water droplet on a pristine AAM fabricated at 40 V showing a low contact angle.

AAMs contain hydroxyl groups on their surfaces and also the inner walls (Jung *et al.*, 2006). This makes silane chemistry a convenient method to modify the wettability of AAMs. The presence of the hydroxyl groups on the AAM surfaces promotes the initial hydrolysis of the silanization reactions. Previous attempt by using 3-aminopropyltriethoxysilane and pentafluorophenyldimethylchlorosilane have shown successful grafting of silane functional groups on the AAM surfaces and along pore walls (Mutalib Md Jani *et al.*, 2009). In this PhD work, two methods were attempted to alter the wettability of AAMs, i.e. by using different silane precursors that have different terminating functional groups and by changing the composition of the precursor solution containing two different silane compounds.

Figure 5.2 shows the contact angle of water on 40 V AAMs that were surface modified by the silane compounds listed in Table 3.3. It clearly demonstrates that the measured contact angle (63° to 120°) is positively correlated to the reported water contact angle on the self-assembly monolayer of the corresponding silanes. However, the measured contact angle is consistently higher than the literature contact angle values tabulated in Table 3.3, in the range of 4° to 12°. The likely reason for this observation is the formation of multiple cross-linked silane layers instead of the desirable monolayer, as depicted in Figure 5.3 (Almanza-Workman *et al.*, 2002). The presence of multiple cross-linked layers enriches the concentration of hydrophobic hydrocarbon or fluorocarbon groups on the surface. Even for the 3-cyanopropyltrichlorosilane which ends with hydrophilic group, the contact angle obtained is also higher than literature contact angle. This increase is due to the cross-linked silanes can increase the exposure to the side chains, i.e. the hydrophobic propyl groups, shielding the effect of the terminal functional (-CN) group.

The cross-linking of the silane precursors is due to the susceptibility of the silicon-chloride bond to hydrolysis. The control of the precursor concentration is very important to limit the degree of cross-linking. A wiping method has shown to provide a good control over the dipping method, where an ellipsometric study showed consistently lower thickness of the silane grafted layer (Lim *et al.*, 2006). However, the wiping method has not been adopted in this work because it would not allow silanization of the pore walls.

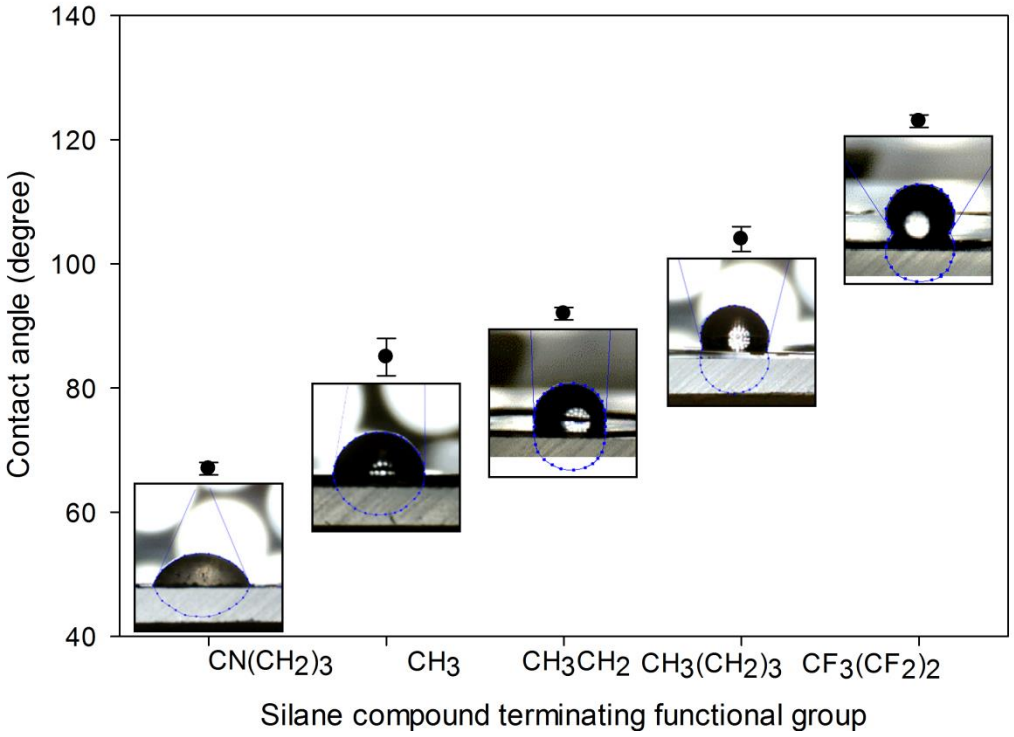

Figure 5.2 Water contact angles of 40 V AAMs after being modified by silanes with different terminating functional groups.

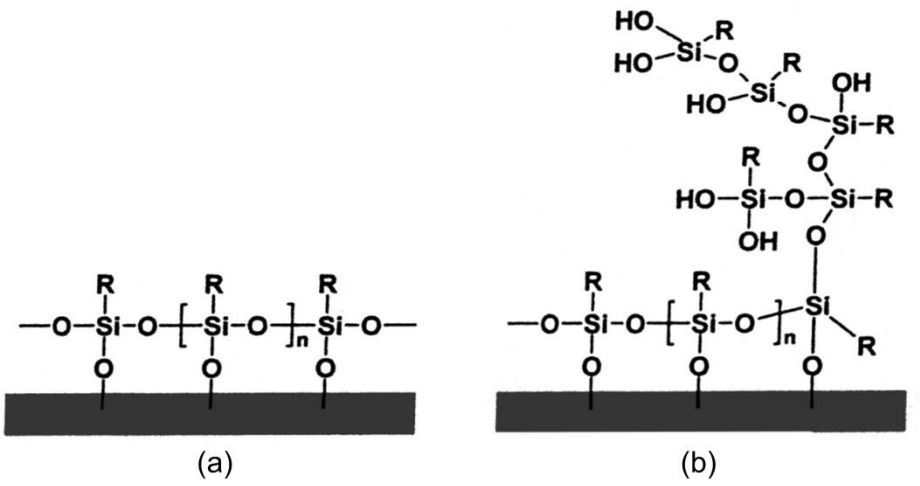

Figure 5.3 The formation of (a) monolayer and (b) multilayer film by silane chemistry (Almanza-Workman *et al.*, 2002).

In Figure 5.4, the water contact angle of the mixed butyltrichlorosilane and 3-cyanopropylsilane grafted layers are shown as a function of different composition in the deposition solution. The reported values of the water contact angle for monolayers formed from 3-cyanopropyltrichlorisilane and butyltrichlorosilane are

59° and 98°, respectively. Thus, when these two silanes are mixed to prepare the deposition solution, the water contact angle for the grafted layer formed is expected to vary between these two values. The water contact angle of the grafted layer, as expected, is increasing with the composition of butyltrichlosilane. Using the dipping method, in agreement with a previous study (Lim *et al.*, 2006), the observed correlation is non-linear.

This non-linearity can be attributed to the disparity of the reaction kinetics between the two silanes. It was found that, in non-polar environments, molecules with polar groups are less stable than molecules with non-polar groups, which induces the faster physisorption of polar molecules onto the substrate (Offord and Griffin, 1993). In this case, in hexane, the polar group containing silane, 3-cyanopropylsilane is more reactive than the non-polar butyltrichlorosilane. Therefore, the surface is preferentially occupied by the polar molecules, resulting in a water contact angle closer to that of a pure 3-cyanotrichlorosilane-grafted layer. Nevertheless, the increment of butyltrichlorosilane concentration in the solution will increase its reactivity and hence its density on the grafting surface.

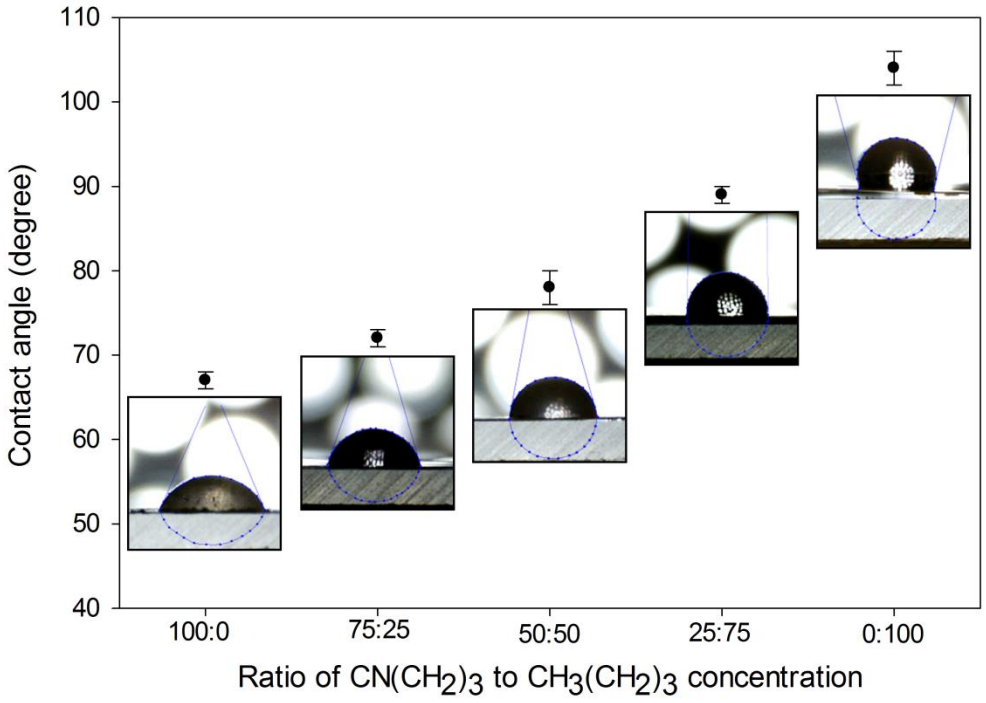

Figure 5.4 Water contact angles of 40 V AAMs after being modified by silane mixture of butyltrichlorosilane and 3-cyano-propyltrichlorosilane at different composition.

5.1.2 Chemical vapour deposition

As described in Section 3.4.1, CVD was used to deposit carbon coating on the AAMs. There have been a number of previous reports on carbon coating for AAMs. The most prevalently reported method was as described in Section 3.4.1. Previous reports show successful coating has been obtained on commercial AAMs, namely Anodiscs® with 200 nm average pore diameter and 60 μm thickness (Figure 5.5).

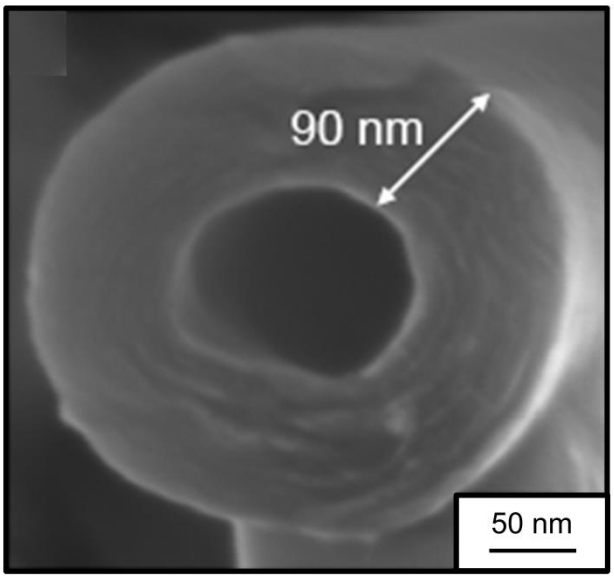

Figure 5.5 SEM micrograph of a released carbon nanopipe produced by a prolonged CVD process of 200 nm Anodisc showing 90 nm of carbon layer thickness (230,000X magnification) (Mattia, 2007).

Based on this CVD condition, a number of attempts have been performed on 40 V AAMs, which have smaller pore diameter and well-ordered pore structure. However, after the carbon coating, fluid flow measurement shows either no or extremely low water flow despite of the high transmembrane pressure applied. Observation under FESEM (Figure 5.6) showed a deposited carbon layer sitting on top of the membrane surface, blocking the porous structure. This provided a simple explanation for the low fluid flow observed in these membranes. The reason for this contrasting result obtained for a 200 nm Anodisc® and a 40 V membranes is likely to be the difference in pore diameter. The four to five times smaller pore diameter can be translated into at least 20 times higher transport resistance for the gas to pass through the membrane channels/pores. Therefore, the carbon preferentially deposits on the surface than on the inner pore wall.

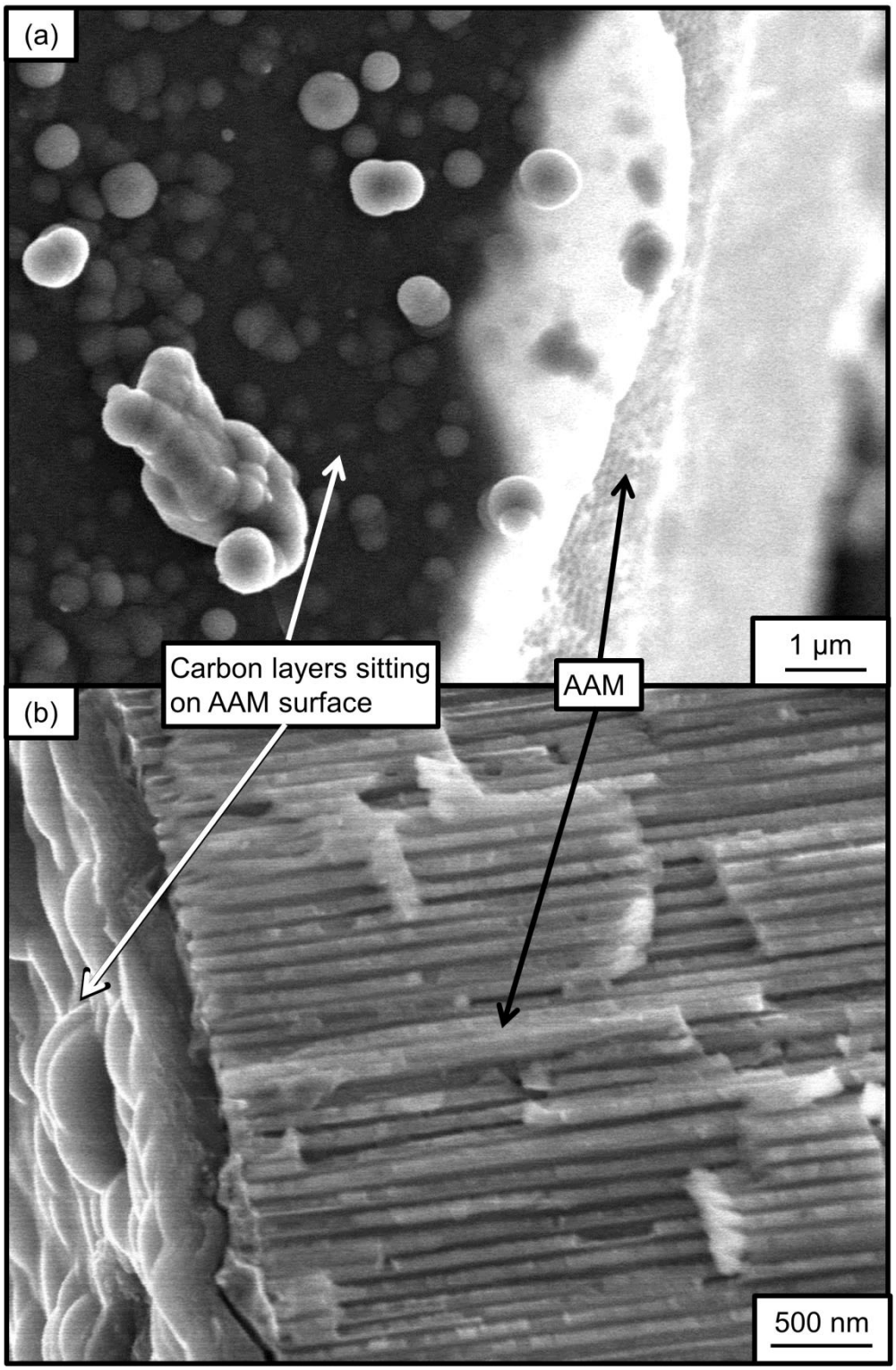

Figure 5.6 SEM micropgraphs showing the (a) top surface (12,000X magnification) and (b) cross-section (30,000X magnification) of carbon coated 40 V AAM. The surface of the membrane is blocked by a deposited carbon layer.

To improve the carbon deposition, the CVD process parameters were modified based on Whitby *et al.*, 2008. In particular, a higher gas flow rate was used. The ethylene and helium flow rate are increased by three times to 18 sccm and 42 sccm, respectively. Moreover, a 50 V AAM was used rather than a 40 V one for the larger pore diameter without compromising the ordered pore structure. As can be seen in Figure 5.7(a), most of the pores of the carbon coated membrane now remain open with only a small fraction of blocked pores. Based on image analysis, after carbon coating, the membrane average pore diameter and porosity have reduced from 58 ± 6 nm and 0.166 to 45 ± 4 nm and 0.092, respectively. The 13 nm-reduction of average pore size indicates the average thickness of the carbon coating is approximately 6.5 nm. Therefore, after the coating, there is no measureable difference in membrane thickness, staying at 80 μm.

A fluid flow measurement was conducted using the carbon coated 50 V AAM (please see Section 5.2.6). However, the permeability obtained is 29% below the estimation based on the surface morphology. Therefore, the carbon nanopipes were released and examined under TEM to observe the interior structure. As can be seen in Figure 5.7(b), some pipes are open through, but exhibit some surface roughness. Other pipes have internal blockage, reducing the percentage of pores for fluid transport across the membrane. Despite the improvement gained by alteration of the CVD process parameters, there are still undesirable structures present within the pore channel that have significant effect on the overall flow behaviour.

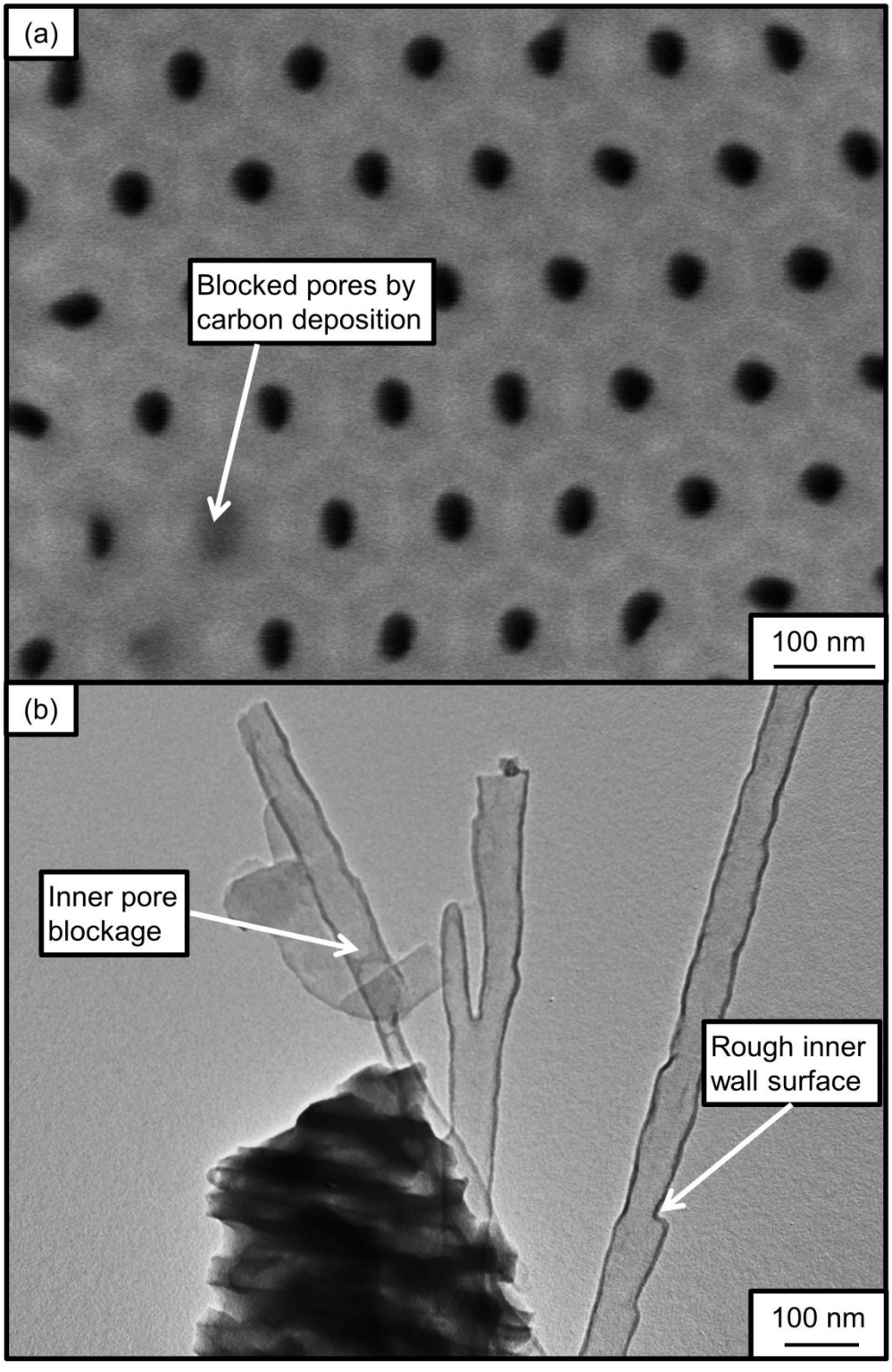

Figure 5.7 (a) SEM micrograph showing the top surface of a carbon coated 50 V AAM (150,000X magnification) and (b) TEM micrograph showing a released carbon nanopipe (110,000X magnification). The CVD condition was improved by increasing the gas flow rate by three fold.

5.2 Fluid flow measurement

As mentioned in Section 2.2.3.1, the occurrence of flow enhancement effect has been repeatedly reported, predominantly in carbon nanotubes (Whitby and Quirke, 2007). This effect has been attributed to nanoscale confinement (Thomas and McGaughey, 2009), surface chemistry and structure (Joseph and Aluru, 2008). However, so far, there has been no experimental study investigating the variation of flow enhancement effect with different nanotube diameters. Thus, there is still a lack of systematic study to verify the computational results reported. Moreover, carbon nanotubes/nanopipes have been the only material being used for investigation so far. While it is generally accepted that the flow enhancement effect is attributed to the slippage of water molecules on the hydrophobic surface of carbon nanotubes, its occurrence on hydrophilic surfaces is still a matter of debate (Neto *et al.*, 2005).

In this section, a systematic study of pressure-driven water flow through hydrophilic AAMs with pore diameters ranging from 100 nm to 20 nm is presented.

5.2.1 Experimental apparatus

A highly sensitive and precise measurement rig is necessary for the fluid flow measurements in AAMs, to study the nanoscale flow with a limited membrane area. After a few stages of modification for measurement accuracy improvement, Figure 5.8 shows the final outcome of the constructed apparatus. The rig is predominantly built using SS316 grade ¼ inch tubing and parts supplied from Swagelok®. Ultrapure water (Milli-Q, 18.2 MΩ cm^{-1} at 25 °C) in a stainless syringe with 225 ml capacity is dispensed by a high force syringe pump (Nexus 6000), to ensure a pulseless flow and capability of measurement at higher pressure. Two pressure transducers (Swagelok®, industrial standard, ±5 kPa) are installed before and after the membrane holder to measure the pressure difference across the membrane. Both pressure transducers are connected from the bottom to eliminate the chances of gas bubble being trapped and altering the measurement. A rugged pipe plug thermocouple probe (Omega, T-type) is installed to provide temperature reading, which enables the measured flow rate being normalized to the standard testing condition. Two gas purge lines and a

water pre-filling line are added for pre-filling the system with water in each experimental run. The water permeate is collected in an oil containing beaker held within a balance (Mettler Toledo®, AB304S). The oil layer is to prevent water loss by evaporation.

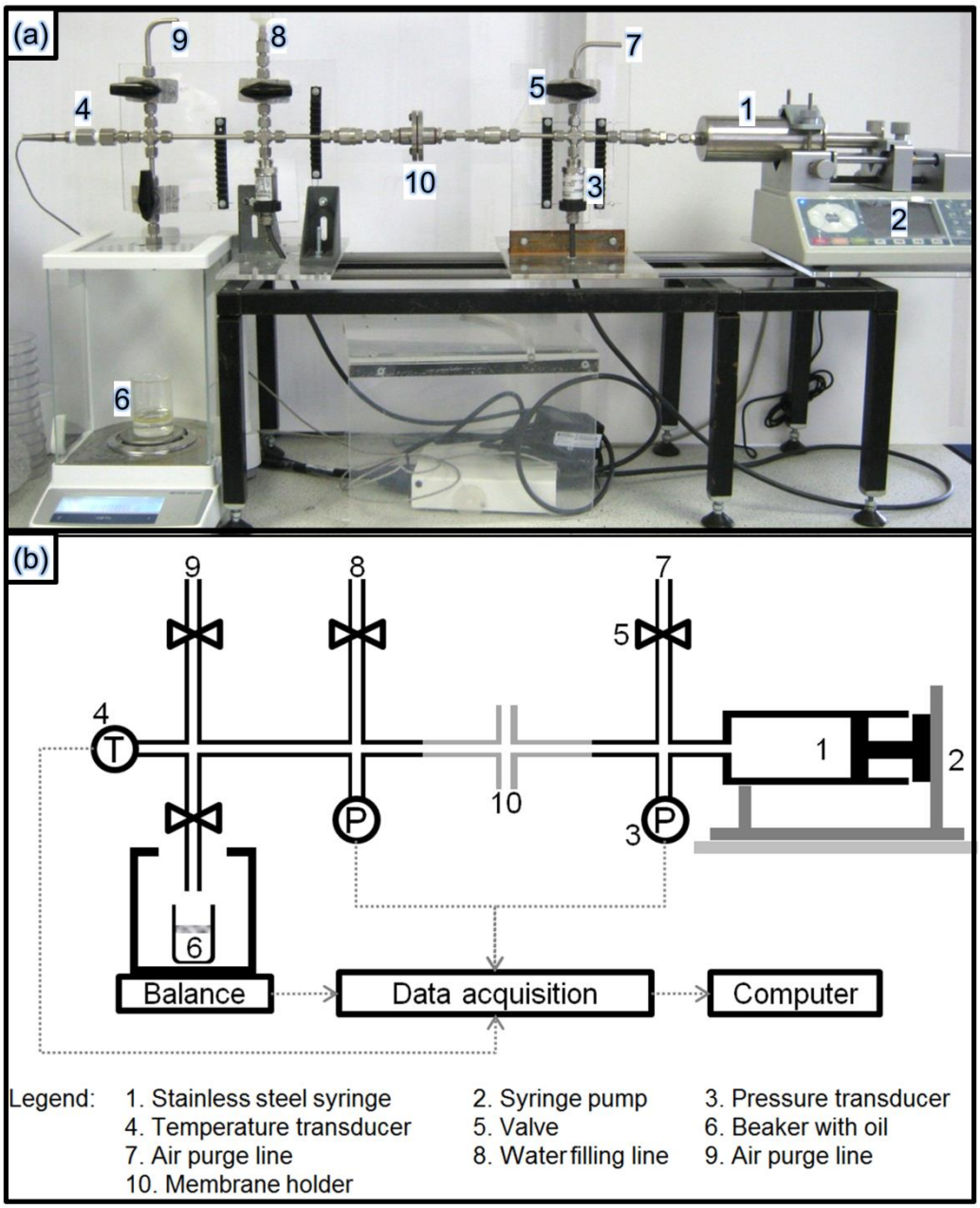

Figure 5.8 (a) The picture and (b) the schematic diagram of the fluid flow measurement apparatus. The apparatus was designed and built in house to provide high sensitivity and accuracy of the measurement.

Each AAM is securely clamped in a custom made membrane holder, consisting of two stainless steel flanges (Figure 5.9). Two silicone rubber annuluses (5 mm inner diameter effective area for water permeation) are used to prevent membrane fracture and to ensure a tight sealing, preventing water slippage around the membrane. For measurements at higher pressures, the membrane is supported using a highly porous and hydrophilic polypropylene mesh (Vyon®, 1-10 µm pore size), without appreciable effect on the flow. The membrane holder is connected to the fluid flow measurement apparatus using Swagelok® quick connect.

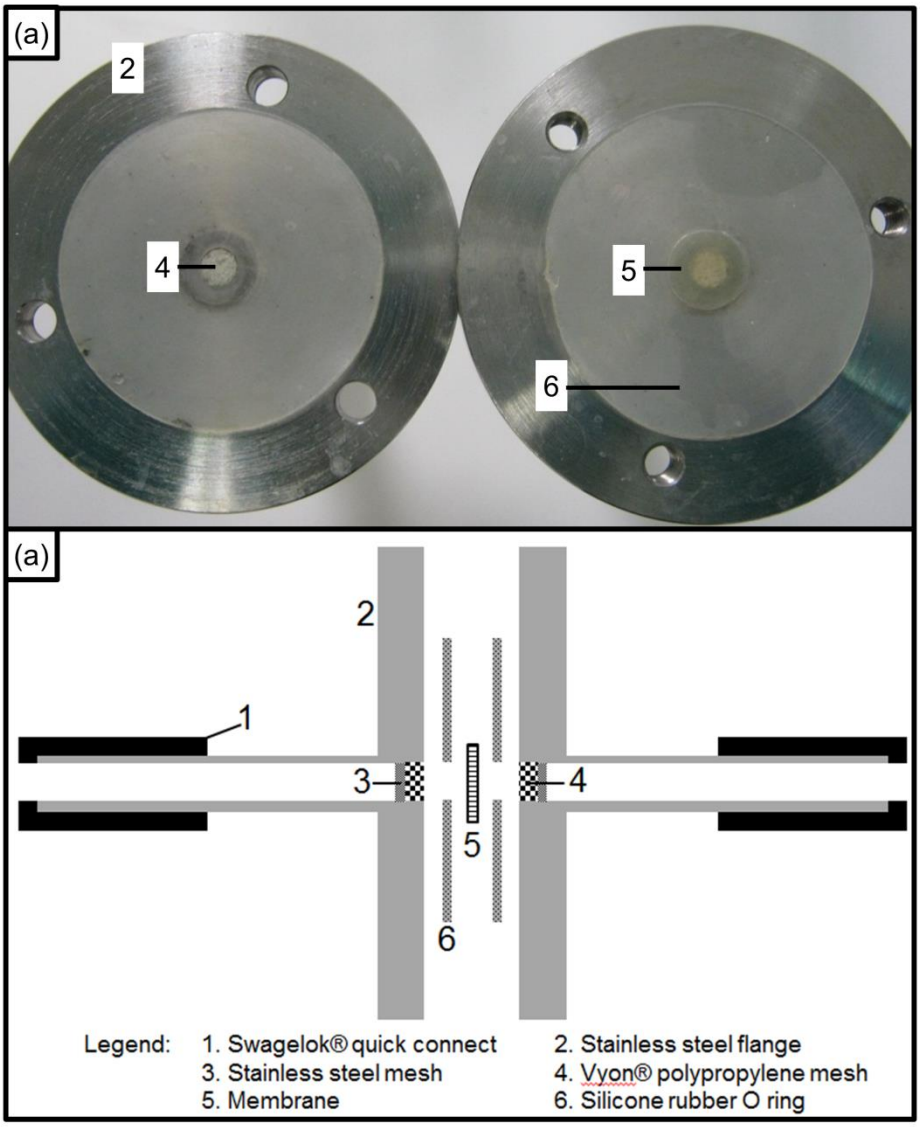

Figure 5.9 (a) The picture and (b) the schematic diagram of the custom made flange type membrane holder.

5.2.2 Measurement procedures

Several precautions have to be taken to ensure accurate measurements. Before starting a measurement, the system was pre-filled with the Milli-Q water and air bubbles were purged away. The air in the feed line (before the membrane) is purged by pump imposed flow at a rate of 2 ml min^{-1}.The air in the permeate line (after the membrane) is purged via manual water feeding by a syringe. As such, this will minimise the lag time to fill the hold-up volume in the system.

To check the effectiveness of the sealing, the AAMs were placed into the membrane holder just after aluminium removal, prior to oxide barrier layer removal (the pores are blocked). Even at a pressure of 700 kPa, water flow was completely blocked. In addition, after a normal experimental run, a visible 5 mm diameter circular wetted area on the membrane can be noticed, ensuring a good sealing around the effective permeation area.

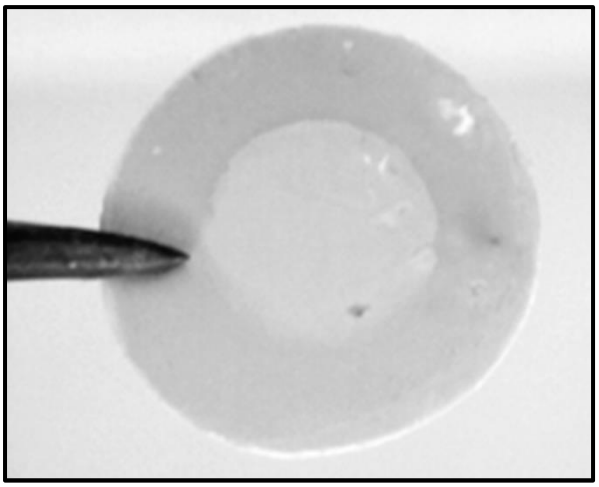

Figure 5.10 Membrane (10 mm diameter) with a 5 mm diameter circular water mark after a flow measurement.

The key variable measured in the fluid flow experiments was the steady-state pressure difference across the membrane, at a given imposed water flow rate. For each membrane, four flow rate settings were tested and each run was for at least 45 min after the pressure had stabilized. All real-time measurements, i.e. pressure, temperature and accumulated mass of water permeate are recorded via a data acquisition system (Labview, National Instruments).

5.2.3 Apparatus calibration

To verify the precision of the apparatus for measurement, regenerated cellulose ultrafiltration (UF) membrane disc (Millipore, PLTK, MWCO = 30 kDa) was used for calibration experiments. According to the product specification, the membrane has a permeability of 1.41 ml min^{-1} cm^{-2} at 55 psi, which can be translated into a permeability of 6.19 x 10^{-10} m^3 m^{-2} s^{-1} Pa^{-1}.

The membrane was tested with a range of flow rates (from 20 to 200 µl min^{-1}). The transient permeate mass and pressure differential profile is illustrated in Figure 5.11. Data should only be extracted during steady-state, to minimise the effect of lag time from delayed responses, as the liquid hold up volume between the membrane and the balance is about 5 ml, a considerable amount relative to the flow rate of the experiment. The gradient of the mass against time plot at each steady-state is obtained as its flow rate. Then, the average pressure at the steady-state is taken. Similarly, the average temperature is taken to correct the flow rate according to its viscosity at referenced temperature, 25°C. Flow rate and viscosity has an inverse proportional relationship as described by the Hagen-Poiseuille equation. According to Hagen-Poiseuille equation, plot in Figure 5.12 should theoretically end at the origin. However, the slightly negative y-axis and positive x-axis interceptions account for the small pressure loss along the tubing and also the Vyon® porous popypropylene mesh support. Specifically, the pressure loss is negligibly small, i.e. less than 1 % when comparing to the pressure resistance caused by the AAMs.

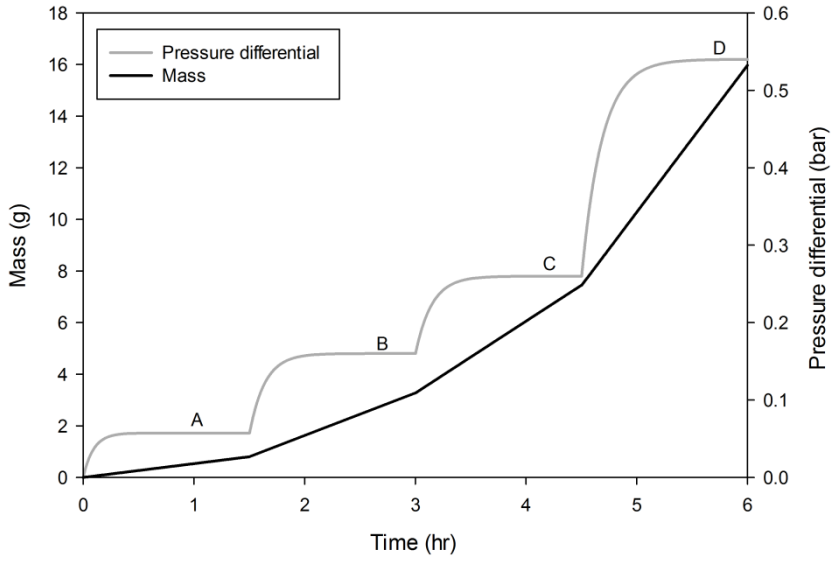

Figure 5.11 Data recorded during a calibration measurement: The accumulated water permeate mass and pressure differential profile plotted against time.

Table 5.1 Gradient of regression line, average pressure differential and average temperature at each steady-state (corresponding to Figure 5.11) and its temperature-corrected mass flow rate.

Steady-state	Gradient of regression line(R^2 factor) ($g\ hr^{-1}$)	Average pressure differential (bar)	Average tempe-rature (°C)	Viscosity (x 10^{-3} Pa s)	Normalised mass flow rate ($g\ hr^{-1}$)
A	0.5353 (0.9966)	0.0574	23.9	0.9150	0.5492
B	1.6510 (0.9967)	0.1600	22.9	0.9368	1.7342
C	2.7900 (0.9988)	0.2600	21.3	0.9710	3.0377
D	5.7060 (0.9997)	0.5390	20.9	0.9815	6.2796

According to the data tabulated in Table 5.1, a plot of corrected mass flow rate against average pressure differential is constructed, as depicted in Figure 5.12. The area-dependent permeability can be obtained from the gradient of the regression line. In this case, it is 11.928 g h^{-1} bar^{-1}. The high regression factor, R^2 value, 0.9996 shows that all the data points closely tally with the regression equation. Taking the effective membrane area for permeation into account, the volumetric permeability obtained is 6.58 x 10^{-10} m^3 m^{-2} s^{-1} Pa^{-1}, which is 6% above the product specification. A number of repeated runs (as tabulated in Table 5.2) were performed to ensure the result is reproducible.

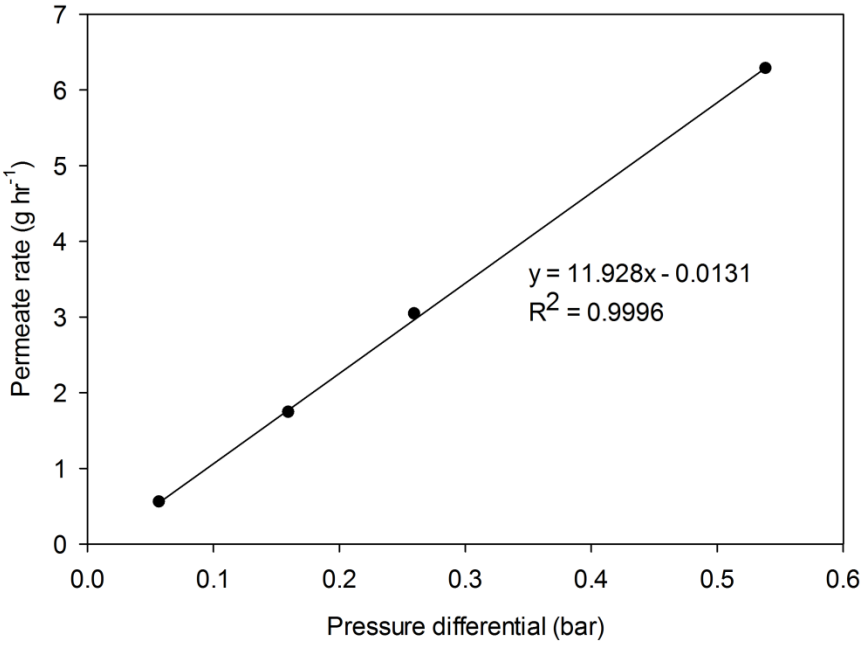

Figure 5.12 Plot of normalised water premeate rate against pressure differential based on Table 5.1.

Table 5.2 Results of repeated calibration experiments.

Run	Measured permeability ($x10^{-10}$ m^3 m^{-2} s^{-1} Pa^{-1})	Deviation from specification (%)
1	6.57	6.10%
2	5.59	-9.80%
3	5.61	-9.70%
4	6.72	8.40%
5	5.64	-9.10%
6	5.68	-8.40%

As can be seen in Table 5.2, all runs yielded results within 10% accuracy of the specification of the membrane. There are a few reasons for the deviation. First, the pressure transducers have a discrepancy range of ±5 kPa. Furthermore, the membrane area tested is rather small, meaning the measurement is very sensitive to error. However, this is inevitable as the system is designed for AAMs, which are fabricated with rather small area at a laboratory scale.

5.2.4 Theoretical and experimental permeability of AAMs

The theoretical permeability of AAMs can be calculated based on equation 2.16. The terms on the right hand side of the equation have all been measured, pore size and porosity in Table 4.1 as well as membrane thickness in Table 4.2. The resulted theoretical permeability of each AAM is tabulated in Table 5.3. The viscosity of water at 25°C, 0.891 x 10^{-3} Pa s was used. The error span presented was originated from the errors in pore diameter and membrane thickness.

Using the protocols developed for fluid flow measurement, the permeability of the AAMs was measured. The measurement data obtained from one of the AAMs is shown in Figure 5.13, in analogy to those shown for the calibration measurement (Figure 5.11 and Figure 5.12). The calculated experimental permeability for all 14 AAMs are summarised in Table 5.4. The theoretical permeability is also included in the table, in order to calculate the flow enhancement factor, as defined by equation 2.17.

Table 5.3 The theoretical permeability of each AAM estimated based on the porosity, pore diameter and membrane thickness.

AAM		φ	D_p	δ_m	L_p
No	Voltage	(-)	(nm)	(±5 μm)	x 10^{-10} m^3 m^{-2} s^{-1} Pa^{-1}
1	25 V	0.121	31±4	55	0.65±0.22
2	25 V	0.142	29±3	55	0.87±0.35
3	30 V	0.157	35±4	60	1.12±0.40
4	30 V	0.153	36±4	65	1.07±0.36
5	40 V	0.149	48±5	80	1.51±0.45
6	40 V	0.153	47±2	80	1.48±0.24
7	50 V	0.166	56±6	80	2.28±0.70
8	50 V	0.167	60±5	105	2.01±0.47
9	60 V	0.155	70±5	130	2.05±0.40
10	60 V	0.155	69±6	135	1.92±0.44
11	70 V	0.175	86±8	115	3.95±0.98
12	70 V	0.166	82±10	130	3.01±0.93
13	80 V	0.178	96±8	145	3.97±0.85
14	80 V	0.168	96±10	120	4.53±1.23

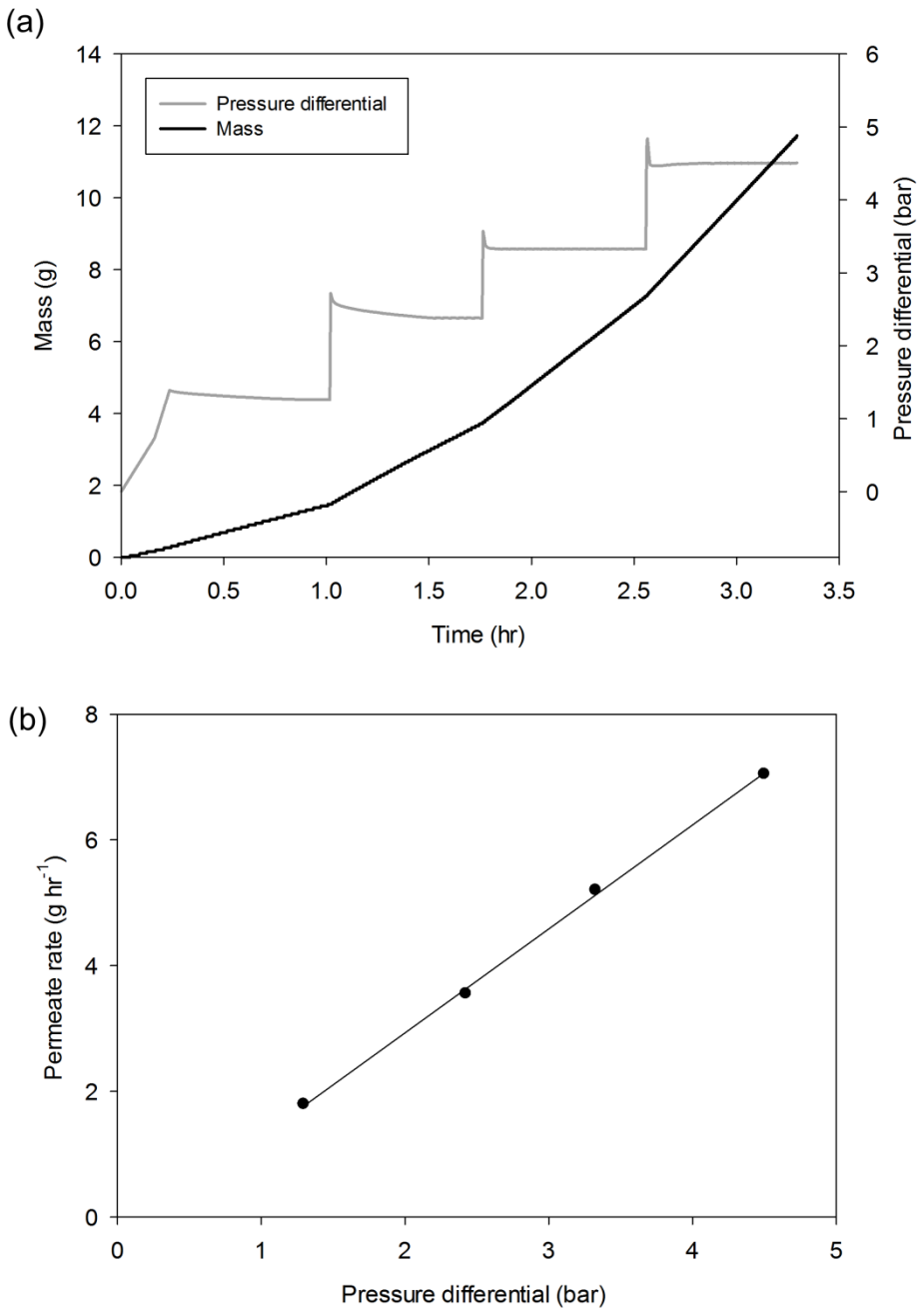

Figure 5.13 (a) Data recorded during a fluid flow measurement of a 40 V AAM: (a) the pressure difference and mass of water profiles and (b) plot of normalised flow rate against the measured pressure difference.

Table 5.4 Experimental permeability and flow enhancement factor of each AAM.

AAM		Experimental L_p[a]	Theoretical L_p	ε
No	Voltage	x 10^{-10} m^3 m^{-2} s^{-1} Pa^{-1}		(-)
1	25 V	1.71±0.09	0.65±0.22	2.64±0.77
2	25 V	2.24±0.12	0.87±0.35	2.57±0.95
3	30 V	2.42±0.13	1.12±0.40	2.15±0.68
4	30 V	2.21±0.12	1.07±0.36	2.07±0.30
5	40 V	2.32±0.12	1.51±0.45	1.54±0.41
6	40 V	2.32±0.12	1.48±0.24	1.57±0.28
7	50 V	2.86±0.15	2.28±0.70	1.25±0.34
8	50 V	2.47±0.13	2.01±0.47	1.23±0.28
9	60 V	2.34±0.12	2.05±0.40	1.14±0.23
10	60 V	2.18±0.11	1.92±0.44	1.14±0.25
11	70 V	4.06±0.21	3.95±0.98	1.03±0.24
12	70 V	3.26±0.17	3.01±0.93	1.08±0.29
13	80 V	3.92±0.21	3.97±0.85	0.99±0.21
14	80 V	4.67±0.25	4.53±1.23	1.03±0.26

[a] The experimental permeability obtained is an average of two measurements.

5.2.5 Flow enhancement factor of AAMs

The calculation of flow enhancement factor is shown in Table 5.4. The data obtained is plotted in two ways, for convenience of analysis (Figure 5.14). As can be seen in Figure 5.14(a), the flow enhancement factor is larger than one for almost all the AAM pore diameters examined. It also increases with decreasing pore diameter. The error bars for the flow enhancement originate from the error accumulation of all measuring devices, while those for the pore diameters arise from the statistical image analysis of SEM micrographs. In Figure 5.14(b), the whole data set is presented (nearly 1300 data points), highlighting the fact that each membrane consists of a distribution, albeit narrow, of pore diameters.

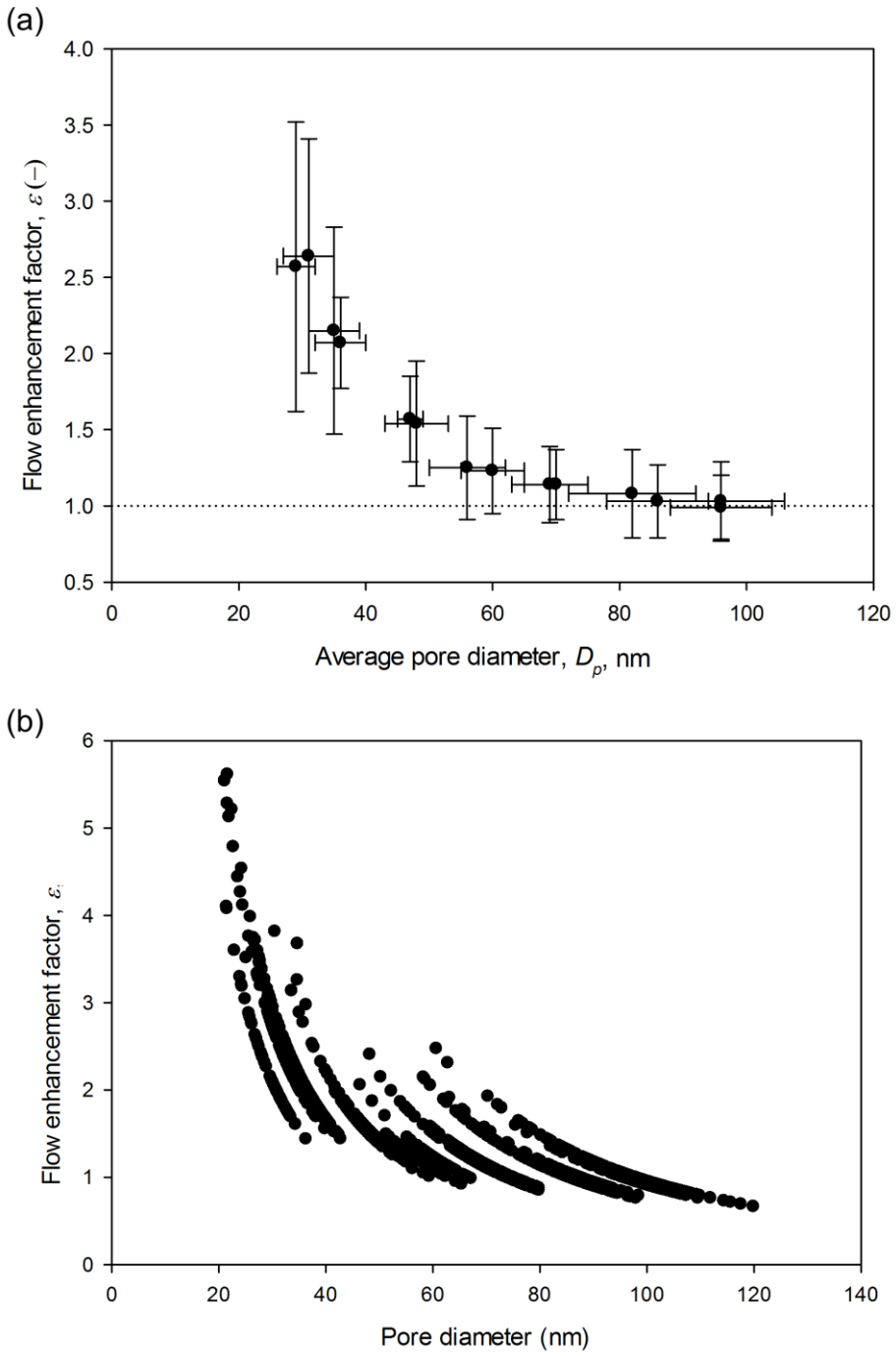

Figure 5.14 Plot of flow enhancement against pore diameter of each AAM based on (a) mean pore diameter with error span and (b) the distribution of pore diameter.

As shown in both plots, a significant flow enhancement effect can be observed for the membranes with smaller pore diameters. As expected, the enhancement decreases with increasing pore diameter, with $\varepsilon \rightarrow 1$ for $D_p \rightarrow 100$ nm. This trend, where the flow enhancement factor is decreasing with increasing pore diameter,

is in good agreement with both molecular dynamics simulations (Thomas and McGaughey, 2008, 2009; Joseph and Aluru, 2008) and experimental results (Sinha *et al.*, 2007) for CNTs. It is apparent from these results that the flow enhancements observed for water through alumina nanochannels are much smaller than those reported for carbon nanotubes. Though small, the flow enhancements reported here are nonetheless larger than unity, signifying that even for hydrophilic materials, slippage of water can occur in channels in the nanometre range.

A flow enhancement approaching unity for channels with a diameter approaching 100 nm is in agreement with observation that no slip was noticed for pressure driven flow of water in a hydrophilic photoresist coated rectangular channel with a hydraulic diameter of ~ 84 nm (Cheng and Giordano, 2002). So far, no other experimental studies for hydrophilic channels with characteristics size below 100 nm have been reported in the literature for water slippage behaviour. This is therefore the first report of water slippage behaviour on hydrophilic surface.

In this study, three factors affecting the extent of flow enhancement have been decoupled, namely the pore diameter, the length of the nanochannels and their wettability. Thomas and McGaughey, 2008 concluded that the size limit for continuum hydrodynamics is 2 nm. Extrapolation of data in Figure 5.14(a) down to this continuum limit yields a flow enhancement effect of about 400 ($\varepsilon \rightarrow 400$ as $D_p \rightarrow 2$ nm). The dependence scales with the square of the tube diameter, explaining why little to no enhancement is observed in channels with diameters above 100 nm. This result is entirely consistent with the Hagen-Poiseuille no-slip model (equation 2.16) for large channels.

Recently, a MD simulation suggested that the flow enhancement factor has a positive correlation with the length of nanotubes or nanochannels (Nicholls *et al.*) This is indirectly confirmed by comparing results for short.(Holt *et al.*, 2006; Thomas and McGaughey, 2008) and long (Majumder *et al.*, 2005; Du *et al.*, 2011) carbon nanotubes, with the latter being two to three orders of magnitude higher than the former. A similar conclusion has been obtained in this case of alumina nanochannels. In fact, although the variation in thickness between each membrane tends to be small, once the flow enhancement data presented in Figure 5.14(b) is normalised to the respective membrane thickness, all the data points collapse into a single curve Figure 5.15.

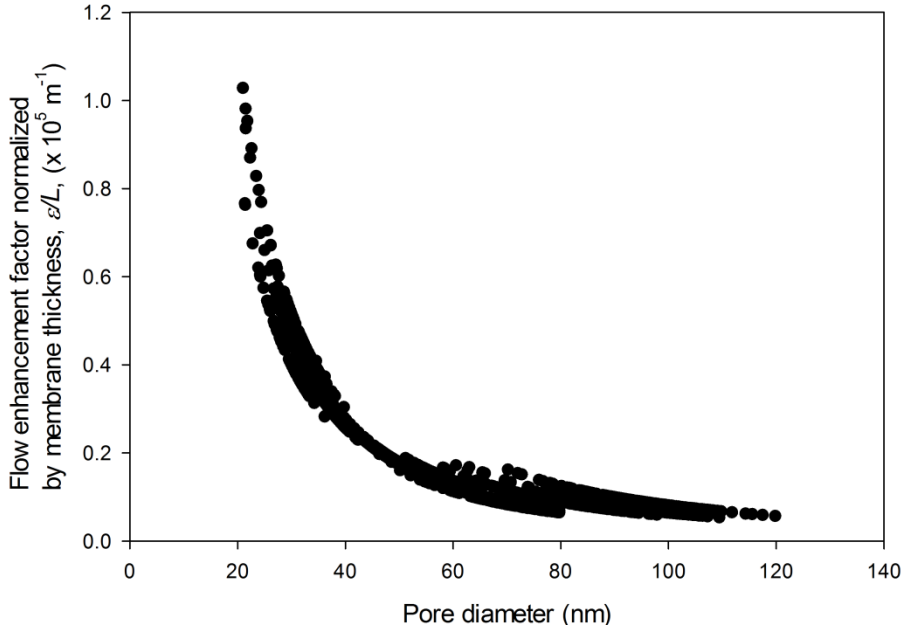

Figure 5.15 Plot of flow enhancement factor normalised by membrane thickness against pore diameter of each AAM based on the distribution of pore diameter.

Finally, by comparing the flow enhancement factor for alumina and carbon nanotube channels of similar diameter and length, it is clearly shown here that the more hydrophilic the material, the lower the flow enhancement. For example, the average flow enhancement for a 40 nm diameter alumina channel normalised by its length is approximately 0.25 x 10^5 m^{-1} (Figure 5.15). This is approximately one order of magnitude smaller than what has been reported for ~44 nm diameter hydrophobic carbon nanopipes, which is about 4 ~ 5 x 10^5 m^{-1} (Whitby and Quirke, 2007). A similar difference is obtained when comparing the enhancement values for ~ 2 nm tubes using the extrapolated data from Figure 5.15 and data for carbon nanotubes both from experiments (Holt *et al.*, 2006) and MD simulation (Joseph and Aluru, 2008).

The above calculations are in agreement with a recent MD article that relates the occurrence of hydrodynamic slippage, and hence the flow enhancement effect, to the magnitude of solid-liquid molecular interactions and the proximity of preferential adsorption sites on the channel wall that promote the migration of water molecules from one to the next (Ho *et al.*, 2011). In fact, the adhesion energy of water on alumina is about 800 mJ m^{-2} (Hobbs and Kinloch, 1998), while it is ~100 mJ m^{-2} on graphite (Fowkes, 1971). This shows significantly lower solid-liquid interaction at the molecular level for water and graphite. In addition, the surface diffusion of water on graphite is also promoted by the

smaller distance between the neighbouring atoms, 0.14 nm (Desch, 1934), comparing to that of alumina, 0.18 nm (Adiga *et al.*, 2006).

Recently, a mathematical model capable of explaining both size confinement and solid-liquid interaction effects on flow in nanochannels has been proposed (Mattia and Calabrò, 2012). In the article, the proposed model was verified by using the large wealth of literature flow enhancement values reported for carbon nanotubes as described before. This mathematical expression is shown as equation 2.17. To focus on the contribution of size confinement effect for flow enhancement, equation 2.17 can be rearranged:

$$\varepsilon \frac{W_a}{LD_s} = \frac{8\mu}{r_p^2} \qquad 5.1$$

Based on the right hand side of this equation, the theoretical values are plotted as the solid line in Figure 5.16, taking the water viscosity at room temperature. On the other hand, the data points shown for AAMs, are obtained by normalising the data points in Figure 5.15, by work of adhesion and surface diffusion, as expressed on the left hand side of equation 5.1. The values for the surface diffusion and the work of adhesion used are 2 x 10^{-9} m^2 s^{-1} and 0.8 J m^{-2}, respectively (Hobbs and Kinloch, 1998). As can be seen in Figure 5.16, the experimental data obtained from AAMs is well-aligned with the mathematical model. This shows the capability of the model in describing the flow enhancement effect for different materials, including hydrophilic material (e.g. alumina) and hydrophobic material (e.g. carbon nanotubes).

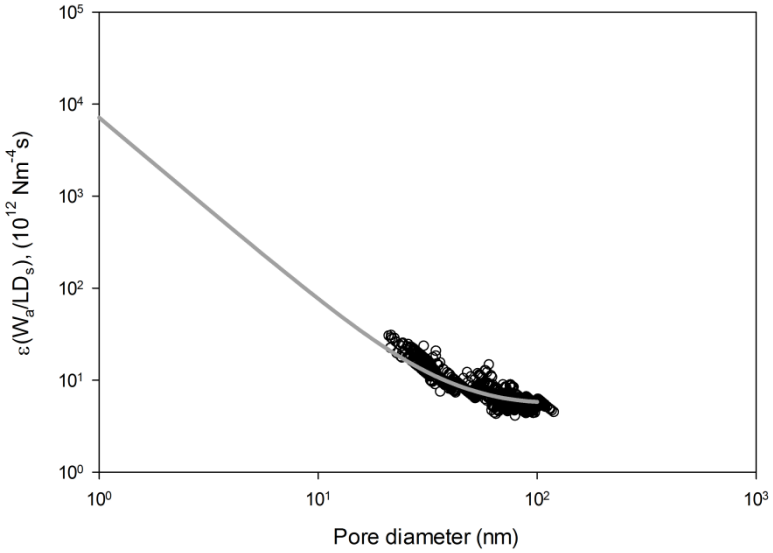

Figure 5.16 Normalised flow enhancement as a function of pore diameter, which the solid grey line shows the theoretical prediction and the scattered points are the data points for AAMs.

5.2.6 Fluid flow measurement in carbon coated AAMs

Previously, a fluid flow study in carbon coated AAMs was reported. This carbon coated AAMs with carbon-nanotube-like structure, are known to be 'carbon nanopipes'. The less-ordered carbon structure as compared to conventional carbon nanotubes, carbon nanopipes give significantly lower flow enhancement effect. Nevertheless, the value reported is still as high as 44 (Whitby *et al.*, 2008). Therefore, it was attempted to reproduce this result and study the effect of varying pore diameter.

The nature and uniformity of the carbon coating produced by CVD has been described in Section 3.4.1. As discussed, initially, the CVD was performed with ethylene and helium flow rate of 6 and 14 sccm, respectively. It is a well-established protocol that was reported in several publications (Mattia, 2007; Sinha *et al.*, 2007; Rossi *et al.*, 2004). However, two 40 V AAMs carbon coated under this CVD condition have shown very low or no fluid flow. As can be seen in Figure 5.17, one of the carbon coated samples shows no flow despite the high pressure (consistently higher than 7 bar) after 24 hours of experiments. On the other hand, the other carbon coated sample shows very low flow rate. The flow rate was only 2 µl min^{-1} even at 6 bar, which indicates virtually 70 times lower flow rate when compared to a pristine 40 V membrane.

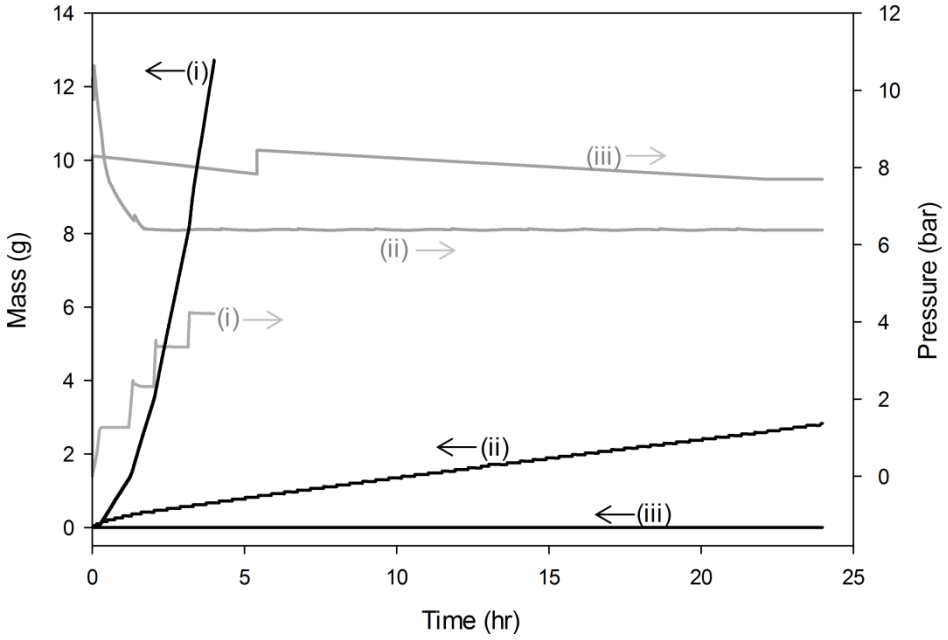

Figure 5.17 Data recorded during fluid flow measurement for two carbon coated 40 V AAMs. (i) shows the data for a pristine 40 V AAM without carbon coating for comparison; (ii) a carbon coated sample shows very low flow; and (iii) the other carbon coated sample shows no flow.

As discussed, this behaviour has been convincingly assigned to a blocking layer formed during CVD. After this, the CVD was performed with tripled gas flow rate, i.e. 18 sccm of ethylene and 42 sccm of helium, as described by Whitby *et al.*, 2008. In this case, the fluid flow was measureable using the established measurement protocol, as shown in Figure 5.18. As can be seen, the measurement shows a drop of more than five times, in permeability, before and after the carbon coating. Despite the decreased pore diameter and porosity after carbon coating, the permeability of carbon coated membrane is still lower than the theoretically expected value, by about 29%. The flow enhancement effect described by Whitby *et al.*, 2008 is not observed here.

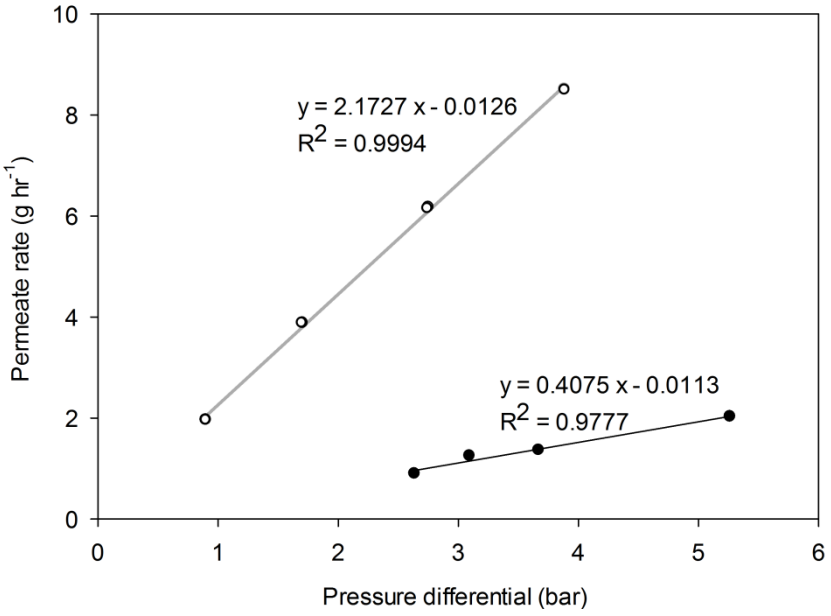

Figure 5.18 Permeability measurement plot for a 50 V AAM, before (open circles) and after (filled circles) carbon coating. The CVD was performed at higher gas flow rate.

Table 5.5 The comparison of flow enhancement effect before and after carbon coating of a 50 V AAM.

Membrane	φ (-)	D_p (nm)	δ_m (±5 µm)	$L_{p,\,theoretical}$ x 10^{-10} m^3 m^{-2} s^{-1} Pa^{-1}	$L_{p,\,exp}$	ε (-)
Pristine	0.166	58±6	80	2.45±0.60	3.07±0.15	1.26±0.31
carbon coated	0.092	45±4	80	0.82±0.38	0.58±0.04	0.71±0.22

As already described in Section 5.1.2.1, under FESEM, the surface of the carbon coated membrane is open, showing homogenous carbon coating. However, further analysis on released carbon nanopipes using transmission electron microscopy (TEM) show, while some of them are thoroughly open, but some of them exhibiting internal blockage. Moreover, the inner pipe wall is not completely smooth and straight, and hence causes additional friction for fluid flow. These reasons are therefore suggested for the reduced permeability observed, contrary to previous report (Whitby *et al.*, 2008).

5.2.7 Fluid flow measurement in silanized AAMs

According to equation 2.17, the flow enhancement effect is dependent on the solid surface-liquid interaction. The wettability of AAMs can be altered by silanization, as described before. Therefore, fluid flow measurements were conducted for silanized AAMs to investigate the flow behaviour of water in nano-channels with varying surface properties.

Figure 5.19 shows some examples of the recorded data during fluid flow measurement for AAMs modified by silanization. However, as can be seen, all silanized samples show no flow despite the high pressure applied after 24 hours of experiments regardless of the silane precursor used. The AAM topographies and cross-sections were checked under FESEM and open through pores like pristine AAMs were observed. The possible explanation for this result is likely due to the hydrophobicity of the pore wall. This high hydrophobicity could be originated from the adopted dipping method for silanization. After the dipping, the AAM samples were rinsed with acetone to remove excessive silane compounds. However, this rinsing has probably only effectively removed the excessive silane reactants on the surfaces, but not within the pore. Therefore, it causes severe cross-linking and forms a multilayer film (Figure 5.3), which increases the hydrophobicity. The contact angles within the pore wall could not be measured due to technical limitations. Nevertheless, the pore walls are likely to exhibit higher hydrophobicity than the surfaces. According to Young-Laplace equation, even if the silanized AAMs are slightly hydrophobic and having a contact angle of about 95°, this can be translated into a critical pressure of at least 500 kPa to wet an AAM with 50 nm pore diameter. This value could be higher if the contact

angle is higher. Therefore, this hydrophobicity poses a lot of resistance for the water flow.

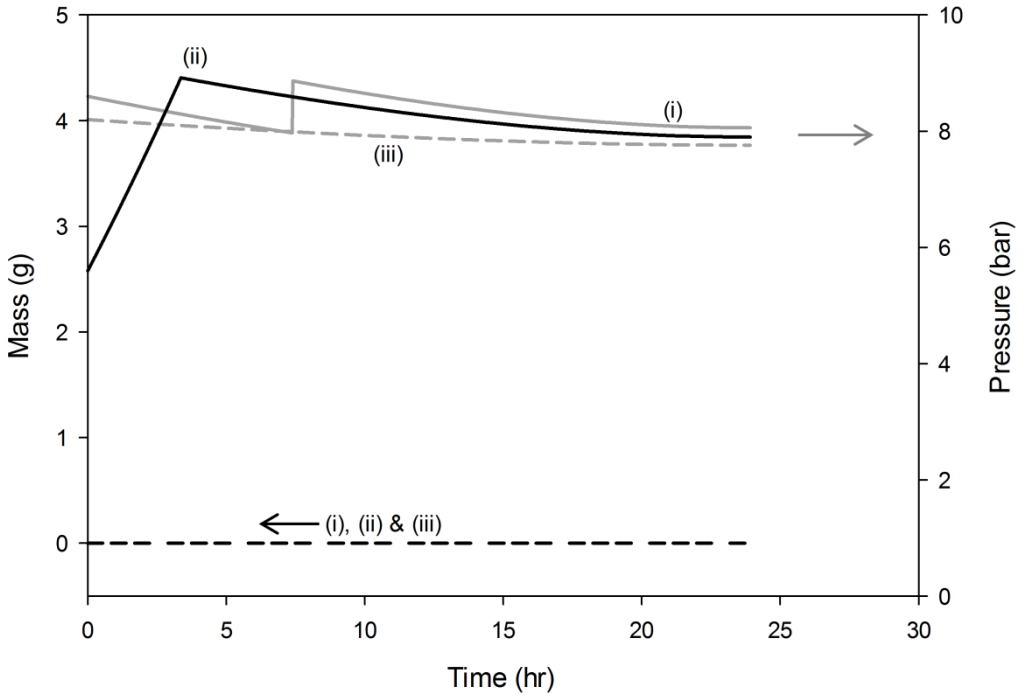

Figure 5.19 Data recorded during fluid flow measurement for three silanized 40 V AAMs by (i) ethyltrichlorosilane; (ii) methyltrochlorosilane and (iii) 50:50 mixture of butyltrichlorosilane and 3-cyano-propyltrichlorosilane.

5.3 Summary

Following the accomplishment in controlled fabrication of flat AAMs with uniform pore structure, this chapter presents the surface modification and fluid flow measurement of the flat AAMs.

AAMs are intrinsically hydrophilic. However, the wettability of AAMs can be readily altered by silane chemistry due to the presence of hydroxyl groups on the alumina surface. Trichlorosilanes with different terminating functional groups can be grafted to the AAM surface and alter the wetting properties. By using different trichlorosilanes for grafting, a wide spectrum of contact angle values (63° to 120°) can be obtained. Alternatively, a mixture of two or more silanes of different composition can also be used to obtain different wettability of the AAM surface. However, the dipping method used here is promoting the cross-linking of silane reactants and therefore the measured contact angle is about 4° to 12° higher than that is expected if only a monolayer was grafted. In particular, due to

inefficient removal of excessive reactants within the pore channel after the dipping, severe cross-linking has caused the pore wall to exhibit higher hydrophobicity than the surface. This subsequently increases tremendous resistance to flow as high critical pressure is required to wet the AAMs.

For carbon coating of AAM by CVD, the gas flow rate is an important parameter to control the resulting morphology. When the gas flow rate is too low, the carbon is deposited on the surface and forms a layer blocking the porous structure. Higher gas flow rate has shown improved carbon deposition, i.e. open pore structure, homogenous deposition, the thickness of carbon coating reduces the pore diameter and porosity. Nevertheless, some inner wall surface roughness and internal blockage are still observed. These undesirable structures of the carbon coated AAMs cause lower than expected permeability obtained in a later fluid flow measurement. Therefore, the attempts to reproduce the flow enhancement effect obtained by Whitby *et al.*, 2008 are unsuccessful.

Finally, a systematic analysis of pressure-driven water flow through AAMs with pore size in the 20 nm to 100 nm range is reported. Results have shown that flow enhancements, though smaller than for hydrophobic materials such as carbon nanotubes, can be observed for hydrophilic materials as well. The results also confirm that the enhancement increases with decreasing diameter and are a function of the channel length (or membrane thickness), as predicted by recent MD simulation. Moreover, the analysis shows good agreement with a recently proposed mathematical model that associates flow enhancement effect with pore size and length, work of adhesion and surface diffusion of the fluid with the pore wall.

6 Tubular AAMs: Morphology and Ultrafiltration

Due to the limited available surface area of the flat AAMs and low mechanical stability, tubular AAMs were designed and fabricated for potential scale-up. Two applications have been tested to probe the membrane potential: ultrafiltration as discussed in this chapter, and membrane emulsification in the next chapter. The procedures to fabricate tubular AAMs are detailed in Section 3.2. Due to the difference in geometry, there are a number of different inherent challenges in making tubular AAMs. Moreover, due to the difference in starting material purity, the pore structure of the tubular membranes was analysed and compared with flat AAMs. Both symmetric and asymmetric tubular AAMs were fabricated with a range of anodization parameters to probe the range of potential pore sizes, with a specific aim for the lower end, i.e. below 10 nm of UF. Particularly, it is the first report of the fabrication of asymmetric tubular AAMs, and therefore the testing for UF performance. The morphology of the membranes and pore size distribution were characterized by SEM and MWCO measurements. Hydraulic permeability and BSA filtration were performed to compare the permeability and selectivity performance with other UF membranes. Finally, fouling testing was performed on AAMs with average pore diameter comparable to the BSA size. By performing these tests, the suitability of AAMs for practical UF application, from the perspectives of perm-selectivity performance, mechanical and fouling resistance was assessed. The results included in this chapter have been recently published in *Journal of Membrane Science* (Lee and Mattia, 2013).

6.1 Stability of anodization

The current density profile, during the anodization of aluminium alloy tubes, shows similar pattern to that of flat aluminium discs. Figure 6.1 shows an example of the current density profile when an asymmetric membrane was formed by continuous voltage reduction after a long period of potentiostatic anodization. Before the voltage reduction, the current density profile is the one typically observed for the formation of symmetric membranes.

During anodization, effective heat removal is required. Therefore, a high recirculation of the acidic electrolyte is needed; considering that the surface area of anodization for tubular geometry is significantly higher (20 times) than the flat ones. The heat removal at high anodization voltage was, however, insufficient

due to the limitation of the experimental set-up, i.e. the peristaltic pump capacity and the big pressure drop due to the small tube diameter. An attempt to lower the concentration of electrolyte at high anodization voltage resulted in a distorted pore structure due to the insufficient dissolution rate of the oxide (Figure 6.2). Therefore, high voltage anodization was avoided in making tubular AAMs. In this work, the maximum anodization voltage used is 50 V.

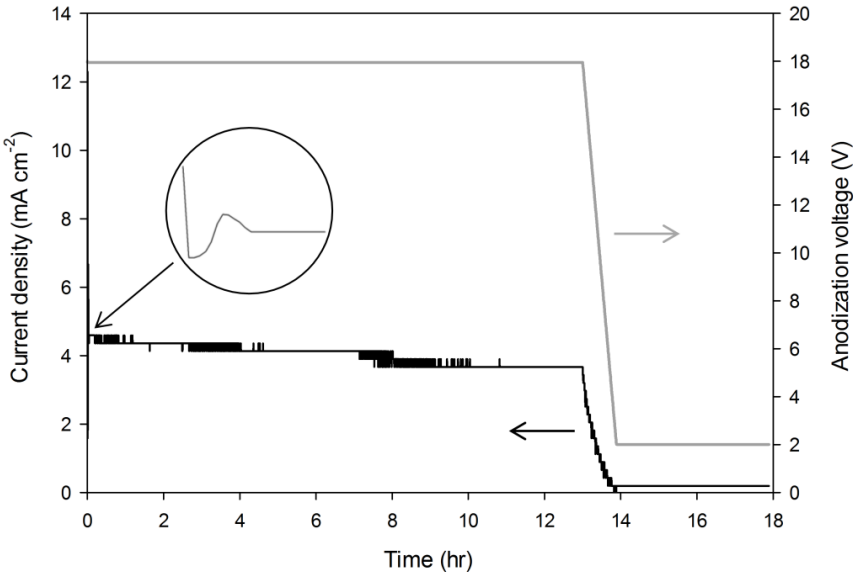

Figure 6.1 Current density profile recorded during the anodization of an A1050 aluminium alloy tube in 1.0 M H_2SO_4 at 0°C, for an asymmetric membrane which the voltage is continuously reduced to 2 V after being kept at 18 V for 13 hours.

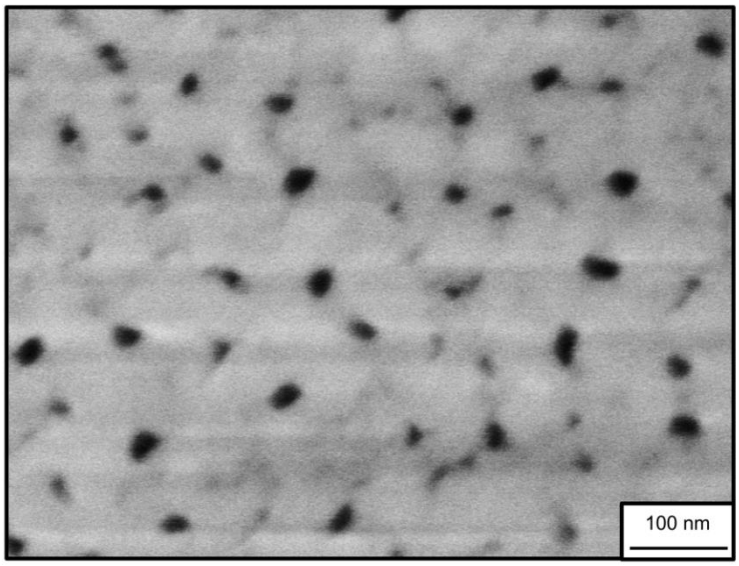

Figure 6.2 SEM micrograph showing distorted pore structure of an 80 V tubular AAM anodized in 0.1 M oxalic acid at 0°C (170,000X magnification). The low quality of the structure organisation is due to the low concentration of electrolyte to facilitate the oxide dissolution.

In addition, it is very important to vent off the hydrogen formed during anodization. The trapped gas bubbles on the tube surface will cause inhomogeneous anodized surface (Figure 6.3(a)). Moreover, the build-up of gas bubbles will increase the pressure within the tube, and negatively affect the recirculation of the electrolyte during anodization, resulting in insufficient heat removal and electrolyte depletion. A number of modifications were performed to improve the system, as illustrated in Figure 6.3(b). Briefly, the system was designed so that the hydrogen and electrolyte exit the tube at the top. While the hydrogen was vented off, the electrolyte was collected and recirculated.

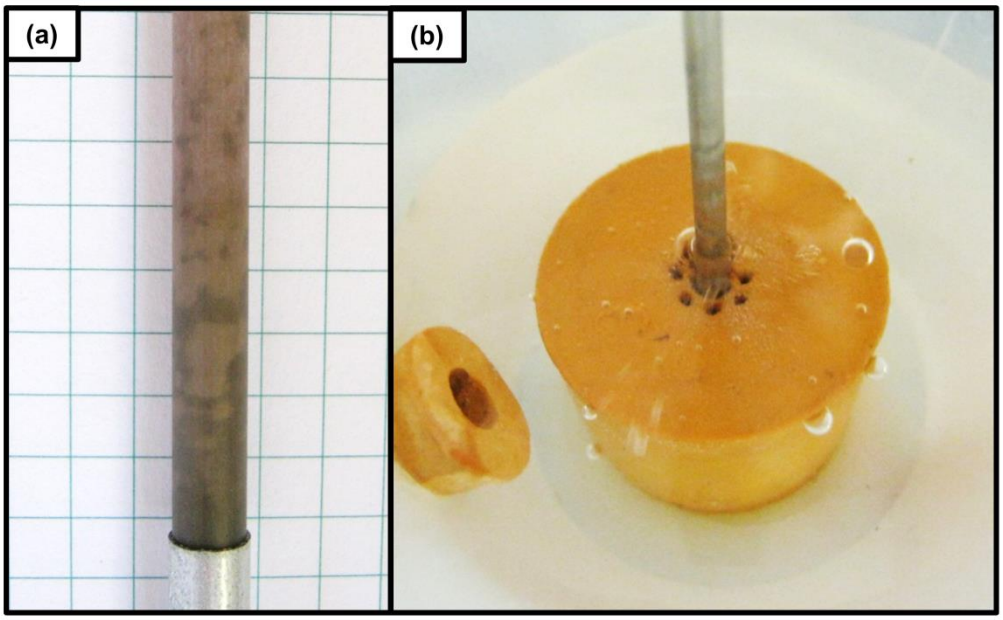

Figure 6.3 Images of (a) a tubular AAM sample showing inhomogeneous surface due to inefficient removal of hydrogen gas bubbles during anodization and (b) improved hydrogen gas bubbles venting after modification.

For tubular AAMs, sealing is normally satisfactory. However, particular care has to be given to the cutting of the tubes. The tube end was physically polished by using sand paper. This is to eliminate sharp pointed edges that could lead to a very high local current density, resulting in overly aggressive aluminium consumption (Figure 6.4).

Figure 6.4. Aggressive aluminium consumption due to high local current density for an aluminium tube having sharp-pointed edges at tube ends.

6.2 Morphological comparison with flat AAMs

Field emission SEM was used to investigate the morphology of the tubular AAMs. The imaging was challenging due to the curvature of the surface which increases inhomogeneous charging of the surface of a material that is on its own non-conductive. Nevertheless, reasonable image quality was obtained by operating the FESEM at low accelerating voltage and short working distance.

6.2.1 Inner surface

Anodization was initiated at the inner surface of the tube, forming the 'top surface' of the AAMs. Since no noticeable difference in permeability for samples prepared by one-step and two-step anodization, only one-step anodization samples were prepared in tubular geometry. Figure 6.5 illustrates the top surface morphology of the membranes and flat AAM samples with similar preparation procedures are included for comparison. As it can be observed, the top surfaces of the two samples are similar. The pore structure was less organised as normally expected for one-step anodization. While the pore shape has high circularity, the pore arrangement deviates significantly from hexagonal packing and a substantial number of branched pores can be observed.

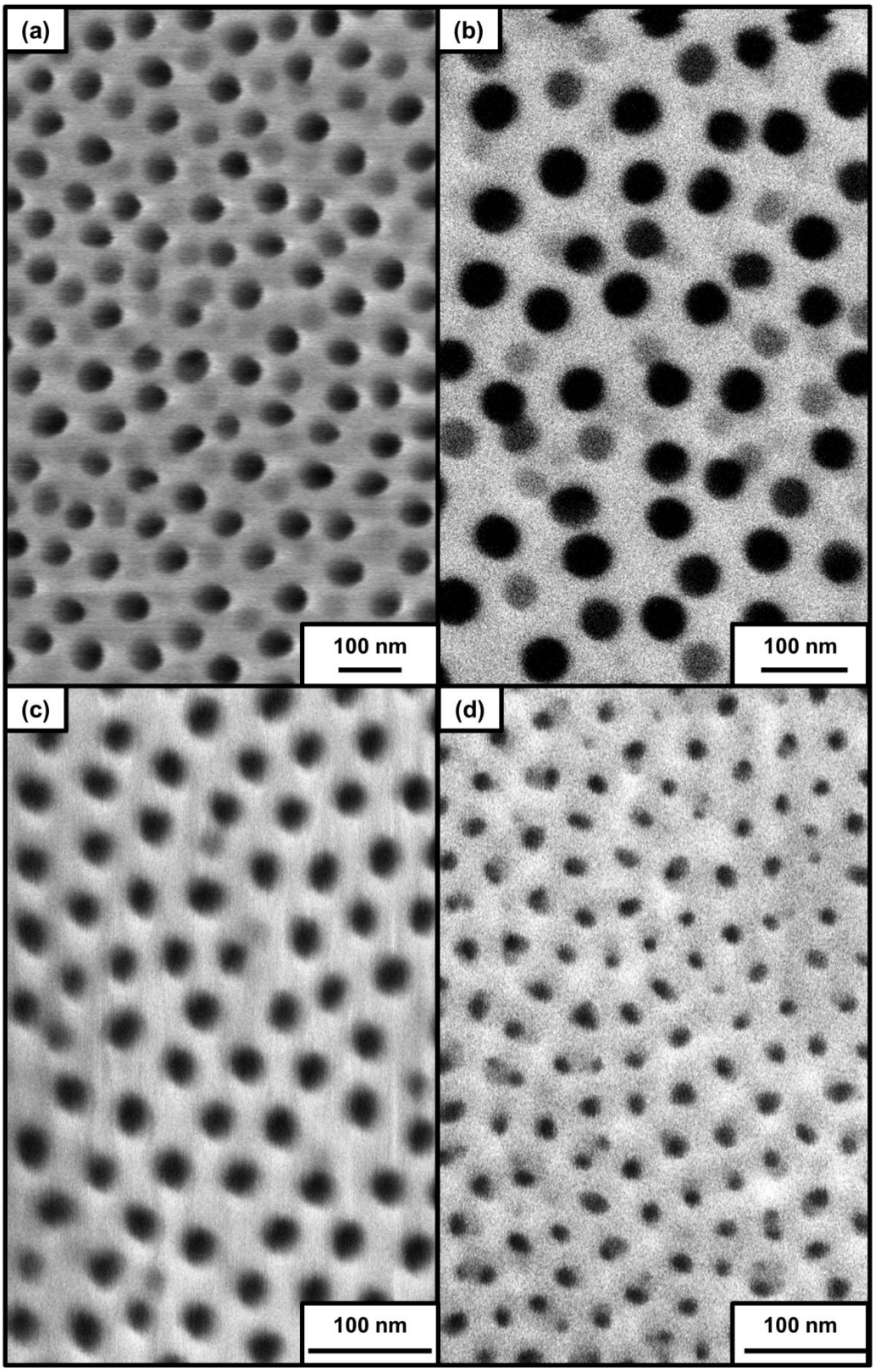

Figure 6.5 SEM micrographs comparing the top surfaces of tubular ((a) and (c)) and flat AAMs ((b) and (d)) fabricated via 1-step anodization. (a) (100,000X magnification) and (b) (140,000X magnification) were anodized at 50 V in 0.3 M oxalic acid whereas (c) (200,000X magnification) and (d) (200,000X magnification) were anodized at 20 V in 0.5 M sulphuric acid.

6.2.2 Outer surface

The outer surface of the tubular AAMs, being analogous to the 'bottom surface' of the flat AAMs, is covered by the oxide barrier layer which is subsequently removed by wet chemical etching. Control of this process is very important to prevent under- or over-etching which would cause significantly reduced permeability in the former case or reduced separation performance in the latter one. While an electrochemical method was developed for flat AAMs to monitor this process, it has been impossible to adapt for tubular AAMs due to the difficulty of insulating the non-removed aluminium at both ends, i.e. interrupting the current detection. Therefore, the optimum removal conditions were investigated by performing wet-chemical etching at different time intervals. As shown in Figure 6.6(a), the barrier layer was still present after 10 min of etching. Then, the barrier layer was gradually removed after 20 min of etching (Figure 6.6(b)) and completely removed after 30 min (Figure 6.6(c)). Excessive etching leads to rapid pore widening and pitting of the membranes (Figure 6.6(d)), not commonly observed in flat AAMs. This is attributed to the use of an aluminium alloy as a starting material and the consequent accumulation of other elements such as Si, Mg, and Cu at the oxide barrier layer (Zaraska *et al.*, 2010a). Generally, the etching time is positively related to the thickness of the oxide barrier layer, and hence the final anodization voltage. As an example, only 1 min was needed to remove the oxide barrier layer for an asymmetric membrane with 1 V final anodization voltage.

Figure 6.7 illustrates the bottom surface morphology of the membranes and flat AAM samples with similar preparation procedures are included for comparison. Usually, a good pore structure is expected at the bottom surface of AAMs fabricated at optimum anodization condition (Figure 6.7(b) and (d)). However, the presence of alloying elements in the A1050 affects the pore circularity and regularity of pore arrangement. As a result, some branching and deflection of pores are observed, in contrast to membranes prepared from highly pure aluminium. This somewhat lower quality structure is the price paid for using lower grade aluminium, which is in favour for potential scale-up production.

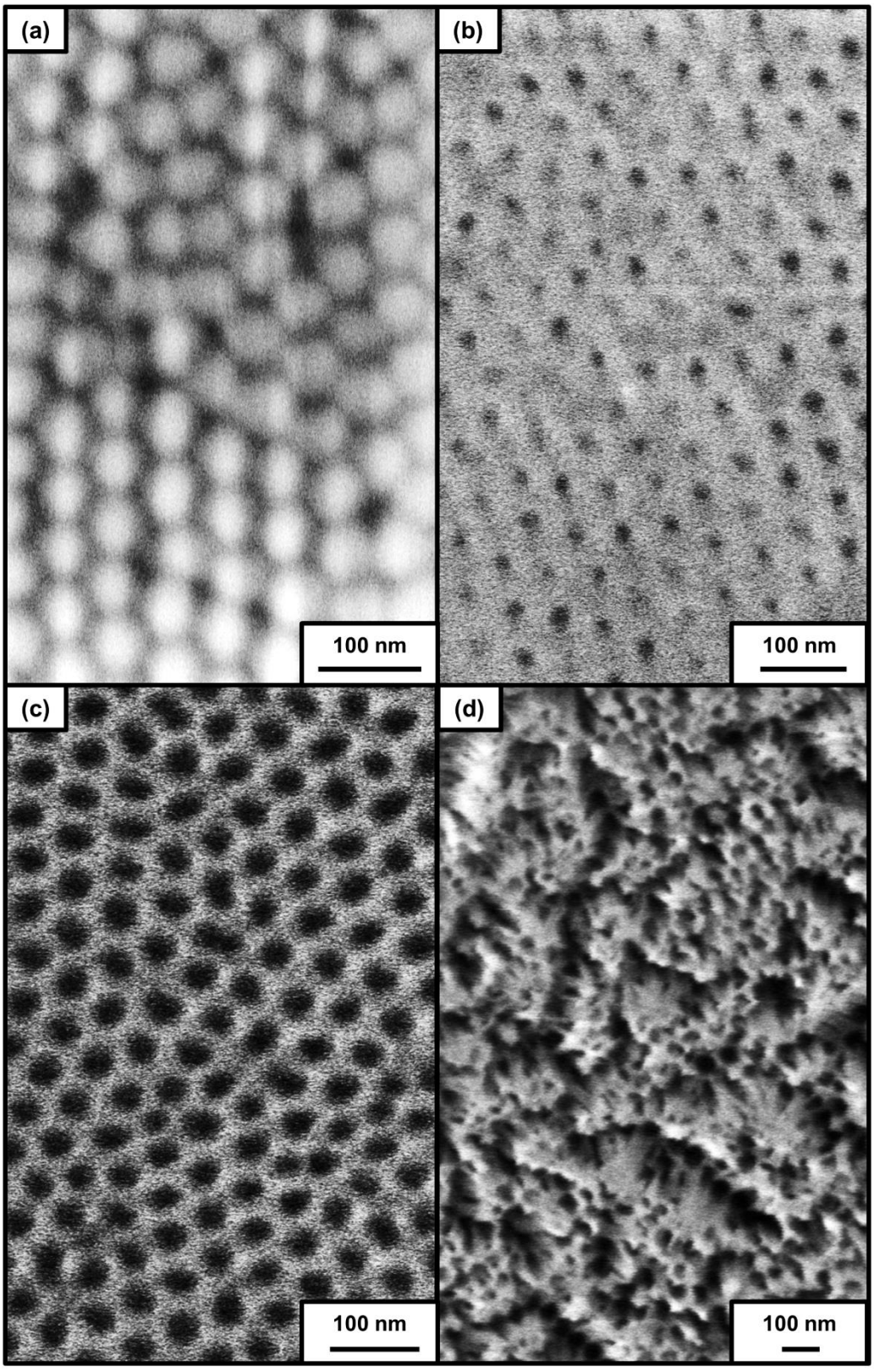

Figure 6.6 SEM micrographs of a tubular AAM anodized at 25 V in 0.5 M sulphuric acid at 0°C. The removal of the oxide barrier layer was performed at 25°C using 6 wt% phosphoric acid for (a) 10 min (170,000X magnification); (b) 20 min (140,000X magnification); (c) 30 min (140,000X magnification) and (d) 40 min (60,000X magnification).

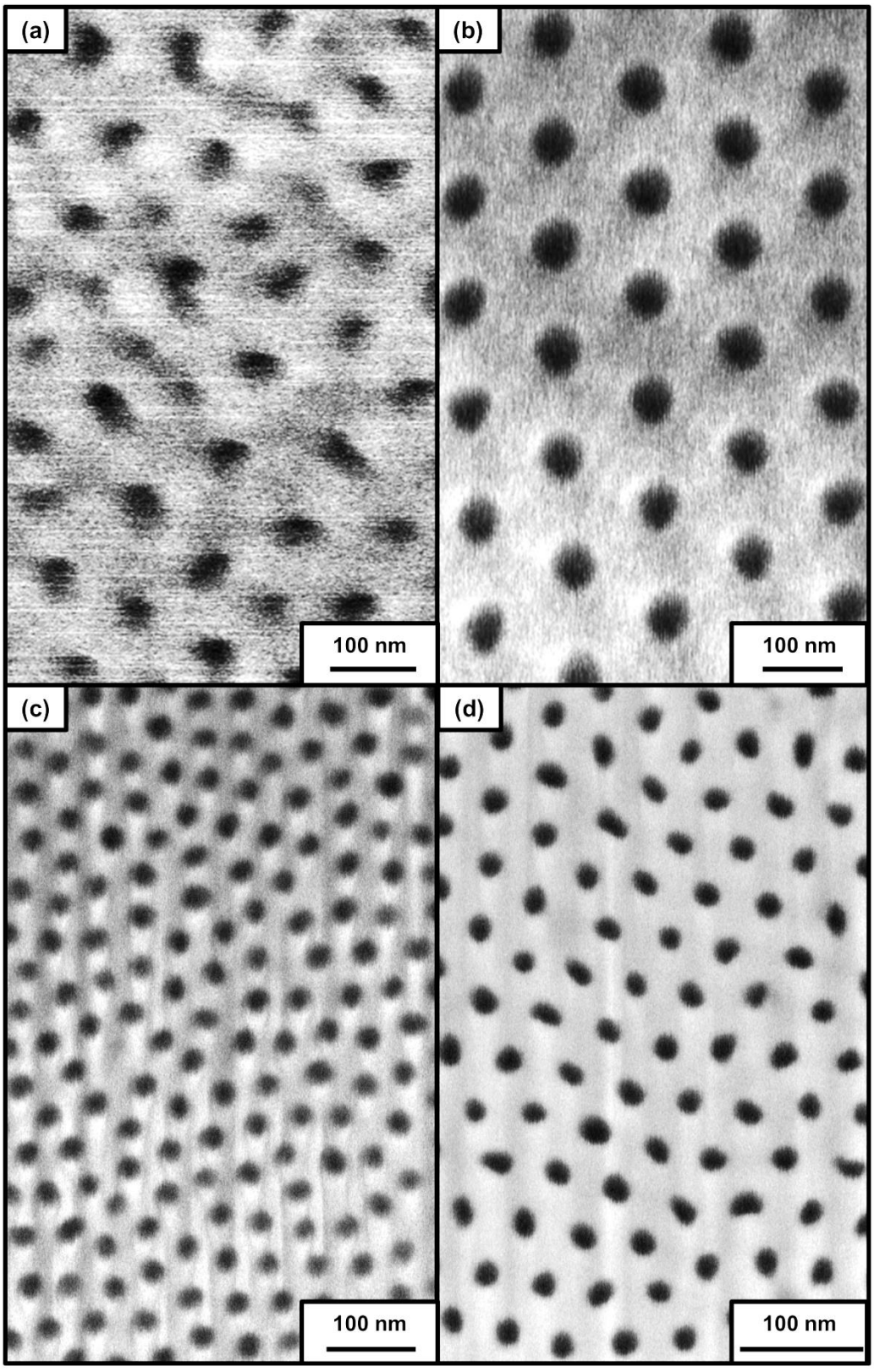

Figure 6.7 SEM micrographs comparing the bottom surfaces of tubular ((a) and (c)) and flat AAMs ((b) and (d)) fabricated via 1-step anodization. (a) (140,000X magnification) and (b) (130,000X magnification) were anodized at 50 V in 0.3 M oxalic acid while (c) (140,000X magnification) and (d) (200,000X magnification) were anodized at 20 V in 0.5 M sulphuric acid.

As discussed before, the impurities present in the starting materials cause the occasional non-even etching of the oxide barrier layer. Despite the mild etching process (lower temperature and lower acid concentration), in contrast to the etching process for flat AAMs, defects are still observed in some samples but in marginal area of membrane (Figure 6.8). These defects were harder to be controlled, and hence causing varying rejection performance of individual membrane, even fabricated at the same anodization condition (See section 6.3, 6.4 and 6.5).

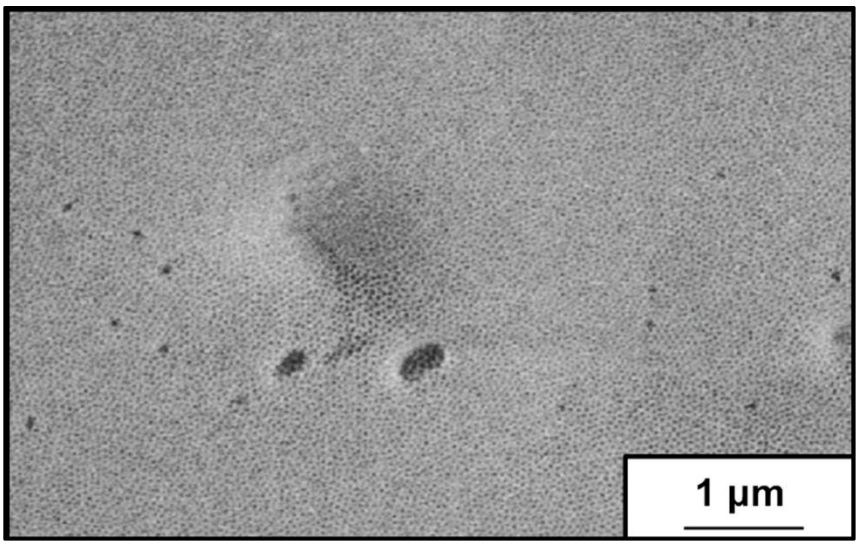

Figure 6.8 SEM micrographs showing a tubular AAM sample with some overly etched spots (17,000X magnification).

6.2.3 AAM pore diameter and thickness

Despite the less ordered pore structure, the linear dependence of the average pore diameter on the anodization voltage is also observed for tubular AAMs, similar to flat AAMs. Figure 6.9 shows the topography of membranes anodized at different voltages. As can be seen, the optimum anodization voltage for-self-assembly, similar to flat AAMs, are 40 V and 20 V for membranes fabricated by oxalic acid and sulphuric acid, respectively. From image analysis, the mean pore diameter for tubular AAMs is tabulated in Table 6.1. However, for asymmetric membranes, the pore diameter at the active layer (formed by final anodization voltage) cannot be quantified, due to the resolution limitation of FESEM which could not provide images of sufficient quality for analysis (Figure 6.10). Therefore, the rejection capability of these asymmetric membranes was examined by molecular weight cut-off (MWCO) tests (See Section 6.3).

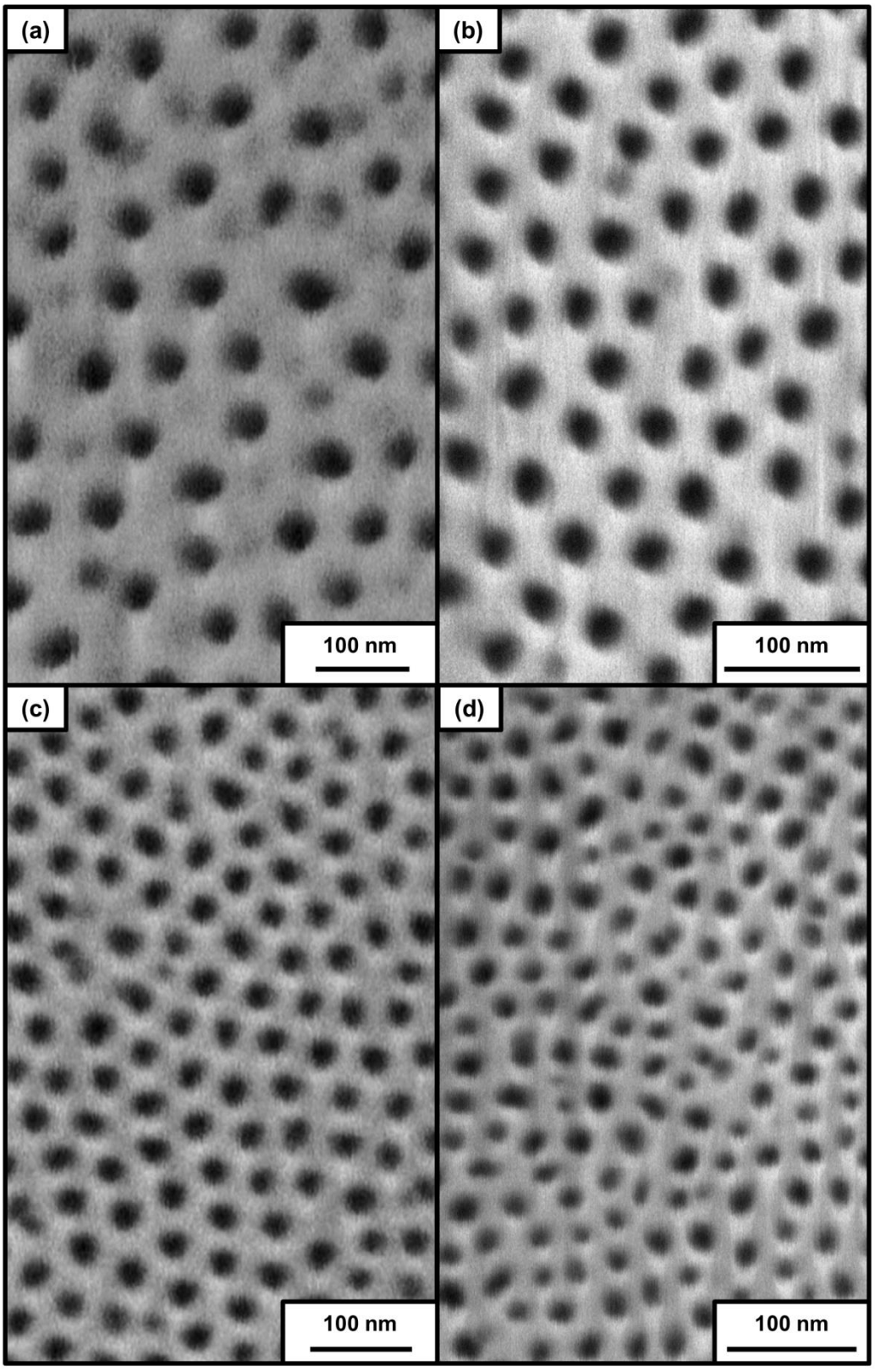

Figure 6.9 SEM micrographs showing the top surface of membranes anodized at (a) 40 V (150,000X magnification); (b) 25 V (220,000X magnification); (c) 20 V (160,000X magnification) and (d) 10 V (210,000X magnification).

Table 6.1 Mean pore diameter, membrane thickness and failing hydraulic pressure for tubular AAMs fabricated at different anodization conditions.

	Anodization voltage (V)		Mean pore diameter (nm)	Thickness (±1 μm)	Failing hydraulic pressure (±10 kPa)
	Initial	Final			
Symmetric	50	-	62±8	62	150
	40	-	49±5	43	120
	25	-	31±3	71	200
	20	-	25±3	32	100
	15	-	19±2	38	120
	12	-	15±2	27	80
	10	-	12±3	21	50
Asymmetric	18	5	-	56	130
	18	2	-	53	130
	18	1	-	50	130

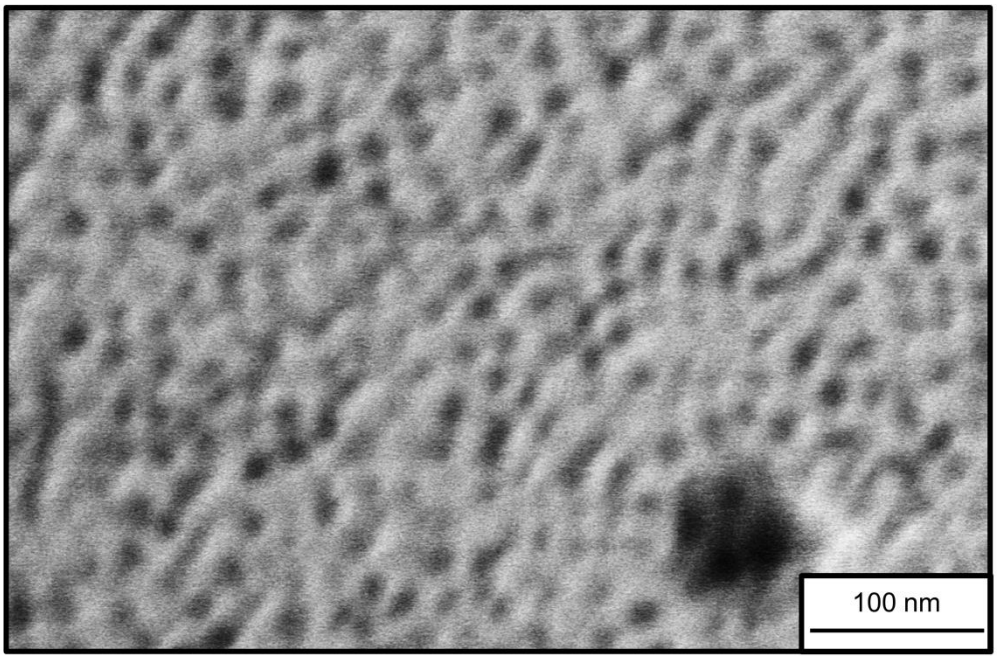

Figure 6.10 SEM micrograph showing insufficient image quality of the bottom surface for an asymmetric AAM fabricated with a final anodization voltage of 2 V (230,000X magnification). However, a porous structure can be roughly observed.

Due to their geometry, the thickness of tubular AAMs was measured by direct observation of cross-section in FESEM rather than using a micrometer. Figure 6.11 shows the two examples of the measurement. For symmetric membranes, subject to the electrolyte used, the thickness of the membrane is generally reduced accordingly to the applied voltage. The increased strength in acidity of electrolyte causes 25 V and 15 V AAMs to have higher thickness than some membranes fabricated at higher voltages. For asymmetric AAMs, it is important to distinguish the thickness of the active layer which was formed during the final anodization voltage. As shown in Figure 6.12, the contrast of this active layer is distinctive due to the significant pore density difference. This thickness is an important parameter for the later perm-selectivity analysis (See Section 6.4).

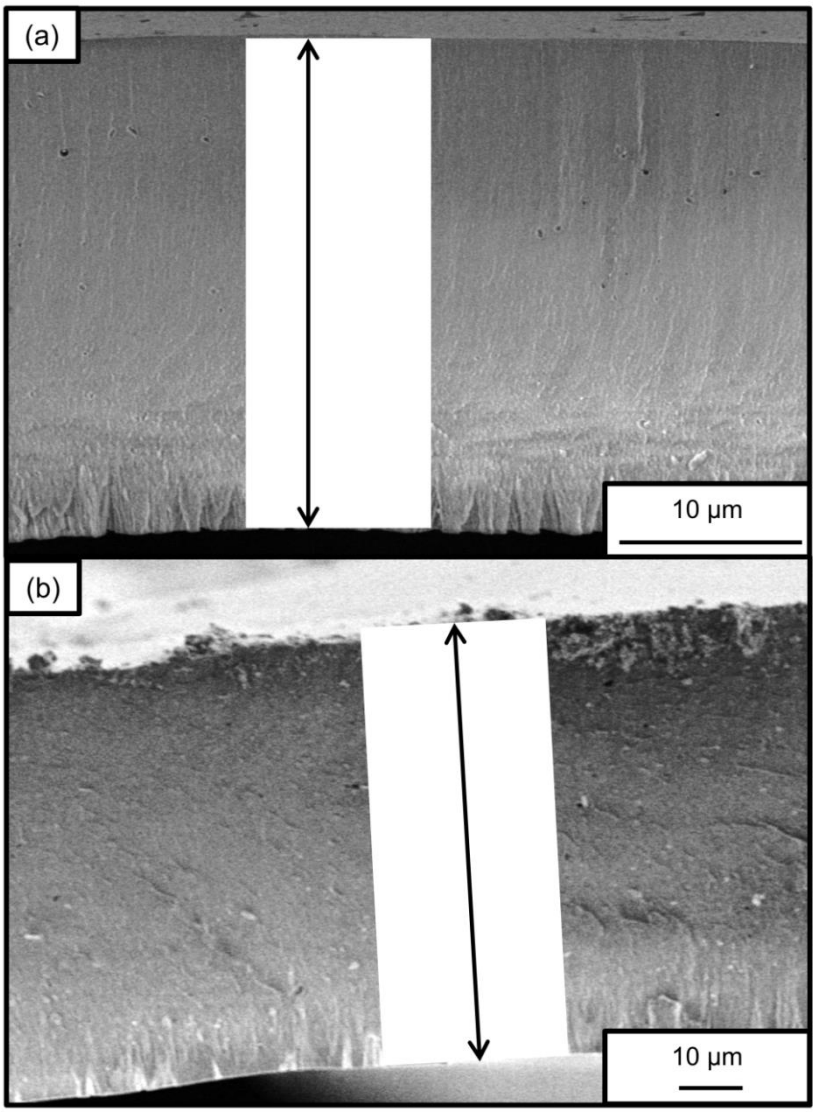

Figure 6.11 The measurement of tubular AAM thickness by direct observation in FESEM. The membranes shows are fabricated at (a) 25 V (2,500X magnification) and (b) 12 V (800X magnification).

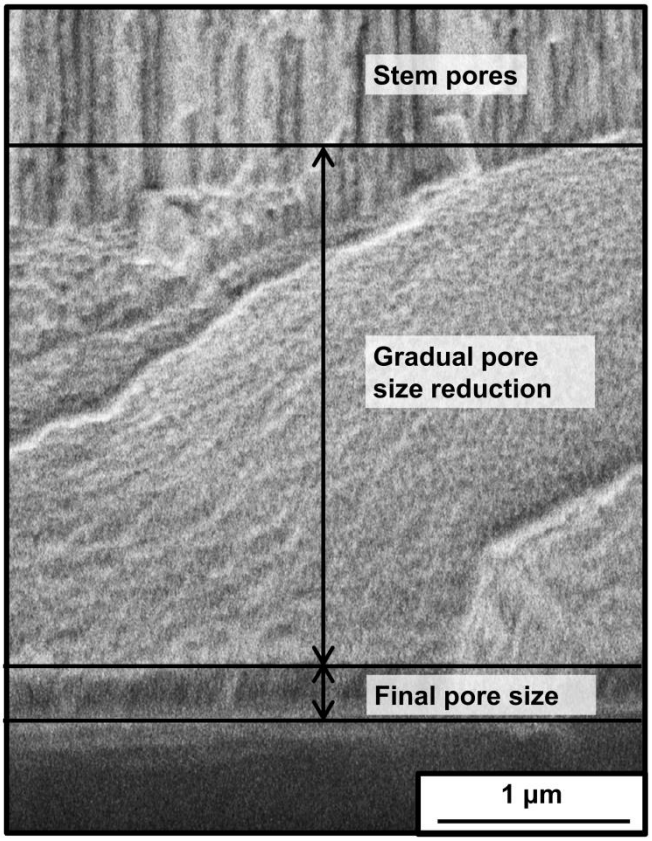

Figure 6.12 The measurement of thickness of the active layer for asymmetric AAMs (25,000X magnification).

6.2.4 AAM mechanical strength

The mechanical strength of membrane is an important durability indicator for practical application. Since the tubular AAMs are going to be used for liquid processes, namely ultrafiltration and membrane emulsification, the mechanical strength of the tubular AAMs were examined by the failing hydraulic pressure, also known as bursting pressure. Basically, failing hydraulic pressure is used to describe the hydraulic pressure which the AAMs can withstand before mechanical failure (Figure 6.13). Hydraulic pressure, induced by water pressurised by compressed air, was applied to the outer surface of the membrane at an interval of 10 kPa. The inner side of the membrane was filled with water at ambient pressure. As tabulated in Table 6.1, as expected, the failing hydraulic pressure is increasing with the thickness of the membranes. Membrane fabricated at 25 V, having the thickest membrane layer, exhibits the highest failing hydraulic pressure of 200±10 kPa. This shows that AAMs are

relatively brittle. This limits the range of applicable transmembrane pressure and extra care is needed for handling and stable operation.

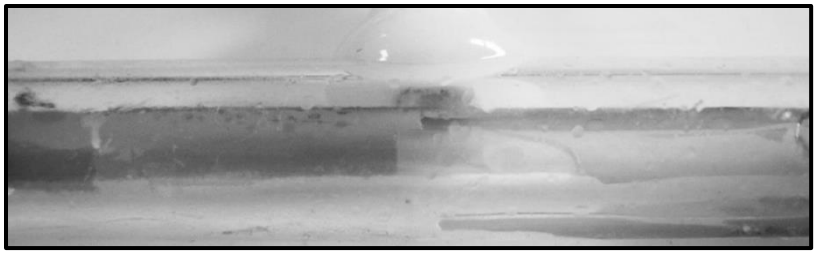

Figure 6.13 Picture showing a failed tubular AAM after hydraulic pressure test.

On the other hand, the vertical tensile of the strength is also measured to assess the rigid for membrane handling. AAM samples were bonded to a nylon cord by using epoxy (Araldite) to ensure a good alignment during the test (Figure 6.14). The test was performed using an electromechanical system (Instron, 3369). Since the material is delicate, the displacement speed was set at 1 mm min^{-1}. The load increased until the membrane failed, as shown in Figure 6.14(c). Due to the limited accessibility of the equipment, tests were only performed for three samples (Table 2) to be sufficiently indicative.

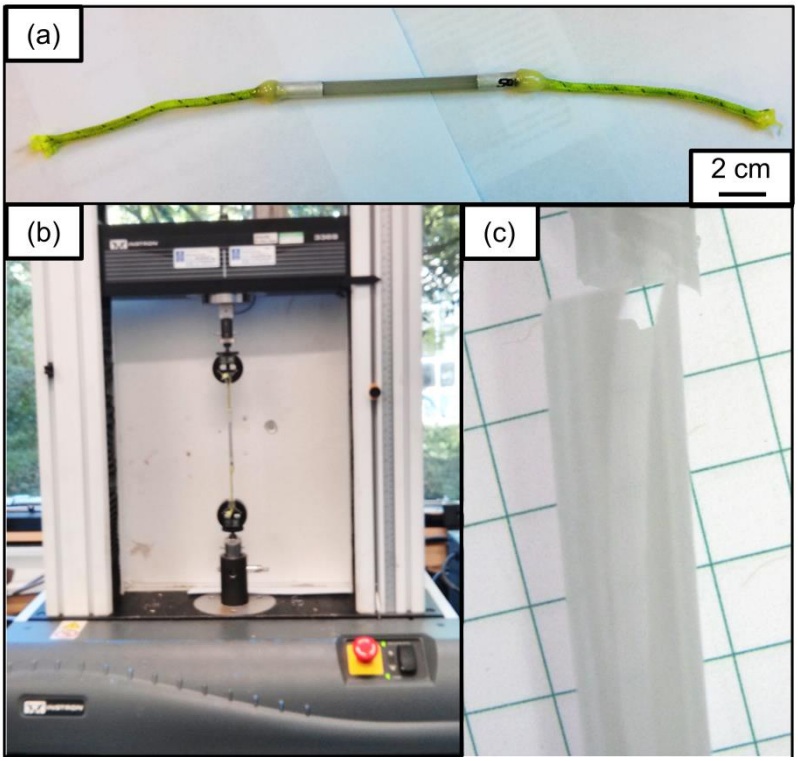

Figure 6.14 Pictures showing (a) a tubular AAM sample bonded with nylon cord to (b) facilitate a good alignment of the sample with the loads during the test without breaking the membranes and (c) the failed sample at the end of the test.

No tensile strength of porous AAM was found in the literature for comparison. The tensile strength for nonporous anodic alumina is in the range of 200 to 500 MPa (Grasing, 2007). The readings here are in the same order of magnitude but slightly lower which can be attributed to the porosity. The sample fabricated in oxalic acid (S50) also has a higher tensile strength, more than double of those made in sulphuric acid. This is likely caused by the slight difference in the elemental composition of the resulting material, but further verification is needed.

Table 6.2 The tensile strength measurement for three AAM samples.

Samples	Thickness (μm)	Load (N)	Tensile strength (MPa)
S50	62	167	297
S15	38	48	139
A18-1	53	61	127

6.3 Molecular Weight Cut Off (MWCO)

To further validate the pore size distribution obtained via image analysis of FESEM micrographs, MWCO tests were carried out to characterise the separation ability of the asymmetric membranes.

6.3.1 Methodology

Two asymmetric AAM samples were prepared for each specific anodization condition. The solutes chosen for the MWCO tests include 10 kDa ± 15% polyethylene glycol (PEG, Aldrich), and 27.8 ± 10%, 51.5 ± 10%, 95 ± 10% and 140 ± 10% kDa polyethylene oxide (PEO, Phenomenex). The distribution span was obtained from the supplier's specification. To avoid interaction among the solutes of different molecular weight, filtration was carried out with a new sample each time with the solution containing a single solute at the concentration of 1000 mg L-1. Ultrapure Milli-Q water (18.2 MΩ cm-1 at 25°C) with 0.05 wt% of sodium azide (99%, Sigma) added was used to prepare the solutions. Using compressed air, dead-end filtrations were performed at 50 kPa. The feed entered at the shell-side and permeated through the membrane into the inner bore. Each experiment was run for an hour and permeates were collected at 10 minute intervals. The feed and permeate samples were analysed by a high performance liquid chromatography (HPLC) system (Shimadzu, SCL-10A_{VP} system controller, SIL-

$10AD_{VP}$ auto injector, LC-$10AD_{VP}$ liquid chromatograph, RID-10A refractive index detector) with an incorporated size exclusion column (TSKgel G3000PW). The flow rate through the column was set to 0.8 ml min^{-1}.

In Figure 6.15, the chromatograms obtained for a blank and 1000 mg L^{-1} 10 kDa solution were illustrated. Comparing these two chromatograms, it is obvious that there is a distinctive peak at 8.477 min corresponding to the 10 kDa PEG. Similarly, the elution time for other solutes, are as summarised in Table 6.3. For each solute, a different solution was prepared for measurement in order to establish the calibration curve. As can be seen in Figure 6.16, a positive linear relationship can be obtained by correlating the area under the peak of the chromatogram with the solution concentration.

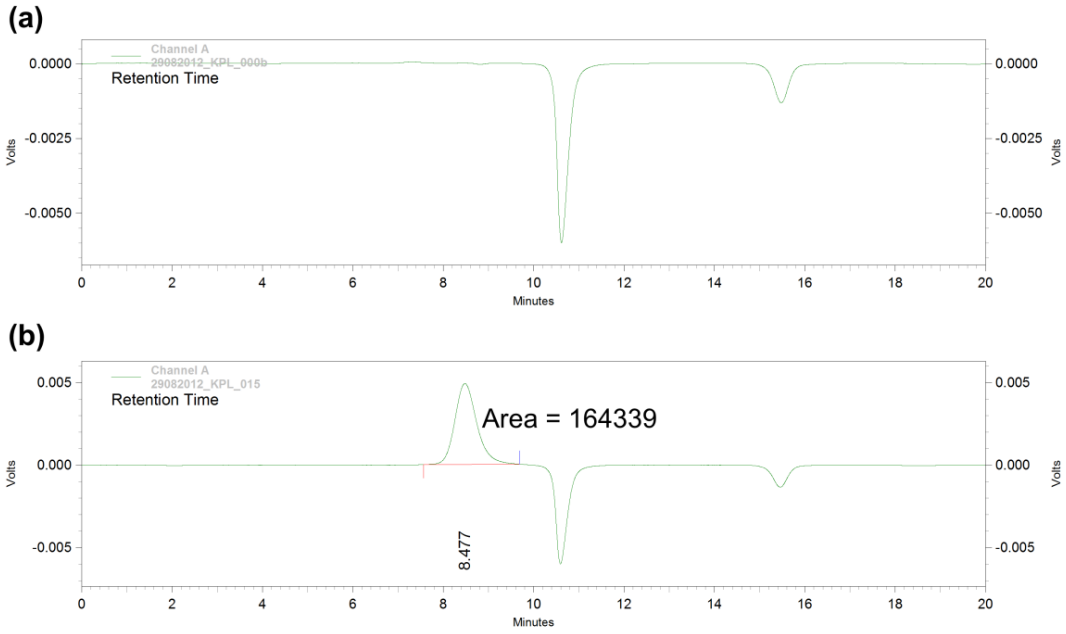

Figure 6.15 Examples of chromatograms obtained from the HPLC for (a) blank and (b) 1000 mg L^{-1} 10 kDa solution.

Table 6.3 The elution time for PEG and PEO solutes of different molecular weight in HPLC analysis.

Solute	Elution time (min)
10 kDa PEG	8.477
28 kDa PEO	7.708
51.5 kDa PEO	7.123
95 kDa PEO	6.667
140 kDa PEO	6.205

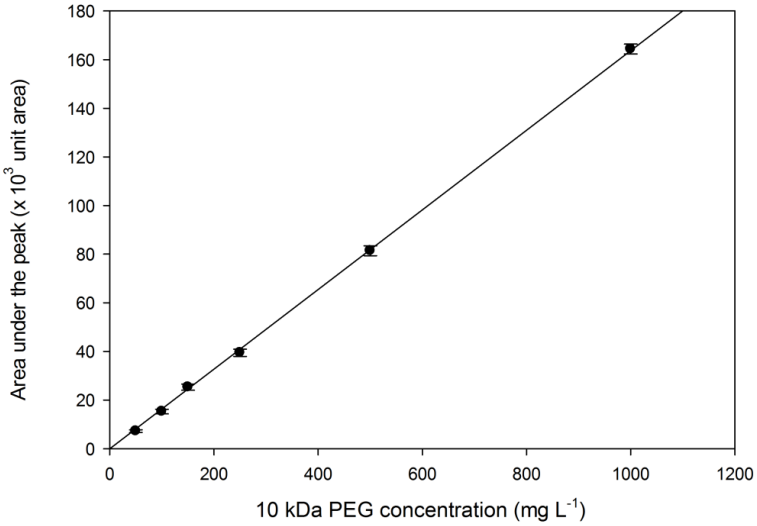

Figure 6.16 An example of calibration curve established to correlate the chromatogram data with the 10 kDa PEG concentration.

Finally, the MWCO data can be used to estimate the membrane pore size based on the following equations (Arkhangelsky *et al.*, 2012; Aimar *et al.*, 1990):

$$d_{50} = 0.11(MW_{50})^{0.46} \quad 6.1$$

$$d_{90} = 0.066(MW_{90})^{0.46} \quad 6.2$$

where d_{50} is the mean pore diameter (in nm), d_{90} is the diameter (in nm) of the solute that is 90% rejected, (i.e. large proportion of pores have diameter less than d_{90}), MW_{50} and MW_{90} are the molecular weight of the solute that displays 50% and 90% rejection capability, respectively. The similarity in d_{50} and d_{90} indicates a narrow pore size distribution. Both equations were derived empirically based on dilute aqueous solution of polysaccharides (Ioan *et al.*, 2000, Aimar *et al.*, 1990). Nevertheless, Arkhangelsky et al. (2000) has used the equations for other polymer standards, particularly PEG and PEO. Good agreement was obtained between the estimation based on the above equations for PEG or PEO rejection and rejection of nano-particles with defined diameter.

6.3.2 MWCO values and corresponding pore size

Figure 6.17 shows the MWCO curves of asymmetric AAMs where two sets of data were obtained for membranes prepared for each specific anodization condition. The MW_{50} and MWCO are both tabulated in Table 6.4. All six membranes tested provide very similar MWCO values, where the cut-off curves

of four membranes are very sharp, indicating a narrow pore size distribution as would be expected. Though having less sharp cut-off curve, the other two samples are still considered to have a narrow pore size distribution when comparing to commercial ceramic UF membranes with similar pore size range (Calvo *et al.*, 2008). While this wider pore size distribution has led to a doubling of the MWCO value compared to the other four samples, very similar rejection properties are observed for all asymmetric AAMs tested, irrespective of the different final anodization voltage. An average pore diameter for the skin layer of 10 ± 2 nm was calculated from MWCO data using the two models in equations 6.3 and 6.4. This result confirms previous observations of a breakdown of the linearity between anodization voltage and pore diameter below the anodization voltage of 10 V (Ding *et al.*, 2010), with a minimum attainable pore size of about 10 nm. Therefore, AAMs anodized below 10 V have similar mean pore size in the range of 10 ± 2 nm and their selectivity is expected to be very close. Despite having similar synthesis procedures, two membranes exhibit higher MWCO and broader cut-off curves. As discussed before (see Figure 6.8), this is attributed to intrinsic structural properties of the membranes, which could be due to the presence of defects and flaws in the aluminium alloy as the starting material. In addition, the effects of pre-treatment such as annealing and, especially, electro-polishing can vary considerably and hence affect the anodization process.

The permeate samples collected at different time interval was compared and show reproducible readings within the sensitivity margin of ±5%. Thus, the effect of solute deformation or concentration polarisation during the test is negligible.

Table 6.4 MWCO values of asymmetric AAMs and the pore diameter estimation based on equations 6.1 and 6.2.

Sample[a]	MW_{50} (±1000)	MWCO (±1000)	d_{50} (±1 nm)	d_{90} (±1 nm)
A18-1a	21100	39700	11	9
A18-1b	24000	73800	11	11
A18-2a	21800	42900	11	9
A18-2b	21300	43400	11	9
A18-5a	22500	44400	11	9
A18-5b	27200	75300	12	12

[a] The sample labelling scheme: A denotes asymmetric membranes. The former number indicates the initial anodization voltage whereas the later one shows the final anodization voltage. The ‘a’ or ‘b’ at the end is to differentiate different samples prepared under the same condition.

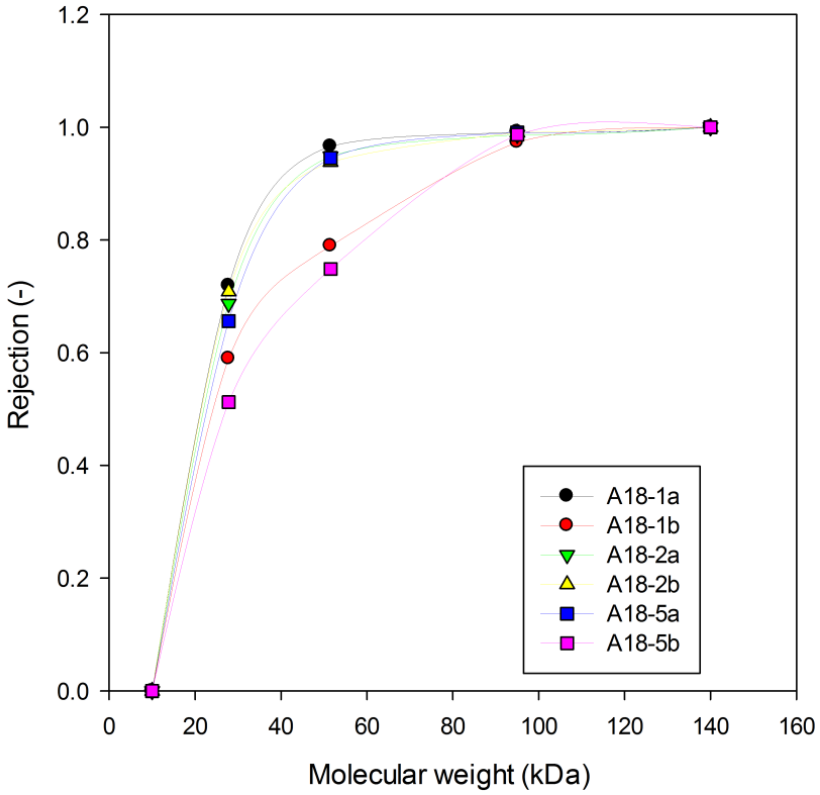

Figure 6.17 MWCO curves of asymmetric AAMs fabricated at different final anodization voltages.

6.4 Permeality-selectivity analysis

Permeability and selectivity, or perm-selectivity, are important indicators of membrane performance. Specifically, permeability shows the membrane productivity whereas selectivity shows the membrane separation capability. As discussed in Section 2.2, Mehta and Zydney, 2005 developed a framework to compare various commercial UF membranes. Kanani *et al.*, 2010 further improved the model by considering the porous structure of the membranes. These two frameworks form the basis for the permeability-selectivity analysis in this chapter.

6.4.1 Methodology

The pure water permeability measurement for tubular AAMs was performed using similar apparatus and procedures to that of flat AAMs (See Section 5.2.2). Briefly, the tubular membranes were housed individually in a custom made mini

'shell and tube' module (Figure 6.18). One end of the membrane was sealed with a silicone sealant to facilitate dead-end permeation. For each tubular AAM, four different flow rate settings were tested and each run lasted at least an hour after the pressure had stabilised. Kanani *et al.*, 2010 rearranged the Darcy's law equation or Hagen-Poiseuille equation, to correlate the flux through the membrane (J_w), transmembrane pressure (ΔP), the viscosity of water (μ), the thickness and porosity of the membrane (δ_m, φ) with the scaled hydraulic permeability (β):

$$\beta = \frac{\mu \delta_m J_w}{\varphi \Delta P} \qquad 6.3$$

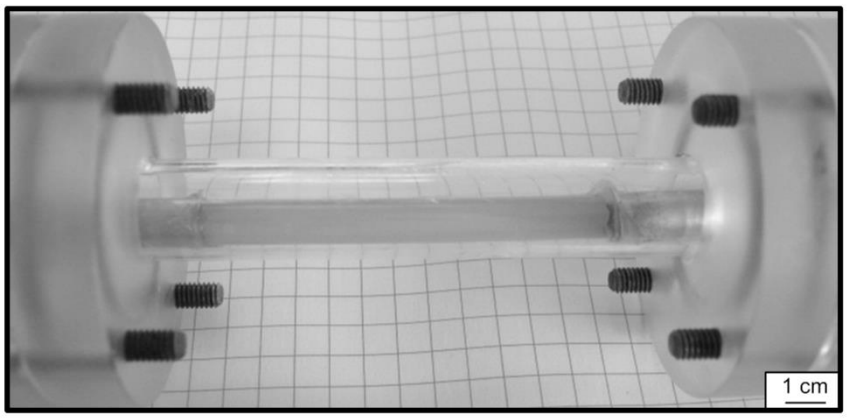

Figure 6.18 A tubular AAM housed in the mini 'shell and tube' module.

Bovine serum albumin (BSA) was used as the model solute to assess the selectivity performance in the developed frameworks (Mehta and Zydney, 2005; Kanani *et al.*, 2010). The BSA (>98%, Sigma-Aldrich) solution was prepared at the concentration of 1000 mg L^{-1} in phosphate buffer saline (PBS, Sigma, pH 7.4) with 0.05 wt% sodium azide (99%, Sigma). The unused solution was stored refrigerated at 4 °C for less than a week. Using compressed air, the dead-end BSA filtrations were performed at 50 kPa for the feed entering at the shell-side and permeate through the membrane in the inner bore. Exceptionally, only 20 kPa of pressure was applied to membranes anodized at 10 V and 12 V because these membranes are insufficiently strong to withstand higher pressure (Table 6.1). Each experiment was run for an hour and permeates were collected at ten minute intervals.

The BSA concentration was analysed by a well-established spectrophotometric method where UV light absorbance of the samples at 280 nm was measured

(Shimadzu UV-1601) (Simonian, 2002). Figure 6.19(a) shows the typical absorbance spectrum obtained for BSA solutions of different concentrations. The peak is located close to 280 nm, corresponding to the fluorescence emission band of tryptophan, a peptide that is present in BSA (Simonian, 2002). The absorbance is positively correlated with the BSA concentration. A linear relationship can be established, and Figure 6.19(b) shows the calibration curve for later measurements. The average of three repeated readings was taken for each sample, and the error bars presented are the standard deviation.

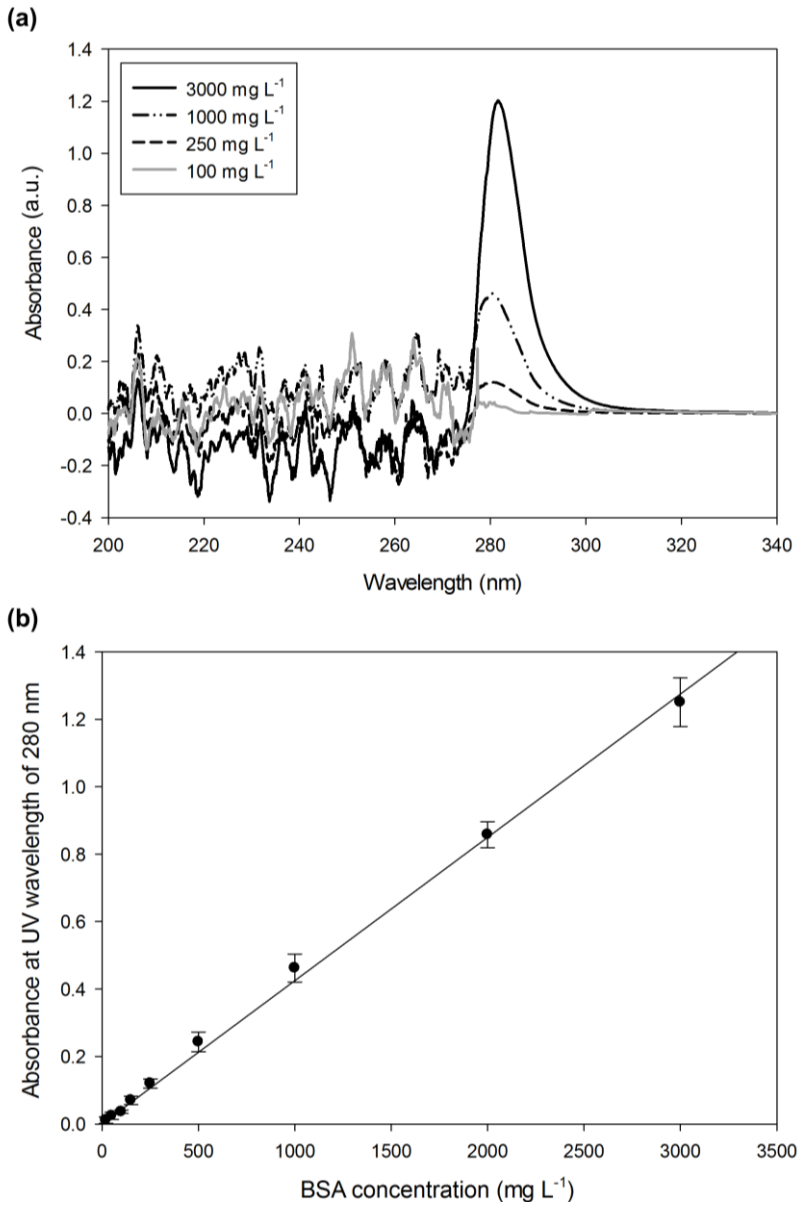

Figure 6.19 (a) UV absorbance spectra for BSA solutions of different concentrations and (b) the calibration curve established to correlate the UV absorbance with the BSA concentration.

The observed sieving coefficient (S_o), actual sieving coefficient (S_a) and rejection (R) can be obtained by:

$$S_o = \frac{C_p}{C_F};\ S_a = \frac{S_o}{(1-S_o)e^{\frac{J}{k}}+S_o};\ R = 1 - S_o \qquad 6.4$$

where C_p and C_F are the concentration of BSA in permeate and feed, respectively; J is the filtrate flux and k is the mass transfer coefficient for different modules (Zeman and Zydney, 1996).

6.4.2 Experimental results

The samples are labelled according to their structure. The starting letters ‘S’ or ‘A’ correspond to symmetric or asymmetric structure, respectively. For symmetric membranes, the number following the letter ‘S’ indicates the anodization voltage (i.e. S25). For asymmetric membranes, the number before the hyphen is the initial anodization voltage and the number after the hyphen represents the final anodization voltage (i.e. A18-2).

The results of the permeability-selectivity measurements are summarised in Table 6.5. The rejection of BSA by S25 and S20 remains low due to their relatively large pore size when compared to the hydrodynamic diameter of BSA, which is about 7.3 nm (Kanani et al., 2010).The higher rejection (21%) of one of the S25 samples is likely due to the incomplete removal of the barrier layer, causing the outer surface of the membrane to have a smaller average pore diameter, as evidenced by the lower hydraulic permeability. As the pore diameter is reducing, the rejection of BSA is increasing as expected. It is especially obvious when the pore diameter of the membrane goes below 20 nm. Nevertheless, the rejection of BSA by symmetric AAMs did not go beyond 90% for effective separation. For asymmetric AAMs, all membranes except one, have achieved consistently higher than 90% BSA rejection. The odd result could be attributed to structural defects and flaws present in this particular membrane (See Figure 6.8).

Table 6.5 The measured pure water permeability and BSA rejection. Multiple samples have been tested for each anodization condition. Please see note for the sample labelling method.

Samples[a]	BSA rejection[b]	Observed & actual sieving coefficient	Separation factor	Hydraulic permeability ($\times 10^{-9}$ m s^{-1} Pa^{-1})
S25	0.03	0.97	1.03	0.17
	0.09	0.91	1.10	0.14
	0.01	0.99	1.01	0.17
	0.21	0.79	1.27	0.05
S20	0.17	0.83	1.20	0.24
	0.25	0.75	1.34	0.20
	0.21	0.79	1.27	0.20
S15	0.61	0.39	2.54	0.17
	0.54	0.46	2.15	0.17
	0.56	0.44	2.27	0.10
S12	0.72	0.28	3.52	0.15
	0.59	0.41	2.47	0.19
S10	0.86	0.14	7.25	0.11
	0.83	0.17	5.84	0.10
A18-5	0.93	0.07	13.53	0.12
	0.93	0.07	14.22	0.12
	0.94	0.06	16.84	0.08
A18-2	0.96	0.04	26.60	0.13
	0.98	0.02	58.14	0.15
	0.92	0.08	12.44	0.22
A18-1	0.98	0.02	48.31	0.14
	0.80	0.20	4.94	0.19
	0.99	0.01	84.75	0.12

[a] The sample labelling scheme: S and A denotes symmetric and asymmetric membranes respectively. For symmetric membranes, the number followed is the anodization voltage. For asymmetric membranes, the former number indicates the initial anodization voltage whereas the later one shows the final anodization voltage.

[b] Given a sensitivity of up to 20 mg L^{-1} for the photometric method used for the BSA concentration determination, the error for the BSA rejection is ± 0.02 for a BSA feed solution concentration of 1000 mg L^{-1}.

When converting the observed sieving coefficients into the actual ones using equation 6.4, there was no noticeable difference. This is mainly due to the low membrane flux and hence the denominator of the equation approaching to unity. As for hydraulic permeability, there is no observable correlation with pore diameter or anodization condition. While the porous model generally estimates that hydraulic permeability (equation 2.16) is inversely correlated to the square of the pore diameter, this was not observed in this study due to the complexity of the membrane thickness and possible flow enhancement effects (See Section 5.2.5), which both affect permeability: the lower the anodization voltage is, the lower the membrane thickness is. The flow enhancement effect also increases with decreasing pore diameter, especially when the average pore diameter is below 30 nm, as discussed in Section 5.2.5. Therefore, the overall permeability of AAMs does not show a significant trend with anodization condition.

6.4.3 Estimation of flow resistance at each layer

As observed from FESEM micrographs, the thickness of the skin layer is only about 500 nm (0.5 μm) out of the overall membrane thickness of 50 μm (Figure 4.23). The support layer hence has a thickness of about 49.5 μm. The skin layer has an average pore diameter of about 10 nm (see Section 6.3) whereas the support layer average diameter is 20 nm. The pressure drop is mainly contributed by three factors, the expansion of pore diameter at the pore branching region and resistance at the skin and support layers. The flow within the pore channel is laminar (Re < 50), hence the pressure drop due to pore expansion is negligible as compared to the resistance caused by the pore wall. To compare the transport resistance at each layer, any flow enhancement effect is neglected. It is because the flow enhancement effect is proportional to length of pore channel and inversely proportional to the pore diameter (See section 5.2.5). Therefore, while the skin layer has a smaller diameter, the short pore length has limited the flow enhancement effect. Similarly, while the support layer has a longer pore length, its pore diameter is larger. Therefore, the no-slip Hagen Poiseuille equation is used for this evaluation.

Resistance at skin layer : Resistance at support layer

$$\frac{32\mu\delta_{skin}}{\varphi_{skin}Ad_{skin}^2} : \frac{32\mu\delta_{support}}{\varphi_{support}Ad_{support}^2}$$

For AAMs, the porosity can typically be assumed as 10% due to their self-assembled hexagonal arrangement (Nielsch *et al.*, 2002) (Please see Section 2.2.5.3). Thus, the porosities of the two layers are similar ($\varphi_{skin} \approx \varphi_{support}$):

$$\frac{\delta_{skin}}{d_{skin}^2} : \frac{\delta_{support}}{d_{support}^2}$$

$$\frac{500}{10^2} : \frac{49500}{20^2}$$

$$1 : 24.75$$

In percentage:

$$\frac{3.9}{100} : \frac{96.1}{100}$$

For asymmetric membranes fabricated here, the support layer is the major contributor to flow resistance as demonstrated by the calculation above. The support layer has twice bigger pore size than the active layer but accounts for more than 97.5 % of the total membrane thickness (see Figure 6.12). This translates, using the Haagen-Poiseulle equation separately for the support and active layer, in the former accounting for more than 96% of the total membrane resistance. This is because the support layer predominantly consists of very small pore channels (20 nm). In contrast, commercial UF membranes, especially polymeric ones, have highly porous support layer, i.e. high porosity (> 20%) and large pore diameter (> 1µm). Therefore, most commercial UF membranes's skin layer accounts for most of the transport resistance (Zeman and Zydney, 1996).

6.4.4 Permeability-selectivity framework

Mehta and Zydney, 2005 developed a comparison framework based on the performance of various commercial UF membranes. Based on this, the data tabulated in Table 6.5 has been included into the original plot, as shown in Figure 6.20. Due to the significant membrane thickness, similar to other commercial ceramic membranes, the AAMs are less permeable than polymeric membranes, which normally have a highly porous support layer and ultra-thin active layer. Nevertheless, the selectivity compares well to that of polymeric membranes, and the separation performance of AAMs is superior to that of other commercial ceramic membranes included in the plot.

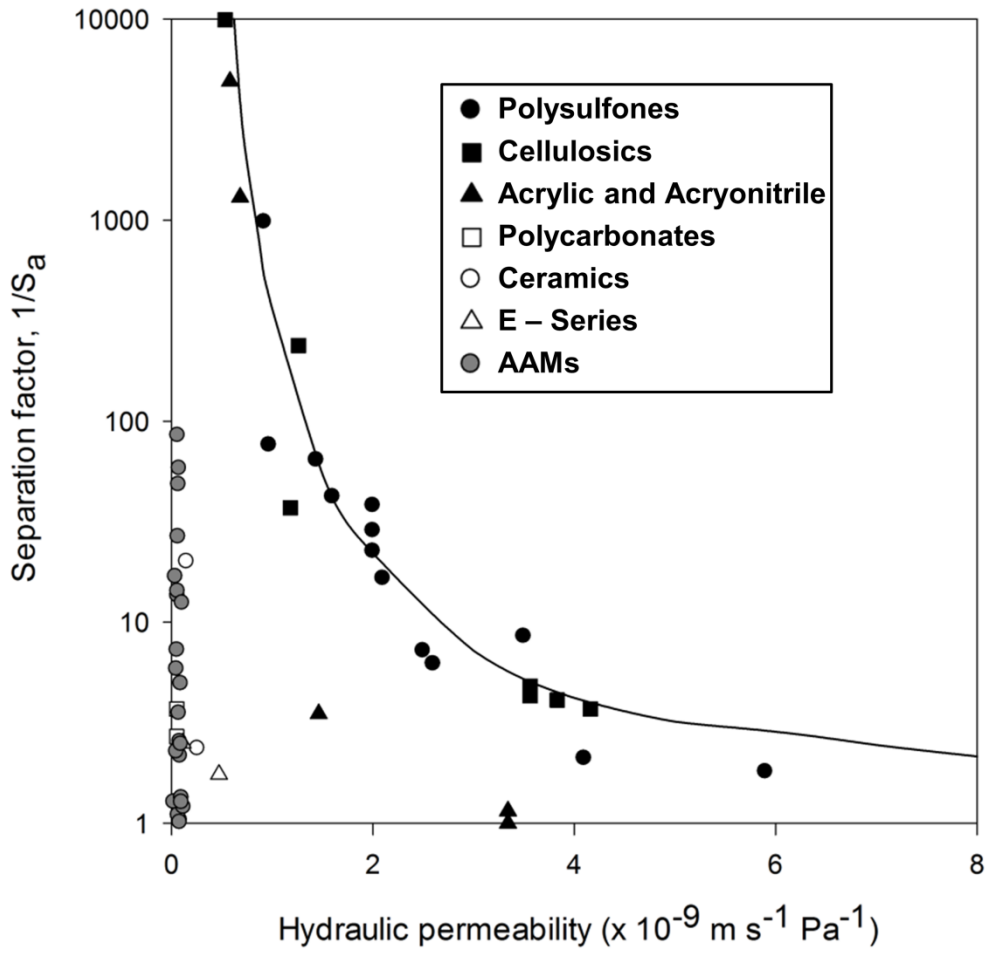

Figure 6.20 Selectivity-permeability trade-off for UF membranes using BSA as the model protein. (Adapted from Mehta and Zydney, 2005)

While the previous plot provides a straight forward framework for UF membrane comparison, Kanani *et al.*, 2010 replaced hydraulic permeability with scaled permeability to observe the effect of pore geometry on membrane performance. Data for both symmetric and asymmetric AAMs was re-arranged to fit this new framework (Figure 6.21). Based on equation 6.3, the hydraulic permeability in Table 6.5 was normalised by membrane porosity and thickness to obtain the scaled permeability. The porosity is taken as 0.20 (the most conservative value within the experimental range of 0.10-0.20), since overall porosity is difficult to obtain for asymmetric membranes due to the structural difference. For asymmetric membranes, the total thickness is still used in lieu of the skin layer thickness alone due to the fact that the support layer of the membrane is still the major contributor to transport resistance, as discussed in Section 6.4.3.

Other than experimental data included, from the original plots and current work, a theoretical model (line curve in Figure 6.21) derived by calculating the scaled permeability (equation 2.24) and the separation (equations 2.22 and 2.24) based on original pore model. While Figure 6.20 provides a straight forward framework to compare practical UF membrane performance, Figure 6.21 enables the comparison between the theoretical and experimental performance of the membranes. It can be observed that the performance of symmetric AAMs is generally following the theoretical trend, with most of the data points falling on the right side of the theoretical curve. This can be explained by the flow enhancement effect, where previous investigation (see Section 5.2.5) has shown more than doubling of the flow enhancement has been obtained in AAMs with pore diameter 30 nm and below. For asymmetric AAMs, the performance is beyond the expectation from the theoretical model. This is attributed to the asymmetric structure of the membrane. The presence of an active layer with smaller pore diameter has substantially improved the separation performance of the membrane without compromising the permeability of the membrane, as discussed in Section 6.4.3. This has therefore shifted the membrane separation factor upwards, beyond the the theoretical model curve.

These results imply that the performance of asymmetric AAMs can be enhanced by improving the permeability of the support layer. While this could be achieved by increasing the pore diameter and porosity of the support layer by increasing the initial anodization voltage, the ramp rate used to achieve the final anodization voltage have to be optimised as well. If the ramp rate is too high, the pore structure will be affected since it cannot respond accordingly to the rapid change of anodization voltage (Lee *et al.*, 2012a). If the ramp rate is too slow, the increased thickness of the transition section will negate any meaningful increase in permeability. An alternative method could be pore-widening of the support layer by wet chemical etching. However, this will weaken the mechanical strength of the support layer, decreasing its usefulness as mechanical support.

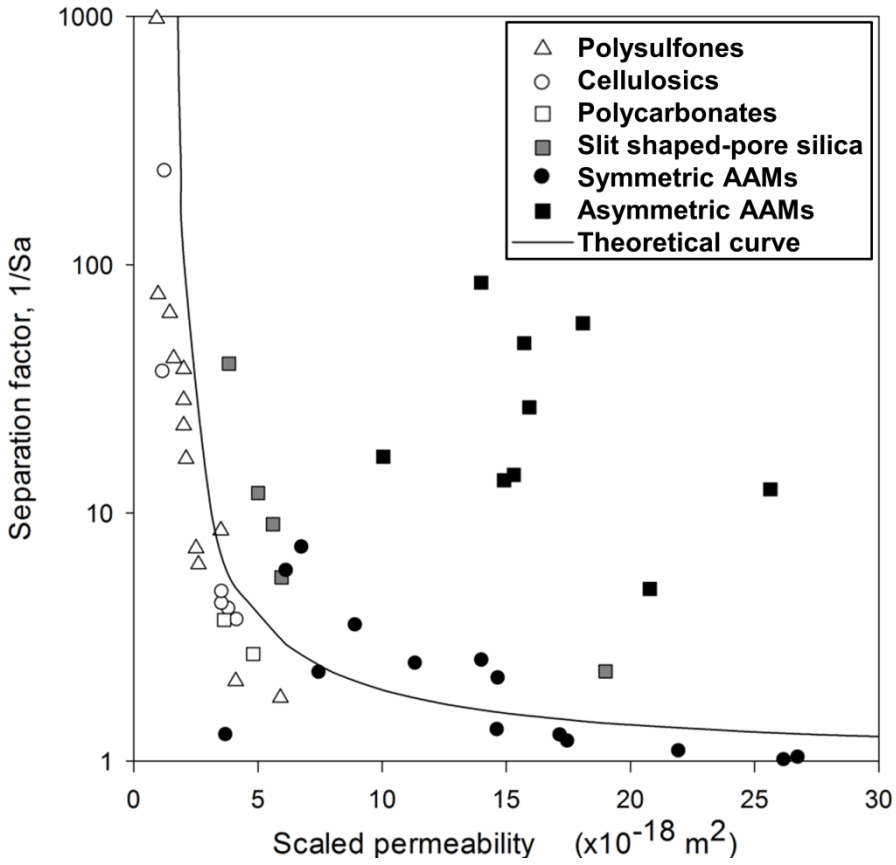

Figure 6.21 Selectivity-scaled permeability trade-off for UF membranes using BSA as the model protein. The line curve is plotted based on theoretical pore model. (Adapted from Kanani *et al.*, 2010)

6.5 Fouling mechanism

Previously, the BSA fouling behaviour of pristine and surface modified 200 nm flat disc symmetric AAMs (commercial Anopore™ membranes) showed good agreement with the standard pore blocking model (Yeu *et al.*, 2009). This can be attributed to the fact that the membrane pore diameter is at least 20 times bigger than the size of BSA, facilitating the attachment of the solute onto the pore wall. However, there has been no study reported before on BSA fouling of AAMs with smaller pore diameter or in tubular geometry. Since only the asymmetric AAMs show promising results for separation of BSA (see Section 6.4), fouling tests were not performed on symmetric AAMs.

6.5.1 Methodology

The experiments performed were similar to that of BSA filtration (see Section 6.4.1), with a couple of differences. First, the inner bore of the membrane (permeate side) was prefilled with clean PBS. This was done to eliminate the lag time for the permeate to fully fill the tube bore, as the initial change in flux is crucial for fouling modelling. Secondly, the permeate was collected in a beaker placed on a high precision balance (Mettler Toledo, MS304S/01, 0.1 mg precision). The beaker was pre-filled with oil to minimise water loss by evaporation. All real-time measurements, *i.e.* pressure, temperature and mass of water permeate were recorded *via* a data acquisition system. The experiments were performed for 4 to 20 hours at 100±2 kPa and 21±1°C. SigmaPlot 12.3 was used for fitting of data into the fouling models listed in Table 2.6 and Table 2.7, to understand the fouling mechanism of BSA on asymmetric AAMs.

6.5.2 Fouling modelling

Model fitting was performed on the cumulative permeate volume profiles to understand which fouling mechanism dominates the flux decline. Of the four popular Hermia's classical fouling mechanisms found in the literature (see Table 2.6), none of them provided a satisfactory fitting for the data. Therefore, combined fouling models were investigated. The results indicate that the complete pore blocking – cake filtration model (see Table 2.7) consistently gives the most satisfactory fittings over the range of data obtained (Figure 6.22), with R^2 consistently higher than 0.99. Despite the long period of experiment, the flux sustained at a steady-state rate (J_{ss}) and did not reduce to zero. Hence, the complete pore blocking – cake filtration model with steady-state flux being taken into account are used to describe the flux decline (Cheryan, 1998):

$$V = \frac{J_o}{K_b}\left[1 - e^{\frac{-K_b}{K_c J_o^2}\left(\sqrt{1+2K_c J_o^2 t}-1\right)}\right] + J_{ss}t \qquad 6.5$$

where V is the accumulated permeate volume ($m^3\ m^{-2}$), J_0 is the initial flux ($m\ s^{-1}$), J_{ss} is the steady-state flux ($m\ s^{-1}$), K_b is the complete pore blocking constant (s^{-1}), K_c is the cake filtration constant ($s\ m^{-2}$), and t is the time (s).

(a)

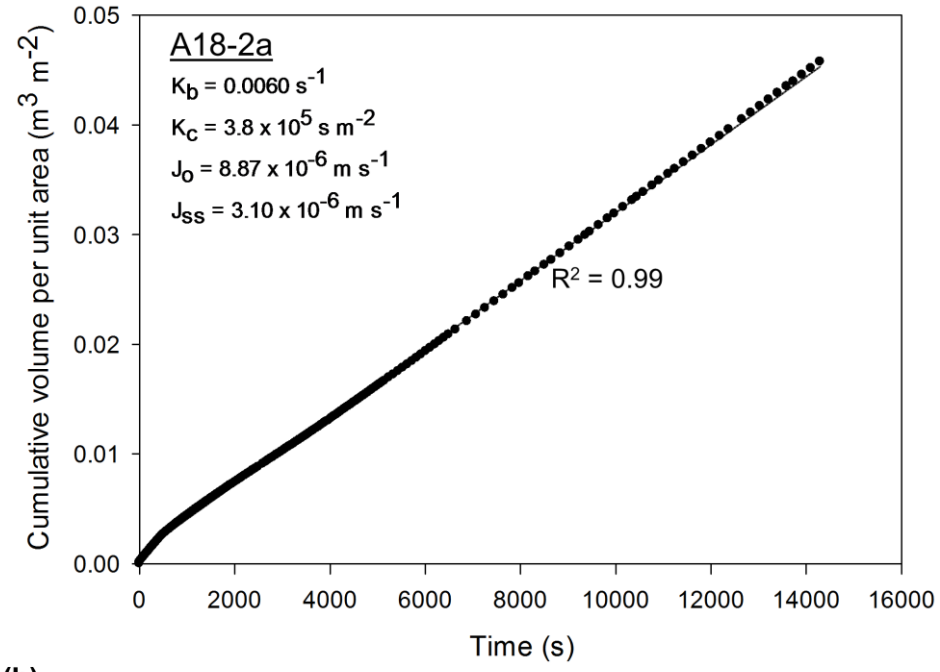
A18-2a
K_b = 0.0060 s^{-1}
K_c = 3.8 x 10^5 s m^{-2}
J_o = 8.87 x 10^{-6} m s^{-1}
J_{ss} = 3.10 x 10^{-6} m s^{-1}
R^2 = 0.99
Cumulative volume per unit area (m^3 m^{-2})
Time (s)
0.00
0.01
0.02
0.03
0.04
0.05
0
2000
4000
6000
8000
10000
12000
14000
16000

(b)

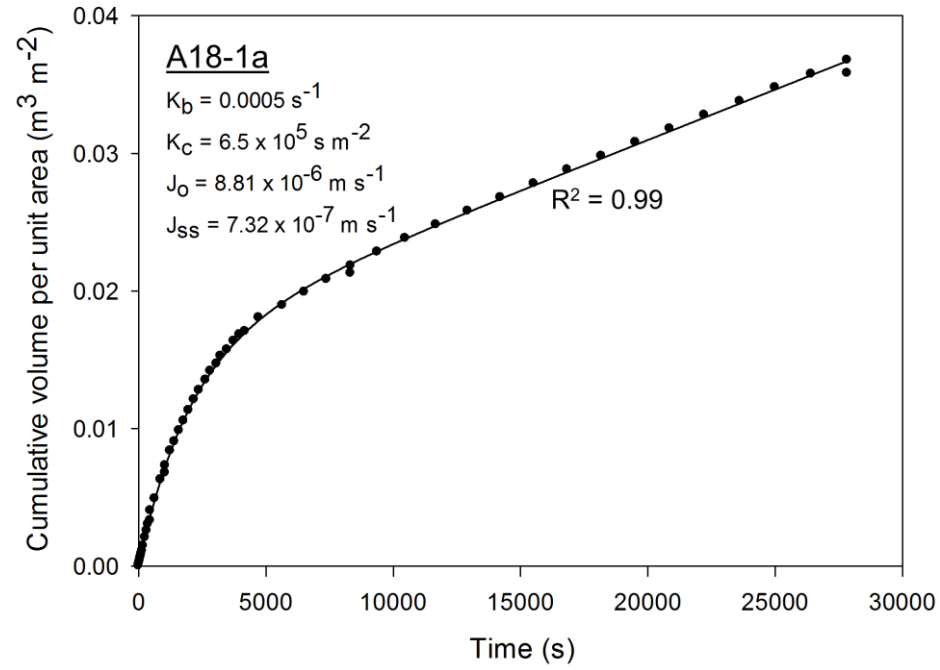
A18-1a
K_b = 0.0005 s^{-1}
K_c = 6.5 x 10^5 s m^{-2}
J_o = 8.81 x 10^{-6} m s^{-1}
J_{ss} = 7.32 x 10^{-7} m s^{-1}
R^2 = 0.99
Cumulative volume per unit area (m^3 m^{-2})
Time (s)
0.00
0.01
0.02
0.03
0.04
0
5000
10000
15000
20000
25000
30000

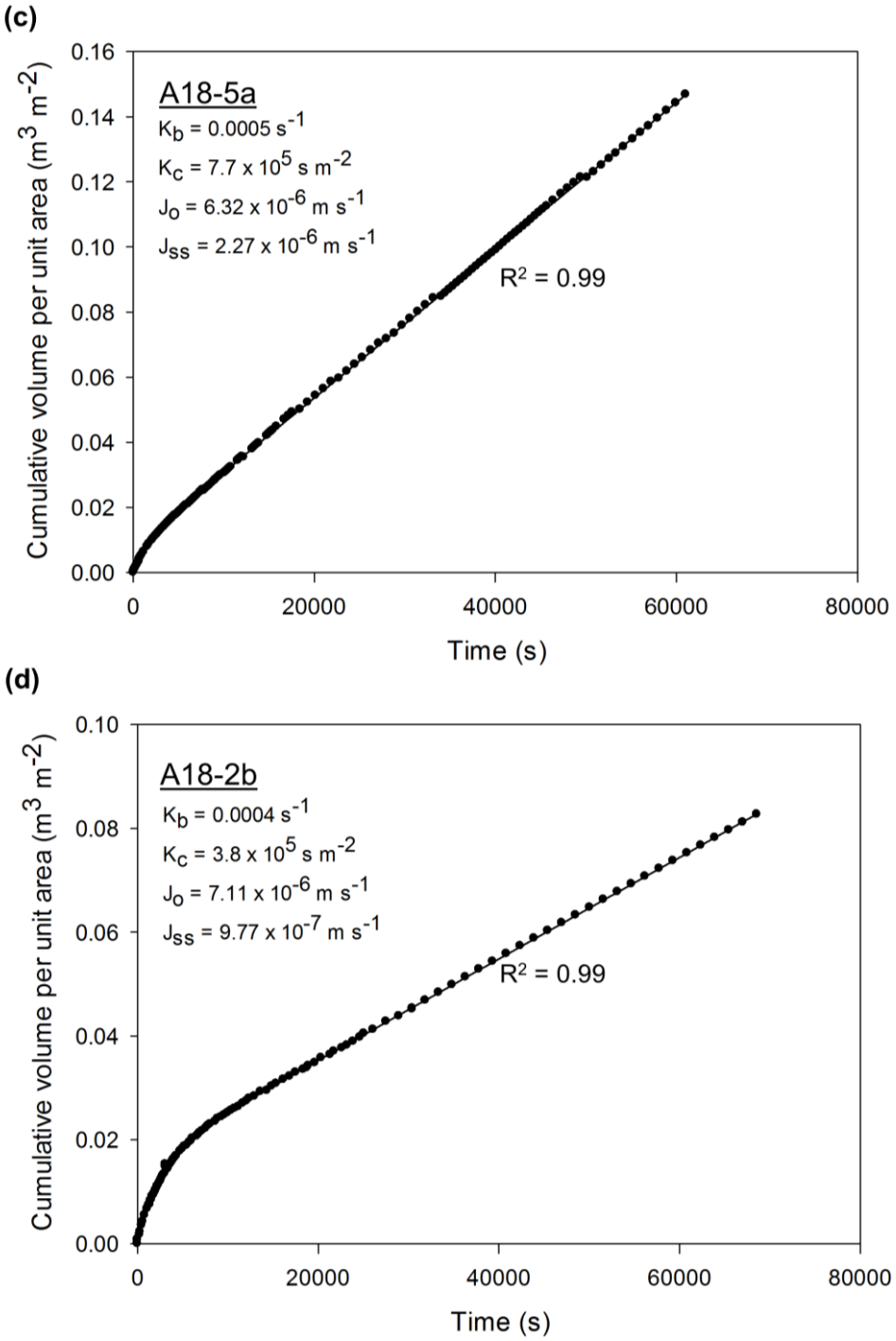

Figure 6.22 The cumulative permeate profiles during BSA filtration and the data was fitted by the complete pore blocking - cake filtration model with fitting parameters labelled in each plot which represents an individual asymmetric AAM: (a) A18-2a; (b) A18-1; (c) A18-5 and (d) A 18-2b. See notes under Table 6.4 for corresponding membrane preparation condition.

There is ample evidence in the literature that the type of combined fouling behaviour discussed here can occur either in sequence or simultaneously (van Reis and Zydney, 2007). In the former case, the initial flux decline is dominated

by the pore blocking mechanism followed by cake filtration, with the formation of cake layer facilitated by the pore blockage. In the latter case, the flux decreases through a reduction in area by complete pore blockage or an increase in resistance through caking or cake thickening (Bolton *et al.*, 2006). When K_b is high, flux decline is dominated by complete pore blocking whereas the cake filtration mechanism is dominating when K_c is high. It is obvious to see that in Figure 6.22(a), when K_b is high, the flux declines sharply as shown by the corresponding curve in Figure 6.23. This can be attributed to the initial rapid loss of available pore area. In Figure 6.22(b) and (d), K_c is large, with cake formation dominating and resulting in relatively low steady-state flux as compared to the other two cases. For the case in Figure 6.22(c), both mechanisms contribute to the flux decline. The different flux decline behaviour among different asymmetric AAMs (i.e. even different membranes under the same anodization conditions) is likely due to structural differences between the membranes: For example, slightly over-etching of the skin layer would cause pore widening for a certain depth in the active layer. When filtration is performed, the solute will be able to enter the pore until it is blocked by the non-widened part of the active layer. This will reduce the likelihood of cake formation. Other reasons include the presence of defects within the membrane or incomplete removal of the oxide barrier layer.

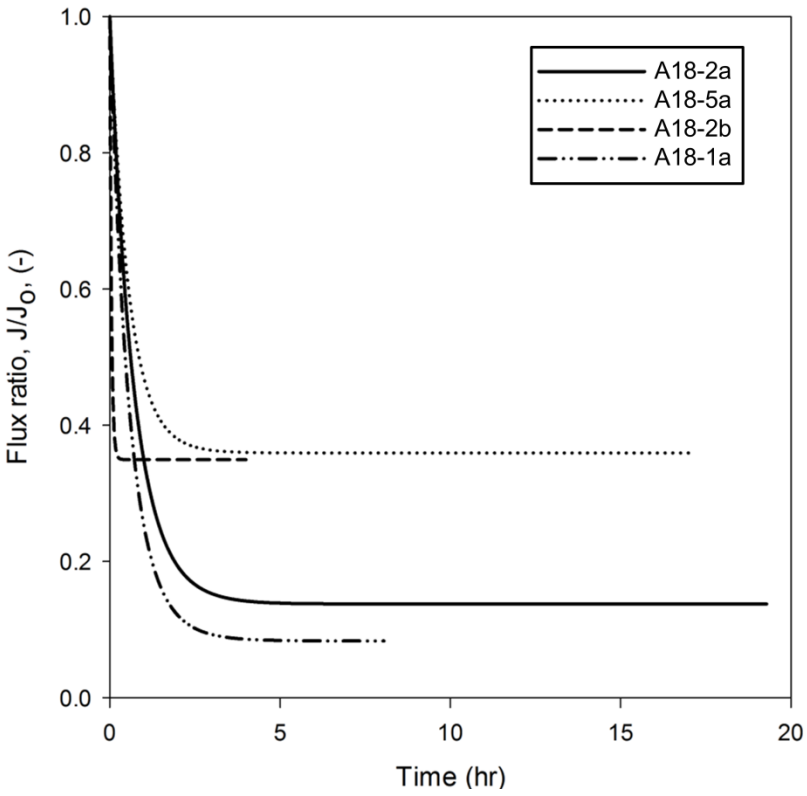

Figure 6.23 Flux decline profile over the course of BSA filtration.

6.6 Summary

In this chapter, the fabrication, characterisation and applications of both symmetric and asymmetric tubular AAMs have been discussed. Despite the use of an aluminium alloy, the resulting porous structure obtained is regular and similar to membranes obtained using highly pure - and more expensive - aluminium. The presence of stem pores in asymmetric membranes effectively increases the thickness of the tubular AAMs for enhanced handling robustness.

The MWCO tests show consistent separation results for asymmetric AAMs with average pore size of 10 ± 2 nm, showing a breakdown of the linear dependence of the pore diameter with anodization voltage below 10 V. While most symmetric AAMs show limited rejection of BSA, asymmetric AAMs reliably reject more than 90% of BSA. As for selectivity-permeability analysis, the asymmetric AAMs outperform other commercial ceramic membranes although they still have very low flux relative to polymeric ones. On the other hand, selectivity-scaled permeability analysis shows great potential for asymmetric AAMs if the porous structure of the support layer can be engineered to improve the permeability. The flux decline during BSA filtration can be described by combined complete pore blocking-cake filtration model. Further improvements such as surface modification by coating or grafting are needed to mitigate fouling and bring AAMs to commercial application.

Despite the consistent performance shown by most of the tests performed on asymmetric AAMs, the presence of structural flaws and defects were found in a number of samples. These defects are likely to be inherited from the starting materials, which is in the form of alloy as the defects are not observed in flat AAMs which are fabricated using highly pure aluminium. This causes a trade-off between the cost of production and quality control.

7. Tubular AAMs: Membrane Emulsification

A regular and circular pore structure is highly desirable to obtain emulsions with narrow droplet size distribution via membrane emulsification (Joscelyne and Trägårdh, 2000). Most of the relevant work has been done by using commercial Shirasu Porous Glass (SPG) and PCTE membranes. Despite the highly ordered pore structure of symmetric AAMs through the entire thickness, very limited experimental results have been reported on the topic of emulsification, especially those in nanoporous range (<100 nm). There have been some previous attempts in the literature using flat AAMs with bigger pore sizes (> 100 nm) to synthesise polymer nanoparticles with defined size by dead-end membrane emulsification (Yanagishita *et al.*, 2010). Therefore, AAM is expected to be a good candidate for membrane emulsification to produce emulsions with defined droplet size. In this chapter, membrane emulsification using only symmetric tubular AAMs with different pore diameter (at the smaller range, 20 to 60 nm), in cross-flow and dead-end modes, is demonstrated. The aim of this chapter is to capitalize the uniform pore structure of AAMs in order to obtain emulsions with nanometre droplet size by controlling the process parameters such as cross-flow velocity and membrane pore diameter. The results obtained have been recently accepted for the publication in journal *Industrial & Engineering Research Chemistry*.

7.1 Methodology

Due to the highly hydrophilic nature of AAMs, only oil in water (o/w) emulsions were investigated. Sunflower oil (SFO) for domestic use and Milli-Q water were used as oil and aqueous phase, respectively. The interfacial tension (IFT) was measured to optimise the dosage of surfactants. Experiments on both dead-end and cross-flow membrane emulsification were performed and compared.

7.1.1 Interfacial tension measurement

In a previous study, the use of 4 v/wt% Span 80 (Sigma) and 4 v/w% Tween 20 (Sigma) as surfactants in the oil and aqueous phase, respectively, has shown good and stable droplet formation (Wagdare *et al.*, 2010). Both Span 80 (sorbitan (z)-mono-9-octadecenoate) and Tween 20 (polyoxyethylene (20) sorbitan monolaurate) are non-ionic surface active agents with molecular formula

$C_{24}H_{44}O_6$ and $C_{58}H_{114}O_{26}$, respectively. They are both clear yellow viscous liquids with a density of 986 and 1100 kgm^{-3}, respectively. Their high level of stability and low level of toxicity make them suitable to be used for domestic and food products (Hancocks, 2011).

Based on this emulsion formulation, Wagdare *et al.*, 2010 used MF membranes with relatively large pore size, 5 μm, and hence the minimum pressure required for droplet formation was small (see equation 2.26). In current study, the AAMs used have much smaller pore size, and therefore the IFT should be minimised to lower the critical pressure for droplet formation.

Different compositions (0, 1, 2, 4, 6, 10 v/w%) of Span 80 (Sigma) in SFO (Co-operative, UK) were prepared. Tween 20 (Sigma) was added into Milli-Q water in the same range of composition. The IFT between each pair of oil/aqueous solutions were measured using a goniometer (Dataphysics OCA20), based on pendant drop method. Briefly, the pendant drop method uses a high resolution camera to obtain a defined interfacial contour of the droplet (Drelich *et al.*, 2006). The pendant drop method was chosen because it offers high accuracy (0.1 mN m^{-1}), and is very suitable for liquid-liquid systems where surfactant solutions are used. Based on the droplet shape and size, the IFT can be calculated based on this equation:

$$\gamma = \frac{\Delta \rho g D_d^2}{H} \qquad 7.1$$

where γ is the IFT, $\Delta\rho$ is the density difference between the two liquids, g is the gravity, D_d is the droplet diameter (see Figure 7.1) and H is a shape dependent empirical parameter depending on a shape factor, $S = d/D_d$. Nevertheless, the goniometer (Dataphysics OCA20) comes with a software that analyse the results automatically based on this theory.

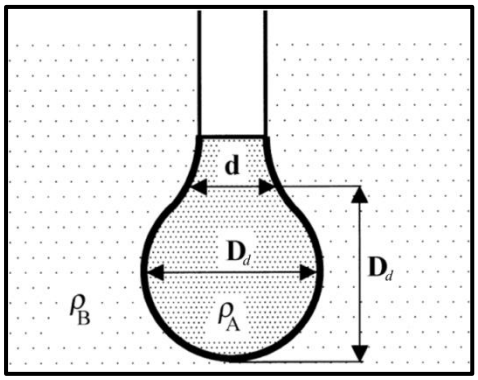

Figure 7.1 Schematic of a pendant drop (Drelich *et al.*, 2006).

7.1.2 Dead end membrane emulsification

Figure 7.2 shows the picture and schematic of the experimental apparatus built for dead-end membrane emulsification. As can be seen, the inner bore of the membrane was filled with the oil phase (disperse). Vertically, the top of the membrane was connected to compress air (upto 400 kPa) via a regulator to control the transmembrane pressure. A pressure transducer (Swagelok, industrial standard, ±5 kPa) was connected to monitor the pressure settings. Then the membrane was positioned to be totally submerged into a 10 ml borosilicate glass test tube containing continuous aqueous phase, which position was fixed by clamp.

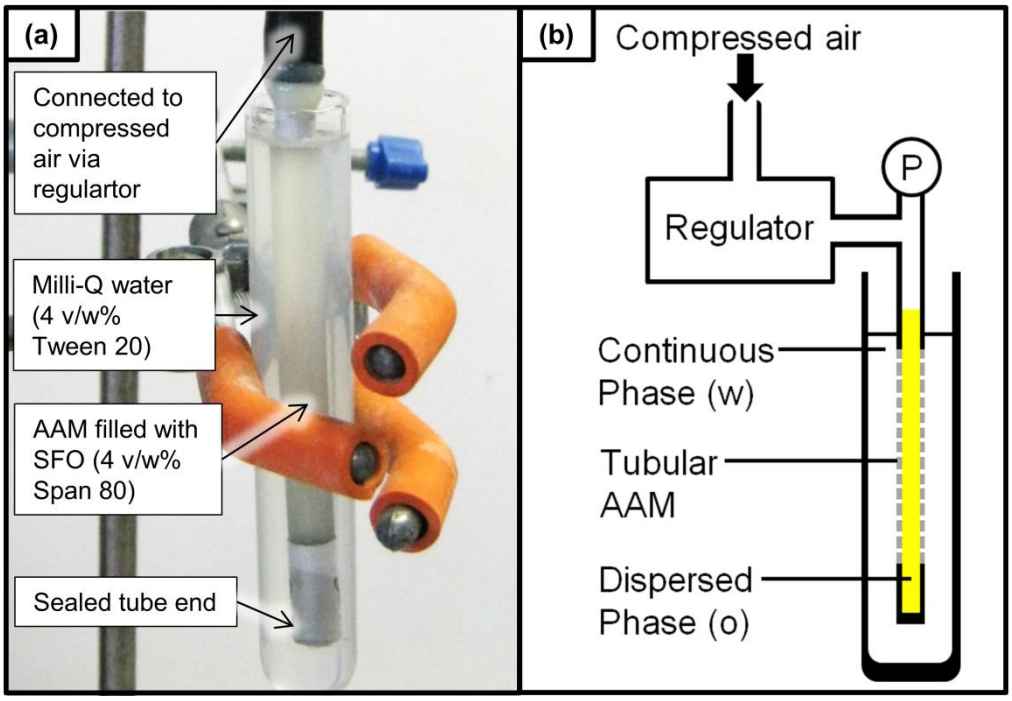

Figure 7.2 The (a) picture and (b) schematic of membrane emulsification in dead-end configuration.

Once the experimental set-up was ready, the pressure was slowly increased to the set point, i.e. 50 kPa or 80 kPa to avoid membrane failure by sudden pressure pulsation. Then the dispersed phase within the inner bore of the membrane would permeate through the membrane. Due to stringent requirement of pore structure homogeneity for membrane emulsification, only membranes with optimum porous structure (i.e. anodized at 20 V in sulphuric acid as well as 40V and 50 V in oxalic acid) were tested. The experiment was conducted for an hour.

7.1.3 Cross-flow membrane emulsification

In the cross-flow configuration, the membrane was mounted in a mini module such that a continuous phase liquid could be flowed along the membrane surface, whilst the dispersed phase is pressurised through the membrane from the outer side. The tubular AAMs were housed individually in a mini-module made of 13 mm inner diameter acrylic tube by using epoxy adhesive (Araldite) (Figure 7.3). As shown in Figure 7.4, the inner bore of the tubular AAM was connected to a stainless steel syringe pump with 225 ml capacity. The gap between the acrylic tube and AAM surface was filled with dispersed oil phase, which was connected to compressed air via a regulator. The continuous aqueous phase was dispensed by pulseless flow driven by a syringe pump (Nexus 4000).

After the experimental apparatus is ready, the syringe pump was started to make sure the inner bore of tubular AAM was completely filled with continuous aqueous phase. The pressure was then gradually increased to the set point, i.e. 50 kPa or 80 kPa. Then the dispersed oil phase would start to permeate through the membrane, forming droplets that were detaching from the membrane surface. Multiple sets of experiments were performed to investigate the effects of membrane pore diameter, transmembrane pressure and effect of wall shear on the resulting emulsion. As summarised in Table 7.1, the main parameters investigated include membrane pore diameter, transmembrane pressure and cross-flow velocity. The first 50 ml of resulting emulsion samples was purged in each experiment. Subsequently, three batches of 50 ml samples were collected, in order to verify steady-state has been attained.

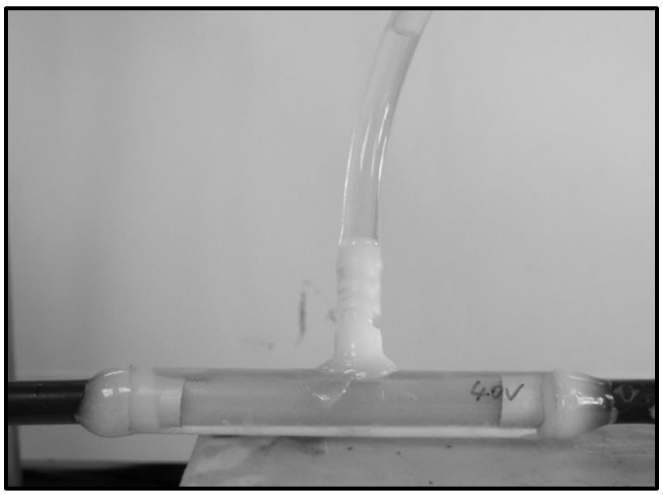

Figure 7.3 Picture of a tubular AAM housed in an acrylic tube filled with dispersed oil phase.

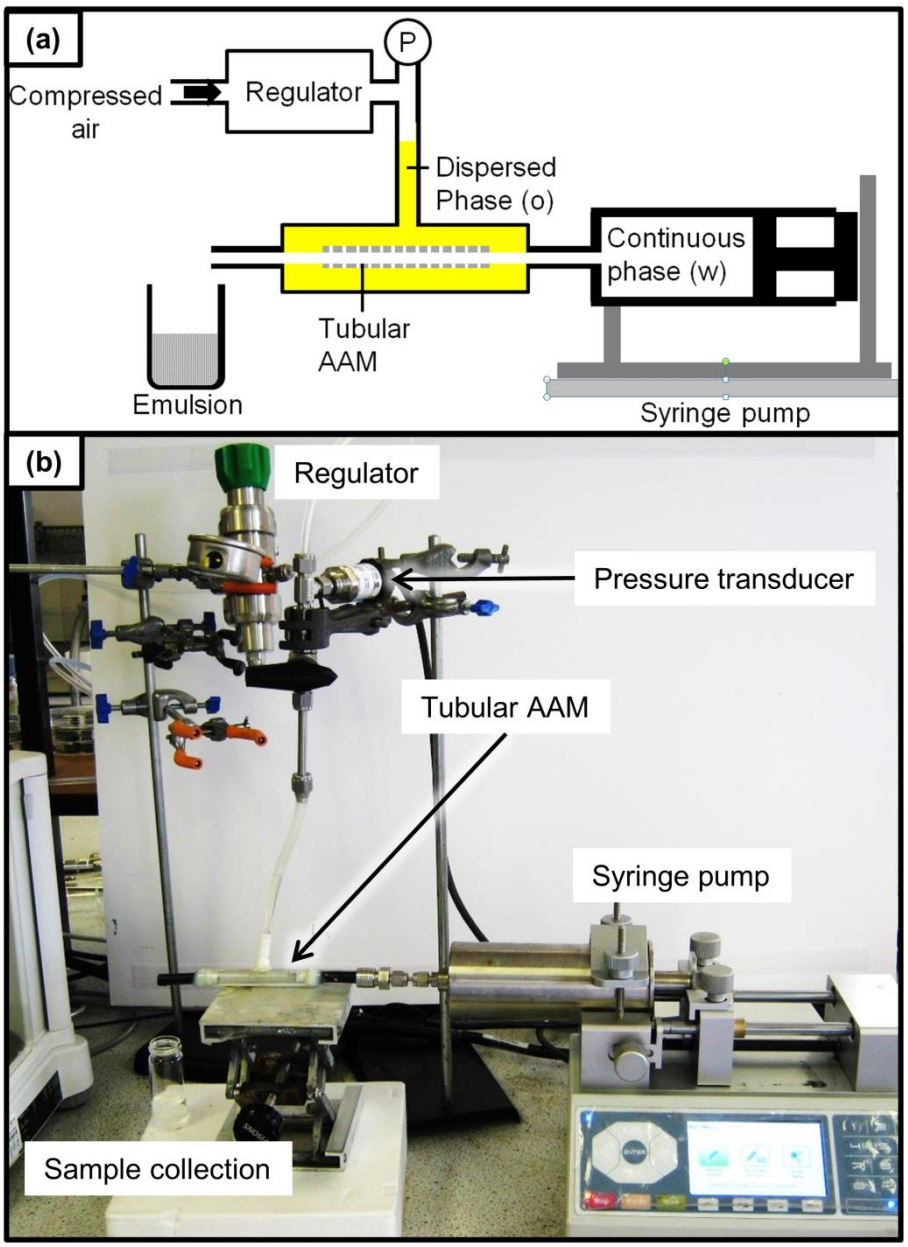

Figure 7.4 The (a) schematic and (b) picture of membrane emulsification in cross-flow configuration.

Table 7.1 The operating parameters investigated for membrane emulsification

AAM anodization voltage (mean pore diameter)	Transmembrane pressure (± 5kPa)	Cross-flow velocity[a] ($m\ s^{-1}$)
20 V (25±2 nm)	80	0, 0.01, 0.02, 0.04, 0.1
40 V (50±3 nm)	80	0, 0.01, 0.02, 0.04, 0.1
50 V (60±5 nm)	50	0, 0.01, 0.02, 0.04, 0.1
50 V (60±5 nm)	80	0, 0.01, 0.02, 0.04, 0.1

[a] 0 $m\ s^{-1}$ cross-flow velocity is equivalent to dead-end membrane emulsification.

7.1.4 Dynamic light scattering (DLS) analysis

The size and distribution of the droplets in the resulting o/w emulsions were analysed using dynamic light scattering technique (Zetasizer Nano-ZS, Malvern Instruments Ltd.). DLS measures Brownian motion and relates this to the size of the particles or droplets. It does this by illuminating the particles with a laser and analysing the intensity fluctuations in the scattered light. Briefly, particles/droplets suspended in a liquid are constantly moving due to random Brownian motion. An important feature of Brownian motion for DLS is that small particles move quickly and large particles move more slowly. When laser is shined through the emulsions, a speckle pattern will also appear to move. As a result, the constructive and destructive phase addition of the scattered light causes the change of intensity at any particular point to fluctuate. The rate of the intensity fluctuation is measured in a DLS system which is used to calculate the size of the particles/droplets (Malvern, 2009).

The Zetasizer Nano-ZS can measure particle in the size range of 0.3 nm to 10 μm. If the sample is too concentrated, the occurrence of multiple scattering i.e. the light scattered by one particle will itself be scattered by another, will be promoted. Therefore, the collected emulsion samples have been significantly diluted for reliable measurement. Nevertheless, alerts would be raised from the device if the concentrations of the samples are too high or too low.

The addition of surfactants into the SFO or water has negligible effect on their refractive index, as verified after the measurement using a refractometer. The refractive indices for SFO and water are 1.47 and 1.33, respectively, at 25 °C. Three measurements were repeated for each sample tested.

7.2 Interfacial tension measurement

Figure 7.5 illustrates the IFT measured for different SFO/water solutions with varying surfactant concentration. Figure 7.6 shows the images captured by the high resolution camera for the IFT measurement. When no surfactant was used, the IFT between pure SFO and water obtained was 24.37 mN m^{-1}. This is very close to the literature value of approximately 25 mN m^{-1} (Barfod, 1995). The picture in the middle shows a smaller SFO (containing 4 v/w% of Span 80) droplet formed in a water bath (containing 4 v/wt% of Tween 20). The

comparison between the top and middle images illustrates the principle of pendant drop measurement, where the droplet size and droplet shape are closely related to the liquid-liquid IFT. The image at the bottom shows an image captured where high concentration of Span 80 was added to the SFO (10 v/wt%). This high concentration of surfactant has significantly reduced the IFT between the two phases and inhibited the formation of a spherical droplet. In this case, the IFT is very low and close to the point where the two phases can be nearly miscible. This image shows that it is not possible to measure the IFT using the pendant drop method for such high surfactant concentrations.

As expected, the IFT is decreasing with increasing dosage of either Span 80 or Tween 20 in SFO and water, respectively. In good agreement with previous studies (Wagdare *et al.*, 2010), the IFT between 4 v/wt% of Span 80 in SFO and 4 v/wt% of water is very low, 0.47 mN m^{-1}. Further increase in surfactant dosage has minimal effect in reducing the IFT. Therefore, the emulsion formulation is based on using 4 v/wt% of Span 80 in SFO as the dispersed phase and 4 v/wt% of water as the continuous phase.

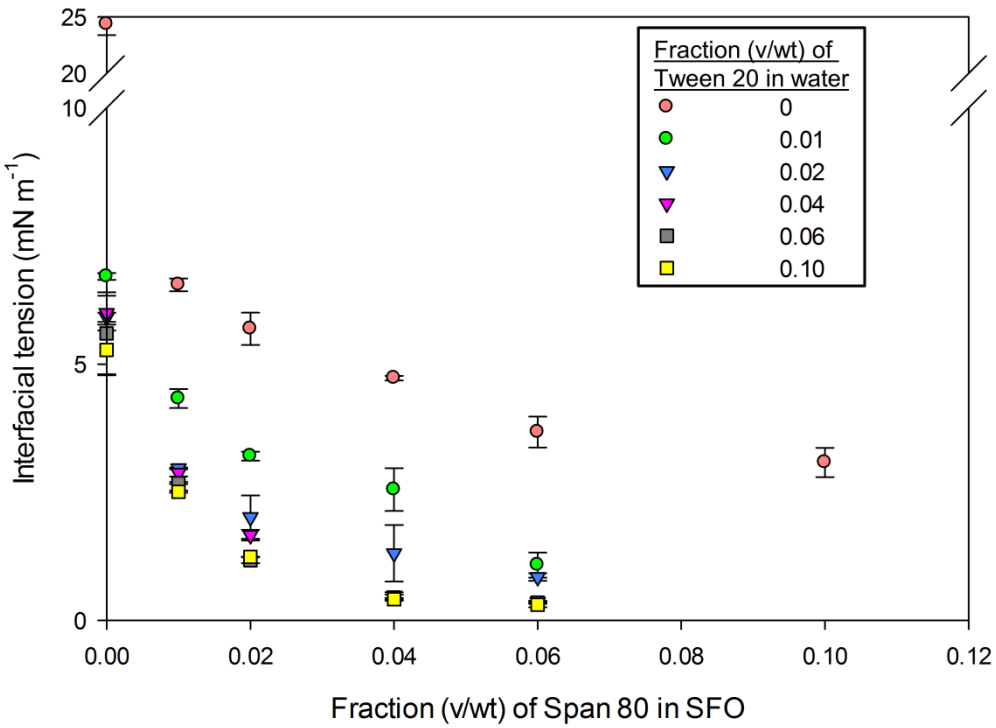

Figure 7.5 The IFT between SFO and water with varying concentration of surfactants in each phase.

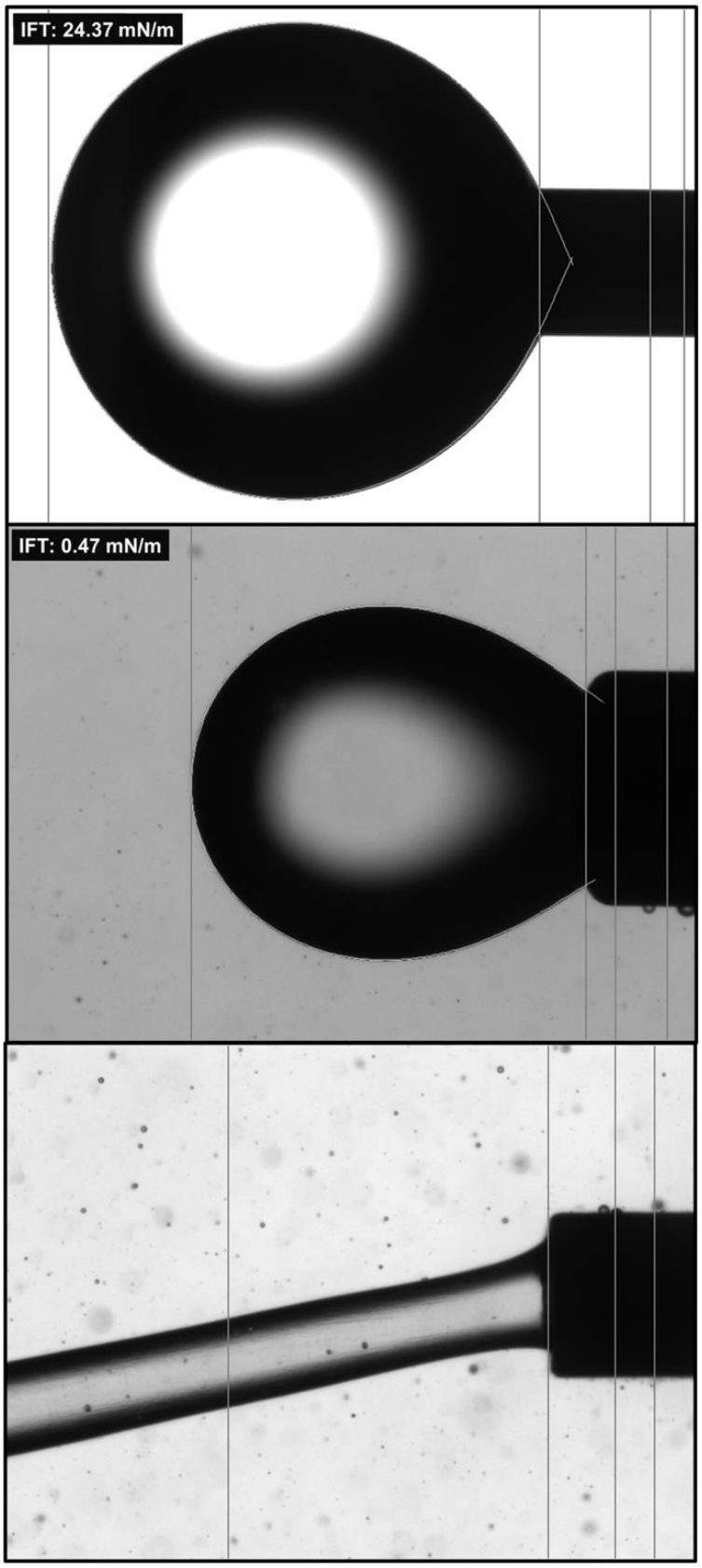

Figure 7.6 Pictures of SFO droplet in water during IFT measurement using pendant drop method. Top: pure SFO and pure water; middle: 4 v/wt% Span 80 in SFO and 4 v/wt% Tween 20 in water; and bottom: 10 v/wt% Span 80 in SFO and 4 v/wt% Tween 20 in water.

7.3 Characterisation of emulsions

For the dead-end configuration, the emulsions appeared to be increasingly milky with time (Figure 7.7(a)). This is attributed to the small and fixed volume (10 ml) of the continuous phase. Therefore, when the concentration of the dispersed droplets increases, the continuous phase turns milky. The emulsion colour is homogenous throughout the continuous phase in the test tube. This implies the droplets formed are small and Brownian motion is dominating the droplet motion instead of buoyancy which could cause the lighter dispersed phase to move upwards. In Figure 7.7(b), in contrast to the milky colour of emulsion obtained from dead-end configuration, cross-flow emulsification in this case results in a clear and transparent liquid. This is mainly due to the smaller droplet size and lower concentration of the droplets present in the continuous phase.

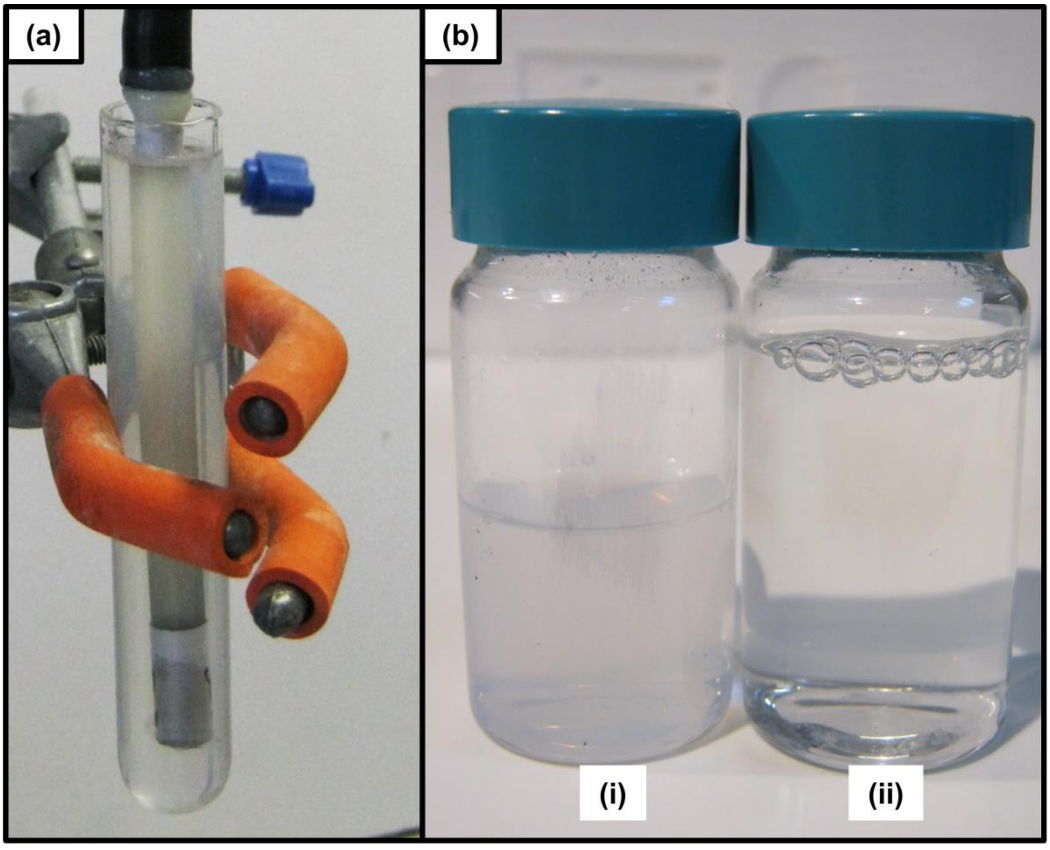

Figure 7.7 (a) Dead-end emulsification after 30 mins and (b) emulsion samples collected from (i) dead-end emulsification and (ii) cross-flow emulsification.

From DLS raw data analysis, some preliminary conclusions can be drawn, as illustrated in Figure 7.8. Firstly, the result quality is an important indicator of the reliability of the analysis. In short, to meet quality criteria, the following should be avoided:

- The particle size is beyond the range of measurement (< 0.3 nm or >10 μm)
- The sample is too polydispersed for DLS analysis (polydispersity index (PDI) > 0.7).
- Detection of multiple scattering due to high concentration or the sample concentration is too low for sufficient count rate to obtain statistically reliable results.
- Significant errors during cumulative and multimodal fittings due to high polydispersity.

In all cases, only results that satisfied the above requirements were extracted for further analysis. Initially, the particle size distribution and average particle size (Z-average) were obtained based on the intensity of light scattered. However, large particles scatter much more light than small particles as the intensity of scattering of a particle is proportional to the sixth power of its diameter ($\sim D_d^6$). This alters the size distribution, giving a higher weight to larger particles. Therefore, the size distribution data by volume which can be exported to spreadsheet, was extracted for further analysis. Based on this data, the average particle size by volume, $D_{4,3}$ was obtained. Finally, the polydispersity of the sample was evaluated based on the polydispersity index (PDI) or width of the size distribution. In particular, the calculation of PDI was based on ISO standard documents 13321:1996 and 22412. It is suggested that a sample can be categorised as monodispersed if the PDI is smaller than 0.2 (Malvern, 2009).

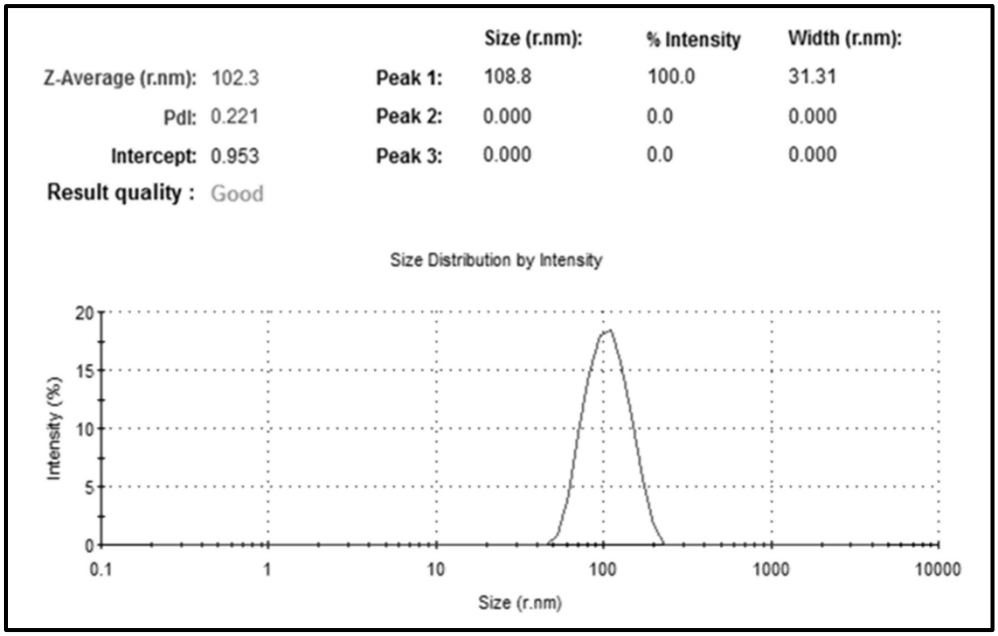

Figure 7.8 A preliminary report from DLS analysis indicating the quality of the analysis. This analysis was based on a sample obtained from 50 V membrane, operated at 50 kPa with 0.01 ms^{-1} cross-flow velocity.

To verify the particle size results obtained from DLS, cryogenic FESEM was used to examine the solidified emulsion samples. Nevertheless, operating the FE-SEM at cryogenic condition poses a number of challenges for good imaging. The presence of solidified water vapour at the surface causes serious charging issues for imaging. The nano-crystal-structure formed during the freezing of the emulsion samples also increases the complexity to distinguish the SFO droplets. The low concentration of the SFO droplets in the continuous phase also increases the difficulty to identify them. Therefore, the image quality obtained from cryogenic FE-SEM was rather unsatisfying due to these limitations. Nevertheless, as shown in Figure 7.9, in some images, the SFO droplets could be identified. Despite these limitations for analysis, it can be concluded that the droplets shown are in the sub-micrometre range. For example, in Figure 7.9(b), the droplet contour is better-defined and the droplet diameter could be estimated in the range of 200 to 300 nm, in reasonable agreement with the DLS report (Figure 7.8).

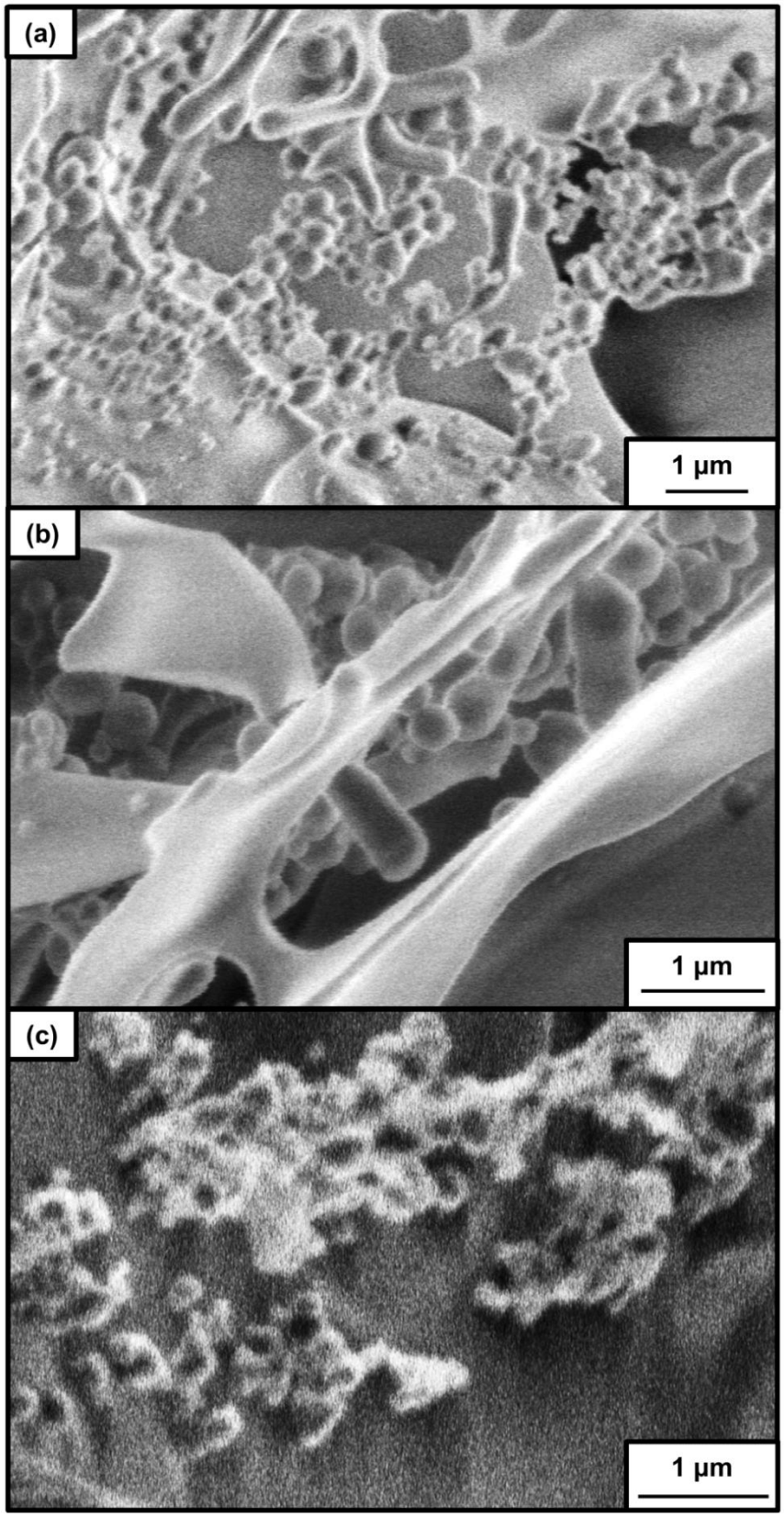

Figure 7.9 SEM micrographs captured under cryogenic condition showing SFO droplets in the emulsion samples prepared by dead-end mode using (a) 50 V (12,000X magnification), (b) 40 V (18,000X magnification) and (c) 20 V membranes (19,000X magnification). Despite the insufficient image quality, the droplet size observed is complementing with results from DLS.

7.4 Dependence of droplet size on process parameters

The DLS analysis of three different batches of samples collected at different time intervals in the same experiment was used to evaluate that the experiments had achieved steady state when samples were collected. The volume for each batch of sample collected was 50 ml. As can be seen from Table 7.2, both the average droplet diameter and the mod obtained for different batches are within 10% span. The PDIs were in the same range too. Therefore, it can be concluded that after purging the first 50 ml, the emulsification process has already reached steady-state.

Table 7.2 DLS analysis results for different batches of samples collected at different time interval during cross-flow membrane emulsification using 20 V membrane at 80 kPa.

Cross-flow velocity ($m\ s^{-1}$)	Average droplet diameter (nm)	PDI (-)	Peak or Mod (nm)
0.01	139	0.260	161
	135	0.234	158
	134	0.243	161
0.02	121	0.229	145
	116	0.228	144
	129	0.236	153
0.04	119	0.222	141
	116	0.221	143
	124	0.233	150
0.1	125	0.204	138
	126	0.209	144
	127	0.183	143

Table 7.3 summarises the results obtained from DLS analysis for each sample prepared based on different membrane emulsification process parameters. In all cases, only a single peak was obtained from the size distribution curve, which is presented in the following sub-sections. Specifically, the proportionality constant that correlates the pore diameter and average droplet diameter, is calculated based on equation 2.31.

Table 7.3 The average droplet diameter, polydispersity index and proportionality constant values obtained from DLS analysis for experiments based on different process parameters.

AAMs[a]	Trans-membrane pressure	Cross-flow velocity[b]	Average droplet diameter[c]	PDI	Proportionality constant
(-)	(± 5kPa)	(m s^{-1}, Pa)	(nm)	(-)	(-)
20 V (25±2 nm)	80	0 (0)	175±7	0.271	7.0
		0.01 (0.012)	136±3	0.234	5.4
		0.02 (0.024)	122±6	0.228	4.9
		0.04 (0.049)	120±4	0.204	4.8
		0.10 (0.120)	124±3	0.206	5.0
40 V (50±3 nm)	80	0 (0)	247±5	0.243	4.9
		0.01 (0.012)	173±2	0.238	3.5
		0.02 (0.024)	164±1	0.231	3.3
		0.04 (0.049)	158±1	0.226	3.2
		0.10 (0.120)	159±2	0.183	3.2
50 V (60±5 nm)	50	0 (0)	304±10	0.258	5.1
		0.01 (0.012)	204±3	0.237	3.4
		0.02 (0.024)	170±7	0.226	2.8
		0.04 (0.049)	157±2	0.232	2.6
		0.10 (0.120)	160±3	0.227	2.7
50 V (60±5 nm)	80	0 (0)	313±2	0.302	5.2
		0.01 (0.012)	221±3	0.253	3.7
		0.02 (0.024)	182±1	0.231	3.0
		0.04 (0.049)	161±1	0.228	2.7
		0.10 (0.120)	162±1	0.233	2.7

[a] The bracketed number shows the mean pore diameter.

[b] 0 m s^{-1} cross-flow velocity is equivalent to dead-end membrane emulsification. The bracketed number is the equivalent shear stress.

[c] The error span is the standard deviation based on the three repeated measurement from DLS.

7.4.1 Effect of membrane pore size

Membrane pore diameter is an influential factor for the resulting emulsions' droplet size. To visualise the effect of the membrane pore diameter, the data from Table 7.3 was extracted to construct the plots in Figure 7.10. As can be seen, there is an apparent positive correlation between the average droplet size and pore diameter. However, this positive correlation is non-linear, as evidenced by the varied proportionality constants obtained for different membranes or cross-flow velocity. The latter factor will be discussed in Section 7.4.3.

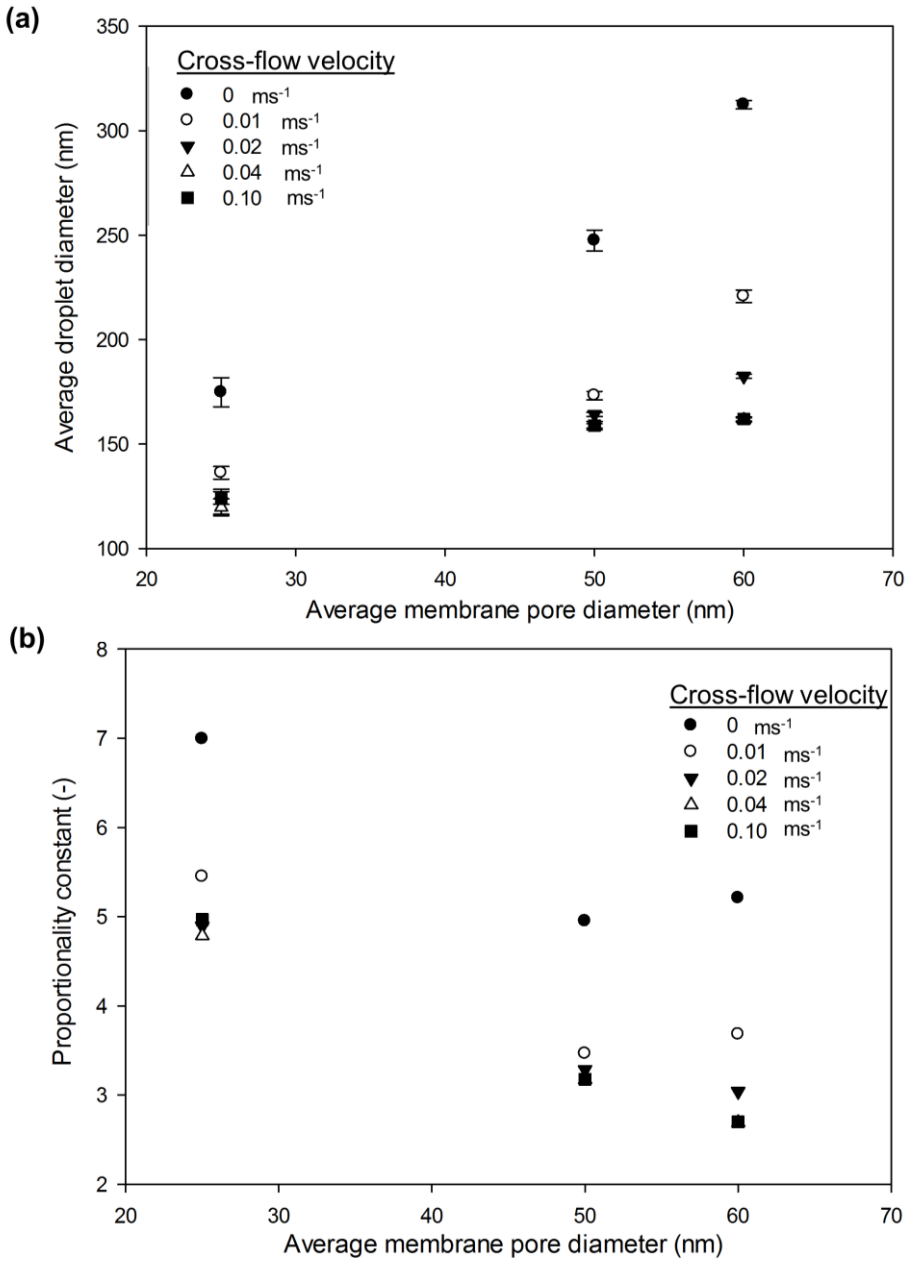

Figure 7.10 (a) The dependence of obtained average droplet size and (b) proportionality constant on membrane pore diameter. For each membrane pore diameter, different cross-flow velocities were investigated.

Despite the non-linearity, the proportionality constants obtained are well-aligned with the literature reported range of 3 to 10, for membranes with regular and circular pore structure (Peng and Williams, 1998). Nevertheless, in some cases, the presence of higher shear by cross-flow velocity has reduced the proportionality constants to just below 3. This extraordinary achievement, especially for submicron droplet formation, can be attributed to the highly-ordered pore structure and the predominant circular pore shape as compared to other membranes. For example, the commercial SPG membranes have very narrow pore size distribution and are by far the most popular choice for membrane emulsification. However, as can be seen in Figure 7.11 (a), the interpore distance and the pore shape is less regular than AAMs. Therefore, the droplets formed by AAMs have a smaller proportionality constant as compared to other membranes. Similarly, PCTE membranes also have highly monodispersed pore diameter with circular pore geometry (Figure 7.11(b)), therefore very low proportional constants (<3) has been previously achieved (Kobayashi *et al.*, 2002).

Existing literature for membranes with pore size in the micrometre range, reports that the correlation between the pore diameter and droplet size is linear (Asano and Sotoyama, 1999). In particular, this has been found to be the case for SPG and PTCE membranes (Vladisavljević and Williams, 2005). However, most of these previous studies focused on membranes with pore diameter above 1 μm. A study that uses commercial alumina membranes (Membraflow) in sub-micrometre range (0.1 and 0.8 μm), however, shows non-linear trend, similar to what obtained in the current study (Schröder and Schubert, 1999). As shown in Table 7.4, there is a significant difference (4- to 5-fold) between the proportionality constants obtained for the two different membrane diameters tested. This is, however, less significant (less than 2-fold) in the current study on AAMs and can be attributed to the superior pore structure regularity of AAMs compared to commercial alumina membranes.

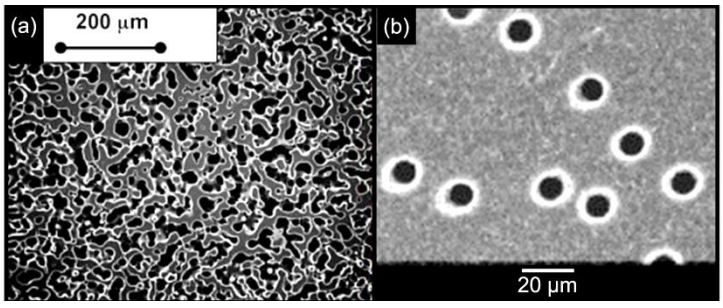

Figure 7.11 SEM micrograph of a (a) 15 μm SPG membrane and (b) 10 μm PCTE membrane (Vladisavljević *et al.*, 2007; Kobayashi *et al.*, 2002).

Table 7.4 The non-linearity of proportionality factor according to data obtained from (Schröder and Schubert, 1999) for commercial Membraflow alumina membranes.

Shear stress (Pa)	0	2	5	10	20	30
0.1 μm pore membrane	40.3	32.8	30.7	31.3	28.8	25.6
0.8 μm pore memrbane	11.5	10.2	8.8	7.6	6.8	5.9

In Figure 7.12, size distribution of the droplets formed using membranes of different pore diameter are shown. As expected, the larger the membrane pore diameter, the bigger the produced droplet, especially for dead-end mode. Increasing the pore size also increases the minimum droplet size attainable. It is also noted that the 40 V membrane with average membrane pore diameter of 50±3 nm has the narrowest droplet size distribution, which is also indicated by the smaller PDI (Table 7.3). This can be attributed to the high uniformity and circularity of the membrane pore structure, as compared to the other two membranes (See section.4.2)

As predicted by the Hagen-Poiseuille equation, a larger pore size generally increases the trans-membrane flux, i.e. the dispersed phase flow rate. In addition, the critical pressure is the highest for the smallest membrane pore diameter (equation 2.26), i.e. approximately 60, 30 and 25 kPa for 25, 50 and 60 nm AAMs, respectively. This greatly reduces the effective driving pressure for the permeation. Although the dispersed rate was not monitored during the experiment, the concentration of the SFO droplets can be directly compared by visual observation. As can be seen in Figure 7.13, the membrane emulsion formed with a 20 V membrane is the most transparent, and hence with the lowest concentration. In contrast, the emulsion formed by a 50 V membrane is the most milky due to the higher SFO content.

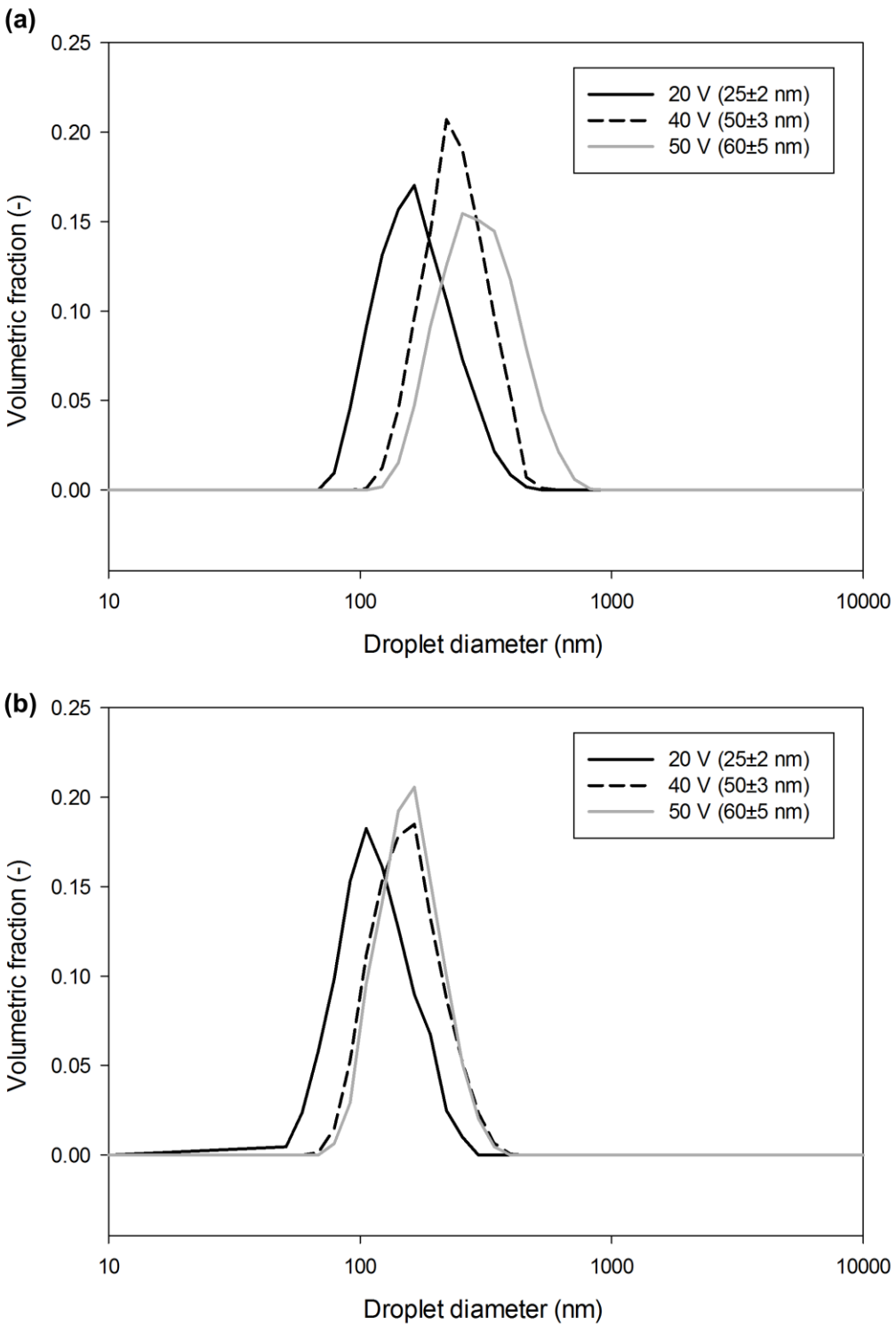

Figure 7.12 Some examples of droplet size distribution curves produced by membrane emulsification using different pore size of tubular AAMs at 80 kPa in (a) dead-end mode and (b) cross-flow mode with 0.4 m s^{-1} cross flow velocity.

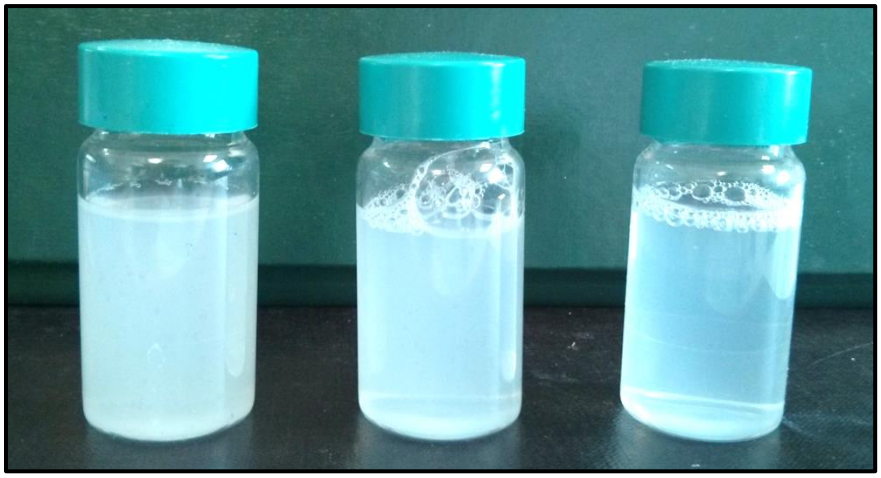

Figure 7.13 The resulting emulsions formed after one hour in dead-end mode using 50 V (left), 40 V (middle) and 20 V (left) AAMs.

7.4.2 Effect of applied pressure

The membranes with smaller pore size (and so the anodization voltage), as discussed before, have relatively high critical pressure, but lower mechanical strength (Table 6.1). This limits the range of applicable pressures for membranes with smaller pore diameter. Therefore, only a 50 V AAM was used to investigate the effect of applied pressure, at 50 and 80 kPa.

The pressure applied to the dispersed phase (SFO) to force it through the membrane pores governs the dispersed phase flow rate (Peng and Williams, 1998). As the applied pressure increases, the dispersed phase flow rate increases, but the time of the droplet detachment is hardly affected. Overall, the net effect is that final droplet volume increases. However, when cross-flow velocity is increased, the dominance of shear stress will reduce the droplet detachment period. Thus, this would reduce the differences between the final volume/size of droplets formed under different applied pressures (Peng and Williams, 1998).

As can be seen in Figure 7.14, in good agreement with literature, the obtained droplet size is smaller with lower applied pressure during the absence of cross-flow velocity. Moreover, the lower applied pressure also has a narrower droplet size distribution. As shear is introduced into the emulsification process (0.1 ms^{-1} continuous phase cross-flow velocity), the size distribution of droplet is converging, even at higher applied pressure. Nevertheless, the average droplet size remains larger at higher applied pressure. When the cross-flow velocity is

further increased, the effect of applied pressure is diminishing. The two size distribution curves corresponding to different applied pressures nearly overlap.

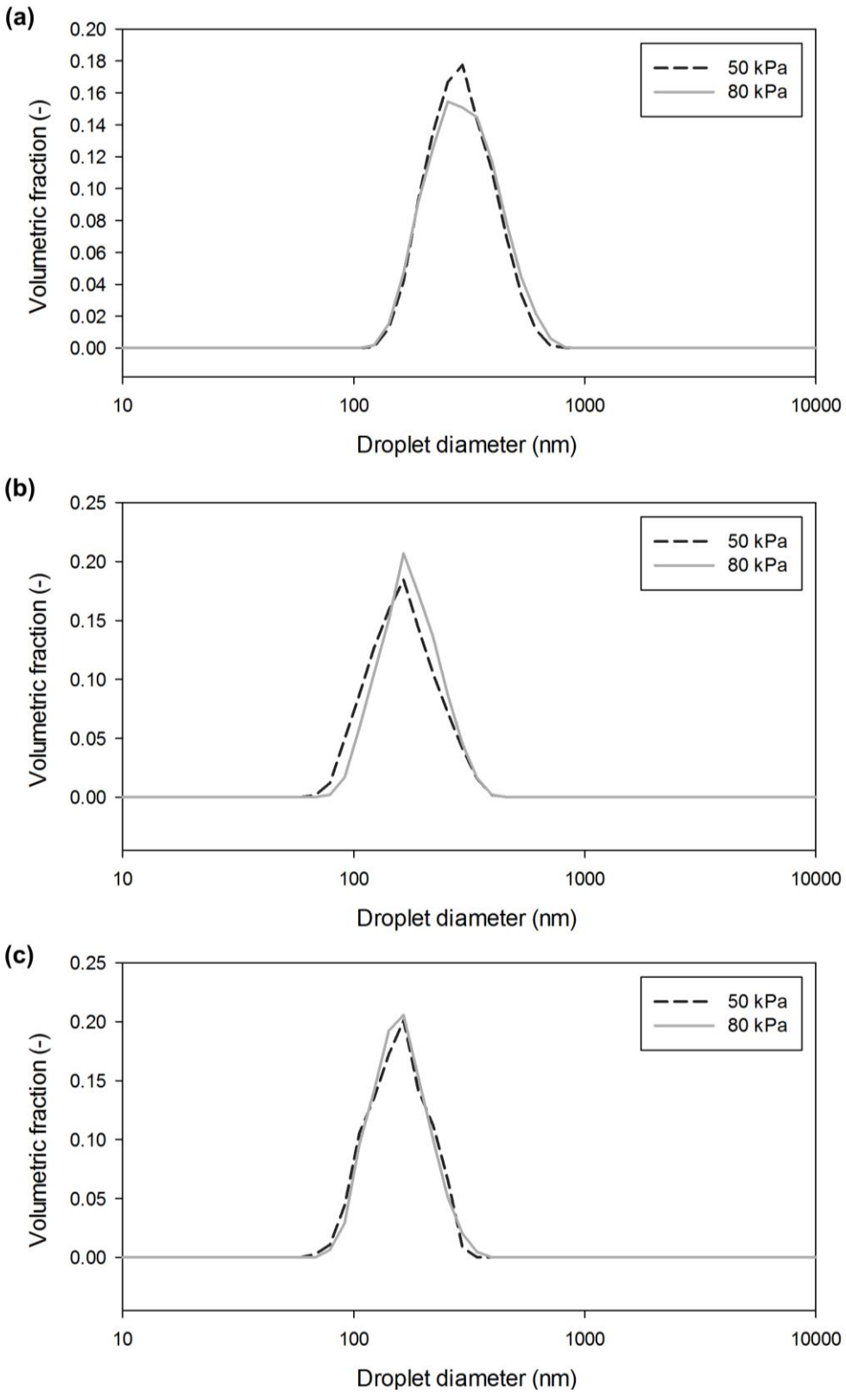

Figure 7.14 Some examples of droplet size distribution curves produced by 50 V membranes in (a) dead-end mode, and cross flow mode with (b) 0.1 and (c) 0.4 ms^{-1} cross-flow velocity.

7.4.3 Effect of cross-flow velocity

As discussed before, the presence of wall shear stress causes the resulting drag force that dominates the droplet formation (see Section 2.4.2). In this study, the shear-stress is introduced by the presence of cross-flow velocity. In laminar regime, the wall shear stress applied can be correlated with the cross-flow velocity by this equation (Peng and Williams, 1998):

$$\tau_w = \frac{8V_c\mu}{D_H} \qquad 7.2$$

where τ_w is the wall shear stress and D_H is the hydraulic diameter of the flow channel, i.e. inner diameter of the membrane tube. In this study, the range of cross-flow velocity investigated was in laminar flow (65<Re<650). As shown in equation 7.2, the wall shear stress is directly proportional to the cross-flow velocity.

Table 7.5 The wall shear stress at each cross-flow velocity.

Cross-flow velocity (ms^{-1})	0	0.01	0.02	0.04	0.10
Wall shear stress (Pa)	0	0.01	0.02	0.05	0.12

As can be seen in Figure 7.15, the droplet size distribution curves are shifting towards the left side when the cross-flow velocity is increasing. As the wall shear stress is facilitating the detachment of the droplet from the pores, the droplets formed are smaller in diameter with increasing cross-flow velocity. However, as can be seen in Figure 7.16, the significance of the effect is reducing and eventually diminishing, with increasing cross-flow velocity (or shear stress). As compared with dead-end operation, cross-flow operation at 0.01 ms^{-1} velocity provides a significant droplet size reduction, of about 25 to 50%. The effect of shear stress is diminishing when the cross-flow velocity reaches 0.04 ms^{-1}. Further increase of cross-flow velocity to 0.10 ms^{-1} does not give any meaningful reduction in droplet size.

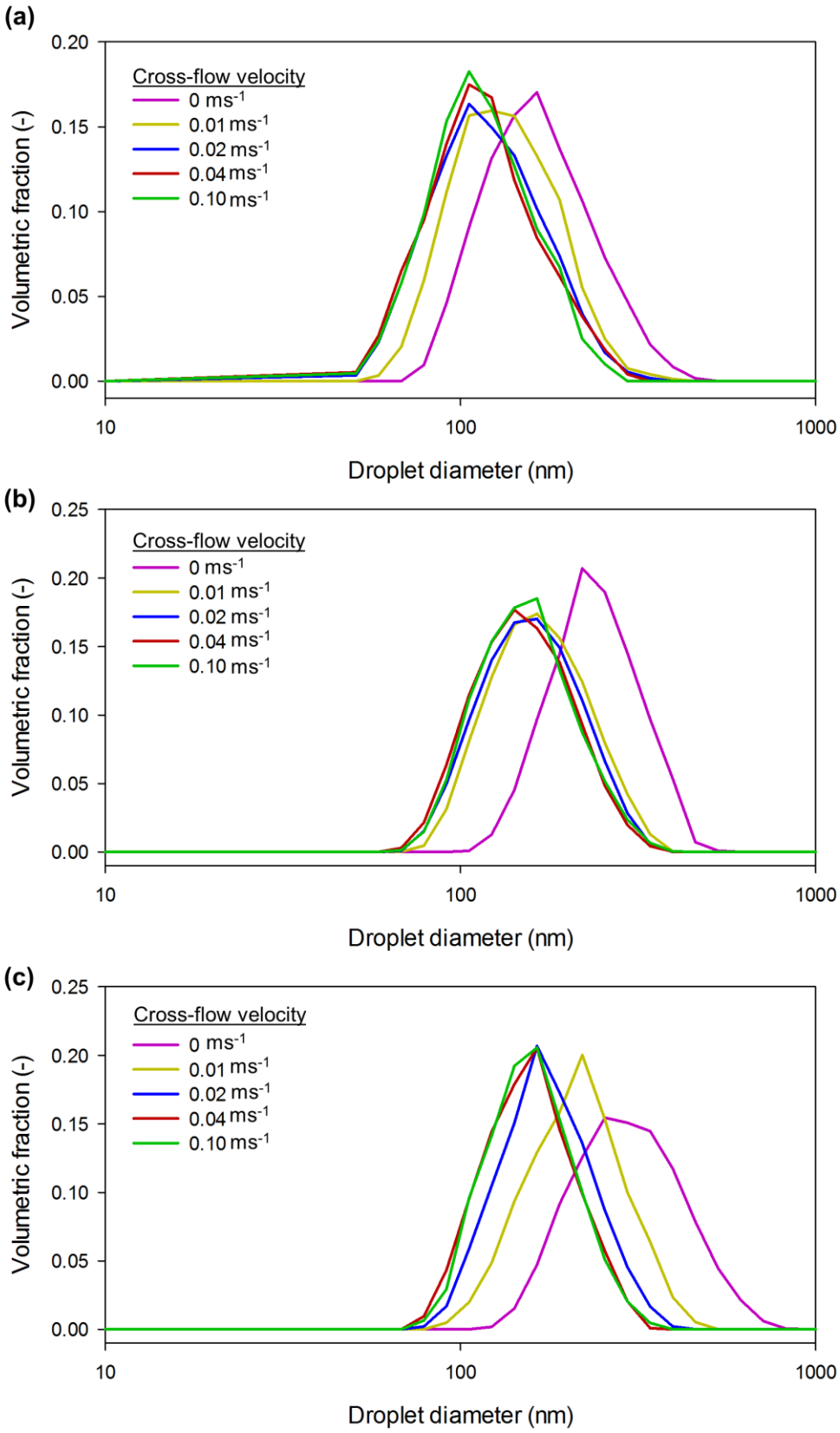

Figure 7.15 The droplet size distribution curves obtained for emulsion formed at different cross-flow velocity, using (a) 20 V, (b) 40 V and (c) 50 V AAMs. For each membrane pore diameter, different cross-flow velocities were investigated.

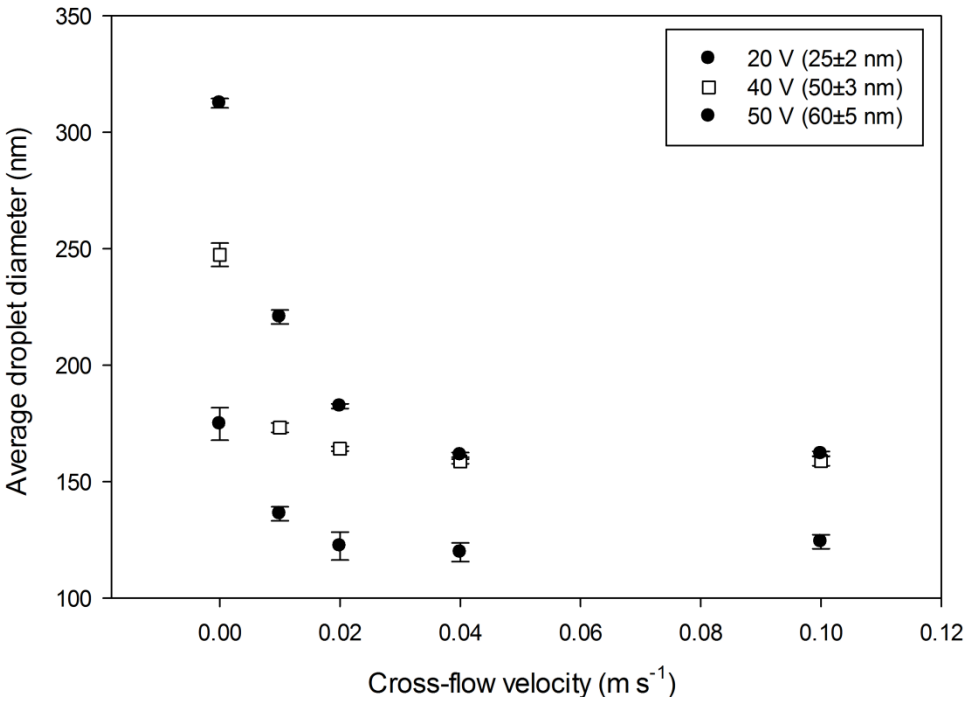

Figure 7.16 The influence of cross-flow velocity on average droplet size.

The droplet size decreases with increasing cross-flow velocity because of the increase of the resulting drag force. On the other hand, though, there is a lower limit on the droplet size due to the membrane surface roughness and the forming droplets hindering each other in detaching from the pores (Schröder and Schubert, 1999). Existing literature results are inconclusive on the value of maximum shear stress needed to minimise the droplet size. For example, two similar membrane emulsification studies using 0.1 μm ceramic alumina membranes are compared here (Schröder and Schubert, 1999; Joscelyne and Trägårdh, 1999). Despite the different emulsion formulation, the IFT reported were both in the range of 3 to 7 mN m^{-1}. However, Schröder and Schubert, 1999, and Joscelyne and Trägårdh, 1999 concluded that the effect of shear stress becomes negligible at 2 and 137 Pa, respectively. So far, there is no explanation offered for this difference.

In the current study, it is found that the effect of shear stress fades off at a shear stress as low as 0.05 Pa. Even for dead-end membrane emulsification, small droplets (sub-micron) were easily obtained. The droplets of this size are likely to have nearly the same dimension to the membrane roughness. Therefore, the introduction of shear is overcome by the presence of the roughness, and hence diminishing the effect of further increment in shear stress.

7.5 Process modelling

During membrane emulsification, the dispersed droplet detachment occurs when the IFT is overcome by the drag force, buoyant force and inertial force (Peng and Williams, 1998). In cross-flow membrane emulsification, the buoyant and inertial forces are usually negligibly small relative to drag force. For example, this can be verified by using the experimental results obtained from emulsion formed using a 50 V membrane with 0.01 m s^{-1} cross-flow velocity at 80 kPa. According to the results tabulated in Table 7.3 and equations 2.27, 2.28, 2.29 and 2.30, the forces caused by drag, interfacial tension, buoyancy and inertia are 4.7x 10^{-15}, 9.0x 10^{-11}, 4.5 x 10^{-18} and 1.8 x 10^{-19} N, respectively. The drag force is at least three orders of magnitude higher than buoyant and inertial force, and hence the dominating factor for the droplet formation.

In first approximation, the force balance can be simplified as:

$$F_d = F_\gamma$$

Replacing the above equation by equations 2.27 and equation 2.28, the following equation can be obtained to predict the droplet size (Rayner and Trägårdh, 2002):

$$D_d = \sqrt{\frac{4D_p\gamma}{6k_x\tau_w}} \qquad 7.3$$

This equation has been generally used in literature to design membrane emulsification process to achieve a desired droplet diameter. This has been previously used to fit the experimental data obtained from emulsions formed using 0.1 μm alumina membranes and 30 μm micro-engineered membrane (Rayner and Trägårdh, 2002; Stillwell *et al.*, 2007). As demonstrated in Figure 7.17, the experimental results are reasonably close to the prediction by the model. However, the attempt to fit the data from previous reported experiments, as listed in Table 7.6, shows significant discrepancy from equation 7.3. Interestingly, even in Peng and William, 1998, this equation overestimates the experimental data by a factor of 4 to 5 .The results summarised in Table 7.6 cover a range of varied process parameters, including the membrane type and wall shear stress. Even for membranes with uniform structure, such as SPG, PCTE and micro-engineered membranes, equation 7.3 always overestimates the resulting droplet size, mostly in the range of three to five. Although Schröder and Schubert, 1999 showed some data points in good agreement with equation 7.3, this data is generated at very high wall shear stress which is beyond the shear-

dependent regime. At lower wall shear stress (<10 Pa), the discrepancy is still significant, ranging from two to four times.

While the validity of the model is questionable for emulsions with larger droplet size (> 1 μm), the gap between the model and experiment is even larger for sub-micron emulsion systems. When using equation 7.3 to estimate the droplet size based on the process parameters in the current work, the resulted discrepancy increases dramatically to 50 to 180 times. Even the droplet size obtained from dead-end mode (<350 nm) is substantially smaller than estimated values based on cross-flow emulsification (>6 μm). For further verification, the droplets obtained by dead-end emulsification using AAM of 220 nm have an average diameter of approximately 600 nm (Yanagishita *et al.*, 2009), well below the estimated value for the current system. Therefore, it is obvious that the model does not work for sub-micron emulsion system. Further investigation is needed to understand the formation mechanism for sub-micron droplets in order to develop an equivalent mathematical model. At this size range, however, it is not possible to image the droplet formation using high resolution camera. This poses the insurmountable challenge for further investigation.

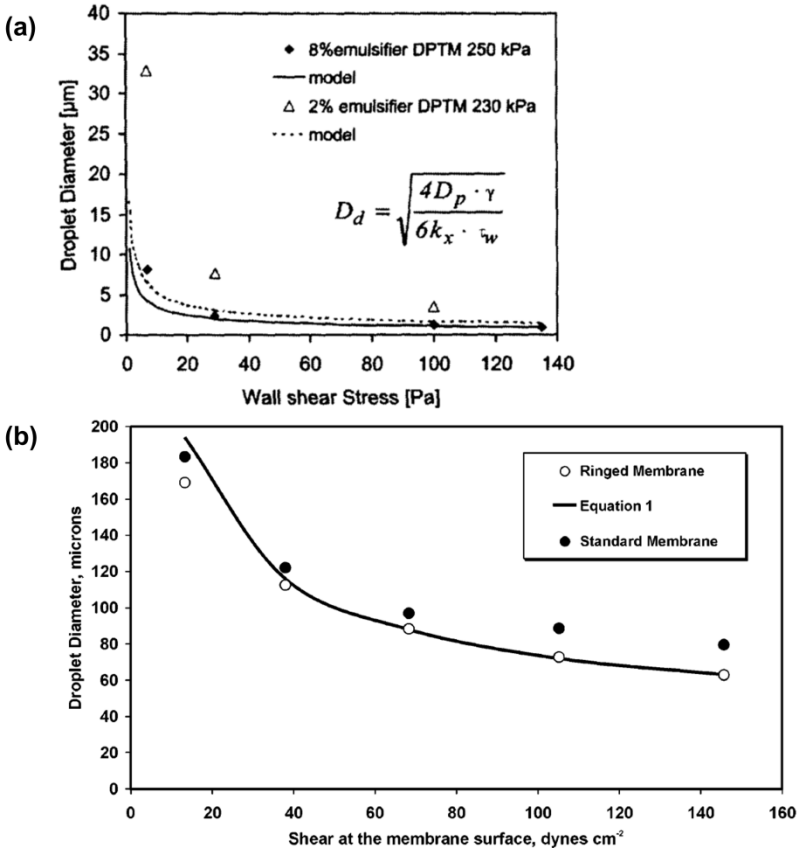

Figure 7.17 The fitting of experimental data into the mathematical model by (a) (Rayner and Trägårdh, 2002) and (b) (Stillwell *et al.*, 2007).

Table 7.6 Summary of previous and current membrane emulsification results with comparison to the mathematical model prediction.

Membrane properties	Process conditions	Experimental and theoretical droplet size	Discrepancy
SPG membrane D_p = 0.1 μm	τ_w = 0.32-1.96 Pa γ ≈ 5.0 mN m^{-1}	$D_{d,exp}$ = 2- 14μm $D_{d,theo}$ = 32-78 μm	5 - 16 times (Hancocks, 2011)
Alumina membrane D_p = 0.1 & 0.8 μm	τ_w = 2-34 Pa γ ≈ 5.0 mN m^{-1}	$D_{d,exp}$ = 2.5-8.0 μm $D_{d,theo}$ = 2.4-28.0 μm	1 - 4 times (Schröder and Schubert, 1999)
Micro-engineered membrane D_p = 0.5 μm	τ_w = 0.71 Pa γ ≈ 1.5 mN m^{-1}	$D_{d,exp}$ = 20 μm $D_{d,theo}$ = 64 μm	3.2 times (Wagdare *et al.*, 2010)
PCTE membrane D_p = 10 μm	τ_w = 0.15-4.58 Pa γ ≈ 4.4 mN m^{-1}	$D_{d,exp}$ = 20-70 μm $D_{d,theo}$ = 61-344 μm	3 - 5 times (Kobayashi *et al.*, 2002)
Single microchannel D_p = 45.6 μm	τ_w = 0.03-0.19 Pa γ ≈ 6.0 mN m^{-1}	$D_{d,exp}$ = 160-456 μm $D_{d,theo}$ = 744-1842 μm	4 - 5 times (Peng and Williams, 1998)
AAM D_p = 0.025-0.060 μm	τ_w = 0.3-0.12 Pa γ ≈ 0.48 mN m^{-1}	$D_{d,exp}$ = 0.12-0.32 μm $D_{d,theo}$ = 6-31 μm	50 - 180 times (Current work)

Equation 7.3 was developed based on the assumption of significant shape deformation during droplet formation as a result of high shear stress (Peng and Williams, 1998). The height of the droplet is approximated as the pore radius, as a result of such deformation. However, in the current study, this assumption might not hold, especially the range of shear rate investigated was at the lower end (< 1 Pa). In addition, a recent computational fluid dynamics (CFD) study showed that 'jetting' (Figure 7.18(a)) can occur at either high dispersed phase flow rate or very low interfacial tension (Pathak, 2011). When 'jetting is occurring, the droplet height is often more than double that of radius of the droplet, as can be seen in Figure 18(a). Two dimensionless numbers, i.e. Weber number (*We*) and Capillary number (*Ca*) are used to describe the 'jetting' phenomena (Pathak, 2011). As demonstrated by equations 7.4 and 7.5, *We* and *Ca* numbers illustrate the relative importance of inertia force and viscous force, respectively, compared to the surface tension:

$$We = \frac{\rho_d V_d^2 D_p}{\gamma} \quad 7.4$$

$$Ca = \frac{\mu_c V_c}{\gamma} \quad 7.5$$

As shown in Figure 7.18(b), according to Pathak, 2011, the 'jetting' occurs when the both the *We* and *Ca* numbers are high. In the current study, though the *We* is relatively low, (10^{-12} – 10^{-10} as compared to 0.009 – 0.182 in Pathak, 2011), the *Ca* is very high when compared to simulation results from Pathak, 2011 (0.019 – 0.186 as compared to 0.004 – 0.040). The low IFT between the continuous and dispersed phase, as a denominator in equations 7.4 and 7.5, signifies the large *We* and *Ca* number and hence the occurrence of jetting.

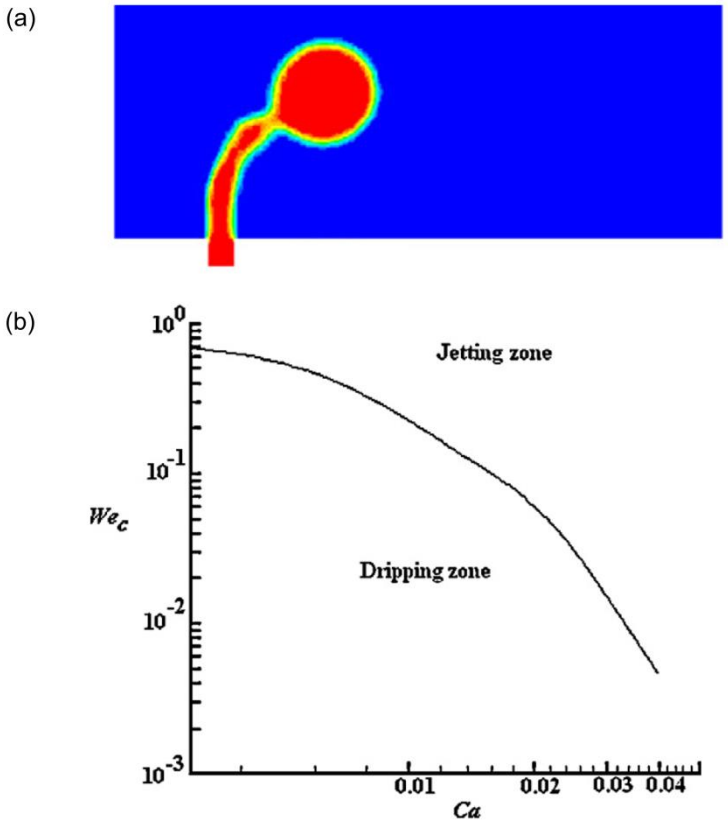

Figure 7.18 (a) The occurrence of 'jetting' during droplet formation and (b) Mapping of the regions for occurrence of 'dripping' and 'jetting' based on the critical *We* and *Ca* for the (Pathak, 2011).

In that case, the droplet height during the droplet detachment cannot be approximated to the membrane pore radius as illustrated in Peng and William,

1998. In that case, the full expression of the torque balance equation has to be used (Peng and Williams, 1998):

$$(F_d + F_b)h = F_\gamma r_p \quad 7.6$$

where h is the height of the droplet. F_d, F_γ and F_b are the forces caused by drag, interfacial tension and buoyancy, as defined in equations 2.27, 2.28, 2.29, respectively. However, the 'droplet radius' term can no longer be used to approximate the droplet height. Therefore, it is proposed here to replace 'r_p' with 'h', as shown in the following equation:

$$F_\mathrm{d} = 3\pi f k_x \rho V_c^2 h^2 = 10.205\pi h^2 \tau_w \quad 7.7$$

where the final expression on the right is simplified by inserting the value for the wall correction factor, k_x and the friction factor, f has been replaced by term wall shear stress, τ_w according to Moody's friction law for laminar flow (Peng and Williams, 1998).

On the other hand, the droplet volume can be related to the height of droplet by (Peng and Williams, 1998):

$$Volume = \frac{4}{3}\pi r_d^3 = \frac{\pi}{6}h\left(3r_p^2 + h^2\right) \quad 7.8$$

Combining equations 2.28, 2.29 and 7.7 into equation 7.6, and inserting the known process parameters such as wall shear stress, wall friction factor, densities of the two phases, IFT and membrane pore diameter, an equation containing two unknown variables, namely r_d and h, will be obtained. On the other hand, knowing the membrane pore diameter, equation 7.8 can be similarly simplified into an equation containing only r_d and h as unknowns. For example, in the current study, for a membrane with 60 nm pore diameter and cross-flow velocity of 0.1 ms^{-1} (τ_w = 0.12 Pa according Table 7.5), the equations 7.6 and 7.8 can be simplified into the following equations:

$$\left(3.8472h^2 + 3.3367 \times 10^3 r_d^3\right)h = 2.7143 \times 10^{-18} \quad 7.9$$

$$4.1888r_d^3 = 1.4137 \times 10^{-15}h + 0.5236h^3 \quad 7.10$$

Using an iterative solver (Wolfram Mathematica 9.0), the solution for the above equation system was obtained. In this case, the obtained D_d=$2r_d$=4.4561 x 10^{-7} m and h = 8.9022 x 10^{-7} m. Based on this method, the estimation of D_d and h for all different cases studied experimentally are tabulated in Table 7.7.

Table 7.7 Comparison between the droplet size obtained from experiments and estimation based on torque balance.

		Membrane pore diameter (nm)								
		25	50	60	25	50	60	25	50	60
		Experimental droplet diameter (nm)			Estimated droplet diameter (nm)			Estimated droplet height (nm)		
Cross-flow velocity (m s^{-1})	0.01	138	173	221	535	849	959	1070	1697	1917
	0.02	124	164	182	425	674	761	849	1348	1522
	0.04	126	159	161	337	535	604	674	1070	1208
	0.10	124	159	162	248	395	446	497	788	890

The estimated droplet diameter based on the torque balance and correlation between the droplet volume with the height of droplet provide a closer estimation than the well-known model based on equation 7.3 (Figure 7.19). Despite the improved accuracy, the estimated droplet diameter is still consistently 2-5 times bigger than the droplet diameter obtained from experimental study. This level of accuracy is, however, similar to the accuracy obtained by equation 7.3 for emulsions with micrometre droplet size (see Table 7.6). The discrepancy arisen in the current study could be attributed to two factors:

- The wall correction factor, k_x value used in equation 7.7 is 1.7, which is a value commonly used for spherical particle. However, clearly, the droplet shape is not entirely spherical, but rather elliptical with longer dimension at the radial direction (height) than axial direction. In this case, the k_x value would be expected to be larger (Khan and Quddus, 2010) due to the elongated shape and larger surface area in contact with the continuous phase. However, no exact number could be found in the literature that is applicable for the current calculation due to most previous investigations being based on system where the particle size is at least 20% of the tube diameter. In the present case, the droplet size is less than 0.02% of the membrane tube diameter.

- Peng and William, 1998 proposed the correlation between droplet volume with the droplet height based on equation 7.8. This equation assumes

that the geometric shape of the forming droplet to be half cylindrical and half spherical. Despite the improved accuracy of this assumption as compared to assuming a perfect spherical droplet shape, this approximation is yet to be validated.

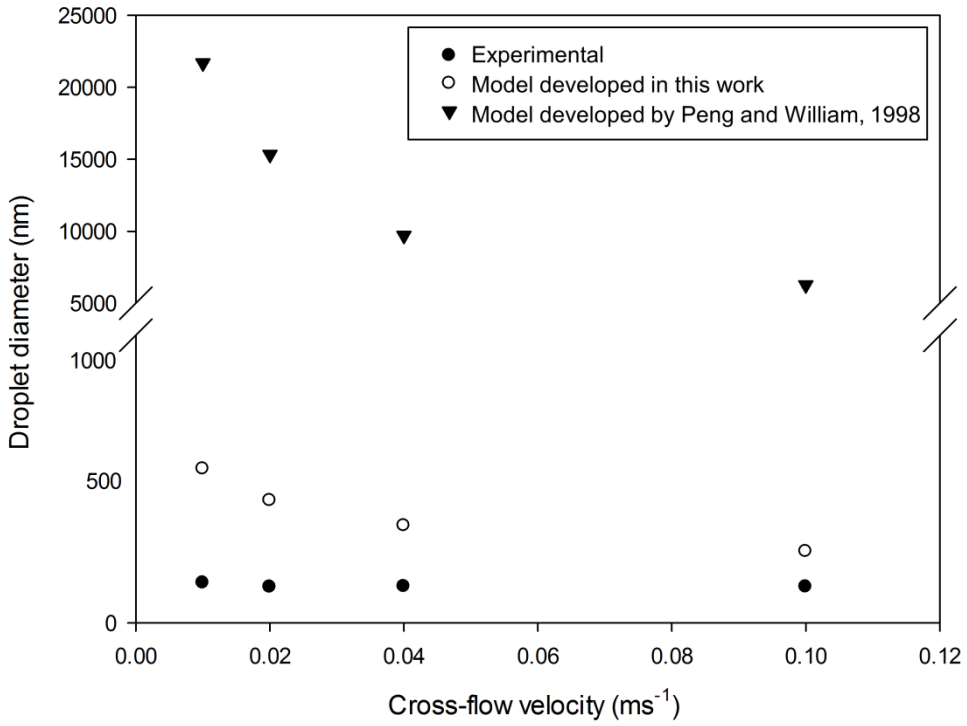

Figure 7.19 The experimental and estimated droplet size for emulsions produced by AAMs with 25 nm pores at different continuous phase cross-flow velocity. One of the estimations is based on equation 7.3 and the other is based on equations 7.6 and 7.8.

7.6 Summary

Symmetric tubular AAMs, due to the uniform pore structure and circular pore geometry, were used to produce oil in water emulsions at the submicron level with narrow size distribution. In this study, only AAMs fabricated at optimum anodization conditions, i.e. 20 V, 40 V, and 50 V were used for investigation.

The formulation of the emulsion was based on a previously studied system where stable emulsions were obtained. The dosage of surfactant was optimised to obtain a low IFT, which is important to reduce the critical pressure since the membranes used in this study have very small pore size. The disperse phase was SFO containing 4 v/wt % of Span 80 whereas the continuous phase was Milli-Q water containing 4 v/wt % of Tween 20. Both dead-end and cross-flow

membrane emulsification were systematically studied to verify the effect of pore diameter, applied pressure and cross-flow velocity on the resulting emulsions.

As expected, the resulting emulsion average diameter has a positive relation with membrane pore diameter. However, the correlation is not linear, with higher proportionality constants obtained for membranes with smaller pore diameter. In cross-flow emulsification, shear is introduced to facilitate the detachment of SFO droplets from the pores. This has a significant effect in reducing the average droplet diameter, as compared to dead-end operation. Similar to other studies, the effect of reduction of droplet size is decreasing for further increases in shear stress. In the current study, no meaningful reduction of droplet size was observed beyond the shear stress of 0.05 Pa. The applied pressure, among the process parameters, has the least effect on the characteristics of the resulting emulsions. It has small but noticeable effects for dead-end operation, i.e. the formed droplets have a bigger diameter with increasing applied pressure. However, in cross-flow operation, the shear-stress is the dominant factor for droplet formation, and hence the effect of the applied pressure is negligible.

Based on the simplified force balance, a previously proposed model tends to significantly overestimate the droplet size of the formed emulsion. In particular, for the current work which has sub-micron droplet sizes, the disparity between the estimation and experimental result is particularly substantial. This can be attributed to the invalid approximation in assuming the droplet height is similar to the membrane pore radius. A new estimation model was developed based on the full torque balance equation and introducing the droplet height as an individual variable. This model enables a very much closer approximation after taking into consideration of the non-spherical shape of the droplet, over the period of droplet growth at the membrane surface.

In general, AAMs are a good candidate for membrane emulsification, due to their homogeneous pore structure. The PDIs for the emulsions formed are mostly in the range of 0.2 to 0.3. For all membranes, emulsions obtained from dead-end operation have the highest PDI rating. Similar to average droplet size, the PDI is generally reducing with increasing cross-flow velocity. Using a 20 V membrane, the smallest average droplet size was obtained, at the range of approximately 120 nm. So far, this is likely to be the smallest achieved average droplet size by cross-flow membrane emulsification being reported.

8. Conclusions and Suggestions for Future Work

Anodic alumina membrane (AAM) is a unique nano-structured material that exhibits self-ordered pore structure. In particular, it offers the advantage of an easy control of the pore structure by altering the anodization conditions. However, the usage of AAMs is still limited to small scale applications such as nano-fabrication and laboratory scale filtration. Considering the uniform pore structure and the ease of precisely controlling it at the nanoscale, AAM is a good candidate membrane material for membrane filtration and emulsification processes. The aim of this PhD project is hence to propose anodic alumina membranes for the applications of these membrane processes. To achieve this, the focus of this project has been placed on the fabrication and optimisation of the membranes in tubular form, which can be potentially scaled up, as well as examining the membrane performance for filtration and emulsification. This chapter concludes the key findings from each chapter and suggests possible avenues for future research.

8.1 Conclusions

There are a number of novel findings or achievement of this work. Firstly, it was demonstrated experimentally for the first time, water slippage can occur in hydrophilic nanochannels. This information is useful for development of nanofluidics devices or high throughput membranes. Then, asymmetric tubular AAMs were developed. This development combines the advantages of high selectivity by layer anodized at low voltage and enhanced mechanical strength by the thicker layer anodized at high voltage. Last but not least, emulsions with well-defined nanometre droplet size have been successfully created using AAMs. To highlight, it is the smallest droplet size achieved so far by cross-flow membrane emulsification. Nevertheless, the above are the highlights from many observations and outcomes of the completed work. They are summed up as followed:

Fabrication and morphology of AAMs

In this work, the development and optimisation of aluminium anodization produced highly controlled and reproducible flat sheet and tubular membranes with nanoscale precision. The two-step anodization, having pre-textured the surface for second step of anodization, is a method to fabricate AAMs with a higher degree of pore structure homogeneity through the thickness of the membrane relative to one-step anodization. To avoid under- or over-etching during the pore opening process, the optimum time for wet chemical etching has been successfully obtained by electrochemical detection and SEM observation, for flat and tubular membranes, respectively.

For both flat and tubular membranes, the strong linear correlation obtained between membrane pore diameter and anodization voltage enables the precise control of pore structure by altering the anodization voltage, down to 10 nm. Particularly, the optimum voltages for self-ordered pore arrangement are 20 V and 40 V for sulphuric and oxalic acid, respectively. The pore structure is more uniform for flat membranes than the tubular membranes. This is attributed to the different grade of starting materials used, i.e. a high purity aluminium sheet for flat membranes and an alloy for tubular membranes. Despite the loss of pore circularity and hexagonal arrangement, the pore size distribution remains small for tubular membranes. It is important to fabricate the membranes using economical starting materials without overly compromising the uniform structure. The less expensive alloy was chosen in consideration of potential scale-up.

The growth rate of the AAM layer, which is a function of temperature, electrolyte type and concentration, and the anodization time are the important parameters determining the membrane thickness. Despite long anodization period (>24 hrs), the membrane thickness obtained at low anodization voltage (<15 V) is still insufficient to be handled robustly. Therefore, there is a technical limitation to make sufficiently strong membranes with small pore diameter. However, by manipulating the anodization voltage, asymmetric membranes consists of stem pores (higher anodization voltage) and active pores (lower anodization voltage) have been made to overcome this limitation. Two types of asymmetric membranes with distinctive structure have been successfully fabricated. The first method produces AAM with a defined pore branching region where multiple branched pores can be formed by sudden voltage reduction. The second method creates continual pore branching by gradual ramp down of anodization voltage.

Fluid flow measurement and surface modification for flat AAMs

Following the accomplishment in controlled fabrication of AAMs with uniform pore structure, surface modification and fluid flow measurement have been performed using flat AAMs. AAMs are intrinsically hydrophilic. A systematic analysis of pressure-driven water flow through pristine AAMs with pore size in the 20 nm to 100 nm range shows that flow enhancements, though smaller than for hydrophobic materials such as carbon nanotubes, can be observed for hydrophilic materials as well. The results also confirm that the enhancement increases with decreasing diameter and are a function of the channel length (or membrane thickness), as predicted by recent MD simulations. Moreover, the analysis shows good agreement with a recently proposed mathematical model that associates flow enhancement effect with pore size and length and solid-liquid molecular interactions.

For surface modification, both silane chemistry and chemical vapour deposition have been performed to alter the surface chemistry of AAMs. Due to the presence of hydroxyl groups, trichlorosilanes with different terminating functional groups have been grafted on the AAM surface and a wide spectrum of contact angle values (63° to 120°) can be obtained. Alternatively, a mixture of two or more silanes of different composition can also be used to obtain different wettability of the AAM surfaces. However, the dipping method used here is promoting the cross-linking of silane reactants. In particular, due to inefficient removal of excessive reactants within the pore channel after the dipping, severe cross-linking has caused the pore wall to exhibit higher hydrophobicity than the surface. This subsequently increased the resistance to flow to a level where the pressure required to overcome the capillarity resistance was higher than the mechanical resistance of the membrane.

For carbon coating of AAM by CVD, the gas flow rate is an important parameter to control the resulting morphology. When the gas flow rate is too low, the carbon is deposited on the surface and forms a layer blocking the porous structure. Higher gas flow rate has shown improved carbon deposition, i.e. open pore structure, homogenous deposition, the thickness of carbon coating reduces the pore diameter and porosity. Nevertheless, some inner wall surface roughness and internal blockage are still observed. These undesirable structures of the carbon coated AAMs cause lower than expected permeability obtained in a later fluid flow measurement. Therefore, the attempts to reproduce the flow

enhancement effect obtained by Whitby *et al.*, 2008 on a wider range of CNT diameters are unsuccessful.

Ultrafiltration performance of tubular AAMs

The MWCO tests show consistent separation results for asymmetric AAMs, in the range of 39 to 76 kDa. This can be translated to an average pore size of 10 ± 2 nm for the active layers. This result shows a breakdown of the linear dependence of the pore diameter with anodization voltage below 10 V. While most symmetric AAMs show limited rejection of BSA, asymmetric AAMs reliably reject more than 90% of BSA. Moreover, asymmetric membranes are mechanically strengthened by the presence of stem pores, i.e. it can sustain at least double the hydraulic pressure that a symmetric AAM with equivalent rejection capability can sustain.

As for selectivity-permeability analysis, the asymmetric AAMs outperform other commercial ceramic membranes although they still have very low flux relative to polymeric ones. On the other hand, the selectivity-scaled permeability analysis shows great potential for asymmetric AAMs if the porous structure of the support layer can be engineered to improve the permeability. The asymmetric membranes fabricated here have stem pores with diameter of about 20 nm, which contribute substantially to the resistance for flow.

The flux decline during BSA filtration can be described by the combined complete pore blocking-cake filtration model. However, the dominating mechanism varies among samples, even different membranes fabricated under the same anodization conditions. This is likely to be attributed to some structural differences resulted from intrinsic structure of starting materials, control of pre- or post-treatment during membrane fabrication. Nevertheless, further improvements such as surface modification by coating or grafting are needed to mitigate fouling and bring AAMs to commercial application.

Despite the consistent performance shown by most of the tests asymmetric AAMs, the presence of structural flaws and defects were found in a number of samples. These defects are likely to be inherited from the starting materials, which is in the form of alloy as the defects are not observed in flat AAMs which are fabricated using highly pure aluminium. This causes a trade-off between the cost of production and quality control.

Membrane emulsification using tubular AAMs

Symmetric tubular AAMs fabricated at optimum anodization conditions, i.e. 20 V, 40 V and 50 V, due to their uniform pore structure and circular pore geometry, have been tested for membrane emulsification. The dosage of surfactant has been optimised to obtain a low interfacial tension, which is important to reduce the critical pressure since the AAMs used in this study have very small pore size.

The droplet size of emulsions obtained from dead-end operation shows a strong dependence on membrane pore diameter. The droplet size proportionality constants range from about 5 to 7, and the higher value is corresponding to smaller pores as expected. When shear stress is introduced by the tangential flow of the continuous phase (cross-flow mode), this facilitates the droplet detachment and effectively reduces the droplet size. Nevertheless, the effect of reduction of droplet size is decreasing for further increases of the shear stress. In the current study, no meaningful reduction of droplet size was observed beyond the shear stress of 0.05 Pa. The applied pressure, among the process parameters, has the least effect on the characteristics of the resulting emulsions. In cross-flow operation, the shear-stress is the dominant factor for droplet formation, and hence the effect of the applied pressure is negligible.

Based on force balance, a previously proposed model tends to significantly overestimate the droplet size of the formed emulsion. In particular, for the current work which has sub-micron droplet size, the disparity between the estimation and experimental result is particularly substantial. . The approximation that assumes the droplet height is similar to the membrane pore radius is therefore questionable. An alternative model has been proposed based on the full torque balance equation. This model enables a closer approximation and reduces the overestimation to 2-5 times, in line with the accuracy obtained by fitting previous models for micrometre droplets.

In general, AAM is a good candidate for membrane emulsification, due to the uniform pore structure. The PDIs for the emulsions are mostly in the range of 0.2 to 0.3. Using a 20 V membrane, the smallest average droplet size was obtained, at the range of approximately 120 nm. So far, this is likely to be the smallest achieved average droplet size by membrane emulsification being reported. This implies that using AAMs for membrane emulsification shows great potential in the areas where controlled and well-defined droplet size is important, such as nanoparticles production, nutraceuticals and nanocapsules for drug delivery.

8.2 Future work

The investigation in this work has been proven to yield valuable information on stable fabrication of AAMs and their performance for membrane filtration and emulsification. Nevertheless, the work here could be extended in various directions to bring AAMs closer to the industrial interest.

Optimisation of CVD process

In the current work, the carbon coating of AAM by CVD has been improved by increasing the gas flow rate. However, some inner wall surface roughness and internal blockage are still observed. Further investigation of CVD process parameters will be needed to improve the coating quality:

- Different carbon source such as acetylene and methane;
- Variation of gas flow rate;
- Dwell at different temperatures.

The aim of the investigation is to obtain homogenous and smooth carbon coating on AAMs. As the non-catalytic CVD process yields turbostratic structure, graphitisation can improve the carbon structure (Mattia *et al.*, 2006). For this, due to the high annealing temperature needed for graphitisation (>1200 °C), there is a technical challenge to avoid deformation of the AAMs during the phase change from amorphous to α-alumina structure.

Subsequently, the coated samples should be examined by fluid flow measurement. This is to attempt to reproduce the results by Whitby *et al.*, 2008, in a wider range of diameters and surface structures. Furthermore, higher flow enhancement effect can be expected from successfully graphitised samples. This result can be potentially beneficial for the development of high flux membranes.

On the other hand, significant flow enhancement effect in silicon carbide (SiC) nanotubes has also been concluded by MD simulation (Khademi and Sahimi, 2011). However, this is yet to be verified by experimental study. Some preliminary synthesis work has been performed during a research visit to Fraunhofer IKTS, Hermsdorf, Germany (see Appendix A). Nevertheless, further work in fluid flow measurement is needed. Other than the flow enhancement

effect, potentially, SiC also exhibits photocatalytic behaviour which would be an interest of wide scientific communities.

Modular design and fabrication of AAMs

The fabrication of tubular AAMs in this work marks the first step of scalable production of AAMs. Nevertheless, currently, the anodization has been only performed at the dimension of 5.75 mm (D) x 100 mm (L). It is still too small for applications in the industrial scale. Some preliminary work has been done to fabricate tubular AAMs with smaller tube diameter (See Appendix B). This can potentially increase the mechanical strength of the membranes and potentially packed into capillary modular form.

Here, it is proposed to fabricate membranes with a shell and tube configuration. Initially, the aluminium (alloy) tubes will be assembled together by either gluing or welding into perforated plate. After annealing, the electropolishing, anodization, aluminium removal and pore opening will be performed sequentially to all the tubes at the same time. A lot of process optimisation will be needed to ensure homogeneity of each process, i.e. temperature control, electrolyte recirculation, etc.

Some residual aluminium would be selectively protected from aluminium removal. This is to further increase the mechanical strength of the membranes. Figure 8.1 shows an example how this could be patterned. The pattern will be optimised based on the trade-off between the available membrane surface area and the mechanical stability of the membranes.

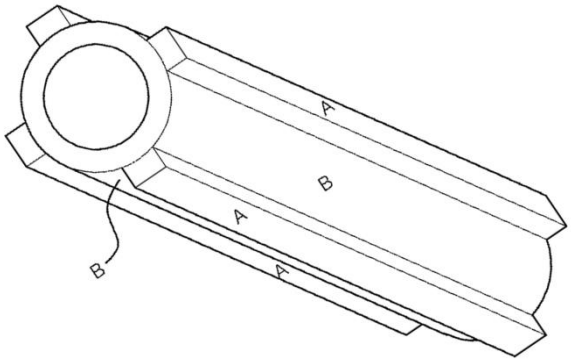

Figure 8.1 Schematic of a tubular AAM with some residual aluminium preserved for mechanical strength improvement. A is the residual aluminium and B is the anodized oxide layer.

Structural optimisation of asymmetric AAMs for ultrafiltration

Finding in this work concludes that the support layer of the asymmetric AAMs fabricated has an undesirable high resistance to fluid flow. Therefore, the permeability of the asymmetric AAMs can be improved by increase the porosity of the support layer.

As such, it is proposed to start anodization at high voltage (i.e. 200 V) to create large pore diameter, which are less resistant for fluid flow. Voltage will be subsequently reduced to a low value (i.e. <20 V) to create the active layer which is responsible for good rejection capability. For this work, there will be a couple of foreseen challenges. First, different electrolytes will need to be used for different voltage regimes to ensure a uniform porous structure as well as anodization stability. Therefore, changing of electrolyte will be required for the anodization voltage transition of 200 V to below 20 V. Moreover, the voltage reduction rate is important to ensure the transition layer is not too thick (i.e. resistant to fluid flow) if it is too slow. At the same time, sufficient time is needed for the porous structure to reorganise at different voltage.

Computational fluid dynamics (CFD) simulation of droplet formation during membrane emulsification

In this study, it has been found that the emulsions formed by AAMs do not comply with the force balance model developed by Peng and William, 1998. The model significantly overestimates the resulted droplet size. Due to the size range of the droplet formed, it is impossible to observe the droplet formation under high resolution camera. Therefore, CFD is suggested to understand the droplet formation mechanism at the nanoscale and develop a model to describe the emulsification process by using AAMs.In the current study, a model has been developed based on the non-spherical droplet shape during the droplet growth. This model has reduced the gap between the estimation from the experimental data. However, further study is needed to verify the droplet shape on the membrane surface.

The CFD study can be conducted using commercial packages such as Ansys Fluent® or COMSOL Multiphysics®. By replacing the geometry of the AAMs used in current experiments, CFD can provide valuable information such as the variation of force field, flow velocity of each phase, the shear stress at the wall, etc. This can be useful to compare the results obtained experimental here.

References

Abel, M.L., Allington, R.D., Digby, R.P., Porritt, N., Shaw, S.J. & Watts, J.F. 2006. Understanding the relationship between silane application conditions, bond durability and locus of failure. *International Journal of Adhesion and Adhesives,* 26**,** 2-15.

Adiga, S.P., Zapol, P. & Curtiss, L.A. 2006. Atomistic simulations of amorphous alumina surfaces. *Physical Review B,* 74**,** 064204.

Aimar, P., Meireles, M. & Sanchez, V. 1990. A contribution to the translation of retention curves into pore size distributions for sieving membranes. *Journal of Membrane Science,* 54**,** 321-338.

Alam, K.M., Singh, A.P., Bodepudi, S.C. & Pramanik, S. 2011. Fabrication of hexagonally ordered nanopores in anodic alumina: An alternative pretreatment. *Surface Science,* 605**,** 441-449.

Almanza-Workman, A.M., Raghavan, S., Deymier, P., Monk, D.J. & Roop, R. 2002. Water dispersible silanes for wettability modification of polysilicon. *Journal of The Electrochemical Society,* 149**,** H6-H11.

Anton, N., Benoit, J.-P. & Saulnier, P. 2008. Design and production of nanoparticles formulated from nano-emulsion templates—a review. *Journal of Controlled Release,* 128**,** 185-199.

Aran, H.C., Chinthaginjala, J.K., Groote, R., Roelofs, T., Lefferts, L., Wessling, M. & Lammertink, R.G.H. 2011. Porous ceramic mesoreactors: A new approach for gas–liquid contacting in multiphase microreaction technology. *Chemical Engineering Journal,* 169**,** 239-246.

Arkhangelsky, E., Duek, A. & Gitis, V. 2012. Maximal pore size in uf membranes. *Journal of Membrane Science,* 394–395**,** 89-97.

Asano, Y. & Sotoyama, K. 1999. Viscosity change in oil/water food emulsions prepared using a membrane emulsification system. *Food Chemistry,* 66**,** 327-331.

Bacchin, P., Aimar, P. & Field, R.W. 2006. Critical and sustainable fluxes: Theory, experiments and applications. *Journal of Membrane Science,* 281**,** 42-69.

Baker, R.W. 2004. *Membrane technology and application,* England: John Wiley & Sons.

Bandyopadhyay, S., Miller, A.E., Chang, H.C., Banerjee, G., Yuzhakov, V., Yue, D.F., Ricker, R.E., Jones, S., Eastman, J.A., Baugher, E. & Chandrasekhar, M. 1996. Electrochemically assembled quasi-periodic quantum dot arrays. *Nanotechnology,* 7**,** 360.

Barfod, N.M. 1995. Chapter 3 - methods for characterization of structure in whippable dairy-based emulsions. *In:* Anilkumar (ed.) *Characterization of food.* Amsterdam: Elsevier Science B.V.

Bartók, A., Csik, A., Vad, K., Molnár, G., Tóth-Kádár, E., & Péter, L. 2009. Application of surface roughness data for the evaluation of depth profile measurements of nanoscale multilayers. *Journal of The Electrochemical Society,* 156, D253-D260.

Belfort, G., Davis, R.H. & Zydney, A.L. 1994. The behavior of suspensions and macromolecular solutions in crossflow microfiltration. *Journal of Membrane Science,* 96**,** 1-58.

Belwalkar, A., Grasing, E., Van Geertruyden, W., Huang, Z. & Misiolek, W.Z. 2008. Effect of processing parameters on pore structure and thickness of anodic aluminum oxide (aao) tubular membranes. *Journal of Membrane Science,* 319**,** 192-198.

Benum, S. & Nes, E. 1997. Effect of precipitation on the evolution of cube recrystallisation texture. *Acta Materialia,* 45**,** 4593-4602.

Bernardi, D., Pereira, T., Maciel, N., Bortoloto, J., Viera, G., Oliveira, G. & Rocha-Filho, P. 2011. Formation and stability of oil-in-water nanoemulsions containing rice bran oil: In vitro and in vivo assessments. *Journal of Nanobiotechnology,* 9**,** 44.

Bhalodia, D., Shah, P. & Shelat, P. 2010. Nanoemulsion: A pharmaceutical review. *Systematic Reviews in Pharmacy,* 1**,** 24-32.

Bibette, J., Calderon, F.L. & Poulin, P. 1999. Emulsions: Basic principles. *Reports on Progress in Physics,* 62**,** 969.

Bockris, J.O.M., White, R.E. & Conway, B.E. 1989. *Modern aspects of electrochemistry*: Springer.

Bojinov, M.S. 2010. Nanoporous anodic oxides. *In:* Sattler (ed.) *Handbook of nanophysics: Functional nanomaterials.* Boca Raton: Taylor & Francis.

Bolton, G., LaCasse, D. & Kuriyel, R. 2006. Combined models of membrane fouling: Development and application to microfiltration and ultrafiltration of biological fluids. *Journal of Membrane Science,* 277**,** 75-84.

Brainerd, E.L. 2001. Caught in the crossflow. *Nature,* 412**,** 387-388.

Calvo, J.I., Bottino, A., Capannelli, G. & Hernández, A. 2008. Pore size distribution of ceramic uf membranes by liquid–liquid displacement porosimetry. *Journal of Membrane Science,* 310**,** 531-538.

Capannelli, G., Vigo, F. & Munari, S. 1983. Ultrafiltration membranes — characterization methods. *Journal of Membrane Science,* 15**,** 289-313.

Charcosset, C., Limayem, I. & Fessi, H. 2004. The membrane emulsification process—a review. *Journal of Chemical Technology & Biotechnology,* 79**,** 209-218.

Cheng, C.-J., Chu, L.-Y. & Xie, R. 2006. Preparation of highly monodisperse w/o emulsions with hydrophobically modified spg membranes. *Journal of Colloid and Interface Science,* 300**,** 375-382.

Cheng, C.J., Chu, L.Y., Xie, R. & Wang, X.W. 2008. Hydrophobic modification and regeneration of shirasu porous glass membranes on membrane emulsification performance. *Chemical Engineering & Technology,* 31**,** 377-383.

Cheng, J.T. & Giordano, N. 2002. Fluid flow through nanometer-scale channels. *Physical Review E,* 65**,** 031206.

Cheng, Q.-M., Interrante, L.V., Lienhard, M., Shen, Q. & Wu, Z. 2005. Methylene-bridged carbosilanes and polycarbosilanes as precursors to silicon carbide—from ceramic composites to sic nanomaterials. *Journal of the European Ceramic Society,* 25**,** 233-241.

Cheremisinoff, N.P. 1998. Liquid filtration (2nd edition). Elsevier.

Cheryan, M. 1998. *Ultrafiltration and microfiltration handbook*: Taylor & Francis.

Choi, J. 2004. *Fabrication of monodomain porous alumina using nanoimprint lithography and its applications.* Doctorate of Philosophy, The Martin Luther University of Halle-Wittenberg.

Choi, Y.C., Hyeon, J.Y. & Bu, S.D. 2009. Effects of anodizing voltages and corresponding current densities on self-ordering process of nanopores in porous anodic aluminas anodized in oxalic and sulfuric acids. *Journal of Korean Physical Society,* 55**,** 835-840.

Choy, K.L. 2003. Chemical vapour deposition of coatings. *Progress in Materials Science,* 48**,** 57-170.

Chung, C.K., Liao, M.W., Chang, H.C. & Lee, C.T. 2011. Effects of temperature and voltage mode on nanoporous anodic aluminum oxide films by one-step anodization. *Thin Solid Films,* 520**,** 1554-1558.

Cuperus, F.P., Bargeman, D. & Smolders, C.A. 1992. Permporometry: The determination of the size distribution of active pores in uf membranes. *Journal of Membrane Science,* 71**,** 57-67.

de Gennes, P.G., Brochard-Wyart, F. & Quere, D. 2004. *Capillarity and wetting phenomena: Drops, bubbles, pearls, waves*: Springer.

Desch, C.A. 1934. *The chemistry of solids,* Ithaca: Cornell University Press.

Diggle, J.W., Downie, T.C. & Goulding, C.W. 1969. Anodic oxide films on aluminum. *Chemical Reviews,* 69**,** 365-405.

Ding, G., Yang, R., Ding, J., Yuan, N. & Zhu, Y. 2010. Fabrication of porous anodic alumina with ultrasmall nanopores. *Nanoscale Research Letters,* 5**,** 1257 - 1263.

Ding, G.Q., Zheng, M.J., Xu, W.L. & Shen, W.Z. 2005. Fabrication of controllable free-standing ultrathin porous alumina membranes. *Nanotechnology,* 16**,** 1285.

Dollimore, D. & Heal, G.R. 1978. The analysis of gas adsorption data to determine pore structure. *Surface Technology,* 6**,** 231-258.

Donsì, F., Senatore, B., Huang, Q. & Ferrari, G. 2010. Development of novel pea protein-based nanoemulsions for delivery of nutraceuticals. *Journal of Agricultural and Food Chemistry,* 58**,** 10653-10660.

Drelich, J., Fang, C. & White, C.L. 2006. Measurement of interfacial tension in fluid-fluid systems. *In:* Somasundaran (ed.) *Encyclopedia of surface and colloid science.* Taylor & Francis Group.

Du, F., Qu, L., Xia, Z., Feng, L. & Dai, L. 2011. Membranes of vertically aligned superlong carbon nanotubes. *Langmuir,* 27**,** 8437-8443.

Fane, A.G., Wang, R. & Jia, Y. 2008. Membrane technology: Past, present and future. *In:* Wang, Chen, Hung & Shammas (eds.) *Membrane and desalination technologies.* Humana Press.

Field, R. 2010. Fundamentals of fouling. *Membrane technology.* Wiley-VCH Verlag GmbH & Co. KGaA.

Fowkes, F.M. 1971. *Chemistry and physics of interfaces.* Washington D.C.: American Chemical Society.

Friberg, S., Larsson, K. & Sjoblom, J. 2003. *Food emulsions*: Taylor & Francis.

Friedman, A.L., Brittain, D. & Menon, L. 2007. Roles of ph and acid type in the anodic growth of porous alumina. *The Journal of Chemical Physics,* 127**,** 154717-7.

Garcia-Vergara, S.J., Iglesias-Rubianes, L., Blanco-Pinzon, C.E., Skeldon, P., Thompson, G.E. & Campestrini, P. 2006a. Mechanical instability and pore generation in anodic alumina. *Proceedings of the Royal Society A: Mathematical, Physical and Engineering Science,* 462**,** 2345-2358.

Garcia-Vergara, S.J., Skeldon, P., Thompson, G.E. & Habazaki, H. 2006b. A flow model of porous anodic film growth on aluminium. *Electrochimica Acta,* 52**,** 681-687.

Garcia-Vergara, S.J., Skeldon, P., Thompson, G.E. & Habazaki, H. 2008. Behaviour of a fast migrating cation species in porous anodic alumina. *Corrosion Science,* 50**,** 3179-3184.

Garcia-Vergara, S.J., Skeldon, P., Thompson, G.E., Hashimoto, T. & Habazaki, H. 2007. Compositional evidence for flow in anodic films on aluminum under high electric fields. *Journal of the Electrochemical Society,* 154**,** C540-C545.

Glaves, C.L. & Smith, D.M. 1989. Membrane pore structure analysis via nmr spinlattice relaxation experiments. *Journal of Membrane Science,* 46**,** 167-184.

Gong, J., Butler, W.H. & Zangari, G. 2010. Tailoring morphology in free-standing anodic aluminium oxide: Control of barrier layer opening down to the sub-10 nm diameter. *Nanoscale,* 2**,** 778-785.

Grasing, E. 2007. *Effect of processing parameters on mechanical properties and membrane morphology of nanoporous anodic aluminium oxide tube membranes.* MSc, Lehigh University, USA.

Green, D. & Perry, R. 2007. *Perry's chemical engineers' handbook, eighth edition*: McGraw-Hill Education.

Haberman, W.L., Sayre, R.M. & Laboratory, D.W.T.M.B.H. 1958. *Motion of rigid and fluid spheres in stationary and moving liquids inside cylindrical tubes*: Dept. of the Navy, David Taylor Model Basin, Hydromechanics Laboratory.

Hancocks, R.D. 2011. *Controlled emulsification using microporous membranes.* Doctor of Philosophy, University of Birmingham.

Haspert, L. 2010. *My research* [Online]. Available: http://www.terpconnect.umd.edu /~lhaspert/research.html [Accessed 12 February 2013].

Henry, J.D. 1972. Cross flow filtration. *In:* Li (ed.) *Recent developments in separation science.* Cleveland: CRC Press.

Hermia, J. 1982. Constant pressure blocking filtration laws - application to power-law non-newtonian fluids. *Transcations of the Institution of Chemical Engineers,* 60**,** 183-187.

Hirose, M., Ito, H. & Kamiyama, Y. 1996. Effect of skin layer surface structures on the flux behaviour of ro membranes. *Journal of Membrane Science,* 121**,** 209-215.

Ho, C.-C. & Zydney, A.L. 2000. A combined pore blockage and cake filtration model for protein fouling during microfiltration. *Journal of Colloid and Interface Science,* 232**,** 389-399.

Ho, T.A., Papavassiliou, D.V., Lee, L.L. & Striolo, A. 2011. Liquid water can slip on a hydrophilic surface. *Proceedings of the National Academy of Sciences,* 108**,** 16170-16175.

Ho, W.S.W. & Sirkar, K.K. 1992. *Membrane handbook,* New York: Chapman and Hall.

Hoar, T.P. & Mott, N.F. 1959. A mechanism for the formation of porous anodic oxide films on aluminium. *Journal of Physics and Chemistry of Solids,* 9**,** 97-99.

Hobbs, C. Hong, S. & Taylor, J. 2006. Effect of Surface Roughness on Fouling of RO and NF Membranes during Filtration of a High Organic Surficial Groundwater. *Journal of Water Supply: Research and Technology*, 58, 559-570.

Hobbs, P.M. & Kinloch, A.J. 1998. The computational molecular modelling of organosilane primers. *The Journal of Adhesion,* 66**,** 203-228.

Holt, J.K., Park, H.G., Wang, Y., Stadermann, M., Artyukhin, A.B., Grigoropoulos, C.P., Noy, A. & Bakajin, O. 2006. Fast mass transport through sub-2-nanometer carbon nanotubes. *Science,* 312**,** 1034-1037.

Houser, J.E. & Hebert, K.R. 2009. The role of viscous flow of oxide in the growth of self-ordered porous anodic alumina films. *Nat Mater,* 8**,** 415-420.

Howell, J.A., Sanchez, V. & Field, R.W. (eds.) 1993. *Membranes in bioprocessing: Theory and applications,* London: Chapman & Hall.

Huang, Q., Yu, H. & Ru, Q. 2010. Bioavailability and delivery of nutraceuticals using nanotechnology. *Journal of Food Science,* 75**,** R50-R57.

Hwang, S.-K., Jeong, S.-H., Lee, O.-J. & Lee, K.-H. 2005. Fabrication of vacuum tube arrays with a sub-micron dimension using anodic aluminum oxide nano-templates. *Microelectronic Engineering,* 77**,** 2-7.

Ichimura, S., Tsuru, T., Nakao, S. & Kimura, S. 2000. Analysis of linear macromolecule transport through aluminum anodic oxide membranes by pore model. *Journal of Chemical Engineering of Japan,* 33**,** 141-151.

Ioan, C.E., Aberle, T. & Burchard, W., 2000. Structure properties of dextrans 2. Dilute Solution. *Macromolecules*, 33, 5730-5739.

Ismail, A.F., Goh, P.S., Sanip, S.M. & Aziz, M. 2011. Transport and separation properties of carbon nanotube-mixed matrix membrane. *Separation and Purification Technology,* 70**,** 12-26.

Itoh, N., Kato, K., Tsuji, T. & Hongo, M. 1996. Preparation of a tubular anodic aluminum oxide membrane. *Journal of Membrane Science,* 117**,** 189-196.

Itoh, N., Tomura, N., Tsuji, T. & Hongo, M. 1998. Strengthened porous alumina membrane tube prepared by means of internal anodic oxidation. *Microporous and Mesoporous Materials,* 20**,** 333-337.

Jeong, B.-H., Hoek, E.M.V., Yan, Y., Subramani, A., Huang, X., Hurwitz, G., Ghosh, A.K. & Jawor, A. 2007. Interfacial polymerization of thin film nanocomposites: A new concept for reverse osmosis membranes. *Journal of Membrane Science,* 294**,** 1-7.

Jessensky, O., Muller, F. & Gosele, U. 1998. Self-organized formation of hexagonal pore arrays in anodic alumina. *Applied Physics Letters,* 72**,** 1173-1175.

Joscelyne, S.M. & Trägårdh, G. 1999. Food emulsions using membrane emulsification: Conditions for producing small droplets. *Journal of Food Engineering,* 39**,** 59-64.

Joscelyne, S.M. & Trägårdh, G. 2000. Membrane emulsification — a literature review. *Journal of Membrane Science,* 169**,** 107-117.

Joseph, S. & Aluru, N.R. 2008. Why are carbon nanotubes fast transporters of water? *Nano Letters,* 8**,** 452-458.

Jung, H.Y., Jung, S.M., Gu, G.H. & Suh, J.S. 2006. Anodic aluminum oxide membrane bonded on a silicon wafer for carbon nanotube field emitter arrays. *Applied Physics Letters,* 89**,** 013121-3.

Kanani, D.M., Fissell, W.H., Roy, S., Dubnisheva, A., Fleischman, A. & Zydney, A.L. 2010. Permeability–selectivity analysis for ultrafiltration: Effect of pore geometry. *Journal of Membrane Science,* 349**,** 405-410.

Kedem, O. & Katchalsky, A. 1958. Thermodynamic analysis of the permeability of biological membranes to non-electrolytes. *Biochimica et Biophysica Acta,* 27**,** 229-246.

Khademi, M. & Sahimi, M. 2011. Molecular dynamics simulation of pressure-driven water flow in silicon-carbide nanotubes. *The Journal of Chemical Physics,* 135**,** 204509-7.

Khan, M.I. & Quddus, N. Year. Wall correction factors for non-spherical particle moving in a liquid-filled cylindrical capillary. *In:* 13th Asian Congress of Fluid Mechanics, 2010 Dhaka. Bangladesh Society of Mechanical Engineers, 966-969.

Kluth, G.J., Sung, M.M. & Maboudian, R. 1997. Thermal behavior of alkylsiloxane self-assembled monolayers on the oxidized si(100) surface. *Langmuir,* 13**,** 3775-3780.

Kobayashi, I., Yasuno, M., Iwamoto, S., Shono, A., Satoh, K. & Nakajima, M. 2002. Microscopic observation of emulsion droplet formation from a polycarbonate membrane. *Colloids and Surfaces A: Physicochemical and Engineering Aspects,* 207**,** 185-196.

Koroleva, M.Y. & Evgenii, V.Y. 2012. Nanoemulsions: The properties, methods of preparation and promising applications. *Russian Chemical Reviews,* 81**,** 21.

Koros, W.J., Ma, Y.H. & Shimidzu, T. 1996. Terminology for membranes and membrane processes. *Pure & Appl. Chem.,* 68**,** 1479-1489.

Krishnan, R. 2005. *Templated self-assembly of nanoporous alumina: Pore formation and ordering mechanisms, methodologies, and applications.* PhD PhD, Massachusetts Institute of Technology.

Kumar, M., Grzelakowski, M., Zilles, J., Clark, M. & Meier, W. 2007. Highly permeable polymeric membranes based on the incorporation of the functional water channel protein aquaporin z. *Proceedings of the National Academy of Sciences,* 104**,** 20719-20724.

Lambrich, U. & Schubert, H. 2005. Emulsification using microporous systems. *Journal of Membrane Science,* 257**,** 76-84.

Lee, I., Jo, Y., Kim, Y.-T., Tak, Y. & Choi, J. 2012a. Electrochemical thinning for anodic aluminum oxide and anodic titanium oxide. *The Bulletin of the Korean Chemical Society,* 33**,** 1465-1469.

Lee, K.P., Arnot, T.C. & Mattia, D. 2011. A review of reverse osmosis membrane materials for desalination--development to date and future potential. *Journal of Membrane Science,* 370**,** 1-22.

Lee, K.P., Leese, H. & Mattia, D. 2012b. Water flow enhancement in hydrophilic nanochannels. *Nanoscale,* 4**,** 2621-2627.

Lee, K.P. & Mattia, D. 2013. Monolithic nanoporous alumina membranes for ultrafiltration applications: Characterization, selectivity–permeability analysis and fouling studies. *Journal of Membrane Science,* 435**,** 52-61.

Lee, W., Ji, R., Gosele, U. & Nielsch, K. 2006. Fast fabrication of long-range ordered porous alumina membranes by hard anodization. *Nature Materials,* 5**,** 741-747.

Lee, W., Schwirn, K., Steinhart, M., Pippel, E., Scholz, R. & Gosele, U. 2008. Structural engineering of nanoporous anodic aluminium oxide by pulse anodization of aluminium. *Nature Nanotechnology,* 3**,** 234-239.

Leitao, D.C., Ventura, J., Sousa, C.T., Teixeira, J.M., Sousa, J.B., Jaafar, M., Asenjo, A., Vazquez, M., De Teresa, J.M. & Araujo, J.P. 2012. Tailoring the physical properties of thin nanohole arrays grown on flat anodic aluminum oxide templates. *Nanotechnology*, 23, 425701-425706.

Leo, C.P. 2008. *Bimodal porous ceramic membrane via nanosized polystyrene templating: Synthesis, characterization and performance evaluation.* PhD, University of Science, Malaysia.

Li, A.P., Muller, F., Birner, A., Nielsch, K. & Gosele, U. 1998a. Hexagonal pore arrays with a 50--420 nm interpore distance formed by self-organization in anodic alumina. *Journal of Applied Physics,* 84**,** 6023-6026.

Li, D. & Wang, H. 2010. Recent developments in reverse osmosis desalination membranes. *Journal of Materials Chemistry,* 20**,** 4551-4566.

Li, F., Zhang, L. & Metzger, R.M. 1998b. On the growth of highly ordered pores in anodized aluminum oxide. *Chemistry of Materials,* 10**,** 2470-2480.

Li, L., Liu, N., McPherson, B. & Lee, R. 2007. Enhanced water permeation of reverse osmosis through mfi-type zeolite membranes with high aluminum contents. *Industrial & Engineering Chemistry Research,* 46**,** 1584-1589.

Lillo, M. & Losic, D. 2009. Pore opening detection for controlled dissolution of barrier oxide layer and fabrication of nanoporous alumina with through-hole morphology. *Journal of Membrane Science,* 327**,** 11-17.

Lim, J.A., Cho, J.H., Jang, Y., Han, J.T. & Cho, K. 2006. Precise control of surface wettability of mixed monolayers using a simple wiping method. *Thin Solid Films,* 515**,** 2079-2084.

Liu, Y., Alwitt, R.S. & Shimizu, K. 2000. Cellular porous anodic alumina grown in neutral organic electrolyte i. Structure, composition, and properties of the films. *Journal of The Electrochemical Society,* 147**,** 1382-1387.

Lohrengel, M.M. 1993. Thin anodic oxide layers on aluminium and other valve metals: High field regime. *Materials Science & Engineering R-Reports,* 11.

Lopez, C.A., Fleischman, A.J., Roy, S. & Desai, T.A. 2006. Evaluation of silicon nanoporous membranes and ecm-based microenvironments on neurosecretory cells. *Biomaterials,* 27**,** 3075-3083.

Losic, D. 2009. Preparation of porous anodic alumina with periodically perforated pores. *Langmuir,* 25**,** 5426-5431.

Lu, Y., Suzuki, T., Zhang, W., Moore, J.S. & Mariñas, B.J. 2007. Nanofiltration membranes based on rigid star amphiphiles. *Chemistry of Materials,* 19**,** 3194-3204.

Lucas, P. & Marchand, A. 1990. Pyrolytic carbon deposition from methane: An analytical approach to the chemical process. *Carbon,* 28**,** 207-219.

Ma, D., Li, S. & Liang, C. 2009. Electropolishing of high-purity aluminium in perchloric acid and ethanol solutions. *Corrosion Science,* 51**,** 713-718.

Majumder, M., Chopra, N., Andrews, R. & Hinds, B.J. 2005. Nanoscale hydrodynamics: Enhanced flow in carbon nanotubes. *Nature,* 438**,** 44.

Malvern 2009. *Zetasizer nano series - user manual*: Malvern Instruments Ltd.

Mardilovich, P.P., Govyadinov, A.N., Mukhurov, N.I., Rzhevskii, A.M. & Paterson, R. 1995. New and modified anodic alumina membranes part I. Thermotreatment of anodic alumina membranes. *Journal of Membrane Science,* 98**,** 131-142.

Marshall, A.D., Munro, P.A. & Trägårdh, G. 1993. The effect of protein fouling in microfiltration and ultrafiltration on permeate flux, protein retention and selectivity: A literature review. *Desalination,* 91**,** 65-108.

Martin, C.R. 1994. Nanomaterials: A membrane-based synthetic approach. *Science,* 266**,** 1961-1966.

Martin, C.R. & Kohli, P. 2003. The emerging field of nanotube biotechnology. *Nature Reviews Drug Discovery,* 2**,** 29-37.

Martínez-Villa, F., Arribas, J.I. & Tejerina, F. 1988. Quantitative microscopic study of surface characteristics of track-etched membranes. *Journal of Membrane Science,* 36**,** 19-30.

Mason, T.G., Wilking, J.N., Meleson, K., Chang, C.B. & Graves, S.M. 2006. Nanoemulsions: Formation, structure, and physical properties. *Journal of Physics: Condensed Matter,* 18**,** R635.

Masuda, H. & Fukuda, K. 1995. Ordered metal nanohole arrays made by a two-step replication of honeycomb structures of anodic alumina. *Science,* 268**,** 1466-1468.

Masuda, H., Hasegwa, F. & Ono, S. 1997. Self-ordering of cell arrangement of anodic porous alumina formed in sulfuric acid solution. *Journal of The Electrochemical Society,* 144**,** L127-L130.

Mata-Zamora, M.E. & Saniger, J.M. 2005. Thermal evolution of porous anodic aluminas: A comparative study. *Revista Mexicana de Física,* 51**,** 502-509.

Matsuura, T. 2001. Progress in membrane science and technology for seawater desalination -- a review. *Desalination,* 134**,** 47-54.

Mattia, D. 2007. *Templated growth and characterization of carbon nanotubes for nanofluidic applications.* PhD, Drexel University, USA.

Mattia, D. & Calabrò, F. 2012. Explaining high flow rate of water in carbon nanotubes via solid–liquid molecular interactions. *Microfluidics and Nanofluidics,* 13**,** 125-130.

Mattia, D., Rossi, M.P., Kim, B.M., Korneva, G., Bau, H.H. & Gogotsi, Y. 2006. Effect of graphitization on the wettability and electrical conductivity of cvd carbon nanotubes and films. *Journal of Physical Chemistry B,* 110**,** 9850 -9855.

McClements, D.J. 2012. Nanoemulsions versus microemulsions: Terminology, differences, and similarities. *Soft Matter,* 8**,** 1719-1729.

Megias-Alguacil, D., Tervoort, E., Cattin, C. & Gauckler, L.J. 2011. Contact angle and adsorption behavior of carboxylic acids on α-Al_2O_3 surfaces. *Journal of Colloid and Interface Science,* 353**,** 512-518.

Mehta, A. & Zydney, A.L. 2005. Permeability and selectivity analysis for ultrafiltration membranes. *Journal of Membrane Science,* 249**,** 245-249.

Meng, G., Jung, Y.J., Cao, A., Vajtai, R. & Ajayan, P.M. 2005. Controlled fabrication of hierarchically branched nanopores, nanotubes, and nanowires. *Proceedings of the National Academy of Sciences of the United States of America,* 102**,** 7074-7078.

Mulder, M. 1996. *Basic principles of membrane technology,* Netherlands: Kluwer Academic.

Mutalib Md Jani, A., Anglin, E.J., McInnes, S.J.P., Losic, D., Shapter, J.G. & Voelcker, N.H. 2009. Nanoporous anodic aluminium oxide membranes with layered surface chemistry. *Chemical Communications,* 0**,** 3062-3064.

Nakao, S.-I. & Kimura, S. 1981. Analysis of solutes rejection in ultrafiltration. *Journal of Chemical Engineering of Japan,* 14**,** 32-37.

Nakashima, T. & Shimizu, M. 1986. Porous glass from calcium alumino boro-silicate glass. *Caramics Japan,* 21**,** 408-412.

Nakashima, T., Shimizu, M. & Kukizaki, M. 2000. Particle control of emulsion by membrane emulsification and its applications. *Advanced Drug Delivery Reviews,* 45**,** 47-56.

Neto, C., Evans, D.R., Bonaccurso, E., Butt, H.-J. & Craig, V.S.J. 2005. Boundary slip in newtonian liquids: A review of experimental studies. *Reports on Progress in Physics,* 68**,** 2859.

Nicholls, W., Borg, M., Lockerby, D. & Reese, J. Water transport through (7,7) carbon nanotubes of different lengths using molecular dynamics. *Microfluidics and Nanofluidics,* 12**,** 257-264.

Nielsch, K., Choi, J., Schwirn, K., Wehrspohn, R.B. & Gösele, U. 2002. Self-ordering regimes of porous alumina: The 10% porosity rule. *Nano Letters,* 2**,** 677-680.

Nielsch, K., Müller, F., Li, A.P. & Gösele, U. 2000. Uniform nickel deposition into ordered alumina pores by pulsed electrodeposition. *Advanced Materials,* 12**,** 582-586.

Nitzan, B. & Margel, S. 1997. Surface modification. Ii. Functionalization of solid surfaces with vinylic monomers. *Journal of Polymer Science Part A: Polymer Chemistry,* 35**,** 171-181.

O'Neill, M.E. 1967. A slow motion of viscous liquid caused by a slowly moving solid sphere: An addendum. *Mathematika,* 14**,** 170-172.

O'Sullivan, J.P. & Wood, G.C. 1970. The morphology and mechanism of formation of porous anodic films on aluminium. *Proceedings of the Royal Society of London. A. Mathematical and Physical Sciences,* 317**,** 511-543.

Offord, D.A. & Griffin, J.H. 1993. Kinetic control in the formation of self-assembled mixed monolayers on planar silica substrates. *Langmuir,* 9**,** 3015-3025.

Ono, S., Saito, M., Ishiguro, M. & Asoh , H. 2004. Controlling factor of self-ordering of anodic porous alumina. *Journal of The Electrochemical Society,* 151**,** B473-B478.

Pappenheimer, J.R., Renkin, E.M. & Borrero, L.M. 1951. Filtration, diffusion and molecular sieving through peripheral capillary membranes; a contribution to the pore theory of capillary permeability. *American Journal of Physiology,* 167**,** 13-46.

Parkhutik, V.P. & Shershulsky, V.I. 1992. Theoretical modelling of porous oxide growth on aluminium. *Journal of Physics D: Applied Physics,* 25**,** 1258.

Pathak, M. 2011. Numerical simulation of membrane emulsification: Effect of flow properties in the transition from dripping to jetting. *Journal of Membrane Science,* 382**,** 166-176.

Peng, S.J. & Williams, R.A. 1998. Controlled production of emulsions using a crossflow membrane: Part I: Droplet formation from a single pore. *Chemical Engineering Research and Design,* 76**,** 894-901.

Peor, N., Sfez, R. & Yitzchaik, S. 2008. Variable density effect of self-assembled polarizable monolayers on the electronic properties of silicon. *Journal of the American Chemical Society,* 130**,** 4158-4165.

Petukhov, D.I., Napolskii, K.S. & Eliseev, A.A. 2012. Permeability of anodic alumina membranes with branched channels. *Nanotechnology,* 23**,** 335601.

Poinern, G.E.J., Ali, N. & Fawcett, D. 2011. Progress in nano-engineered anodic aluminum oxide membrane development. *Materials,* 4**,** 487-526.

Porter, M.C. 1990. *Handbook of industrial membrane technology*. William Andrew Publishing/Noyes.

Pourbaix, M. 1966. *Atlas of electrochemical equilibria in aqueous solutions*: Pergamon Press.

Qin, X., Yuan, Q., Zhao, Y., Xie, S. & Liu, Z. 2011. Measurement of the rate of water translocation through carbon nanotubes. *Nano Letters,* 11**,** 2173-2177.

Rahimi, M.H., Tabaian, S.H., Marashi, S.P.H., Saramad, S., Arab, M. & Hemasian, A. 2012. Heat treatment of aluminum in preparing porous anodic alumina templates. *Micro & Nano Letters, IET,* 7**,** 125-129.

Rayner, M. & Trägårdh, G. 2002. Membrane emulsification modelling: How can we get from characterisation to design? *Desalination,* 145**,** 165-172.

Renkin, E.M. 1954. Filtration, diffusion, and molecular sieving through porous cellulose membranes. *The Journal of General Physiology,* 38**,** 225-243.

Richardson, J.F., Harker, J.H. & Backhurst, J.R. 1997. Coulson and richardson's chemical engineering volume 2 - particle technology and separation processes (5th edition). Elsevier.

Ricker, R.E., Miller, A.E., Yue, D.F., Banerjee, G. & Bandyopadhyay, S. 1996. Nanofabrication of a quantum dot array: Atomic force microscopy of electropolished aluminum. *Journal of Electronic Materials,* 25**,** 1585-1592.

Rossi, M.P., Ye, H., Gogotsi, Y., Babu, S., Ndungu, P. & Bradley, J.-C. 2004. Environmental scanning electron microscopy study of water in carbon nanopipes. *Nano Letters,* 4**,** 989-993.

Sarbolouki, M.N. 1984. Properties of asymmetric polyimide ultrafiltration membranes. I. Pore size and morphology characterization. *Journal of Applied Polymer Science,* 29**,** 743-753.

Sato, N. 1971. A theory for breakdown of anodic oxide films on metals. *Electrochimica Acta,* 16**,** 1683-1692.

Schröder, V., Behrend, O. & Schubert, H. 1998. Effect of dynamic interfacial tension on the emulsification process using microporous, ceramic membranes. *Journal of Colloid and Interface Science,* 202**,** 334-340.

Schröder, V. & Schubert, H. 1999. Production of emulsions using microporous, ceramic membranes. *Colloids and Surfaces A: Physicochemical and Engineering Aspects,* 152**,** 103-109.

Shaban, M., Hamdy, H., Shahin, F., Park, J. & Ryu, S.-W. 2010. Uniform and reproducible barrier layer removal of porous anodic alumina membrane. *Journal of Nanoscience and Nanotechnology,* 10**,** 3380-3384.

Shiyong, Z., Karen, C., Arthur, Y. & Teodor, V. 2007. Preparation of open-through anodized aluminium oxide films with a clean method. *Nanotechnology,* 18**,** 245304.

Siejka, J. & Ortega, C. 1977. An o18 study of field‐assisted pore formation in compact anodic oxide films on aluminum. *Journal of The Electrochemical Society,* 124**,** 883-891.

Simonian, M.H. 2002. Spectrophotometric determination of protein concentration. *Current protocols in food analytical chemistry* John Wiley & Sons, Inc.

Singh, G.K., Golovin, A.A. & Aranson, I.S. 2006. Formation of self-organized nanoscale porous structures in anodic aluminum oxide. *Physical Review B,* 73**,** 205422.

Sinha, S., Rossi, M.P., Mattia, D., Gogotsi, Y. & Bau, H.H. 2007. Induction and measurement of minute flow rates through nanopipes. *Physics of Fluids,* 19**,** 013603.

Spiegler, K.S. & Kedem, O. 1966. Thermodynamics of hyperfiltration (reverse osmosis): Criteria for efficient membranes. *Desalination,* 1**,** 311-326.

Stillwell, M.T., Holdich, R.G., Kosvintsev, S.R., Gasparini, G. & Cumming, I.W. 2007. Stirred cell membrane emulsification and factors influencing dispersion drop size and uniformity. *Industrial & Engineering Chemistry Research,* 46**,** 965-972.

Strathmann, H. 2001. Membrane separation processes: Current relevance and future opportunities. *AIChE Journal,* 47**,** 1077-1087.

Strathmann, H. & Kock, K. 1977. The formation mechanism of phase inversion membranes. *Desalination,* 21**,** 241-255.

Su, Z., Zhou, W., Jiang, F. & Hong, M. 2012. Anodic formation of nanoporous and nanotubular metal oxides. *Journal of Materials Chemistry,* 22**,** 535-544.

Sulka, G.D. 2008. Highly ordered anodic porous alumina formation by self-organized anodizing. *Nanostructured materials in electrochemistry.* Wiley-VCH Verlag GmbH & Co. KGaA.

Sulka, G.D., Stroobants, S., Moshchalkov, V., Borghs, G. & Celis, J.-P. 2002. Synthesis of well-ordered nanopores by anodizing aluminum foils in sulfuric acid. *Journal of The Electrochemical Society,* 149**,** D97-D103.

Thamida, S.K. & Chang, H.-C. 2002. Nanoscale pore formation dynamics during aluminum anodization. *Chaos: An Interdisciplinary Journal of Nonlinear Science,* 12**,** 240-251.

Thomas, J.A. & McGaughey, A.J.H. 2008. Reassessing fast water transport through carbon nanotubes. *Nano Letters,* 8**,** 2788-2793.

Thomas, J.A. & McGaughey, A.J.H. 2009. Water flow in carbon nanotubes: Transition to subcontinuum transport. *Physical Review Letters,* 102**,** 184502.

Thompson, G.E., Furneaux, R.C., Wood, G.C., Richardson, J.A. & Goode, J.S. 1978. Nucleation and growth of porous anodic films on aluminium. *Nature,* 272**,** 433-435.

Thompson, G.E., Xu, Y., Skeldon, P., Shimizu, K., Han, S.H. & Wood, G.C. 1987. Anodic oxidation of aluminium. *Philosophical Magazine Part B,* 55**,** 651 - 667.

van Reis, R. & Zydney, A. 2007. Bioprocess membrane technology. *Journal of Membrane Science,* 297**,** 16-50.

Velleman, L., Triani, G., Evans, P.J., Shapter, J.G. & Losic, D. 2009. Structural and chemical modification of porous alumina membranes. *Microporous and Mesoporous Materials,* 126**,** 87-94.

Verniory, A., Du Bois, R., Decoodt, P., Gassee, J.P. & Lambert, P.P. 1973. Measurement of the permeability of biological membranes application to the glomerular wall. *The Journal of General Physiology,* 62**,** 489-507.

Vladisavljević, G.T., Kobayashi, I., Nakajima, M., Williams, R.A., Shimizu, M. & Nakashima, T. 2007. Shirasu porous glass membrane emulsification: Characterisation of membrane structure by high-resolution x-ray microtomography and microscopic observation of droplet formation in real time. *Journal of Membrane Science,* 302**,** 243-253.

Vladisavljević, G.T. & Williams, R.A. 2005. Recent developments in manufacturing emulsions and particulate products using membranes. *Advances in Colloid and Interface Science,* 113**,** 1-20.

Wagdare, N.A., Marcelis, A.T.M., Ho, O.B., Boom, R.M. & van Rijn, C.J.M. 2010. High throughput vegetable oil-in-water emulsification with a high porosity micro-engineered membrane. *Journal of Membrane Science,* 347**,** 1-7.

Wasserman, S.R., Tao, Y.T. & Whitesides, G.M. 1989. Structure and reactivity of alkylsiloxane monolayers formed by reaction of alkyltrichlorosilanes on silicon substrates. *Langmuir,* 5**,** 1074-1087.

Wedlock, D.J. 1994. *Controlled particle, droplet, and bubble formation*: Butterworth-Heinemann.

Whitby, M., Cagnon, L., Thanou, M. & Quirke, N. 2008. Enhanced fluid flow through nanoscale carbon pipes. *Nano Letters,* 8**,** 2632-2637.

Whitby, M. & Quirke, N. 2007. Fluid flow in carbon nanotubes and nanopipes. *Nature Nanotechnology,* 2**,** 87-94.

Wu, M.T., Leu, I.C. & Hon, M.H. 2002. Effect of polishing pretreatment on the fabrication of ordered nanopore arrays on aluminum foils by anodization. *Journal of Vacuum Science & Technology B: Microelectronics and Nanometer Structures,* 20**,** 776-782.

Xu, C. & Gao, W. 2000. Pilling-bedworth ratio for oxidation of alloys. *Material Research Innovations,* 3**,** 231-235.

Yanagishita, T., Fujimura, R., Nishio, K. & Masuda, H. 2010. Fabrication of monodisperse polymer nanoparticles by membrane emulsification using ordered anodic porous alumina. *Langmuir,* 26**,** 1516-1519.

Yeu, S., Lunn, J.D., Rangel, H.M. & Shantz, D.F. 2009. The effect of surface modifications on protein microfiltration properties of anopore™ membranes. *Journal of Membrane Science,* 327**,** 108-117.

Zaraska, L., Sulka, G. & Jaskuła, M. 2011. Anodic alumina membranes with defined pore diameters and thicknesses obtained by adjusting the anodizing duration and pore opening/widening time. *Journal of Solid State Electrochemistry,* 15**,** 2427-2436.

Zaraska, L., Sulka, G.D., Szeremeta, J. & Jaskula, M. 2010a. Porous anodic alumina formed by anodization of aluminum alloy (aa1050) and high purity aluminum. *Electrochimica Acta,* 55**,** 4377-4386.

Zaraska, L., Sulka, G.D., Szeremeta, J. & Jaskuła, M. 2010b. Porous anodic alumina formed by anodization of aluminum alloy (aa1050) and high purity aluminum. *Electrochimica Acta,* 55**,** 4377-4386.

Zeman, L.J. & Zydney, A.L. 1996. *Microfiltration and ultrafiltration: Principles and applications*: Marcel Dekker Inc.

Zhang, L., Cheng, B., Shi, W. & Samulski, E.T. 2005. In-situ electrochemical synthesis of 1-dimensional alumina nanostructures. *Journal of Materials Chemistry,* 15**,** 4889-4893.

Appendix A: Silicon carbide coating on AAMs by CVD

Other than carbon nanotubes, significant flow enhancement effect in silicon carbide (SiC) nanotubes has also been predicted by MD simulation (Khademi and Sahimi, 2011). However, this is yet to be verified experimentally. During a research collaboration visit to Fraunhofer IKTS, Hermsdorf, Germany, some preliminary synthesis work was conducted as described in the following section.

In the preparation of SiC coated AAMs, a liquid carbosilane precursor was used. A SiC forming CVD precursor, trade name of CVD-4000, was purchased from Starfire Systems Inc. This is primarily composed of $[SiH_2CH_2]_n$ (n = 4 - 8). As can be seen in Figure A1, an alumina boat filled with 2 ml of the carbosilane precursor was placed in the upstream end of the quartz tube. Similar to carbon coating, the membranes were held in a holder and placed in the centre of the furnace (Figure 3.24). Nitrogen (BOC, research grade, 99.99%) was used as the carrier gas at the flow rate of 40 sccm. After flushing the system for approximately 15 minutes, the furnace was heated to the target temperature (between 700 °C to 900 °C) at the rate of 15 °C min^{-1}. The carbosilane precursor evaporated and was carried to the central high temperature zone, where the reaction occurred. After that, the samples were cooled within the quartz tube overnight under a constant flow of nitrogen.

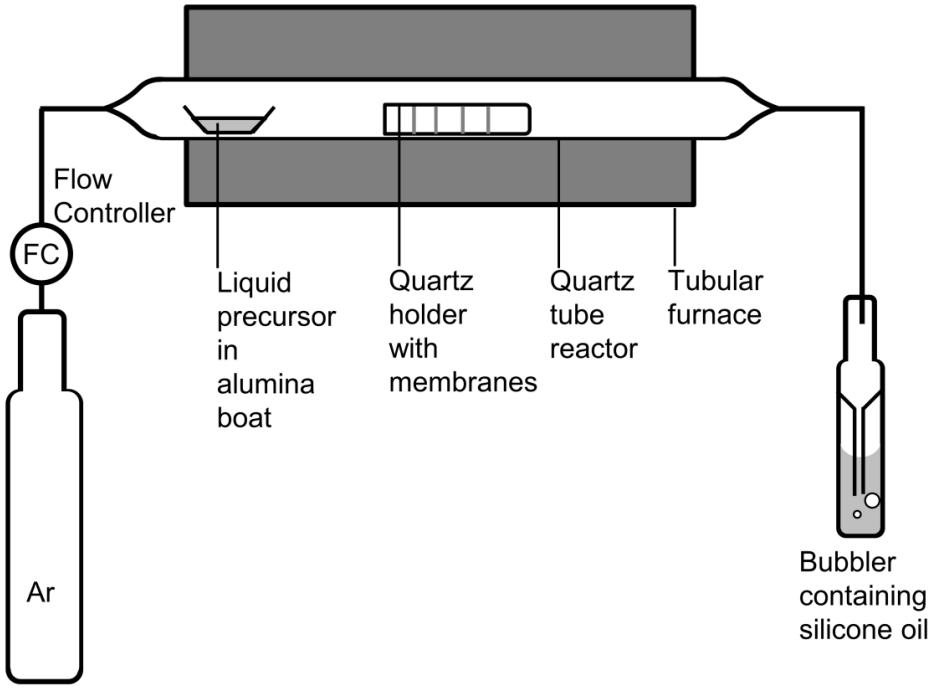

Figure A1. Schematic of the CVD apparatus for deposition of silicon carbide film (Cheng *et al.*, 2005).

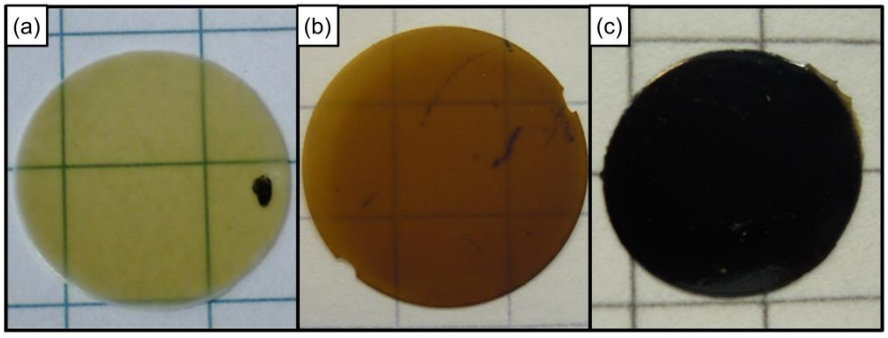

Figure A2. (a) A pristine AAM and, SiC coated AAMs, which CVD was performed at (b) 700 °C and (c) 900 °C.

The coated samples are shown in Figure A2. AAMs within the carbon or silicon carbide membranes can be dissolved by hydrofluoric acid (Cheng *et al.*, 2005) or sodium hydroxide (Martin, 1994) to release the carbon or silicon carbide nanotubes. This was done in this work to verify the coating was homogeneous through the thickness of the AAMs. In short, crushed coated AAMs were immersed in a stirred, 1 M sodium hydroxide solution and heated above 100 °C in refluxing conditions. Nevertheless, the pre-annealing before the CVD process made the alumina templates more crystalline, i.e. more chemically resistant. Therefore, it posed more difficulty to completely remove the alumina templates. Ultra-sonication can significantly speed up the dissolution process. Once the solution cooled down to room temperature, the nanotubes were purified and collected by using a membrane filter under vacuum suction.

Figure A3 illustrates the released SiC nanotubes from the commercial Anodisc templates with 200 nm average diameter. The nanotubes are cylindrical in shape with a relatively short length when compared to the thickness of the Anodisc templates, i.e. 3 to 10 μm compared to 60 μm. The nanotubes were likely broken into shorter lengths by intensive ultrasonication process used to aid the nanotube releasing. To verify the elemental content of the nanotubes, Energy-dispersive X-ray spectroscopy (EDX) was performed (Figure A4). Both samples prepared by CVD at 700 °C and 800 °C show major peaks for silicon and carbon. This confirms that the nanotubes are predominantly silicon carbide. There are also some visible peaks at oxygen and aluminium, which indicate the detection of incomplete removal of Anodisc template during the nanotube releasing process. In particular, as expected the sample prepared at 800 °C has higher aluminium oxide content than the sample prepared at 700 °C. This is attributed to the Anodisc template for the former sample being annealed to a higher temperature, and hence exhibiting a higher order of crystallinity that in turn caused a lower dissolution rate in sodium hydroxide.

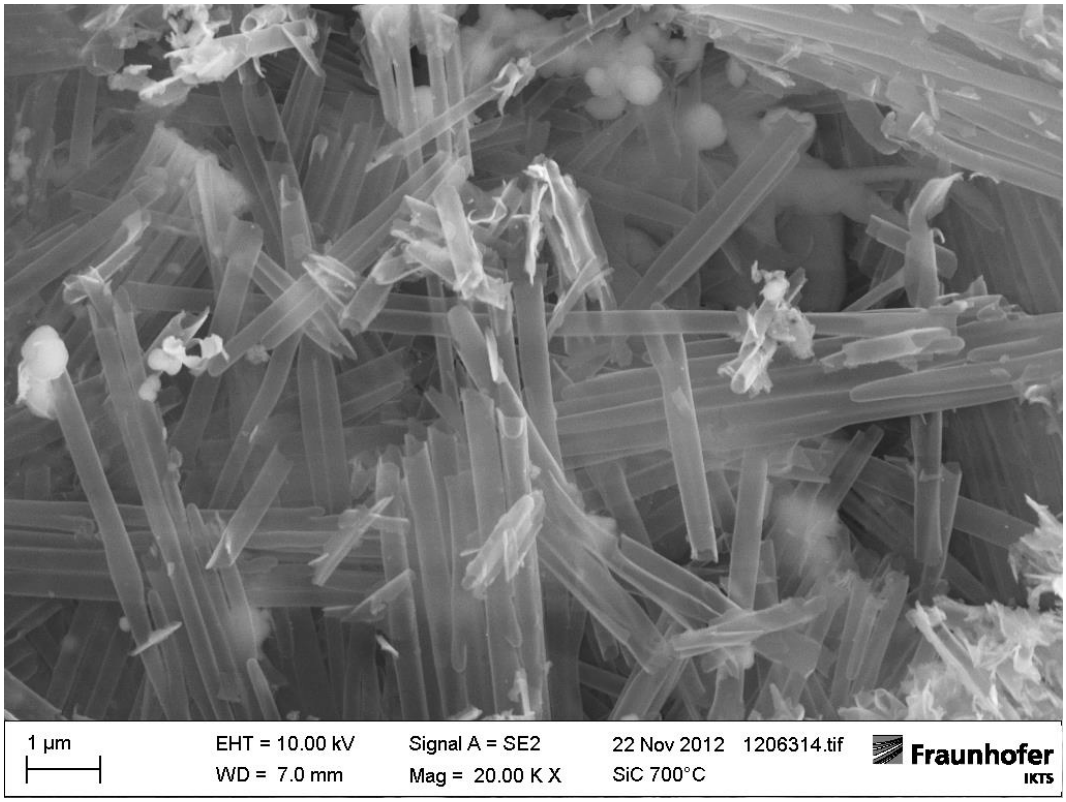

Figure A3. SEM micrographs showing released silicon carbide nanotubes made by CVD coating in Anodisc templates.

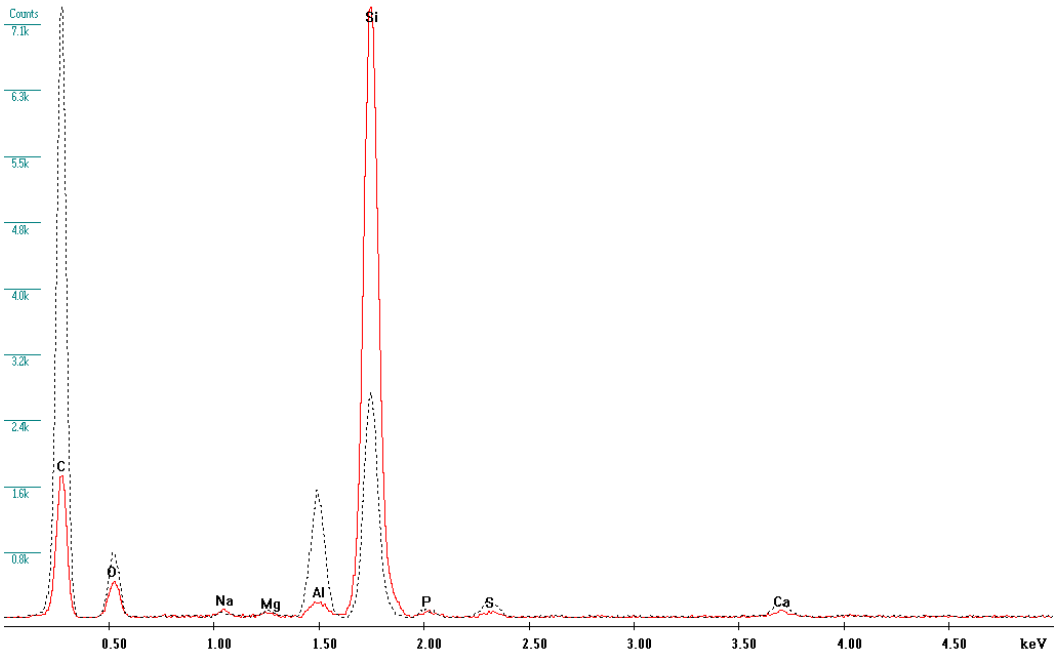

Figure A4. EDX spectra of the released nanotubes. Red line and dotted black line correspond to SiC nanotubes synthesized by CVD at 700 °C and 800 °C, respectively.

Then, SiC coating was performed at 900 °C CVD process using a self-made 50 V AAMs. The AAMs were pre-annealed to just above 900 °C for the process. Consequently, the AAMs were highly crystalline, and posed high difficulty to be dissolved during the nanotube realising process. A long period of treatment in heated sodium hydroxide provides an ideal environment for the formation of silicate by hydrothermal growth. Therefore, as shown in Figure A5, silicate-like structure was obtained. Nevertheless, some non-reacted SiC nanotubes can be observed under the FESEM. The outer diameter of the nanotubes is approximately 60 nm, corresponding to the average pore diameter of a 50 V AAM.

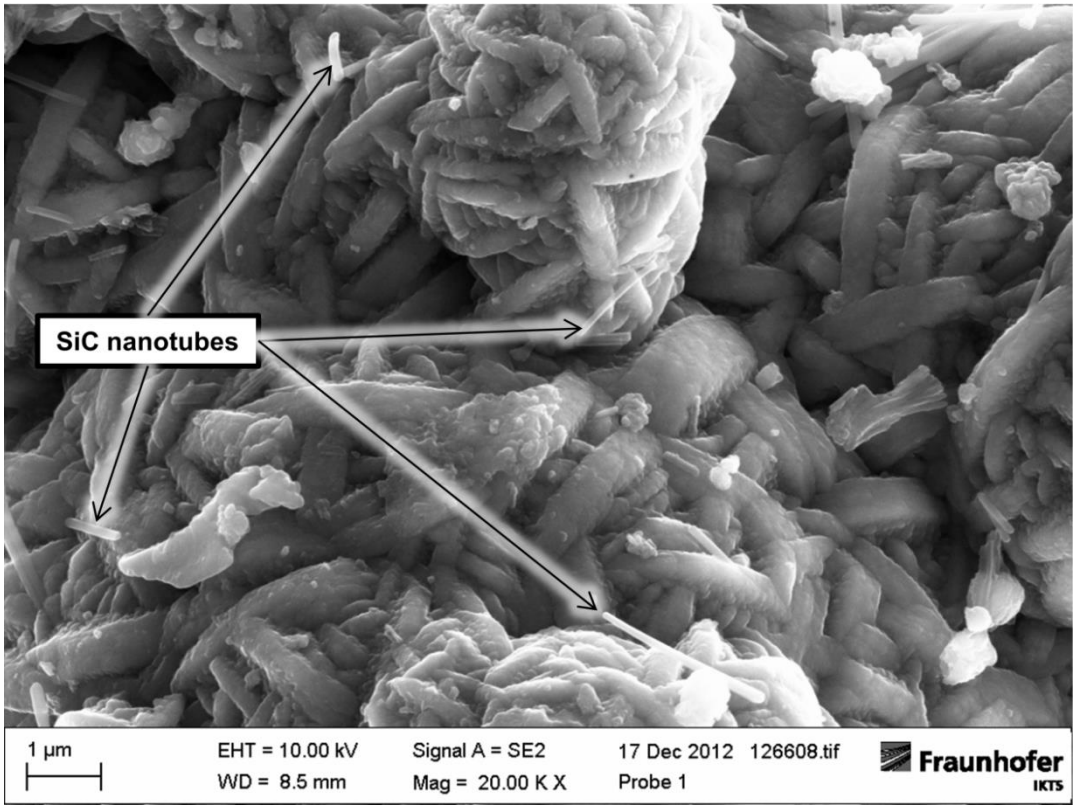

Figure A5. SEM micrographs showing the SiC material was converted into silicates after a long period of treatment in heated sodium hydroxide. Some unreacted SiC nanotubes are still observed.

Therefore, it is believed that the coating of SiC in a 50 V AAM was successful. However, a more controlled nanotube releasing process is needed to prevent the formation of silicates.

Appendix B: Synthesis of tubular AAMs with smaller tube diameter

The fabrication of tubular AAMs in this work marks the first step of scalable production of AAMs. Nevertheless, currently, the anodization has been only performed at the dimension of 5.75 mm (D) x 100 mm (L). It is still too small for applications in the industrial scale. Some preliminary work has been done to fabricate tubular AAMs with smaller tube diameter. This can potentially increase the mechanical strength of the membranes and potentially packed into capillary modular form.

The tubular AAMs with smaller tube diameter were fabricated by following the similar procedures described in Section 3.2. The set-up for anodization was similar, as depicted in Figure 3.14. The starting aluminium alloy tubes have inner and outer diameters of 2.1 mm and 3.0 mm, respectively. Therefore, it is challenging to find a cathode of suitable geometric dimension which position can be fixed and not touching the anode (aluminium alloy tube) during the anodization process. After a number of optimisation process, highly porous alumina hollow fibres were used to shield a stainless steel wire (Figure B1). The presence of the highly porous alumina hollow fibres can prevent the physical contact of the cathode from the anode, which would create a short circuit and prevent the occurrence of anodization. The highly porous nature of the material also has minimal resistant effect for the transport of ions within the electrolyte. This design has been also adapted in electro-polishing pre-treatment to prevent the short circuit during the process.

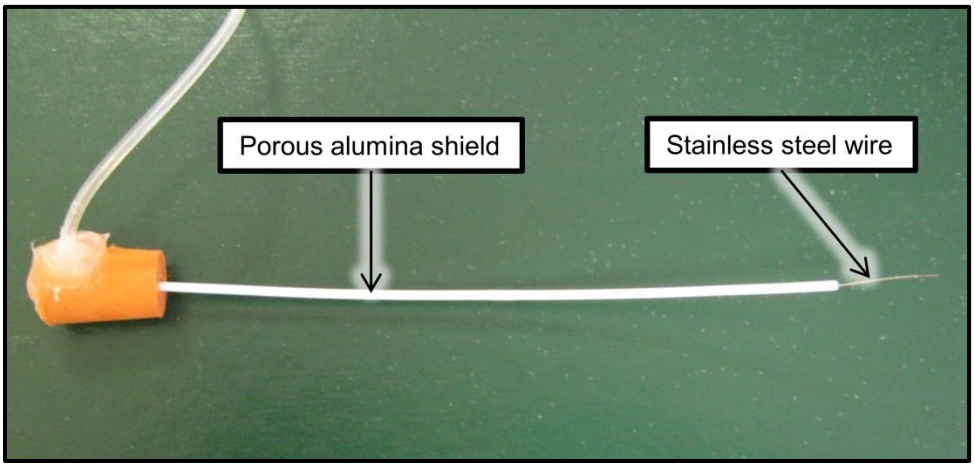

Figure B1. An image showing the cathode (stainless steel wire) shielded by a highly porous alumina hollow fibre.

Figure B2 shows the image of a sample of resulting AAMs with about 2.1 mm tube diameter fabricated at 40 V in oxalic acid. The inhomogeneous colour of the membrane is likely caused by the low quality of the starting material.

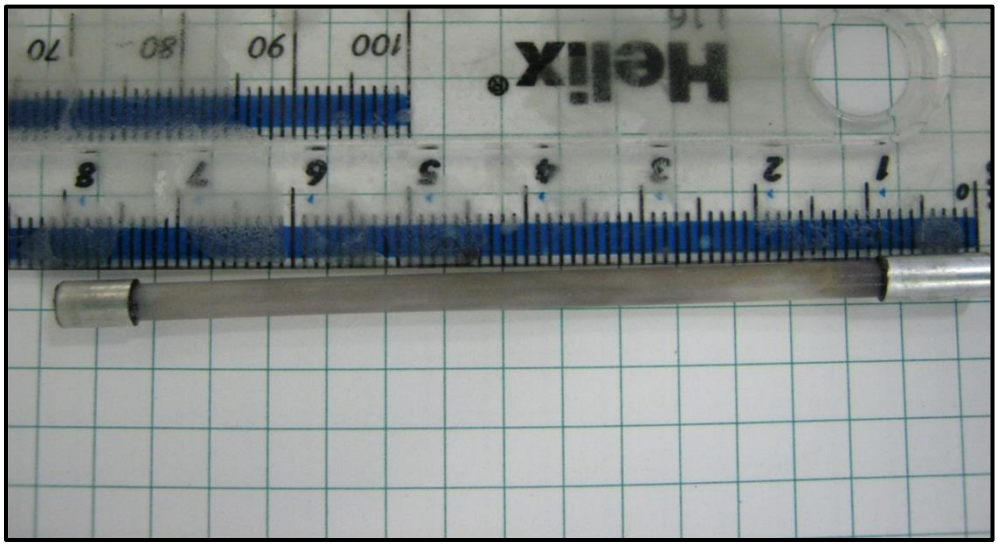

Figure B2. A resulting tubular AAM with 2.1 mm tube diameter.

List of Publications and Presentations

Peer-reviewed journal articles:

Lee, K.P., Arnot, T.C. & Mattia, D. 2011. A review of reverse osmosis membrane materials for desalination--development to date and future potential. *Journal of Membrane Science,* 370**,** 1-22.

Lee, K.P., Leese, H. & Mattia, D. 2012. Water flow enhancement in hydrophilic nanochannels. *Nanoscale,* 4**,** 2621-2627.

Leese, H., Bhurtun, V., **Lee, K.P.** & Mattia, D. 2013. Wetting behaviour of hydrophilic and hydrophobic nanostructured porous anodic alumina. *Colloids and Surfaces A: Physicochemical and Engineering Aspects,* 420**,** 53-58.

Lee, K.P. & Mattia, D. 2013. Monolithic nanoporous alumina membranes for ultrafiltration applications: Characterization, selectivity–permeability analysis and fouling studies. *Journal of Membrane Science,* 435**,** 52-61.

Lee, K.P. & Mattia, D. 2013. Manufacturing of Nano-Emulsions using Nanoporous Anodized Alumina Membranes: Experimental Investigation and Process Modeling. *Industrial & Engineering Research Chemistry* (Manuscript Accepted).

Conference presentations:

Lee, K.P. & Mattia, D. 2012. Tubular nanoporous alumina membranes: Improving ceramic ultrafiltration membranes. Euromembrane – London, UK, September 23rd-27th.

Lee, K.P., Leese, H. & Mattia, D. 2012. Water flow enhancement in hydrophilic nanochannels. 12th International Conference on Inorganic Membranes – Enschede, Netherlands, July 9th-13th.

Lee, K.P. & Mattia, D. 2011. Nanoporous ceramic membranes for water filtration and desalination. SET for Britain 2011 – London, UK, March 14th.

Lee, K.P., Morawska, P.M. & Mattia, D. 2011. Investigation of enhanced fluid transport in nanoporous alumina membranes. International Congress on Membranes and Membrane Processes – Amsterdam, Netherlands, July 23rd-29th.

Lee, K.P., Morawska, P.M. & Mattia, D. 2011. Investigation of enhanced fluid transport in nanoporous alumina membranes. Network Young Membrains 13 – Enschede, Netherlands, July 21st-23rd.

Lee, K.P., Morawska, P.M. & Mattia, D. 2010. Mass transport at the nanoscale. Chemical Engineering Departmental Seminar – University of Nottingham Malaysia Campus, May 29th.